The Biogeochemical Cycling of Particulate Trace Metals off the Southwest African and Peruvian Shelves

Dissertation

zur Erlangung des akademischen Grades eines
Doktors der Naturwissenschaften

– Dr. rer. nat –

an der Mathematisch-Naturwissenschaftlichen Fakultät
der Christian-Albrechts-Universität zu Kiel

vorgelegt von

Ali A. Al-Hashem

Kiel, 2023

Erstgutachter: **Prof. Dr. Eric P. Achterberg**

Zweitgutachterin: **Prof. Dr. Martin Frank**

Tag der mündlichen Prüfung: **10th August 2023**

Abstract

Marine particles in the ocean play an important role in various biogeochemical processes, such as nutrient cycling and primary productivity. While significant progress has been made in recent decades, our understanding of the marine biogeochemical cycling of trace metals remains incomplete. Additionally, particulate trace metal (pTM) datasets from key dynamic regions of the global ocean, such as continental shelves, upwelling sites, and oxygen minimum zones, are lacking, impeding progress toward fully understanding the processes which impact pTM cycling and distributions. To constrain the controls on the broader cycling of TMs in the marine environment and to predict the impact of environmental perturbations on marine ecosystems and global biogeochemical cycles, it is crucial to gather more comprehensive data on pTM distributions across a variety of oceanic regimes. In particular, studies on continental shelves, upwelling zones, and oxygen minimum zones are needed to provide insight into the dynamic processes in these areas that can significantly influence global TM cycling. In such regions, factors such as changes in redox conditions, primary production, biomineralization processes, and different particulate sources can have profound effects on pTM speciation, transformation, and distribution. Furthermore, incorporating the analysis of both labile (L-pTM) and refractory (R-pTM) particulate trace metal fractions will permit a more nuanced understanding of the processes controlling the bioavailability and residence times of these trace metals. This knowledge, in turn, will allow us to better predict how shifts in these processes due to environmental perturbations might affect marine ecosystems and global biogeochemical cycles.

To that end, this thesis focuses on studying the biogeochemical cycling of 17 particulate trace metals (pTMs), including iron (Fe), manganese (Mn), cobalt (Co), aluminum (Al), copper (Cu), nickel (Ni), zinc (Zn), cadmium (Cd), lead (Pb), titanium (Ti), vanadium (V), and particulate phosphorus (P) on the Southwest African and Peruvian shelves, employing a chemical leach to marine particles that were collected on two separate research expeditions. The distributions and biogeochemical cycling of biogeochemical tracers, molybdenum (Mo), barium (Ba), chromium (Cr), tungsten (W), thorium (Th), and uranium (U) are explored only on the Southwest African shelf. The transects from these sites traversed through contrasting biogeochemical regimes with

diverse particle sources, including the Benguela and Humboldt upwelling regions, oxygen minimum zones, and the Congo River plume, offering unique gradients under which particulate trace metal cycling can be studied. The chemical leaching technique allows for differentiation between labile and refractory pTM fractions, providing a more accurate assessment of the biogeochemical behavior and fate of pTMs within the different marine environments. Elemental ratios and particle type proxies were also utilized to determine redox and scavenging processes, and biological uptake of trace metals in the water column. This approach allowed for the identification of the principal carrier phases of pTMs, which is a critical step toward constraining the biogeochemical mechanisms that control their fate and interactions with dissolved phases in the water column.

The elements were broadly categorized into 3 main groups within the discussions of the studies based on shared biogeochemical behaviors and patterns, namely, bio-essential type elements (Zn, Cu, Ni, Cd, Co, and V), lithogenic type elements (Fe, Al, and Ti), and scavenged elements (Pb, Al, Fe, Mn, Cu, and V), with labile Fe and Mn oxides receiving special attention as well. The distributions and biogeochemical cycling of particulate Fe, Mn, Co, Al, Cu, Ni, Zn, Cd, Pb, Ti, and P on the Southwest African and Peruvian shelves are explored and discussed in chapters 3 and 4, respectively. The distributions and biogeochemical cycling of the biogeochemical tracers Mo, Ba, Cr, W, Th, and U on the Southwest African shelf are discussed in chapter 5, for which datasets in the marine environment are severely lacking.

Bio-essential type pTMs (Zn, Cu, Ni, Cd, Co, and V) in surface waters, were ascribed primarily to biogenic particles and were mostly labile (>50%), with some instances of enhanced lithogenic or adsorbed fractions where considerable nepheloid or riverine inputs were apparent. Although, a substantial fraction of biogenic pP was refractory in the productive Benguela upwelling region on the Southwest African shelf, which was not observed in the Humboldt upwelling region off the Peruvian shelf, attributed to possible variations in bulk phytoplankton community compositions. Nepheloid (lithogenic) particles regularly occupied (near-)bottom waters and comprised large fractions of the pTM pools for Al, Ti, Fe, Pb, and V, and often included substantial fractions of labile Fe and Mn oxides and enhanced adsorbed pTM phases. However, within the OMZ, Fe and Mn oxide distributions were apparently decoupled, whereby Fe oxides persisted, and some

instances enhanced, and Mn oxides were depleted. The decoupled distributions were attributed to the faster redox kinetics of Fe which permitted its oxidative precipitation and persistence, compared to Mn oxides which were kept reductively dissolved in the OMZs of both regions due to slower oxidation kinetics. Particulate W and Th were mostly comprised of refractory phases (>90% R-pTM/T-pTM) and predominantly associated with lithogenic material across all biogeochemical settings over the Southwest African shelf. Particulate Ba distributions were primarily associated with barite minerals, though with higher average labile fraction in deep open ocean stations (70.6±11.9% L-pBa/T-pBa), compared to shallow shelf-adjacent stations (48.7±16.5% L-pBa/T-pBa). Particulate U and Mo were largely associated with biogenic particles and exhibited enhanced refractory fractions in the productive Benguela upwelling region. Particulate Cr was seemingly comprised of absorbed phases and enhanced in association with biogenic particles in surface waters of shelf stations and with resuspended benthic nepheloid particles in bottom waters. Although, lithogenic particles from riverine sources apparently dominated the pCr pool in the Congo River plume stations.

This work contributes a valuable set of regional insights into the biogeochemical cycling of particulate trace metals in the Southwest African and Peruvian shelves that can be extended to other regions of the global ocean. The findings presented in this dissertation have far-reaching implications for elucidating the factors that control the distribution and speciation of pTMs and their role in the marine ecosystem. Furthermore, this work has the potential to inform the development of enhanced predictive models of TM biogeochemistry, and to contribute to a better understanding of the complex interaction between dissolved and particulate TMs, and helps advance our insights and knowledge of the global biogeochemical cycling of pTMs.

Zusammenfassung

Marine Partikel im Ozean spielen eine wichtige Rolle bei verschiedenen biogeochemischen Prozessen, wie dem Nährstoffkreislauf und der Primärproduktivität. Obwohl in den letzten Jahrzehnten erhebliche Fortschritte erzielt wurden, ist unser Verständnis des biogeochemischen Kreislaufs von Spurenmetallen im Meer nach wie vor unvollständig. Darüber hinaus fehlen Daten über partikuläre Spurenmetalle (pTM) aus dynamischen Schlüsselregionen des globalen Ozeans, wie z.B. Kontinentalschelfe, Auftriebsgebiete und Sauerstoffminimumzonen, was ein vollständiges Verständnis der Prozesse, die den Kreislauf und die Verteilung von pTM beeinflussen, erschwert. Um die Steuerung des breiteren Kreislaufs von TMs in der Meeresumwelt besser zu verstehen und die Auswirkungen von Umweltstörungen auf die marinen Ökosysteme und die globalen biogeochemischen Kreisläufe vorherzusagen, ist es von entscheidender Bedeutung, umfassendere Daten über die Verteilung von pTMs in einer Vielzahl von Ozeanregimen zu sammeln. Insbesondere Studien über Kontinentalschelfe, Auftriebsgebiete und Sauerstoffminimumzonen sind erforderlich, um einen Einblick in die dynamischen Prozesse in diesen Gebieten zu erhalten, die den globalen TM-Kreislauf erheblich beeinflussen können. In solchen Regionen können Faktoren wie Veränderungen der Redoxbedingungen, der Primärproduktion, Biomineralisierungsprozesse und verschiedene Partikelquellen tiefgreifende Auswirkungen auf die Speziation, Umwandlung und Verteilung von pTM haben. Darüber hinaus wird die Einbeziehung der Analyse sowohl der labilen (L-pTM) als auch der refraktären (R-pTM) partikulären Spurenmetallfraktionen ein differenzierteres Verständnis der Prozesse ermöglichen, die die Bioverfügbarkeit und Verweildauer dieser Spurenmetalle steuern. Dieses Wissen wird es uns wiederum ermöglichen, besser vorherzusagen, wie sich Verschiebungen in diesen Prozessen aufgrund von Umweltstörungen auf marine Ökosysteme und globale biogeochemische Kreisläufe auswirken könnten.

Zu diesem Zweck konzentriert sich diese Arbeit auf die Untersuchung des biogeochemischen Kreislaufs von 17 partikulären Spurenmetallen (pTMs), einschließlich Eisen (Fe), Mangan (Mn), Kobalt (Co), Aluminium (Al), Kupfer (Cu), Nickel (Ni), Zink (Zn), Cadmium (Cd), Blei (Pb), Titan

(Ti), Vanadium (V) und partikelförmigem Phosphor (P) auf dem südwestafrikanischen und peruanischen Schelf mit Hilfe einer chemischen Auslaugung von Meerespartikeln, die auf zwei separaten Forschungsexpeditionen gesammelt wurden. Die Verteilung und der biogeochemische Kreislauf der biogeochemischen Tracer Molybdän (Mo), Barium (Ba), Chrom (Cr), Wolfram (W), Thorium (Th) und Uran (U) werden nur auf dem südwestafrikanischen Schelf untersucht. Die Transekte dieser Standorte führten durch kontrastreiche biogeochemische Systeme mit unterschiedlichen Partikelquellen, darunter die Benguela- und Humboldt-Auftriebsgebiete, Sauerstoffminimumzonen und die Kongo-Flussströmung, die einzigartige Gradienten bieten, unter denen der Kreislauf der partikulären Spurenmetalle untersucht werden kann. Die chemische Auslaugungstechnik ermöglicht die Unterscheidung zwischen labilen und refraktären pTM-Fraktionen, was eine genauere Bewertung des biogeochemischen Verhaltens und des Verbleibs von pTMs in den verschiedenen Meeresumgebungen ermöglicht. Elementverhältnisse und Partikeltyp-Proxys wurden auch verwendet, um Redox- und Scavengingprozesse (Enfternung aus der Wassersäule durch Sorption an Partikeln und Absetzen dieser Partikel) sowie die biologische Aufnahme von Spurenmetallen in der Wassersäule zu bestimmen. Dieser Ansatz ermöglichte die Identifizierung der wichtigsten Trägerphasen von pTMs, was ein entscheidender Schritt zur Eingrenzung der biogeochemischen Mechanismen ist, die ihr Schicksal und ihre Wechselwirkungen mit gelösten Phasen in der Wassersäule steuern.

Die Elemente wurden in den Diskussionen über die Studien auf der Grundlage gemeinsamer biogeochemischer Verhaltensweisen und Muster grob in drei Hauptgruppen eingeteilt, nämlich in bioessentielle Elemente (Zn, Cu, Ni, Cd, Co und V), lithogene Elemente (Fe, Al und Ti) und von Scavengingprozessen beeinflusste Elemente (Pb, Al, Fe, Mn, Cu und V), wobei auch labilen Fe- und Mn-Oxiden besondere Aufmerksamkeit zuteil wurde. Die Verteilung und der biogeochemische Kreislauf von Fe-, Mn-, Co-, Al-, Cu-, Ni-, Zn-, Cd-, Pb-, Ti- und P-Partikeln auf dem südwestafrikanischen und peruanischen Schelf werden in den Kapiteln 3 und 4 untersucht und diskutiert. Die Verteilung und der biogeochemische Kreislauf der biogeochemischen Tracer Mo, Ba, Cr, W, Th und U auf dem südwestafrikanischen Schelf, für die es in der Meeresumwelt nur wenige Daten gibt, werden in Kapitel 5 erörtert.

Bioessentielle pTMs (Zn, Cu, Ni, Cd, Co und V) in Oberflächengewässern wurden in erster Linie biogenen Partikeln zugeschrieben und waren größtenteils labil (>50 %), mit einigen Fällen erhöhter lithogener oder adsorbierter Fraktionen, in denen beträchtliche nepheloide oder Einträge aus Flüssen offensichtlich waren. Im produktiven Benguela-Auftriebsgebiet auf dem südwestafrikanischen Schelf war ein erheblicher Teil des biogenen pP refraktär, was im Humboldt-Auftriebsgebiet vor dem peruanischen Schelf nicht beobachtet wurde, was auf mögliche Unterschiede in der Zusammensetzung der Phytoplankton-Gemeinschaft zurückzuführen ist. Nepheloide (lithogene) Partikel besetzten regelmäßig das (bodennahe) Wasser und machten große Anteile der pTM-Pools für Al, Ti, Fe, Pb und V aus und enthielten oft erhebliche Anteile an labilen Fe- und Mn-Oxiden und verstärkte adsorbierte pTM-Phasen. Innerhalb der OMZ waren die Verteilungen von Fe- und Mn-Oxiden jedoch offenbar entkoppelt, wobei Fe-Oxide bestehen blieben und in einigen Fällen verstärkt auftraten, während Mn-Oxide verarmt waren. Die entkoppelten Verteilungen wurden auf die schnellere Redoxkinetik von Fe zurückgeführt, die seine oxidative Ausfällung und Persistenz ermöglichte, im Gegensatz zu Mn-Oxiden, die aufgrund einer langsameren Oxidationskinetik in den OMZ beider Regionen reduktiv aufgelöst blieben. Partikuläres W und Th bestanden größtenteils aus refraktären Phasen (>90 % R-pTM/T-pTM) und waren in allen biogeochemischen Zonen auf dem südwestafrikanischen Schelf überwiegend mit lithogenem Material verbunden. Die Verteilung von partikulärem Ba war in erster Linie mit Barytmineralien assoziiert, wenn auch mit einem höheren durchschnittlichen labilen Anteil in tiefen Stationen im offenen Ozean (70,6±11,9% L-pBa/T-pBa) im Vergleich zu flachen, an den Schelf angrenzenden Stationen (48,7±16,5% L-pBa/T-pBa). Partikuläres U und Mo waren größtenteils mit biogenen Partikeln assoziiert und wiesen in der produktiven Benguela-Auftriebsregion einen erhöhten Anteil an refraktären Bestandteilen auf. Partikuläres Cr bestand offenbar aus absorbierten Phasen und war in Verbindung mit biogenen Partikeln im Oberflächenwasser der Schelfstationen und mit resuspendierten benthischen nepheloiden Partikeln im Bodenwasser verstärkt vorhanden. Allerdings dominierten lithogene Partikel aus Flussquellen offenbar den pCr-Pool in den Stationen der Kongo-Fahne.

Diese Arbeit liefert wertvolle regionale Einblicke in den biogeochemischen Kreislauf von partikulären Spurenmetallen im südwestafrikanischen und peruanischen Schelf, die sich auf andere Regionen des globalen Ozeans übertragen lassen. Die in dieser Dissertation vorgestellten Ergebnisse haben weitreichende Auswirkungen auf die Klärung der Faktoren, die die Verteilung und Speziation von pTMs und ihre Rolle im marinen Ökosystem steuern. Darüber hinaus hat diese Arbeit das Potenzial, die Entwicklung verbesserter Vorhersagemodelle für die Biogeochemie von TMs zu unterstützen und zu einem besseren Verständnis der komplexen Interaktion zwischen gelösten und partikulären TMs beizutragen und unsere Erkenntnisse und unser Wissen über den globalen biogeochemischen Kreislauf von pTMs zu erweitern.

Acknowledgements

I would like to express my deepest gratitude and appreciation to everyone who supported me to the successful completion of this PhD thesis. First and foremost, I would like to thank my PhD supervisor, Eric Achterberg, for his unwavering support, guidance, and mentorship throughout this journey. Your expertise, patience, and encouragement have been invaluable, and I am truly grateful for the opportunity to learn and grow under your tutelage. I would also like to thank my co-supervisor, Aaron Beck, for his assistance during the course of my research.

I would like to acknowledge the support of Kuwait Institute for Scientific Research, whose financial assistance made this research possible. I am truly grateful for the opportunities and resources provided during my time as a PhD candidate. I would also like to acknowledge the administrative support received from the Kuwait Cultural Office, the Kuwait Health Office, and the Kuwait Embassy throughout my PhD candidacy, and particularly for facilitating logistical support during the periods of extended Covid lockdowns.

I am deeply indebted to my fellow colleagues and researchers, especially Tim Steffens, Stephan Krish, Tom Browning, Mark Hopwood, Kechen Zhu, Mahmoud Altahan, Peter Rowland, and Martha Gledhill, for their camaraderie, stimulating discussions, and assistance during this journey. Your friendship and support have made my experience as a PhD candidate a memorable and enriching one.

I would also like to thank the administrative and technical staff at GEOMAR for their help in ensuring a conducive research environment. A special mention goes to Dominik Jasinski, André Mutzberg, and Birgit Reiner for their invaluable assistance and support throughout my research.

My deepest gratitude goes to my family, especially my parents and brothers, for their unwavering love, support, and encouragement. Your belief in me and my abilities has been the driving force behind my pursuit of this degree. I am also grateful to my wife, Mariam, and daughters, Batool and Sarah, for their understanding, patience, and unwavering love throughout this journey.

Lastly, I would like to thank my close friends, Mohammed Ali, Ali Al-Ali, and Turki Al-Said, for their support, encouragement, and for providing much-needed moments of levity during the most challenging times.

I am grateful to all who have contributed to the success of this PhD thesis in their unique ways. This accomplishment would not have been possible without the collective effort and support of all those mentioned here and many others who have touched my life during this journey.

Contents

List of Figures

Supplementary Figures

List of Tables

Supplementary Tables

List of Abbreviations

AABW	Antarctic Bottom Water
AAIW	Antarctic Intermediate Water
ABF	Angola-Benguela Front
AF	Angola Front
Al	Aluminum
Ba	Barium
BAT	Beam Attenuation
BDL	Below Detection Limit
BUS	Benguela Upwelling System
Cd	Cadmium
Co	Cobalt
Cr	Chromium
CRM	Certified Reference Material
Cu	Copper
dTMs	Dissolved Trace Metals
EBUS	Eastern Boundary Upwelling System
ETSP	Eastern Tropical South Pacific
Fe	Iron
FEP	Fluorinated Ethylene Propylene
H_2O_2	Hydrogen Peroxide
HCl	Hydrochloric Acid
HF	Hydrofluoric Acid
HNLC	High Nutrient Low Chlorophyll
HNO_3	Nitric Acid
ICP-MS	Inductively Coupled Plasma Mass Spectrometry
In	Indium
LDPE	Low Density Polyethylene
L-pTMs	Labile Particulate Trace Metals
Mn	Manganese
Mo	Molybdenum
NADW	North Atlantic Deep Water
Ni	Nickel
NO_2^-	Nitrite
NO_3^-	Nitrate
OMZ	Oxygen Minimum Zone

P	Phosphorus
Pb	Lead
PCA	Principal Component Analysis
PES	Polyethersulfone
PFA	Perfluoroalkoxy
PO_4^{3-}	Phosphate
PPE	Personal Protective Equipment
pTMs	Particulate Trace Metals
Re	Rhenium
R-pTMs	Refractory Particulate Trace Metals
RSD	Relative Standard Deviation
RV	Research Vessel
SACW	South Atlantic Central Water
SD	Standard Deviation
SECC	South Equatorial Counter Current
$Si(OH)_4$	Silicic Acid
ST	Station
STUW	Subtropical Underwater
TE	Trace Element
Th	Thorium
Ti	Titanium
TMs	Trace Metals
T-pTMs	Total Particulate Trace Metals
TSW	Tropical Surface Water
U	Uranium
UCC	Upper Continental Crust
UCDW	Upper Circumpolar Deep Water
V	Vanadium
W	Tungsten
Zn	Zinc
BENG	Benguela (Southwest African) Shelf Region
NORTH	Northern (Southwest African) Shelf Region

Chapter 1: Introduction

1.1 Trace Metals in Seawater

Trace metals (TMs) are metallic elements that are present in seawater at very low concentrations, often below concentrations of ~ 10^{-6} mol kg^{-1} (µM), extending several orders of magnitude to less than 10^{-15} mol kg^{-1} (fM) (Bruland et al., 2014; Bruland & Lohan, 2003; Nozaki, 1997). Despite their low concentrations, several TMs, such as iron (Fe), manganese (Mn), zinc (Zn), cobalt (Co), copper (Cu), cadmium (Cd), nickel (Ni), and vanadium (V), play essential roles in the structure and metabolism of marine organisms (see section 1.2.1), and therefore act as critical regulators of biogeochemical cycles of carbon, nitrogen, and phosphorus (P). Other TMs include pollutants (e.g., lead (Pb)), or are used as tracers to identify TM sources, sinks, or contaminants, as well as specific biogeochemical processes in the modern or paleo-ocean (see sections 1.2 and 5.1). The biogeochemical cycling of trace metals in the marine environment is complex and influenced by a range of frequently interconnected physical, chemical, and biological processes. Marine particles participate in the cycling of most TMs in the ocean, however, the mechanisms which govern solid-solution interactions under different biogeochemical regimes are not fully understood (Charette et al., 2016; Horner et al., 2021; Jeandel et al., 2015; Tagliabue et al., 2016).

The TMs in seawater exist in a size continuum and are operationally defined depending on the method used to separate them (Stemmann & Boss, 2012). Following filtration, marine particles are retained on a filter membrane, typically > 0.2 – 0.45 µm (Figure 1.1), while phases that pass through the membrane are typically referred to as the dissolved fraction (dTMs). Notably, colloidal phases can encompass both dissolved and particulate fractions and are susceptible to exchanges between both fractions depending on marine environmental conditions and (dis-)aggregation dynamics (Burd & Jackson, 2009). Physical processes, such as upwelling, advection, mixing, and particle settling (Burd & Jackson, 2009; Lam et al., 2011; Lam & Bishop, 2008; Liu et al., 2022), contribute substantially to the spatial distribution and transformations of TMs throughout the water column. Biogeochemical processes, such as scavenging (also termed adsorption), precipitation, complexation, redox transformations, and biological uptake and

remineralization, further influence these distributions (Boyd et al., 2010; Gledhill & Buck, 2012; Goldberg, 1954; Jeandel et al., 2015; Sunda, 2012; Vedamati et al., 2014). The source, composition, and abundance of particles, and the biogeochemical environment, also dictate the nature of the interactions between dissolved and particulate phases (e.g. Barrett et al., 2018; Dymond et al., 1997; Honeyman et al., 1988; Scholz et al., 2011; Sherrell & Boyle, 1992; Wuttig et al., 2013).

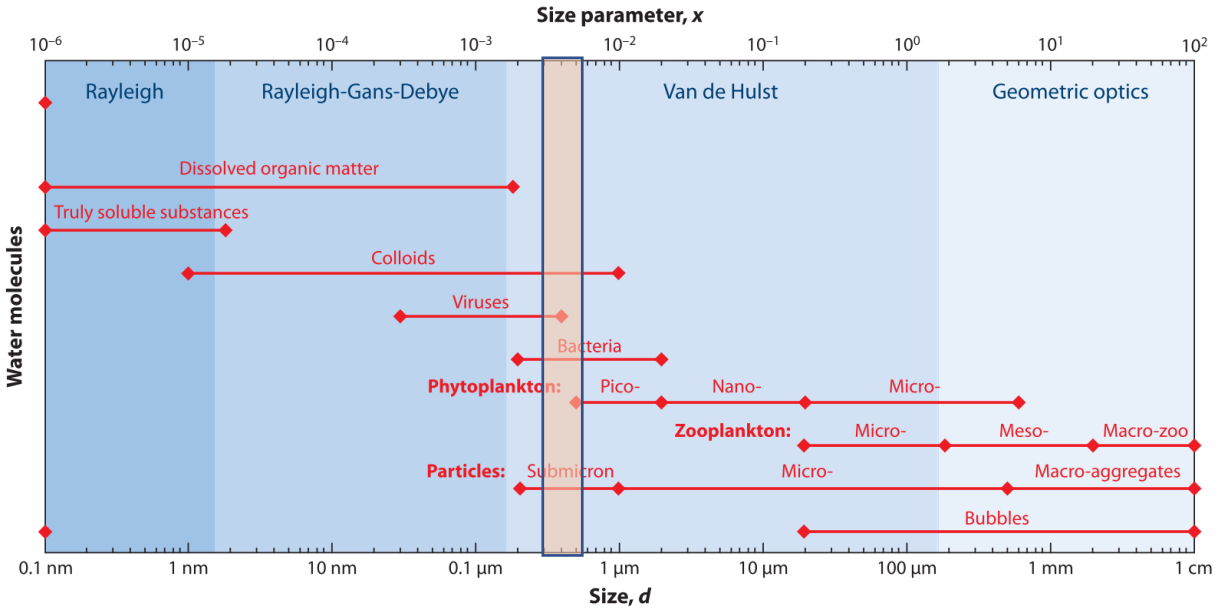

Figure 1.1 – Representative Sizes of Different Constituents in Seawater. The Yellow Box Depicts the Typical Filter Membrane Size Ranges Used to Separate Particulate Trace Metals from Dissolved Trace Metal Phases (0.2-0.45 µm). Note the logarithmic scales. Figure adapted from Stemmann & Boss (2012).

An international program called GEOTRACES was established with the goal of improving our understanding of the distribution, sources, sinks of trace elements and their isotopes in major interfaces of the ocean, as well as their internal biogeochemical cycling processes on a global scale (Figure 1.2) (Anderson, 2020; SCOR Working Group, 2006). This initiative involves a series of international research section cruises carried out in diverse regions of the global ocean, organized by various nations and research groups. The program further includes the development of standard methods and protocols, as well as intercalibrations for trace element measurements in both dissolved and particulate fractions (Cutter et al., 2014, 2017; Morton et

al., 2013; Planquette & Sherrell, 2012; Twining et al., 2015). These expeditions involve meticulous collection of water samples from various depths using state-of-the-art clean handling and analytical techniques. Together with the advancements in analytical technologies with enhanced sensitivity and detection limits, the efforts carried out under the scope of the GEOTRACES program pave the way for novel insights to accurately quantify and understand the biogeochemical cycling of TMs in the ocean and their influence on global climate dynamics.

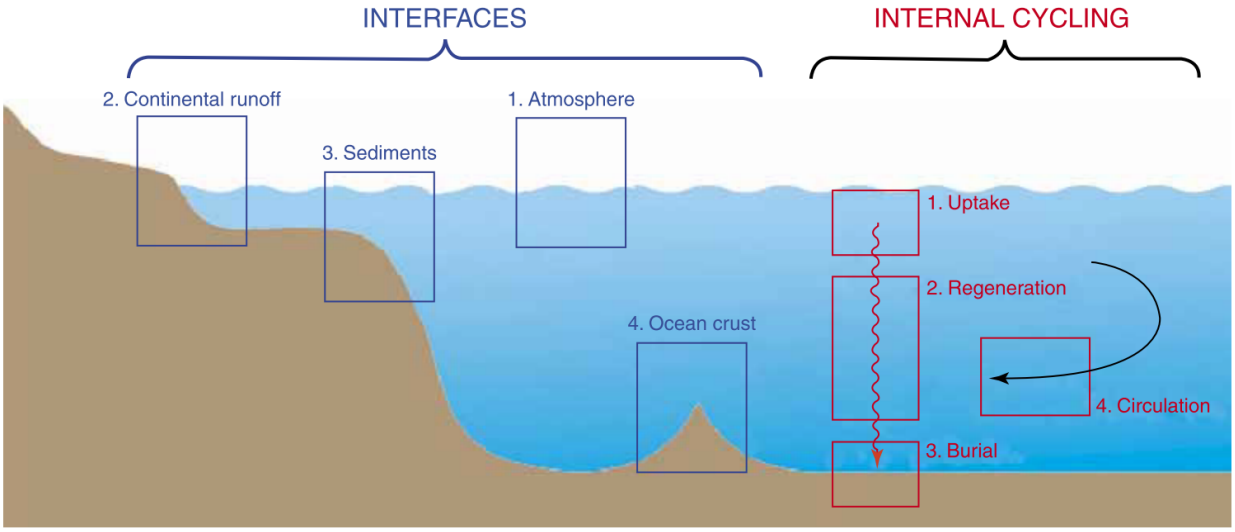

Figure 1.2 – Diagram Illustrating the Major Influences on Trace Metals in the Ocean. Four Major Ocean Interfaces (blue) and Four Major Internal Processes (red) are Responsible for Ocean Trace Metal Patterns. Source: *GEOTRACES Science Plan, SCOR Working Group (2006).*

1.2 Marine Particles: Sources, Composition and Cycling

Marine particles play a critical role in the distribution of most TMs in the marine environment by serving as sources or sinks of TMs throughout the water column via biological incorporation and remineralization, precipitation/dissolution, or sorption. The diverse nature of particles, which vary in their size, origin, composition, and residence time, influence their interactions with TMs in seawater. Marine particles consist of biogenic and abiogenic phases, with internal or external sources. External sources of particles include atmospheric deposition (aerosols), sediment resuspension, riverine particles, hydrothermal vents, ice-rafted debris and volcanoes (Achterberg et al., 2018, 2021; Hunt et al., 2022; Liao & Ho, 2018; Menzel-Barraqueta

et al., 2018). Internal particle sources include bio-assimilation of TMs by primary producers, authigenic precipitation, or scavenging of TMs onto particle surfaces (Boyd et al., 2017; Close et al., 2021; Jeandel et al., 2015; Lam et al., 2015; Lam & Marchal, 2014; Lee et al., 2018). Understanding the intricacies of the interactions between different TMs with particles provides valuable insights into the biogeochemical cycling of TMs around the global ocean.

The TM composition of particles can provide valuable clues about their sources and the mechanisms that introduce or generate the particles, as well as their role in TM biogeochemical cycles through their use as biogeochemical or particle source proxies. Additionally, multivariate statistical tools, such as principal component analysis (Liao & Ho, 2018; Marsay & Achterberg, 2021; Ohnemus & Lam, 2015), or factor analysis (Ohnemus et al., 2019) have been used as effective supplemental tools providing valuable insights into identifying particle associations and biogeochemical cycling processes of TMs. The pTMs associated with particles can broadly be grouped into four main categories (bio-essential, lithogenic, authigenic, and scavenged phases) depending on their origin and behavior within the marine environment.

1.2.1 Biogenic Particles

Biogenic particles are primarily formed through primary production in the surface ocean and include organic matter, skeletal materials of organisms, fecal pellets, and detritus (Boyd & Trull, 2007; Lam et al., 2011; Sanders et al., 2014; Stemmann & Boss, 2012; Turner, 2015). Their interactions with TMs are often governed by biological uptake, complexation with organic ligands, and remineralization processes, which influence the distributions of bio-essential TMs from the sea surface and through the deeper water column (Boyd et al., 2017; Bruland, 1980; Bruland et al., 1994; Morel & Price, 2003; Twining et al., 2015). The dissolved TM pool is usually recognized to comprise the most readily bio-accessible TM pool (e.g., Wells et al., 1995). However, the pTM pool is also recognized as carrying bio-available fractions that are accessible to marine organisms either directly or following remineralization (Boyd et al., 2017; Bruland et al., 1991; Fitzwater et al., 2003; Nakayama et al., 2010; Sugie et al., 2013).

Extensive field and laboratory studies have established the biological requirement of several TMs (such as Fe, Zn, Mn, Ni, Cu, Co, Cd, and V) to marine organisms, revealing their critical role in the synthesis of cellular components and metalloenzymes (e.g., Twining et al., 2014, 2015;

Twining & Baines, 2013). These TMs participate in crucial physiological processes such as photosynthesis, respiration, nitrogen fixation and other important enzymatic reactions (Table 1.1). Furthermore, the availability of TMs, such as Fe, Cu, Co, or Cd, also influences the taxonomic composition of plankton communities (Boyd et al., 2017; Browning et al., 2017, 2021; Huapaya & Echeveste, 2023; Hutchins & Boyd, 2016; Martin et al., 1989; Moore et al., 2013; Sunda, 2012) or toxicity (e.g., Cu, Brand et al., 1986; Bruland et al., 2014). This, in turn, impacts particle composition and their density, whereby bio-aggregated particles may contain ballast minerals such as calcite, aragonite, and opal (Sanders et al., 2010). In turn, these ballast minerals provide a source of excess density and/or protection to bio-aggregated particles promoting deeper particle export and their associated pTMs, which are subsequently remineralized or incorporated into the underlying sediment (Armstrong et al., 2001; Francois et al., 2002; Hayes et al., 2013; Klaas & Archer, 2002; De La Rocha, 2007). Lithogenic particles, such as dust, are also sources of ballast in bio-aggerated particles (Klaas & Archer, 2002). TMs present in the water column, including those released shortly after particle remineralization, can (re-)absorb onto available particle surfaces during sinking (e.g., Fe, Zn, and Cu; Richon & Tagliabue, 2019; Tagliabue et al., 2019; Weber et al., 2018). Additionally, mineral precipitation within microenvironments of organic aggregates and fecal pellets may also play a large role in the marine biogeochemistry of other elements, such as Cd and barium (Ba) (Bianchi et al., 2018; Gonzalez-Muñoz et al., 2012; Martinez-Ruiz et al., 2019; Xie et al., 2019).

Phosphate is widely known for its role as a macronutrient in marine organisms, allowing the use of pP as a biogenic particle proxy. Comparisons of TM/P stoichiometries in marine particles with documented TM/P in various phytoplankton taxa (e.g., Ho et al., 2003; Twining & Baines, 2013) provides valuable clues to the principal carrier phases of associated pTMs pools. However, the TM/P stoichiometries for TMs such as Fe, Mn, Zn, Ni, Cu, Cd, and Co (see table 3.1), are only available for a limited variety of phytoplankton taxa. Other bioactive elements, such as V and molybdenum (Mo), have less commonly available TM/P stoichiometry data (Ho et al., 2003; Klein et al., 2013; Ohnemus et al., 2017).

Table 1.1 - Summary of Common Metalloproteins Present within Phytoplankton and Their Biochemical Functions. Compiled from *Ensign et al. (1993); Frausto da Silva & Williams (2001); Morel et al. (1994); Morel & Price (2003) Twining & Baines (2013)*

Common metalloproteins present in marine phytoplankton		
Metal	**Protein**	**Function**
Fe	Cytochromes	Electron transport in photosynthesis and respiration
	Ferredoxin	Electron transport in photosynthesis and Nitrogen fixation
	Nitrate and Nitrite reductase	Nitrate to Ammonia conversion
	Chelatase	Porphyrin and phycobiliprotein synthesis
	Nitrogenase	Nitrogen fixation
	Catalase	Hydrogen Peroxide to water conversion
	Peroxidase	Reactive oxygen species reduction
	Superoxide dismutase	Superoxide disproportionation to oxygen and hydrogen peroxide
Zn	Carbonic Anhydrase	Carbon dioxide hydration and dehydration
	Alkaline phosphatase	Phosphate ester hydrolysis
	RNA polymerase	Replication and transcription of Nucleic Acid
	tRNA synthetase	tRNA Synthesis
	Reverse transcriptase	Single stranded DNA synthesis from RNA
	Carboxypeptidase	Peptide bond hydrolysis
	Superoxide dismutase	Superoxide disproportionation to oxygen and hydrogen peroxide
Mn	O2-evolving enzyme	Oxidation of water during photosynthesis
	Superoxide dismutase	Superoxide disproportionation to oxygen and hydrogen peroxide
	Arginase	Arginine hydrolysis to ornithine and urea
	Phosphotransferases	Phosphorylation reactions
Ni	Urease	Urea hydrolysis
	Superoxide dismutase	Superoxide disproportionation to oxygen and hydrogen peroxide
Cu	Plastocyanin	Photosynthesis electron transport
	Cytochrome oxidase	Electron transport in mitochondria
	Ascorbate oxidase	Oxidation and reduction of ascorbic acid
	Superoxide dismutase	Superoxide disproportionation to oxygen and hydrogen peroxide
	Multicopper ferroxidase	High-affinity transmembrane Fe transport
Co	Vitamin B12	Carbon dioxide and Hydrogen transfer reactions
Cd	Carbonic anhydrase	Carbon dioxide hydration and dehydration (diatoms)
V	Nitrogenase	Nitrogen fixation
	Haloperoxidase	Halide Ion oxidation
Mo	Nitrogenase	Nitrogen fixation
	Nitrate and Nitrite Reductase	Nitrate to Ammonia conversion

1.2.2 Lithogenic Particles

Lithogenic particles are primarily derived from terrestrial sources, and delivered to the ocean via atmospheric deposition, rivers, or benthic resuspension, and are concentrated near continental margins and the ocean floor (Jickells et al., 2016; Lam et al., 2015; Lee et al., 2018; Lemaitre et al., 2020; Ohnemus & Lam, 2015). These particles consist mainly of silicate minerals, such as quartz, feldspars, clays, but also contain trace metals bound within their crystal lattice or adsorbed onto their surfaces and primarily comprise refractory materials (Baker et al., 2006; Baker & Jickells, 2016; Jickells et al., 2016; McKee et al., 2004). Aluminum (Al) and Titanium (Ti) are common constituents of lithogenic material (e.g., Rudnick & Gao, 2013; Taylor & McLennan, 1995) and therefore they are often employed as lithogenic tracers to estimate lithogenic fractions of other TMs. In such cases, the concentrations of lithogenic tracers (Al or Ti) are typically assumed to exclusively be derived from lithogenic sources. The pTM fractions in marine particles are then estimated by scaling up the average stoichiometric TM/Al abundance ratio values of canonical upper continental crust sources (e.g. Honjo et al., 1995; Lam et al., 2015; Ohnemus et al., 2017; Ohnemus & Lam, 2015; Xiang & Lam, 2020). Although, this estimation technique has uncertainties associated with it due to different elemental compositions of lithogenic source end members (e.g., Borchers et al., 2005; Brumsack, 2006), or due to the inclusion of adsorbed fractions of the lithogenic tracers, which for the pAl pool can be in the average vicinity of 15-20% by some estimates (Al-Hashem et al., 2022; Berger et al., 2008; Rauschenberg & Twining, 2015). This error can be reduced through the application of a suitable chemical leach to marine particles to remove adsorbed fractions (see section 1.3).

1.2.3 Authigenic Particles

Authigenic particles are those that form in-situ within the marine environment as a result of mineral precipitation, such as Fe and Mn oxides, or barite (see section 5.1). This process is often triggered by changes in the redox conditions, pH, or saturation state of the seawater affecting TM solubility. Iron and Mn are arguably the most pertinent of redox sensitive TMs due to their long-recognized role as strong scavengers in seawater (Goldberg, 1954; Turekian, 1977) acting as sinks for other TMs in the ocean, such as Cu, Zn, Co, and V (Charette et al., 2016; Ho et

al., 2018; Homoky et al., 2016; Lee et al., 2018). Their precipitation is partly due to low solubility of the thermodynamically favored Fe(III) and Mn(III/IV) redox states in oxygenated seawater (Bruland et al., 2014; Liu & Millero, 2002; Oldham et al., 2020; Tebo et al., 2004, 2005). However, in reducing environments, such as oxygen minimum zones (OMZs) or within reducing sediments, they are prone to dissolution following their reduction to the more soluble Fe(II) and Mn(II) redox states (Burdige, 1993; Burdige & Komada, 2020; Froelich et al., 1979). Following reductive dissolution, Fe(II) and Mn(II) can be re-oxidized following release from within sediment porewater in the presence of oxygen or other oxidizing agents, such as nitrate, leading to their re-precipitation as Fe and Mn oxides (Heller et al., 2017; Schlosser et al., 2018; Scholz et al., 2016). Although, Mn oxides appear to become less abundant within OMZs, where reducing conditions slows down their precipitation (Jensen et al., 2020; Von Langen et al., 1997; Tebo et al., 2004, 2005). Alternatively, where sulfidic conditions exist, such as within euxinic sediments or microenvironments in bio-aggregated particles, further diagenetic transformation of Fe and other chalcophile TMs (e.g., Cu, Zn, and Cd) to insoluble sulfides is also possible (Janssen et al., 2014; John et al., 2018; Landing & Lewis, 1991; Raven et al., 2021; Xie et al., 2019). The complex biogeochemical cycling of redox sensitive and associated TMs is thus especially important in OMZs, particularly in shelf regions, such as the Peruvian shelf, which are important TM sources to the ocean interior (Homoky et al., 2021; Lam et al., 2020; Rapp et al., 2020). The processes influencing TM export or retention in these regions, however, are not fully constrained (Dale et al., 2015; Henderson & Marchal, 2015; Jeandel et al., 2015).

1.3 Importance of Differentiating Labile and Refractory pTM Phases

The balance of the TM inventory between dissolved and particulate phases is largely determined by the roles of marine particles in the physical and biogeochemical processes of bio-assimilation, dissolution, (co-)precipitation minerals, reversible scavenging, and (dis)aggregation dynamics (see section 1.2). These processes allow a portion of pTMs to act as an exchangeable reservoir with the dTM pools depending on the biogeochemical processes occurring in the water column (Achterberg et al., 2018; Hurst & Bruland, 2007; Lippiatt et al., 2010; Milne et al., 2017). While bulk particulate concentrations provide an overview of the total metal content in particles, they do not provide reliable information about the mobility and bioavailability of these metals.

Distinguishing between the chemically labile and refractory particulate phases allows for a more nuanced understanding of TM dynamics and provides deeper insights into TM bioavailability, TM transformation processes, and their transport pathways, improving the characterization of pTM phases associated with particles. This can be accomplished by using a selective chemical leach on marine particles (Lam et al., 2015; Lippiatt et al., 2010; Milne et al., 2017; Rauschenberg & Twining, 2015).

Several chemical leaches have been developed for the investigating of marine particles (e.g., Chester & Hughes, 1967; Hudson & Morel, 1989; Tessier et al., 1979; Tovar-Sanchez et al., 2003). One leach method by *Berger et al. (2008),* developed based on a widely used *Chester and Hughes (1967)* leach, has become widely adopted by several oceanography working groups and has been evaluated against other leaching methods (Rauschenberg & Twining, 2015), with its use recommended in the latest GEOTRACES standards and protocols (Cutter et al., 2017). This leach method was found to reliably represent reactive pTM fractions associated with biogenic particles, adsorbed phases, and readily reducible Fe and Mn oxides, while leaving lithogenic/refractory particles largely intact (Berger et al., 2008; Rauschenberg & Twining, 2015). Adopting this methodology to evaluate pTM fractions provides several advantages that improve pTM characterization. First, it enables a more reliable use of the lithogenic proxy, pAl, by removing scavenged Al phases in the labile fraction and using the refractory pAl as a lithogenic tracer, preventing overestimation of lithogenic pTM fractions. Second, the biogenic pTM pool is effectively characterized by the leachable bio-essential pTM phases, as evidenced by pTM/pP ratios of leachable particulate Zn, Co, Cu, and Ni in surface waters of the North Atlantic when compared in conjunction with direct cellular quota measurements individually, and with documented phytoplankton pTM/pP quotas (Rauschenberg & Twining, 2015). However, to avoid overestimation of biogenic pTM phases, other abiogenic phases comprised of labile (oxy-)hydroxides and scavenged phases have also to be considered, particularly for Fe and Mn. Third, the refractory pTM pool can effectively represent the fraction of pTMs sequestered in the water column, helping identify the biogeochemical mechanisms which sequester TMs. Additionally, adopting labile and refractory particle fractions for multivariate statistical analysis, rather than bulk particulate fractions, is expected to increase their interpretability.

Of all TMs in the ocean, Fe is arguably the most widely studied and is routinely represented in global ocean biogeochemical models (Dutay et al., 2015; Moore et al., 2004; Tagliabue et al., 2016; Wallmann et al., 2022), while other TMs, such as Mn are not (Anderson & Henderson, 2005; Anugerahanti & Tagliabue, 2023; Henderson & Marchal, 2015; Rijkenberg et al., 2014; Tagliabue, 2019). This is largely due to the paucity of TM datasets that are available for the ocean, notably for particles, and for several critical biogeochemical regimes, such as oxygen minimum zones and upwelling regions. Such processes and particle sources are most frequently evident and concentrated in continental shelf regions, where the strength of particle supply is typically greatest. This makes continental shelves important conduits for the transfer of TMs into the ocean interior (Charette et al., 2016). Despite their importance, continental shelves are still understudied in terms of TM cycling (Charette et al., 2016; Henderson & Marchal, 2015). As a result, studies from productive upwelling shelf regions, such as the Benguela and Humboldt upwelling systems, and their associated OMZs, are needed. These studies would provide valuable insights that would help address significant gaps in our knowledge, particularly regarding the role of physical, chemical, and biological processes in the transformation between labile and refractory fractions and how this affects dissolved TM inventories.

1.4 Objectives and Outline of the Thesis

The primary objective of this thesis is to advance the knowledge of processes controlling internal biogeochemical cycling of particulate trace metals, and the primary mechanisms which influence the trace metal supply, distribution, and partitioning between dissolved and particulate TM phases.

This will be achieved by (1) exploiting naturally contrasting oceanographic conditions and distinctive particle sources from marine particle samples that were collected from the Southwest African and Peruvian shelf regions; (2) applying a chemical leach on marine particle samples to separate reactive and potentially exchangeable particulate trace metals from refractory phases; and (3) utilizing particle type proxies and a suite of other complementary ancillary physical and chemical measurements made on conjointly collected samples.

Chapter 2 briefly describes the methods used for marine particle collection and analysis that were not covered in chapters 3-5 of this thesis. Additionally, a detailed description of the leach and digestion procedure is provided as a practical reference for future researchers working in this area.

Chapter 3 describes the particulate trace metal distributions of Fe, Mn, Al, Ti, Co, Zn, Cd, Ni, Pb, Cu, and of P, along a sampled transect along SW African shelf, which traversed several contrasting oceanographic features, and discusses some of the biogeochemical processes behind the observations. These features include the Benguela upwelling system, oxygen minimum zones, and an anoxic shelf. The sampled region was also susceptible to several enhanced particle sources such as coastal shelf sediment resuspension, dust deposition from the Namib desert, increased primary production, and Congo River plume. Labile and refractory particulate fractions were used to characterize particle types and help provide evidence of redox chemistry influencing dissolution, precipitation, or persistence of redox-sensitive elements (i.e., Fe and Mn) in OMZs, as well as explain some of the distributions of dissolved trace metals as well. Labile and refractory particulate elemental abundance ratios were also utilized to suggest likely regional particulate sources.

Chapter 4 describes the particulate trace metal distributions of Fe, Mn, Al, Ti, Co, Zn, Cd, Ni, Pb, Cu, V, and P off the Peruvian shelf in the Eastern South Pacific Ocean and discusses the possible biogeochemical mechanisms responsible for the observations along sampled cross-shelf transects off the Peruvian shelf. This region is situated along a steep, narrow continental shelf within a coastal upwelling system and is underlaid by oxygen-depleted waters and anoxic sediment. Also, samples were collected during a strong El-Nino event which exhibited higher oxygenation of waters, influencing the distributions of several redox-sensitive trace metals (i.e., Fe, Mn, and Co). This study also aims to focus on investigating solid-solution interactions between the dissolved and particulate trace metal fractions, utilizing labile and refractory particulate fractions and suite of complementary ancillary measurements.

Chapter 5 describes the labile and refractory particulate distributions of biogeochemical tracers, vanadium (V), molybdenum (Mo), tungsten (W), chromium (Cr), uranium (U), thorium (Th), and

barium (Ba) along the same transects of the Southwest African shelf as the third chapter. These elements are understudied in the water column and only a limited number of datasets are available for these elements in marine environments, despite several of these elements having been utilized in (paleo-)oceanographic studies of marine sediment, and some having the potential to serve as biogeochemical proxies for elucidating biogeochemical cycling processes of the modern ocean. This study provides valuable insights into the pTM cycling of these elements, which are critically needed to fully understand the biogeochemical processes governing their distributions in the ocean.

Chapter 6 summarizes the major findings and conclusions drawn from the studies conducted between the two different regions and discusses the key takeaways and applications of the findings, as well as potential implications to other regions. In addition, recommendations are made to improve the efficacy and quality of future efforts to address knowledge gaps regarding the marine biogeochemical cycling of TMs.

References

Achterberg, E. P., Steigenberger, S., Marsay, C. M., Lemoigne, F. A. C., Painter, S. C., Baker, A. R., et al. (2018). Iron Biogeochemistry in the High Latitude North Atlantic Ocean. *Scientific Reports*, *8*(1). https://doi.org/10.1038/s41598-018-19472-1

Achterberg, E. P., Steigenberger, S., Klar, J. K., Browning, T. J., Marsay, C. M., Painter, S. C., et al. (2021). Trace Element Biogeochemistry in the High-Latitude North Atlantic Ocean: Seasonal Variations and Volcanic Inputs. *Global Biogeochemical Cycles*, *35*(3). https://doi.org/10.1029/2020GB006674

Al-Hashem, A. A., Beck, A. J., Krisch, S., Barraqueta, J.-L. M., Steffens, T., & Achterberg, E. P. (2022). Particulate Trace Metal Sources, Cycling, and Distributions on the Southwest African Shelf. *Global Biogeochemical Cycles*, e2022GB007453. https://doi.org/10.1029/2022GB007453

Anderson, R. F. (2020). GEOTRACES: Accelerating Research on the Marine Biogeochemical Cycles of Trace Elements and Their Isotopes. *Annual Review of Marine Science*, *12*, 49–85. https://doi.org/10.1146/annurev-marine-010318-095123

Anderson, R. F., & Henderson, G. M. (2005). Geotraces-A global study of the marine biogeochemical cycles of trace elements and their isotopes. *Oceanography*, *18*(3), 76–79. https://doi.org/10.5670/oceanog.2005.31

Anugerahanti, P., & Tagliabue, A. (2023). Process controlling iron – manganese regulation of the Southern Ocean biological carbon pump.

Armstrong, R. A., Lee, C., Hedges, J. I., Honjo, S., & Wakeham, S. G. (2001). A new, mechanistic model for organic carbon fluxes in the ocean based on the quantitative association of POC with ballast minerals. *Deep-Sea Research Part II: Topical Studies in Oceanography*, *49*(1–3), 219–236. https://doi.org/10.1016/S0967-0645(01)00101-1

Baker, A. R., & Jickells, T. D. (2016). Atmospheric deposition of soluble trace elements along the Atlantic Meridional Transect (AMT). *Progress in Oceanography*. https://doi.org/10.1016/j.pocean.2016.10.002

Baker, A. R., Jickells, T. D., Witt, M., & Linge, K. L. (2006). Trends in the solubility of iron, aluminium, manganese and phosphorus in aerosol collected over the Atlantic Ocean. *Marine Chemistry*, *98*(1), 43–58. https://doi.org/10.1016/j.marchem.2005.06.004

Barrett, P. M., Resing, J. A., Grand, M. M., Measures, C. I., & Landing, W. M. (2018). Trace element composition of suspended particulate matter along three meridional CLIVAR sections in the Indian and Southern Oceans: Impact of scavenging on Al distributions. *Chemical Geology*, *502*, 15–28. https://doi.org/10.1016/j.chemgeo.2018.06.015

Berger, C. J. M., Lippiatt, S. M., Lawrence, M. G., & Bruland, K. W. (2008). Application of a chemical leach technique for estimating labile particulate aluminum, iron, and manganese in the Columbia River plume and coastal waters off Oregon and Washington. *Journal of Geophysical Research*, *113*, 1–16. https://doi.org/10.1029/2007JC004703

Bianchi, D., Weber, T. S., Kiko, R., & Deutsch, C. (2018). Global niche of marine anaerobic metabolisms expanded by particle microenvironments. *Nature Geoscience*, *11*(4), 263–268. https://doi.org/10.1038/s41561-018-0081-0

Borchers, S. L., Schnetger, B., Böning, P., & Brumsack, H. J. (2005). Geochemical signatures of the Namibian diatom belt: Perennial upwelling and intermittent anoxia. *Geochemistry, Geophysics, Geosystems*, *6*(6). https://doi.org/10.1029/2004GC000886

Boyd, P. W., & Trull, T. W. (2007). Understanding the export of biogenic particles in oceanic waters: Is there consensus? *Progress in Oceanography*, *72*(4), 276–312. https://doi.org/10.1016/j.pocean.2006.10.007

Boyd, Philip W., Ibisanmi, E., Sander, S. G., Hunter, K. A., & Jackson, G. A. (2010). Remineralization of upper ocean particles: Implications for iron biogeochemistry. *Limnology and Oceanography*, *55*(3), 1271–1288. https://doi.org/10.4319/lo.2010.55.3.1271

Boyd, Philip W., Ellwood, M. J., Tagliabue, A., & Twining, B. S. (2017). Biotic and abiotic retention, recycling and remineralization of metals in the ocean. *Nature Geoscience*. https://doi.org/10.1038/ngeo2876

Brand, L. E., Sunda, W. G., & Guillard, R. R. L. (1986). Reduction of marine phytoplankton reproduction rates by copper and cadmium. *Journal of Experimental Marine Biology and Ecology*, *96*(3), 225–250. https://doi.org/10.1016/0022-0981(86)90205-4

Browning, T. J., Achterberg, E. P., Rapp, I., Engel, A., Bertrand, E. M., Tagliabue, A., & Moore, C. M. (2017). Nutrient co-limitation at the boundary of an oceanic gyre. *Nature*, *551*(7679), 242–246. https://doi.org/10.1038/nature24063

Browning, T. J., Achterberg, E. P., Engel, A., & Mawji, E. (2021). Manganese co-limitation of phytoplankton growth and major nutrient drawdown in the Southern Ocean. *Nature Communications*, *12*(1), 1–9. https://doi.org/10.1038/s41467-021-21122-6

Bruland, K. W. (1980). Oceanographic distributions of cadmium, zinc, nickel, and copper in the North Pacific. *Earth and Planetary Science Letters*, *47*(2), 176–198. https://doi.org/10.1016/0012-821X(80)90035-7

Bruland, K. W., & Lohan, M. C. (2003). Controls of trace metals in Seawater. *The Oceans and Marine Geochemistry*, *6*, 23–47.

Bruland, K. W., Donat, J. R., & Hutchins, D. A. (1991). Interactive influences of bioactive trace metals on biological production in oceanic waters. *Limnology and Oceanography*, *36*(8), 1555–1577. https://doi.org/10.4319/lo.1991.36.8.1555

Bruland, K. W., Orians, K. J., & Cowen, J. P. (1994). Reactive trace metals in the stratified central North Pacific. *Geochimica et Cosmochimica Acta*. https://doi.org/10.1016/0016-7037(94)90044-2

Bruland, K. W., Middag, R., & Lohan, M. C. (2014). *Controls of Trace Metals in Seawater*. *Treatise on Geochemistry: Second Edition* (2nd ed., Vol. 8). Elsevier Ltd. https://doi.org/10.1016/B978-0-08-095975-7.00602-1

Brumsack, H. J. (2006). The trace metal content of recent organic carbon-rich sediments: Implications for Cretaceous black shale formation. *Palaeogeography, Palaeoclimatology, Palaeoecology*, *232*(2–4), 344–361. https://doi.org/10.1016/j.palaeo.2005.05.011

Burd, A. B., & Jackson, G. A. (2009). Particle aggregation. *Annual Review of Marine Science*, *1*, 65–90. https://doi.org/10.1146/annurev.marine.010908.163904

Burdige, D. J. (1993). The biogeochemistry of manganese and iron reduction in marine sediments. *Earth Science Reviews*, *35*(3), 249–284. https://doi.org/10.1016/0012-8252(93)90040-E

Burdige, D. J., & Komada, T. (2020). Iron redox cycling, sediment resuspension and the role of sediments in low oxygen environments as sources of iron to the water column. *Marine Chemistry*, *223*(September 2019), 103793. https://doi.org/10.1016/j.marchem.2020.103793

Charette, M. A., Lam, P. J., Lohan, M. C., Kwon, E. Y., Hatje, V., Jeandel, C., et al. (2016). Coastal ocean and shelf-sea biogeochemical cycling of trace elements and isotopes: Lessons learned from GEOTRACES. *Philosophical Transactions of the Royal Society A: Mathematical, Physical and Engineering Sciences*, *374*(2081), In press. https://doi.org/10.1098/rsta.2016.0076

Chester, R., & Hughes, M. J. (1967). A chemical technique for the separation of ferro-manganese minerals, carbonate minerals and adsorbed trace elements from pelagic sediments. *Chemical Geology*, *2*(C), 249–262. https://doi.org/10.1016/0009-2541(67)90025-3

Close, H. G., Lam, P. J., & Popp, B. N. (2021). Marine Particle Chemistry: Influence on Biogeochemical Cycles and Particle Export. *ACS Earth and Space Chemistry*, *5*(5), 1210–1211. https://doi.org/10.1021/acsearthspacechem.1c00091

Cutter, G. A., Andersson, P. S., Codispoti, L., Croot, P. L., Francois, R., Lohan, M. C., et al. (2014). Sampling and sample-handling protocols for GEOTRACES cruises, (December), 1–238.

https://doi.org/http://www.geotraces.org/science/intercalibration/222-sampling-and-sample-handling-protocols-for-geotraces-cruises

Cutter, G. A., Casciotti, K., Croot, P. L., Geibert, W., Heimbürger, L.-E., Lohan, M. C., et al. (2017). Sampling and Sample-handling Protocols for GEOTRACES Cruises. Version 3, August 2017. *GEOTRACES Community Practices*, (August), 139pp. & Appendices. Retrieved from http://www.geotraces.org/images/stories/documents/intercalibration/Cookbook.pdf

Dale, A. W., Nickelsen, L., Scholz, F., Hensen, C., Oschlies, A., & Wallmann, K. (2015). A revised global estimate of dissolved iron fluxes from marine sediments. *Global Biogeochemical Cycles*, *29*(5), 691–707. https://doi.org/10.1002/2014GB005017

Dutay, J., Tagliabue, A., Kriest, I., & Van Hulten, M. (2015). Modelling the role of marine particle on large scale 231 Pa, 230 Th, Iron and Aluminium distributions. *Progress in Oceanography*, *133*, 66–72. https://doi.org/10.1016/j.pocean.2015.01.010

Dymond, J., Collier, R., McManus, J., Honjo, S., & Manganini, S. J. (1997). Can the aluminum and titanium contents of ocean sediments be used to determine the paleoproductivity of the oceans? *Paleoceanography*, *12*(4), 586–593. https://doi.org/10.1029/97PA01135

Ensign, S. A., Hyman, M. R., & Arp, D. J. (1993). In vitro activation of ammonia monooxygenase from Nitrosomonas europaea by copper. *Journal of Bacteriology*, *175*(7), 1971–1980. https://doi.org/10.1128/JB.175.7.1971-1980.1993

Fitzwater, S. E., Johnson, K. S., Elrod, V. A., Ryan, J. P., Coletti, L. J., Tanner, S. J., et al. (2003). Iron, nutrient and phytoplankton biomass relationships in upwelled waters of the California coastal system. *Continental Shelf Research*, *23*(16), 1523–1544. https://doi.org/10.1016/J.CSR.2003.08.004

Francois, R., Honjo, S., Krishfield, R., & Manganini, S. (2002). Factors controlling the flux of organic carbon to the bathypelagic zone of the ocean. *Global Biogeochemical Cycles*, *16*(4), 34-1-34–20. https://doi.org/10.1029/2001gb001722

Frausto da Silva, J. J. R., & Williams, R. J. P. (2001). The principles of the uptake and chemical speciation of the elements in biology. *The Biological Chemistry of the Elements: The Inorganic Chemistry of Life*, *02*, 29–82. Retrieved from https://global.oup.com/academic/product/the-biological-chemistry-of-the-elements-9780198508489

Froelich, P. N., Klinkhammer, G. P., Bender, M. L., Luedtke, N. A., Heath, G. R., Cullen, D., et al. (1979). Early oxidation of organic matter in pelagic sediments of the eastern equatorial Atlantic: suboxic diagenesis. *Geochimica et Cosmochimica Acta*, *43*(7), 1075–1090. https://doi.org/10.1016/0016-7037(79)90095-4

GEOTRACES Planning Group. (2006). GEOTRACES Science Plan. *Scientific Committee on Oceanic Research*, 1–87.

Gledhill, M., & Buck, K. N. (2012). The organic complexation of iron in the marine environment: A review. *Frontiers in Microbiology*, *3*(FEB), 1–17. https://doi.org/10.3389/fmicb.2012.00069

Goldberg, E. D. (1954). Chemical Scavengers of the Sea. *The Journal of Geology*, *62*(3), 249–265.

Gonzalez-Muñoz, M. T., Martinez-Ruiz, F., Morcillo, F., Martin-Ramos, J. D., & Paytan, A. (2012). Precipitation of barite by marine bacteria: A possible mechanism for marine barite formation. *Geology*, *40*(8), 675–678. https://doi.org/10.1130/G33006.1

Hayes, C. T., Anderson, R. F., Jaccard, S. L., François, R., Fleisher, M. Q., Soon, M., & Gersonde, R. (2013). A new perspective on boundary scavenging in the North Pacific Ocean. *Earth and Planetary Science Letters*, *369–370*, 86–97. https://doi.org/10.1016/j.epsl.2013.03.008

Heller, M. I., Lam, P. J., Moffett, J. W., Till, C. P., Lee, J. M., Toner, B. M., & Marcus, M. A. (2017). Accumulation of Fe oxyhydroxides in the Peruvian oxygen deficient zone implies non-oxygen dependent Fe oxidation. *Geochimica et Cosmochimica Acta*, *211*(Iii), 174–193. https://doi.org/10.1016/j.gca.2017.05.019

Henderson, G. M., & Marchal, O. (2015). Recommendations for future measurement and modelling of particles in GEOTRACES and other ocean biogeochemistry programmes. *Progress in Oceanography*, *133*, 73–78. https://doi.org/10.1016/j.pocean.2015.01.015

Ho, P., Lee, J. M., Heller, M. I., Lam, P. J., & Shiller, A. M. (2018). The distribution of dissolved and particulate Mo and V along the U.S. GEOTRACES East Pacific Zonal Transect (GP16): The roles of oxides and biogenic particles in their distributions in the oxygen deficient zone and the hydrothermal plume. *Marine Chemistry*, *201*(October), 242–255. https://doi.org/10.1016/j.marchem.2017.12.003

Ho, T.-Y., Finkel, Z. V, Milligan, A. J., Wyman, K., Falkowski, P. G., & Morel, F. M. M. (2003). The elemental composition of some marine phytoplankton. *Journal of Phycology*, *39*, 1145–1159.

Homoky, W. B., Weber, T., Berelson, W. M., Conway, T. M., Henderson, G. M., Van Hulten, M., et al. (2016). *Quantifying trace element and isotope fluxes at the ocean-sediment boundary: A review*. *Philosophical Transactions of the Royal Society A: Mathematical, Physical and Engineering Sciences* (Vol. 374). https://doi.org/10.1098/rsta.2016.0246

Homoky, W. B., Conway, T. M., John, S. G., König, D., Deng, F. F., Tagliabue, A., & Mills, R. A. (2021). Iron colloids dominate sedimentary supply to the ocean interior. *Proceedings of the National Academy of Sciences of the United States of America*, *118*(13). https://doi.org/10.1073/PNAS.2016078118

Honeyman, B. D., Balistrieri, L. S., & Murray, J. W. (1988). Oceanic trace metal scavenging: the importance of particle concentration. *Deep Sea Research Part A, Oceanographic Research Papers*, *35*(2), 227–246. https://doi.org/10.1016/0198-0149(88)90038-6

Honjo, S., Dymond, J., Collier, R., & Manganini, S. J. (1995). Export production of particles to the interior of the equatorial Pacific Ocean during the 1992 EqPac experiment. *Deep-Sea Research Part II*, *42*(2–3), 831–870. https://doi.org/10.1016/0967-0645(95)00034-N

Horner, T. J., Little, S. H., Conway, T. M., Farmer, J. R., Hertzberg, J. E., Janssen, D. J., et al. (2021). Bioactive Trace Metals and Their Isotopes as Paleoproductivity Proxies: An Assessment Using GEOTRACES-Era Data. *Global Biogeochemical Cycles*, *35*(11), 1–86. https://doi.org/10.1029/2020gb006814

Huapaya, K., & Echeveste, P. (2023). Physiological responses of Humboldt current system diatoms to Fe and Cu co-limitation. *Marine Environmental Research*, *187*, 105937. https://doi.org/10.1016/J.MARENVRES.2023.105937

Hudson, R. J. M., & Morel, F. M. M. (1989). Distinguishing between extra- and intracellular iron in marine phytoplankton. *Limnology and Oceanography*, *34*(6), 1113–1120. https://doi.org/10.4319/LO.1989.34.6.1113

Hunt, H. R., Summers, B. A., Sieber, M., Krisch, S., Al-Hashem, A., Hopwood, M. J., et al. (2022). Distinguishing the influence of sediments, the Congo River, and water-mass mixing on the distribution of iron and its isotopes in the Southeast Atlantic Ocean. *Marine Chemistry*, 104181. https://doi.org/10.1016/J.MARCHEM.2022.104181

Hurst, M. P., & Bruland, K. W. (2007). An investigation into the exchange of iron and zinc between soluble, colloidal, and particulate size-fractions in shelf waters using low-abundance isotopes as tracers in shipboard incubation experiments. https://doi.org/10.1016/j.marchem.2006.07.001

Hutchins, D. A., & Boyd, P. W. (2016). Marine phytoplankton and the changing ocean iron cycle. *Nature Publishing Group*, *6*. https://doi.org/10.1038/NCLIMATE3147

Janssen, D. J., Conway, T. M., John, S. G., Christian, J. R., Kramer, D. I., Pedersen, T. F., & Cullen, J. T. (2014). Undocumented water column sink for cadmium in open ocean oxygen-deficient zones. *Proceedings of the National Academy of Sciences of the United States of America*, *111*(19), 6888–6893. https://doi.org/10.1073/PNAS.1402388111/ASSET/64F7D31E-2EAF-4C5B-B7E2-151BBBF860F9/ASSETS/GRAPHIC/PNAS.1402388111I32.GIF

Jeandel, C., Rutgers van der Loeff, M., Lam, P. J., Roy-Barman, M., Sherrell, R. M., Kretschmer, S., et al. (2015). What did we learn about ocean particle dynamics in the GEOSECS-JGOFS era? *Progress in Oceanography*, *133*, 6–16. https://doi.org/10.1016/j.pocean.2014.12.018

Jensen, L. T., Morton, P. L., Twining, B. S., Heller, M. I., Hatta, M., Measures, C. I., et al. (2020). A comparison of marine Fe and Mn cycling: U.S. GEOTRACES GN01 Western Arctic case study. *Geochimica et Cosmochimica Acta*, *288*, 138–160. https://doi.org/10.1016/j.gca.2020.08.006

Jickells, T. D., Baker, A. R., & Chance, R. (2016). Atmospheric transport of trace elements and nutrients to the oceans. *Philosophical Transactions of the Royal Society A: Mathematical, Physical and Engineering Sciences*, *374*(2081), 20150286. https://doi.org/10.1098/rsta.2015.0286

John, S. G., Helgoe, J., Townsend, E., Weber, T., DeVries, T., Tagliabue, A., et al. (2018). Biogeochemical cycling of Zn and Cd and their stable isotopes in the Eastern Tropical South Pacific. *Marine Chemistry*, *201*, 66–76. https://doi.org/10.1016/j.marchem.2017.06.003

Klaas, C., & Archer, D. E. (2002). Association of sinking organic matter with various types of mineral ballast in the deep sea: Implications for the rain ratio. *Global Biogeochemical Cycles*, *16*(4), 63-1-63–14. https://doi.org/10.1029/2001gb001765

Klein, N. J., Beck, A. J., Hutchins, D. A., & Sañudo-Wilhelmy, S. A. (2013). Regression modeling of the North East Atlantic Spring Bloom suggests previously unrecognized biological roles for V and Mo. *Frontiers in Microbiology*, *4*(MAR), 1–12. https://doi.org/10.3389/fmicb.2013.00045

De La Rocha, C. L. (2007). The Biological Pump. *Treatise on Geochemistry*, *6–9*, 1–29. https://doi.org/10.1016/B0-08-043751-6/06107-7

Lam, P. J., & Bishop, J. K. B. (2008). The continental margin is a key source of iron to the HNLC North Pacific Ocean. *Geophysical Research Letters*, *35*(7), 1–5. https://doi.org/10.1029/2008GL033294

Lam, P. J., & Marchal, O. (2014). Insights into Particle Cycling from Thorium and Particle Data. https://doi.org/10.1146/annurev-marine-010814-015623

Lam, P. J., Doney, S. C., & Bishop, J. K. B. (2011). The dynamic ocean biological pump: Insights from a global compilation of particulate organic carbon, CaCO 3, and opal concentration profiles from the mesopelagic. *Global Biogeochemical Cycles*, *25*(3). https://doi.org/10.1029/2010GB003868

Lam, P. J., Twining, B. S., Jeandel, C., Roychoudhury, A., Resing, J. A., Santschi, P. H., & Anderson, R. F. (2015). Methods for analyzing the concentration and speciation of major and trace elements in marine particles. *Progress in Oceanography*, *133*, 32–42. https://doi.org/10.1016/j.pocean.2015.01.005

Lam, P. J., Ohnemus, D. C., & Auro, M. E. (2015). Size-fractionated major particle composition and concentrations from the US GEOTRACES North Atlantic Zonal Transect. *Deep-Sea*

Research Part II: Topical Studies in Oceanography, *116*, 303–320. https://doi.org/10.1016/j.dsr2.2014.11.020

Lam, P. J., Heller, M. I., Lerner, P. E., Moffett, J. W., & Buck, K. N. (2020). Unexpected Source and Transport of Iron from the Deep Peru Margin. *ACS Earth and Space Chemistry*, *4*(7), 977–992. https://doi.org/10.1021/acsearthspacechem.0c00066

Landing, W. M., & Lewis, B. L. (1991). Thermodynamic Modeling of Trace Metal Speciation in the Black Sea. *Black Sea Oceanography*, 125–160. https://doi.org/10.1007/978-94-011-2608-3_8

Von Langen, P. J., Johnson, K. S., Coale, K. H., & Elrod, V. A. (1997). Oxidation kinetics of manganese (II) in sea water at nanomolar concentrations. *Geochimica et Cosmochimica Acta*, *61*(23), 4945–4954. https://doi.org/10.1016/S0016-7037(97)00355-4

Lee, J. M., Heller, M. I., & Lam, P. J. (2018). Size distribution of particulate trace elements in the U.S. GEOTRACES Eastern Pacific Zonal Transect (GP16). *Marine Chemistry*, *201*, 108–123. https://doi.org/10.1016/j.marchem.2017.09.006

Lemaitre, N., Planquette, H., Dehairs, F., Planchon, F., Sarthou, G., Gallinari, M., et al. (2020). Particulate Trace Element Export in the North Atlantic (GEOTRACES GA01 Transect, GEOVIDE Cruise). *ACS Earth and Space Chemistry*, *4*(11), 2185–2204. https://doi.org/10.1021/acsearthspacechem.0c00045

Liao, W.-H., & Ho, T.-Y. (2018). Particulate Trace Metal Composition and Sources in the Kuroshio Adjacent to the East China Sea: The Importance of Aerosol Deposition. *Journal of Geophysical Research: Oceans*, *123*(9), 6207–6223. https://doi.org/10.1029/2018JC014113

Lippiatt, S. M., Brown, M. T., Lohan, M. C., Berger, C. J. M., & Bruland, K. W. (2010). Leachable particulate iron in the Columbia River, estuary, and near-field plume. *Estuarine, Coastal and Shelf Science*, *87*(1), 33–42. https://doi.org/10.1016/j.ecss.2009.12.009

Liu, T., Krisch, S., Xie, R. C., Hopwood, M. J., Dengler, M., Achterberg, E. P., & Liu tliu, T. (2022). Sediment release in the Benguela Upwelling System dominates trace metal input to the shelf and eastern South Atlantic Ocean. *Global Biogeochemical Cycles*, e2022GB007466. https://doi.org/10.1029/2022GB007466

Liu, X., & Millero, F. J. (2002). The solubility of iron in seawater. *Marine Chemistry*, *77*(1), 43–54. https://doi.org/10.1016/S0304-4203(01)00074-3

Marsay, C. M., & Achterberg, E. P. (2021). Particulate iron and other trace elements in near-surface waters of the high latitude North Atlantic following the 2010 Eyjafjallajökull eruption. *Marine Chemistry*, *232*(October 2020), 103959. https://doi.org/10.1016/j.marchem.2021.103959

Martin, J. H., Gordon, R. M., Fitzwater, S., & Broenkow, W. W. (1989). Vertex: phytoplankton/iron studies in the Gulf of Alaska. *Deep Sea Research Part A, Oceanographic Research Papers*, *36*(5), 649–680. https://doi.org/10.1016/0198-0149(89)90144-1

Martinez-Ruiz, F., Paytan, A., Gonzalez-Muñoz, M. T., Jroundi, F., Abad, M. M., Lam, P. J., et al. (2019). Barite formation in the ocean: Origin of amorphous and crystalline precipitates. *Chemical Geology*, *511*(October 2018), 441–451. https://doi.org/10.1016/j.chemgeo.2018.09.011

McKee, Brent A., Aller, R. C., Allison, M. A., Bianchi, T. S., & Kineke, G. C. (2004). Transport and transformation of dissolved and particulate materials on continental margins influenced by major rivers: benthic boundary layer and seabed processes. *Continental Shelf Research*, *24*(7–8), 899–926. https://doi.org/10.1016/J.CSR.2004.02.009

Menzel Barraqueta, J.-L., Schlosser, C., Planquette, H., Gourain, A., Cheize, M., Boutorh, J., et al. (2018). Aluminium in the north atlantic ocean and the Labrador Sea (GEOTRACES GA01 section): Roles of continental inputs and biogenic particle removal. *Biogeosciences*, *15*(16), 5271–5286. https://doi.org/10.5194/bg-15-5271-2018

Milne, A., Schlosser, C., Wake, B. D., Achterberg, E. P., Chance, R., Baker, A. R., et al. (2017). Particulate phases are key in controlling dissolved iron concentrations in the (sub)tropical North Atlantic: Particulate Phases Control dFe. *Geophysical Research Letters*. https://doi.org/10.1002/2016GL072314

Moore, C. M., Mills, M. M., Arrigo, K. R., Berman-Frank, I., Bopp, L., Boyd, P. W., et al. (2013). Processes and patterns of oceanic nutrient limitation. *Nature Geoscience*, *6*(9), 701–710. https://doi.org/10.1038/ngeo1765

Moore, J. K., Doney, S. C., & Lindsay, K. (2004). Upper ocean ecosystem dynamics and iron cycling in a global three-dimensional model. *Global Biogeochemical Cycles*, *18*(4), 1–21. https://doi.org/10.1029/2004GB002220

Morel, F. M. M., & Price, N. M. (2003). The biogeochemical cycles of trace metals in the oceans. *Science*, *300*(5621), 944–947. https://doi.org/10.1126/science.1083545

Morel, F. M. M., Reinfelder, J. R., Roberts, S. B., Chamberlain, C. P., Lee, J. G., & Yee, D. (1994). Zinc and carbon co-limitation of marine phytoplankton. *Nature*, *369*(6483), 740–742. https://doi.org/10.1038/369740a0

Morton, P. L., Landing, W. M., Hsu, S. C., Milne, A., Aguliar-Islas, A., Baker, A. R., et al. (2013). Methods for the sampling and analysis of marine aerosols: Results from the 2008 GEOTRACES aerosol intercalibration experiment. *Limnology and Oceanography: Methods*, *11*(FEB), 62–78. https://doi.org/10.4319/lom.2013.11.62

Nakayama, Y., Kuma, K., Fujita, S., Sugie, K., & Ikeda, T. (2010). Temporal variability and bioavailability of iron and other nutrients during the spring phytoplankton bloom in the Oyashio region. *Deep Sea Research Part II: Topical Studies in Oceanography*, *57*(17–18), 1618–1629. https://doi.org/10.1016/J.DSR2.2010.03.006

Nozaki, Y. (1997). A fresh look at element distribution in the North Pacific Ocean. *Eos*, *78*(21), 221. https://doi.org/10.1029/97eo00148

Ohnemus, D. C., & Lam, P. J. (2015). Cycling of lithogenic marine particles in the US GEOTRACES North Atlantic transect. *Deep-Sea Research Part II: Topical Studies in Oceanography*, *116*, 283–302. https://doi.org/10.1016/j.dsr2.2014.11.019

Ohnemus, D. C., Rauschenberg, S., Cutter, G. A., Fitzsimmons, J. N., Sherrell, R. M., & Twining, B. S. (2017). Elevated trace metal content of prokaryotic communities associated with marine oxygen deficient zones. *Limnology and Oceanography*, *62*(1), 3–25. https://doi.org/10.1002/LNO.10363

Ohnemus, D. C., Torrie, R., & Twining, B. S. (2019). Exposing the Distributions and Elemental Associations of Scavenged Particulate Phases in the Ocean Using Basin-Scale Multi-Element Data Sets. *Global Biogeochemical Cycles*, *33*(6), 725–748. https://doi.org/10.1029/2018GB006145

Oldham, V. E., Lamborg, C. H., & Hansel, C. M. (2020). The Spatial and Temporal Variability of Mn Speciation in the Coastal Northwest Atlantic Ocean. *Journal of Geophysical Research: Oceans*, *125*(1), 1–15. https://doi.org/10.1029/2019JC015167

Planquette, H., & Sherrell, R. M. (2012). Sampling for particulate trace element determination using water sampling bottles: Methodology and comparison to in situ pumps. *Limnology and Oceanography: Methods*. https://doi.org/10.4319/lom.2012.10.367

Rapp, I., Schlosser, C., Browning, T. J., Wolf, F., Le Moigne, F. A. C., Gledhill, M., & Achterberg, E. P. (2020). El Niño-Driven Oxygenation Impacts Peruvian Shelf Iron Supply to the South Pacific Ocean. *Geophysical Research Letters*, *47*(7). https://doi.org/10.1029/2019GL086631

Rauschenberg, S., & Twining, B. S. (2015). Evaluation of approaches to estimate biogenic particulate trace metals in the ocean. *Marine Chemistry*, *171*, 67–77. https://doi.org/10.1016/j.marchem.2015.01.004

Raven, M. R., Keil, R. G., & Webb, S. M. (2021). Microbial sulfate reduction and organic sulfur formation in sinking marine particles. *Science*, *371*(6525), 178–181. https://doi.org/10.1126/SCIENCE.ABC6035/SUPPL_FILE/ABC6035_RAVEN_SM.PDF

Richon, C., & Tagliabue, A. (2019). Insights Into the Major Processes Driving the Global Distribution of Copper in the Ocean From a Global Model. *Global Biogeochemical Cycles*, *33*(12), 1594–1610. https://doi.org/10.1029/2019GB006280

Rijkenberg, M. J. A., Middag, R., Laan, P., Gerringa, L. J. A., Van Aken, H. M., Schoemann, V., et al. (2014). The Distribution of Dissolved Iron in the West Atlantic Ocean. *PLOS ONE*, *9*(6), e101323. https://doi.org/10.1371/JOURNAL.PONE.0101323

Rudnick, R. L., & Gao, S. (2013). *Composition of the Continental Crust*. *Treatise on Geochemistry: Second Edition* (2nd ed., Vol. 4). Elsevier Ltd. https://doi.org/10.1016/B978-0-08-095975-7.00301-6

Sanders, R., Morris, P. J., Poulton, A. J., Stinchcombe, M. C., Charalampopoulou, A., Lucas, M. I., & Thomalla, S. J. (2010). Does a ballast effect occur in the surface ocean? *Geophysical Research Letters*, *37*(8). https://doi.org/10.1029/2010GL042574

Sanders, R., Henson, S. A., Koski, M., De La Rocha, C. L., Painter, S. C., Poulton, A. J., et al. (2014). The Biological Carbon Pump in the North Atlantic. *Progress in Oceanography*, *129*(PB), 200–218. https://doi.org/10.1016/J.POCEAN.2014.05.005

Schlosser, C., Streu, P., Frank, M., Lavik, G., Croot, P. L., Dengler, M., & Achterberg, E. P. (2018). H2S events in the Peruvian oxygen minimum zone facilitate enhanced dissolved Fe concentrations. *Scientific Reports*, *8*(1). https://doi.org/10.1038/s41598-018-30580-w

Scholz, F., Hensen, C., Noffke, A., Rohde, A., Liebetrau, V., & Wallmann, K. (2011). Early diagenesis of redox-sensitive trace metals in the Peru upwelling area - response to ENSO-related oxygen fluctuations in the water column. *Geochimica et Cosmochimica Acta*, *75*(22), 7257–7276. https://doi.org/10.1016/j.gca.2011.08.007

Scholz, F., Löscher, C. R., Fiskal, A., Sommer, S., Hensen, C., Lomnitz, U., et al. (2016). Nitrate-dependent iron oxidation limits iron transport in anoxic ocean regions. *Earth and Planetary Science Letters*, *454*, 272–281. https://doi.org/10.1016/j.epsl.2016.09.025

Sherrell, R. M., & Boyle, E. A. (1992). The trace metal composition of suspended particles in the oceanic water column near Bermuda. *Earth and Planetary Science Letters*, *111*, 155–174. Retrieved from http://ac.els-cdn.com/0012821X9290176V/1-s2.0-0012821X9290176V-main.pdf?_tid=362fe70c-971c-11e7-bb75-00000aab0f01&acdnat=1505153488_611fb430616d3fdcd9d26f5cfb2f3853

Stemmann, L., & Boss, E. (2012). Plankton and particle size and packaging: From determining optical properties to driving the biological pump. *Annual Review of Marine Science*. https://doi.org/10.1146/annurev-marine-120710-100853

Sugie, K., Nishioka, J., Kuma, K., Volkov, Y. N., & Nakatsuka, T. (2013). Availability of particulate Fe to phytoplankton in the Sea of Okhotsk. *Marine Chemistry*, *152*, 20–31. https://doi.org/10.1016/j.marchem.2013.03.005

Sunda, W. G. (2012). Feedback interactions between trace metal nutrients and phytoplankton in the ocean. *Frontiers in Microbiology*, *3*(JUN), 1–22. https://doi.org/10.3389/fmicb.2012.00204

Tagliabue, A. (2019). *Elemental distribution: Overview*. *Encyclopedia of Ocean Sciences* (3rd ed., Vol. 2010). Elsevier Ltd. https://doi.org/10.1016/B978-0-12-409548-9.10774-2

Tagliabue, A., Aumont, O., Death, R., Dunne, J. P., Dutkiewicz, S., Galbraith, E., et al. (2016). How well do global ocean biogeochemistry models simulate dissolved iron distributions? *Global Biogeochemical Cycles*, *30*(2), 149–174. https://doi.org/10.1002/2015GB005289

Tagliabue, A., Bowie, A. R., DeVries, T., Ellwood, M. J., Landing, W. M., Milne, A., et al. (2019). The interplay between regeneration and scavenging fluxes drives ocean iron cycling. *Nature Communications*. https://doi.org/10.1038/s41467-019-12775-5

Taylor, S. R., & McLennan, S. M. (1995). The geochemical evolution of the continental crust. *Reviews of Geophysics*, *33*(2), 241–265. https://doi.org/10.1029/95RG00262

Tebo, B. M., Bargar, J. R., Clement, B. G., Dick, G. J., Murray, K. J., Parker, D., et al. (2004). Biogenic manganese oxides: Properties and mechanisms of formation. *Annual Review of Earth and Planetary Sciences*, *32*(Goldberg 1954), 287–328. https://doi.org/10.1146/annurev.earth.32.101802.120213

Tebo, B. M., Johnson, H. A., McCarthy, J. K., & Templeton, A. S. (2005). Geomicrobiology of manganese(II) oxidation. *Trends in Microbiology*, *13*(9), 421–428. https://doi.org/10.1016/j.tim.2005.07.009

Tessier, A., Campbell, P. G. C., & Bisson, M. (1979). Sequential Extraction Procedure for the Speciation of Particulate Trace Metals. *ANALYTICAL CHEMISTRY*, *51*(7).

Tovar-Sanchez, A., Sañudo-Wilhelmy, S. A., Garcia-Vargas, M., Weaver, R. S., Popels, L. C., & Hutchins, D. A. (2003). A trace metal clean reagent to remove surface-bound iron from marine phytoplankton. *Marine Chemistry*, *82*(1–2), 91–99. https://doi.org/10.1016/S0304-4203(03)00054-9

Turekian, K. K. (1977). The fate of metals in the oceans. *Geochimica et Cosmochimica Acta*. https://doi.org/10.1016/0016-7037(77)90109-0

Turner, J. T. (2015). Zooplankton fecal pellets, marine snow, phytodetritus and the ocean's biological pump. *Progress in Oceanography*, *130*, 205–248. https://doi.org/10.1016/j.pocean.2014.08.005

Twining, B. S., & Baines, S. B. (2013). The Trace Metal Composition of Marine Phytoplankton. *Annu. Rev. Mar. Sci*, *5*, 191–215. https://doi.org/10.1146/annurev-marine-121211-172322

Twining, B. S., Nodder, S. D., King, A. L., Hutchins, D. A., Lecleir, G. R., Debruyn, J. M., et al. (2014). Differential remineralization of major and trace elements in sinking diatoms. *Limnology and Oceanography*, *59*(3), 689–704. https://doi.org/10.4319/lo.2014.59.3.0689

Twining, B. S., Rauschenberg, S., Morton, P. L., Ohnemus, D. C., & Lam, P. J. (2015). Comparison of particulate trace element concentrations in the North Atlantic Ocean as determined with discrete bottle sampling and in situ pumping. *Deep-Sea Research Part II: Topical Studies in Oceanography*, *116*, 273–282. https://doi.org/10.1016/j.dsr2.2014.11.005

Twining, B. S., Rauschenberg, S., Morton, P. L., & Vogt, S. (2015). Metal contents of phytoplankton and labile particulate material in the North Atlantic Ocean. *Progress in Oceanography*, *137*, 261–283. https://doi.org/10.1016/j.pocean.2015.07.001

Vedamati, J., Goepfert, T., & Moffett, J. W. (2014). Iron speciation in the eastern tropical south pacific oxygen minimum zone off peru. *Limnology and Oceanography*, *59*(6), 1945–1957. https://doi.org/10.4319/lo.2014.59.6.1945

Wallmann, K., José, Y. S., Hopwood, M. J., Somes, C. J., Dale, A. W., Scholz, F., et al. (2022). Biogeochemical feedbacks may amplify ongoing and future ocean deoxygenation: a case study from the Peruvian oxygen minimum zone. *Biogeochemistry*, *159*(1), 45–67. https://doi.org/10.1007/s10533-022-00908-w

Weber, T. S., John, S., Tagliabue, A., & DeVries, T. (2018). Biological uptake and reversible scavenging of zinc in the global ocean. *Science*, *361*(6397), 72–76. https://doi.org/10.1126/science.aap8532

Wells, M. L., Price, N. M., & Bruland, K. W. (1995). Iron chemistry in seawater and its relationship to phytoplankton: a workshop report. *Marine Chemistry*, *48*(2), 157–182. https://doi.org/10.1016/0304-4203(94)00055-I

Wuttig, K., Wagener, T., Bressac, M., Dammshäuser, A., Streu, P., Guieu, C., & Croot, P. L. (2013). Impacts of dust deposition on dissolved trace metal concentrations (Mn, Al and Fe) during a mesocosm experiment. *Biogeosciences*, *10*(4), 2583–2600. https://doi.org/10.5194/bg-10-2583-2013

Xiang, Y., & Lam, P. J. (2020). *Size-Fractionated Compositions of Marine Suspended Particles in the Western Arctic Ocean: Lateral and Vertical Sources*. *Journal of Geophysical Research: Oceans* (Vol. 125). https://doi.org/10.1029/2020JC016144

Xie, R. C., Rehkämper, M., Grasse, P., van de Flierdt, T., Frank, M., & Xue, Z. (2019). Isotopic evidence for complex biogeochemical cycling of Cd in the eastern tropical South Pacific. *Earth and Planetary Science Letters*, *512*, 134–146. https://doi.org/10.1016/J.EPSL.2019.02.001

Chapter 2: Methods and Materials

This chapter briefly describes the cleaning procedures, seawater sampling, sample handling and analytical processes for particulate trace metal (pTM) samples that are not completely explained in the subsequent chapters. The reader is referred to the method sections of the main chapters of this thesis and to the GEOTRACES sampling and sample handling protocols (the GEOTRACES 'Cookbook') as reported by Cutter et al. (2014, 2017), which were strictly followed in my research.

The low concentrations of TMs in seawater relative to the prevalence of contamination sources on ships and in traditional laboratories (e.g., dust, rust, galvanized material, brass fittings, paint with zinc and copper antifouling agents, and sacrificial zinc anodes) require strict adherence to proper cleaning and handling procedures during all phases of sampling and analysis. As a result, several precautions were taken throughout the course of work to ensure the accuracy and reliability of the TM data produced, including the proper cleaning of all apparatus used for sampling, handling, and storage of samples, as well as the use of ultra-clean facilities and clean-handling techniques. These practices reduced the contamination risk by ensuring that measured quantities properly reflect the true concentrations of TMs in seawater.

2.1 Sample Collection and Handling

Seawater for trace metal samples was collected using a dedicated TM clean rosette and CTD system equipped with Go-Flo bottles (12 Liter; Ocean Test Equipment), operated with a plastic-coated conducting cable from a mobile winch system from GEOMAR, enabling the collection of surface and deep-water samples under contaminant-free conditions. Before initial sampling, the Go-Flo bottles were pre-cleaned by filling each bottle with (1.2 M) hydrochloric acid, followed by a thorough rinsing and refilling with ultra-pure water (Milli-Q – Millipore). As soon as the CTD-Rosette was recovered and brought onboard after collecting seawater, the Go-Flo bottles were immediately transferred to a containerized clean room (Class 100) for

subsampling. All personnel entering the clean-room and processing trace metal samples were fully suited with nylon body suits and hairnets when working with the samples.

The polyethersulfone (PES) filters used to collect marine particle samples (0.2 µm pore size, 25 mm diameter, Sartorius) were pre-cleaned by soaking them in (1.2 M) hydrochloric acid for 24 hours and thoroughly rinsed with ultra-pure water before being transferred to an ultra-pure water bath until ready to use. The plastic tweezers (chlorotrifluoroethylene (CTFE) or polytetrafluoroethylene (PTFE)) used to handle the filters were stored in (1.2 M) hydrochloric acid baths when not in use, and thoroughly rinsed with ultra-pure water (Milli-Q – Millipore) prior to and immediately after handling each sample filter.

2.2 Marine Particle Digestions

The leach and digestion methods have been thoroughly described in the methods sections of the subsequent chapters 3-5. A detailed step-by-step protocol was prepared during method development which contains in-depth technical information about sample handling and processing, and is provided in the appendix of this chapter. In addition, the protocol offers suggestions to prevent sample contamination, to improve data recording, and working efficiency, and also provides some data recording templates. The procedural blanks and certified reference material recoveries for each element are reported in the chapters where the respective pTM data is presented.

All apparatus used to prepare the leach and digestion reagents that were used (e.g., low density polyethylene (LDPE) and fluorinated ethylene propylene (FEP) bottles, Nalgene) were thoroughly cleaned using a 3-step acid washing procedure by first leaving them to soak in a (2%) Citranox or Mucasol bath for 1 week, followed by a 1 week soak in (6 M) HCl, and finally a 1 week soak in (8 M) HNO_3, rinsing with ultra-pure water before and after each step. Pipette tips that were used to dispense reagents and to dilute samples were first rinsed with (1.2 M) hydrochloric acid then with ultrapure water before withdrawing the desired solution. The 15 ml polypropylene (PP) centrifuge tubes (Metalfree ™, Labcon) used to store redissolved samples after the sample leaching and digestion procedures, as well as the 2 ml centrifuge tubes

(Eppendorf) used to centrifuge leached pTM samples, were cleaned using a 3-step cleaning procedure. The centrifuge tubes were first soaked in a (2%) Citranox or Mucasol bath for 1 day, followed by a 2-day soak in (1.2 M) HCl (Supra grade), and in (1.6M) HNO_3 (Supra grade) heated baths at 60°C, separately, thoroughly rinsing the tubes with ultrapure water before and after each step.

The heating and drying-down steps which involved marine particle leaching and digestions for the labile and refractory pTM fractions were performed in pre-cleaned perfluoroalkoxy (PFA) vials (30ml, Savillex) on a hot-plate (Savillex – HPX-200) with heating blocks (Figure 2.1a) under a custom designed and fabricated transparent polyvinyl-chloride (PVC) plastic cover within a fume cupboard in a TM-clean laboratory (Figure 2.1b and 2.1c), as described in the leaching and digestion protocol in the chapter appendix.

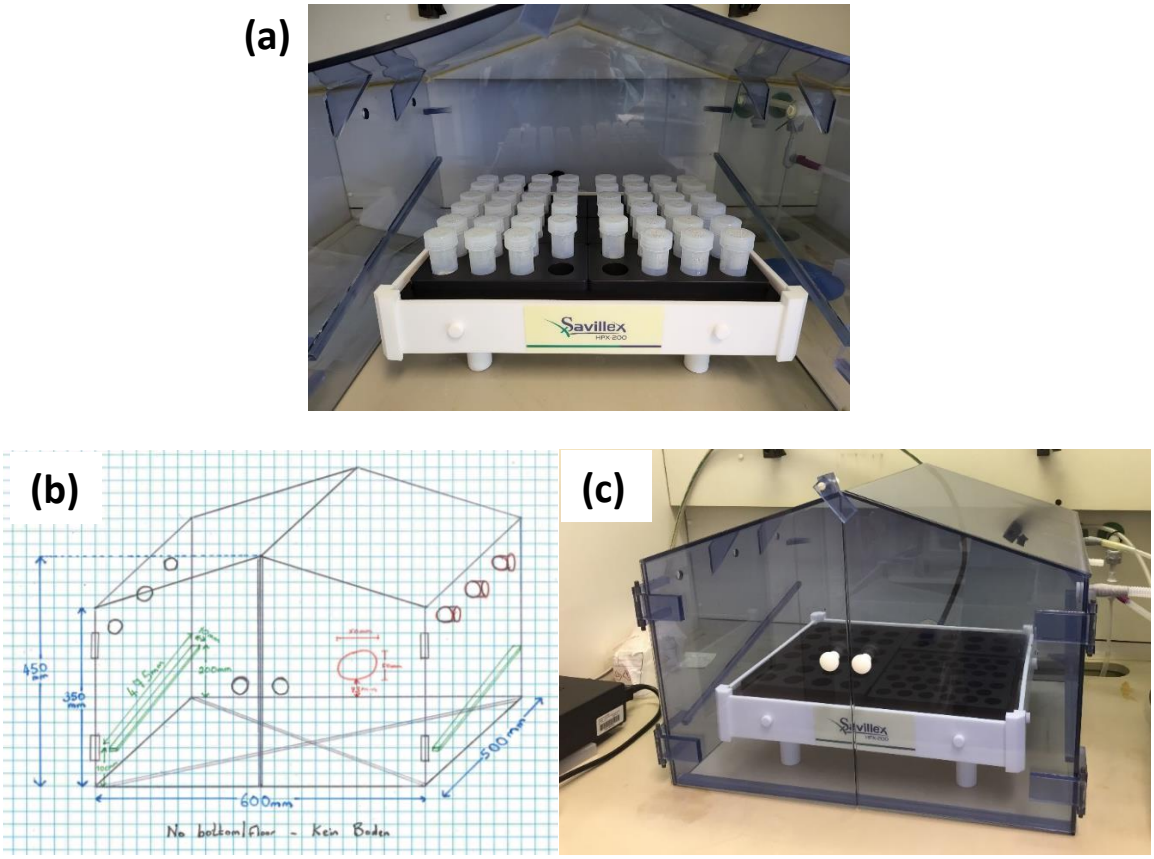

Figure 2.1. (a) Typical Setup of the Savillex HPX-200 Hotplate with Graphite Heating Blocks and Perfluoroalkoxy (PFA) Vials for Marine Particle Digestions. (b) Raw Design of Custom Digestion Hotplate Cover with measurements. (c) Design of Custom Digestion Hotplate Cover used for Marine Particle Digestions After Fabrication.

2.3 Particulate Trace Element Analysis and Calculations

The analytical methods are explained in detail in the methodology sections of chapters 3-5, but they are briefly mentioned here to help clarify the calculation steps for determining particulate trace element concentrations. Briefly, trace element (TE) concentrations were determined following analysis on a high-resolution inductively coupled plasma mass spectrometry (HR-ICP-MS; Element XR, ThermoFisher) dedicated for measurement of seawater samples. To monitor analytical drift, all leached and digested marine particle samples were rediluted using the same (1M) HNO_3 with internally spiked indium (1 µg/L, Inorganic Ventures) prepared for each particle digestion batch. The digestion solution (50% HNO_3/15% H_2O_2, solution volume %) used for refractory particulate digestions was prepared with a 10 ng rhenium (Re) standard spike (Inorganic Ventures) to monitor sample loss. Indium and Re were selected as spikes to monitor drift and sample loss, respectively, since they are not naturally present in any detectable concentrations within the analyzed samples. Element concentrations were quantified using external multi-element calibration with standards (Inorganic Ventures) prepared in a sample-matched matrix (Cullen et al., 2001), and were analyzed each time samples were analyzed.

Each analysis batch typically included samples from the same leach and digestion batch, which were all prepared using the same (1M) HNO_3 with internally spiked indium (1 µg/L, Inorganic Ventures) within the analytical sequence. The redilution acid blanks used for each batch of particle leach and digestions were filled and stored in the same pre-cleaned 15 ml centrifuge vials used for the samples and were later measured alongside the samples in the same analytical sequence. Procedural blanks from blank PES filter digestions were also measured alongside samples in their respective analytical batches for each digestion run. Sample element concentrations that exceeded the concentration of the highest standard in the multi-element calibration samples were further diluted using the same (1M) HNO_3, with internally spiked indium (1 µg/L), following their leach or digestion. This was done to guarantee that the indium concentrations used to monitor instrument drift were identical, and that the acid blanks used to correct the raw sample data were consistently matched for each sample.

Following their analysis via HR-ICP-MS, the raw sample data was generated in counts (cts). Since the instrument signal naturally fluctuates during the analytical run (<2% RSD between each sample), these values were adjusted to account for instrument signal drift by normalizing the generated values to the internally spiked indium standard. To obtain a 'drift-corrected' TE value, an indium correction factor was calculated and applied to the raw sample value (cts) of each unique sample (equation 2.1).

$$\boldsymbol{Drift\ Corrected\ TE}\ [\boldsymbol{cts}] = Raw\ TE\ [cts] \times Indium\ Correction\ factor = Raw\ TE\ [cts] \times \frac{Average\ Indium\ (all\ samples)\ [cts]}{Sample\ Indium\ (individual\ sample)\ [cts]}$$

Equation 2.1 – Drift Correction of Raw ICPMS data [cts].

Following instrument drift correction, the background TE content from the redilution acid used for the samples was subtracted using the mean values of the blank redilution acids from the corresponding digestion batch that stored in the same centrifuge vials as the samples after leach and digestions, yielding a 'sample blank corrected' TE value (cts). This ensured that the acid background TE contributions from each digestion batch were appropriately accounted for, even if there were minor TE differences between digestion batch redilution acids. The instrument detection limit was also determined at this stage as three times the standard deviation of the blank redilution acid data for the acid background correction.

$$\boldsymbol{Sample\ Blank\ Corrected\ TE}\ [\boldsymbol{cts}] = Sample\ Drift\ Corrected\ TE\ [cts] - Average\ Rediltion\ Acid\ Blank\ TE\ [cts]$$

Equation 2.2 – Sample Blank Redilution Acid correction [cts].

The concentrations of the analyzed samples (ng/ml, or ppb) were then calculated by dividing the sample blank corrected TE values (cts) by slopes (cts/ppb) generated from the 20-point external standard addition calibration curve measurements from the analytical sequence batch (Equation 2.3). The external standard addition calibration extended through concentration ranges of 5 orders of magnitude, 0.01 ppb – 750 ppb, with 4-standard points within each order of magnitude. A minimum of a 5-point standard calibration curve slope, which spanned 2 orders of magnitude within the measured sample TE concentration range, was chosen to determine the analyzed TE concentration per sample.

$$\boldsymbol{Analyzed\ TE\ Concentration}\ [\boldsymbol{ng/ml}] = \frac{Sample\ Blank\ Corrected\ TE\ [cts]}{TE\ Calibration\ Curve\ Slope\ [cts/ppb]}$$

Equation 2.3 – Analyzed Sample Trace Element Concentration [ng/ml]

The bulk TE content per sample filter (ng) was then calculated by multiplying the analyzed concentration (ng/ml) with the corresponding dilution factor and the redilution volume (ml) of the digested or leached sample (equation 2.4).

$$\boldsymbol{Bulk\ TE\ Content}\ [\boldsymbol{ng}] = Analyzed\ Concentration\ [ng/ml]\ \times Dilution\ Factor\ \times\ Sample\ Redilution\ Volume\ [ml]$$

Equation 2.4 –Bulk Trace Element Content per Sample Filter [ng]

The measured content from each respective fraction had to be accurately accounted for because the first step of the sequential digestion of the sample filters involved sub-sampling of the leached sample solution (i.e., the leachate) and partial transfer into the residual refractory particulate material. The 'bulk content' of the sample measurement (equation 2.4) from the L-pTM sample fraction was therefore less than the actual concentration, and the TE content from the transferred leachate had to be subtracted from the corresponding refractory sample fraction. The 'leachate transfer corrected bulk labile particulate TE content' (ng) was calculated by multiplying the uncorrected 'bulk content' value (ng) of the sub-sampled leachate (equation 2.4) with a leachate transfer correction factor. The leachate transfer correction factor was calculated by dividing the total volume of the leachate solution (ml) by the volume of the subsampled leachate (ml) after centrifugation, drying, and redilution of the sample labile particle fraction (Equation 2.5). The 'leachate transfer corrected bulk refractory TE content' (ng) was then calculated after subtracting the value for the remainder of the TE content (ng) in the volume of leachate transferred into its associated refractory sample vial (Equation 2.6).

$$\boldsymbol{Leachate\ Transfer\ Corrected\ Bulk\ Labile\ TE\ Content}\ (\boldsymbol{LpTE*})\ [\boldsymbol{ng}] = Uncorrected\ Bulk\ Leached\ TE\ Content\ [ng]\ \times \frac{Total\ Leachate\ [ml]}{Subsampled\ Transferred\ Leachate\ [ml]}$$

Equation 2.5 – Corrected Labile Trace Element Content per Sample Filter [ng]

$$\boldsymbol{Leachate\ Transfer\ Corrected\ Bulk\ Refractory\ TE\ Content}\ (\boldsymbol{RpTE*})\ [\boldsymbol{ng}] = Uncorrected\ Bulk\ Refractory\ TE\ Content\ [ng] - \left(\frac{Leachate\ transfered\ to\ Refractory\ [ml]}{Total\ Leachate\ [ml]} \times Bulk\ Labile\ TE\ Content\ (leachate\ Transfer\ Corrected)[ng]\right)$$

Equation 2.6 – Corrected Refractory Trace Element Content per Sample Filter [ng]

Following the leachate transfer corrections, the TE contributions to each sample filter from the procedural blanks (i.e., sample handling, leaching and digestion reagents, and blank PES filters) were accounted for. This was done by subtracting the median TE values of blank PES

filter samples that were processed alongside the seawater particulate samples for each digestion batch for the labile (Equation 2.7) and refractory (Equation 2.8) sample fractions. At this stage, the procedural detection limit was also determined as three times the standard deviation of the PES filter procedural blanks. The resulting procedurally corrected values (ng) reflect the TE content of the sample particulate matter from the total volume of seawater that was filtered.

$$\boldsymbol{Sample\ Labile\ pTE\ Content}\ [\boldsymbol{ng}] = Leachate\ Transfer\ Corrected\ Bulk\ Labile\ pTE\ [ng] - Median\ Labile\ pTE\ Procedural\ Blank\ [ng]$$

Equation 2.7 – Sample Labile Trace Element Content per Sample Filter [ng]

$$\boldsymbol{Sample\ Refractory\ pTE\ Content}\ [\boldsymbol{ng}] = Leachate\ Transfer\ Corrected\ Bulk\ Refractory\ pTE\ [ng] - Median\ Refractory\ pTE\ Procedural\ Blank\ [ng]$$

Equation 2.8 – Sample Refractory Trace Element Content per Sample Filter [ng]

Finally, the sample particulate TE concentrations were calculated by dividing the filtered seawater volume per sample (liters) with the sample pTE content (ng) for each fraction. These concentrations were then converted to molar concentrations by dividing them by their respective TE molar mass (Equation 2.9). The total particulate TE concentrations were calculated by summing the labile and refractory concentrations of each respective sample together (Equation 2.10).

$$\boldsymbol{Sample\ pTE\ Concentration}\ [\boldsymbol{pM}]: = \frac{Procedural\ Blank\ Corrected\ pTE\ [ng]}{Volume\ Filtered\ [L]} \times \frac{1}{TE\ Molar\ Mass\ [ng/nmol]} \times \frac{1000\ pMol}{1\ nMol}$$

Equation 2.9 – Sample Trace Element concentrations [pM]

$$\boldsymbol{Total\ (Summed)\ Particulate\ TE\ Concentration}\ [\boldsymbol{pM}] = Labile\ pTE\ Concentration\ [pM] + Refractory\ pTE\ Concentration\ [pM]$$

Equation 2.10 – Total Particulate Trace Element Concentration [pM]

Appendix for Chapter 2 Methods and Materials

This appendix contains a detailed step-by-step protocol that was developed while conducting marine particle digestion work for the particulate trace metal cycling research in this thesis. It provides in-depth instructions for handling and processing marine particle samples, along with suggested precautions to prevent contamination. In addition, practical tips for enhancing working efficiency and data recording templates are also included. While the protocol is specific to instrumentation at GEOMAR facilities, it helps promote the reproducibility of the presented research, facilitates understanding of the methods, and is intended to support future research aiming to leach or digest marine particles to determine particulate trace metal content.

Protocol: Processing Marine Particles Collected on Polyethersulfone (PES) Filters to Determine Labile and Refractory Phases using a Hot-Plate

Version 2.4

Prepared by: Ali A. Al-Hashem
(aalhashem@geomar.de)

AG Achterberg Working Group
GEOMAR-Helmholtz Center for Ocean Research – Kiel

Last Revised 16-June-2022

Summarized Steps for Sample Processing (Leach + Digest)

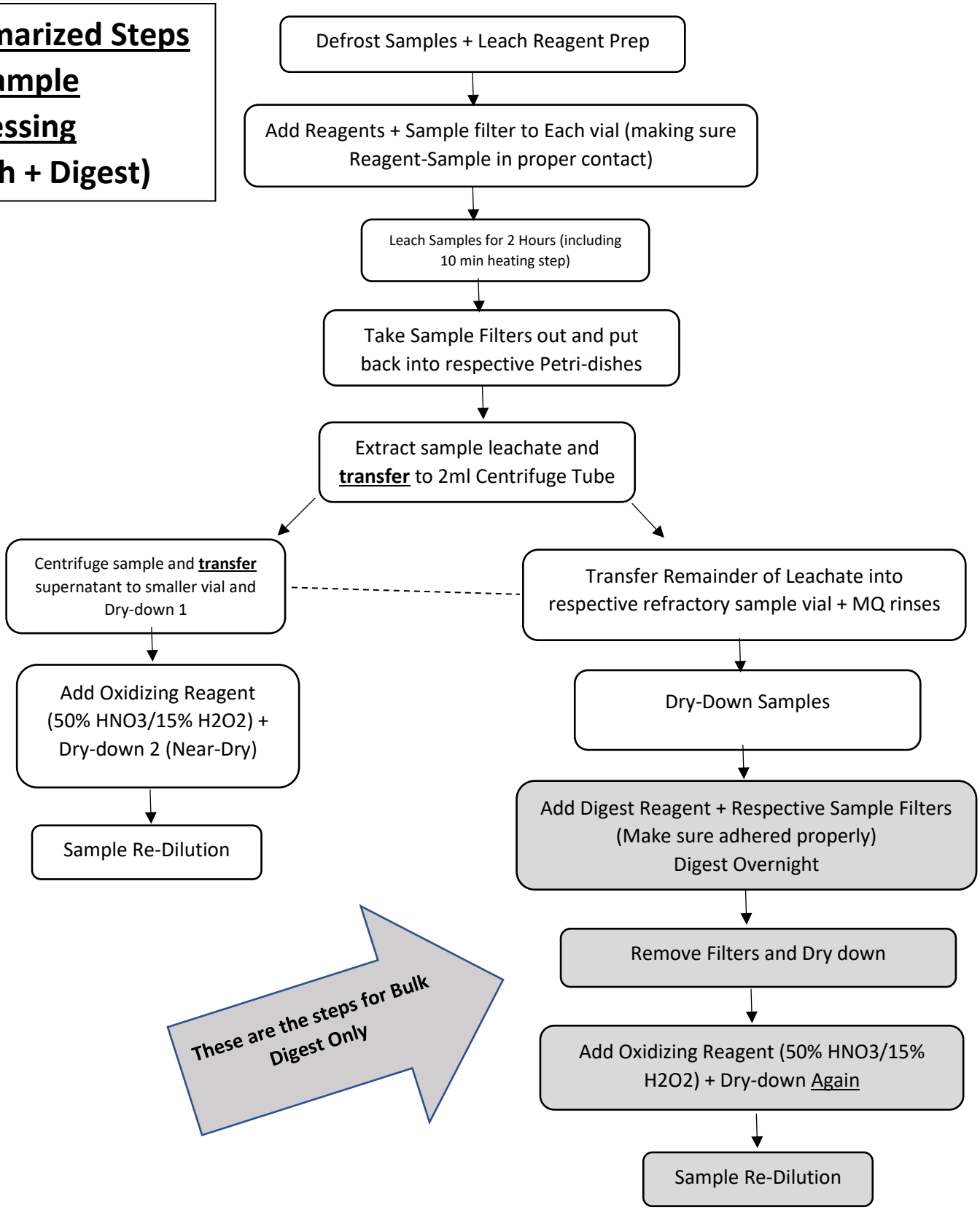

Apparatus and Reagents Necessary

Specific recommendations for some of the products/reagents can be found at the end of the protocol.

- Digestion suitable Hot Plate
- Heating Blocks
- Microbalance
- Sample hot-plate cover and acid vapor neutralization system
- Chemical Resistant Plastic Tweezers
- 2ml Centrifuge tube rack
- 15ml Centrifuge tube rack
- Countdown Timer/Stopwatch
- 1ml Pipette + Tips
- 5 or 10ml Pipette + Tips
- Designated toxic-waste canister (*appropriate for HF waste)

Pre-Cleaned Consumables necessary:

- PFA Digest Vials (30ml Savillex) + respective PFA caps (33mm)
- PFA Digests Vials (7ml Savillex) + respective PFA caps (24mm)

- Pre-prepared **process blank filters** (if not collected on cruise)

- 15ml Centrifuge Tubes
- 2ml Centrifuge [Eppendorf] Tubes
- Plastic disposable weighing spatula/straw
- Clean 1-Liter LDPE bottle for [1M or 2%] Nitric Acid Redilution acid
    - 125ml LDPE working bottle to pipette from
- Clean FEP bottles for Reagent Preparation

Reagents:

- [15.9M] Nitric Acid (Optima; UPA; or Sub-boil distilled)
- [28.9M] Hydrofluoric Acid (Optima or UPA)
- [≥99.9%] Glacial Acetic Acid (Optima or UPA)
- [≥30%] Hydrogen Peroxide (Ultratrace grade)
- [2M] Hydroxylamine Hydrochloride Solution (Pre-prepared using Hydroxylamine Hydrochloride Salt)
- [400ppb] Rhenium (Re) Standard
- [1ppm] Indium (In) Standard

Please observe proper use of PPE's when handling or processing any part of the digestion procedure. This is <u>especially critical for any steps involving the use of Hydrofluoric Acid (HF)</u>. Ensure that you are in compliance with all of the appropriate safety training and handling of HF, and that another qualified person is always present in the lab when working with any step that involves HF.

Labile Fraction on Hot Plate

This technique was adopted from the leaching technique described by Berger et al. 2008.

(1) Take samples out of the freezer to start defrosting them the morning of processing.
(2) Prepare Leaching Reagent (25% Acetic Acid + 0.02M HHCl)

In Pre-Cleaned 125ml Bottle:

- 25ml Acetic Acid [>99.9%] (Optima or UpA Grade recommended)
- 1ml of [2M] Hydroxylamine Hydrochloride (pre-prepared by diluting H.HCl salt in Milli-Q water)
- 74ml Milli-Q water
- Take small sub-sample and measure pH (Should be ~1.8). Record.

(3) Take picture of each filter before starting to process samples.
This step may be useful if they haven't already been photographed after sample collection. The image can be referred back to later, if necessary, when examining your data.
(4) Turn on Hot Plate to 95°C. Make sure heating blocks are properly secured. Allow the temperature read-out to reach 95°C.
(5) Measure out CRMs in designated Savillex Vials* (15-20mg). Record Weight.
* To remove any potential of increasing sample vial blank values, it is recommended to process the CRM's in a set of vials separate from the ones used for samples. The bulk material from CRM materials are much higher relative to the total material from marine particles on low-load filters. Remember to also process a separate CRM process blank using one of the vials designated for CRM work.
(6) Add **<u>2.5ml</u>** Leaching Reagent into each Sample and CRM vial.
(7) Place filters face down into vials. Keep petri-dishes that filters were in – will be used later.

Note: I've found it easier to handle the filters by adding the <u>reagent first</u> and then the filter. It allows for the filter to be guided/pushed down with minimal filter creasing.

(8) Make sure each sample filter is in complete contact with Reagent and no air bubbles are trapped underneath the filter. **<u>Start Timer for 2 Hours (Total Leach time)</u>**
(9) Tightly close vials and place on pre-heated Hot Plate. **<u>Start 2nd Timer for 10 minutes</u>**
(10) After the 10 minute heating time, remove vials and place in working area in the hood.
(11) After 2 Hours have elapsed, gently swirl vials to mix the solution, and remove sample filters and place in respective their petri dishes. (These will be used later for the refractory)

Note: It is easier to extract the filter by maneuvering it onto the side by swirling the vial and tapping the top of closed vial, which will move the filter towards the top of the vial, before pulling it out. Try to avoid getting any leachate under the sample cap.

(12) <u>Slowly</u> extract 1.8ml of leachate and transfer into labelled pre-cleaned 2ml Centrifuge Tube. Try to minimize particles extracted.
The leachate will adhere to the pipette wall, so if you empty the pipette tip too quickly, there will be some solution that will continue to slowly run down the pipette walls and accumulate at the tip. This can be avoided if you <u>slowly</u> withdraw and dispense the solution from the pipette.

(13)Place 2ml tubes in Centrifuge, and repeat steps 10 and 11 for all remaining samples.
(14)Start Centrifuge at 14,500 rpm for 10 minutes.

Make sure you follow proper centrifuge use guidelines, maintaining equal masses in the slots opposite each other in the rotor.

(15)After centrifuge complete –transfer 1.5-1.8ml of supernatant into clean, pre-labeled 7ml Savillex vial, avoiding extraction of any particles at bottom of centrifuge tube.
(16)Place the 7ml savillex vials on hot plate, uncapped, and turn on Hot-plate to 110˚C to dry down samples to near-dryness (~2Hours). Note time and check on samples periodically.

**CRM samples tend to dry quicker than marine particle samples. Keep a closer eye on CRM samples taking care that they do not evaporate to dryness.*

(17)While waiting for samples to dry, continue to process the samples for the refractory fraction (discussed in next section), and label the pre-cleaned 15ml sample vials that will later be used for sample redilution.
(18)When samples dry down to appropriate level, remove from hot plate, loosely cap vials and allow to cool to room temperature.
(19)While waiting for samples to cool-down, prepare Oxidizing Reagent (50%HNO3 : 15% H2O2 solution (v/v)).

In clean 30ml FEP bottle:

- 7ml Milli-Q water
- 3ml Hydrogen Peroxide (Ultratrace grade)
- 10ml Conc. Nitric Acid (Sub-boil distilled or Optima)

(20)After samples have cooled, slowly add 0.5ml of oxidizing reagent to each vial.

*The samples typically react very quickly and froth. Be careful not to keep the pipette tip too close to the sample when adding the reagent, or else aerosols from the bursting frothed bubbles could contaminate your pipette tip.

(21)Loosely cap the sample vials and allow to sit for 30 minutes.
(22)Removing caps and re-placing the sample vials on hot plate allow samples to dry at 110˚C until a very small oily drop remains at the bottom of the vial (~35-45mins)
(23)Remove the dried-down sample from the hot plate and allow to cool to room temperature.
(24)Prepare a 1-Liter [1M] Nitric Acid solution with 1-ppb In spike.

- 63ml Conc. Nitric Acid (Sub-boil distilled or Optima
- 936ml Milli-Q water
- 1ml [1ppm] Indium Standard (pre-prepared from stock standard)

(25)Add 4.5ml of the prepared [1M] Nitric Acid to each vial to re-dilute samples.
(26)Tightly cap then shake each sample vial, and place on the Hot plate and heat to 80 ˚C for 1 hour to fully dissolve contents in vial.
(27)Remove vials from hot plate and allow to cool to room temperature. Shake vials, and then transfer to pre-cleaned, pre-labeled 15ml Centrifuge tubes.
(28)Fill 3x pre-cleaned 15ml Centrifuge vials with re-dilution acid blanks.
(29)Clean sample vials according to protocol described below.

Refractory Fraction on Hot Plate:

This technique was adapted from the Digestion technique described by Cullen and Sherrell 1999.

(1) Transfer the remaining leached solution from the 2ml centrifuge tube back into the original 30ml sample vial.
(2) Rinse each 2ml centrifuge vial with 3x 0.5ml separate rinses of Milli-Q water and transfer each rinse into each respective sample vial.
(3) Repeat for all remaining samples, then set the uncapped sample vials onto the hot plate.
(4) Turn on Hot-Plate at 110 C and heat to near-dryness (~90 minutes).
(5) While waiting for samples to dry, Prepare 10%HF:50%HNO3 Digest reagent.

In Pre-Cleaned 125ml FEP Bottle:

- 50ml HNO3 (sub-boil distilled)
- 10ml HF (Optima)
- 39ml Milli-Q water
- 1ml [400ppb] Re Standard Spike

(6) After Samples dry-down, remove from hot plate and allow to cool (~10 minutes)
(7) Re-insert each sample filter into its respective Refractory vial.
(8) Add **2.5ml** of Digest Reagent to each of the Sample vials.
(9) Close the vials and maneuver filters to the vial walls, sample side pointing inwards, by gently swirling around the vial and tapping the vial to work the filters towards the top. Do not tap too hard to avoid getting digest reagent underneath the cap.

Note: Many of the sample filters may be creased. They will require CAREFUL handling and pressing and flattening them against the vial wall using the tweezers. Be careful to avoid "rubbing-off" any of the filter material and be sure to always rinse tweezers thoroughly after every sample.

What I found to work great is pressing the very outer edge of the filter against the wall and maneuvering it upwards and against the wall. If at first it doesn't fully adhere, try rotating the filter using one of the tweezer tips with the moistened filter against the vial wall, and you will almost always find a "sweet spot" where the filters will securely stay in place.

(10) Check each vial and make sure the sample filter is adhered to vial wall. Leave between 0.5-1 cm distance between the top of the filter upper edge of the vial. Maneuver filter by swirling and tapping as necessary and note any abnormalities with any samples (Scrunched filter etc).
(11) Make sure the vials are capped VERY tightly. Place samples onto hot plate and turn on at 150°C and allow to reflux overnight [15 Hours].
(12) Next morning, turn off hot-plate (if not automatic) and allow samples to cool to room temperature.
If you take them off the Hot-plate and place them in the hood, they will cool faster, but wait at least 30 minutes before working with them.

(13) Before uncapping each sample individually, gently tap top of vial lids and twist the vials as you do so, so that condensed drops underneath the cap may trickle down to bottom. Unscrew the cap very slowly**, slightly tilted, with your gloved hand away from underneath the cap.

***The vials will commonly have a slight buildup of pressure. Any drops underneath the cap could be pushed out into the screw threads of the vial, or leak off the cap while opening the vials. This is why it is important to make sure you really minimize the droplets at the bottom of the vial cap.*

(14) Uncap sample vial, and using the pre-cleaned tweezers remove the filter from vial and transfer to small 125ml pre-filled waste beaker with Milli-Q water.

(15) Repeat for each sample.

(16) Place vials on hot plate and turn on to 110 and allow samples to dry-down to near dryness (~2 Hours).

(17) Discard the liquid from small waste beaker from step (14) into HF waste container. Rinse waste beaker twice by filling half way with Milli-Q water, gently swirling to rinse filters, and discard rinses into HF waste container. Then transfer filters into zip lock bag, and double-bag, then discard through appropriate laboratory waste.

(18) When samples have reached near-dryness, remove from hot plate, cover with caps and allow to cool to room temperature.

(19) While waiting for samples to cool, Prepare Oxidizing reagent (50%HNO_3 : 15% H_2O_2 solution)

In clean 30ml FEP bottle:

- 7ml Milli-Q water
- 3ml Hydrogen Peroxide (Ultratrace grade)
- 10ml Conc. Nitric Acid (Sub-boil distilled or Optima)

(20) After samples have cooled, slowly add 0.5ml of oxidizing reagent to each vial.

*The samples typically react very quickly and will froth. Be careful not to keep the pipette tip too close to the sample when adding this reagent, or aerosols from the frothed bubbles could contaminate your pipette tip.

(21) Loosely cap the sample vials and allow to sit for 30 minutes before removing caps and re-placing the sample vials on hot plate.

(22) Allow samples to dry at 110˚C until a very small oily drop remains at the bottom of the vial (~35-45mins)

** This would be a good time to label the vials you will be storing your rediluted samples in (e.g., 15 ml centrifuge vials)*

(23) Remove the dried-down sample from the hot plate and allow to cool to room temperature.

(24) Add 4.5ml of pre-prepared [1M] Nitric Acid to each vial to re-dilute samples.

(25) Tightly cap then shake each sample vial, and place on the Hot plate and heat to 80 ˚C for 1 hour to fully dissolve contents in vial.

(26) Remove vials from hot plate and allow to cool to room temperature. Shake vials, and then transfer to pre-cleaned, pre-labeled 15ml Centrifuge tubes.

(27) Fill 3x pre-cleaned 15ml Centrifuge vials with re-dilution acid blanks.

(28) Clean sample vials according to protocol described below.

Digest Vial Cleaning

New Vials:

(1) Place vial in 2% Citranox (or 2% Mucasol) bath for 24 hours.
(2) Rinse vials thoroughly with Milli-Q (at least 5 times) to ensure all detergent is removed.
(3) Fill vials half full with 50% HNO3/10% HCl/2% HF (v/v/v%) and close tightly with caps.
(4) Place on Hot plate and heat at 150°C and leave on overnight.
(5) NEXT DAY: Turn off Hot-Plate and take off vials and placing them on bench (working area), keeping then in the fume hood. Let cool down for 1 hour.
(6) Place HF/Toxic Waste container in fume hood, and a pre-filled plastic beaker with Milli-Q water and place in fume-hood (e.g., 3 Liter beaker filled with 2-Liters of Milli-Q).
(7) One-by-one: Uncap vials, and discard solutions into the Toxic waste container. Use Milli-Q rinse bottle to rinse the inside of the vial and cap 3 times, and discard rinses into HF waste container.
(8) Place the rinsed vials + caps into the prefilled beaker with milli-Q water, Repeat step (7) for each vial until all vials have been washed, or beaker is full.
(9) Take plastic beaker to the designated washing area, carefully pouring out water, and then filling it with Milli-Q water and allowing it to overflow.
(10) Repeat step (9) until 3x rinsing cycles have been completed.
(11) Rinse each vial and cap 3x with Milli-Q water, and place in tray.
(12) Transfer vials and caps into 15% HCl bath and place in hot-plate for heated cleaning at 65°C overnight.
(13) NEXT DAY: Turn off hot-plate and allow bath to cool.
(14) Remove vials and caps from bath and wash each 5x individually with Milli-Q water.
(15) Repeat Steps 3-15 a second time. After done proceed to Step 16.
(16) Place in Laminar flow hood and allow to air-dry.
(17) After drying, they are ready for use, or should be double-bagged and stored for future use.

After Digestions:

After completion of sample re-dilutions:

(1) Place vials in Plastic beaker pre-filled with Milli-Q.
(2) Take vials to designated washing area and carefully pour out water, and then fill with Milli-Q water and allowing it to overflow. Then pour out water again.
(3) Clean the insides of the vial using Berkshire tissue, Kimwipes or other appropriate tissues to remove any residual material. Take care not to scratch the surfaces and be sure to use a different 'clean section' of the tissue for each vial.
(4) Repeat step (3) for every vial.
(5) Rinse each vial 3 times with Milli-Q water, then take to fume hood.
(6) Fill vials 1/4 - 1/3rd full with 50% HNO3/10% HCl/2% HF (v/v/v%) and tightly close with caps.
(7) Place on Hot plate and heat at 150°C and leave on overnight.
(8) NEXT DAY: Turn off Hot-Plate and take off vials and placing them on bench (working area), keeping then in the fume hood. Let cool down for 1 hour.

(9) Place HF/Toxic Waste container in fume hood, and a pre-filled plastic beaker with Milli-Q water and place in fume-hood (eg. 3 Liter beaker filled with 2-Liters of Milli-Q).
(10) One-by-one: Uncap vials, and discard solutions into the Toxic waste container, and use Milli-Q rinse bottle to rinse the inside of the vial and cap 3 times, and discard rinses in waste container. Then put vials + caps in to the pre-filled beaker.
(11) Repeat step (10) for each vial until all vials have been washed, or beaker is full.
(12) Take plastic beaker to the designated washing area, carefully pouring out water, and then filling it with Milli-Q water and allowing it to overflow.
(13) Repeat step (12) until 3x rinsing cycles have been completed.
(14) Rinse each vial and cap 3x with Milli-Q water, and place in tray.
(15) Transfer vials and caps into 15% HCl bath and place in hot-plate for heated cleaning at 65°C overnight.
(16) NEXT DAY: Turn off hot-plate and allow bath to cool.
(17) Remove vials and caps from bath and wash each 5x individually with Milli-Q water.
(18) Place in Laminar flow hood and allow to air-dry.
(19) After drying, they are ready for use, or should be double-bagged and stored for future use.

Further Notes and Recommendations:

Hot Plate Selection:

This protocol describes the processes as they are carried out on a Savillex HPX-200 hot-plate (with graphite heating blocks) for processing marine particles collected on 25mm PES filters.

Initial testing found that using non-digestion specialized hot-plates (ie, from IKA®) - without heating blocks - had limited sample capacity and underwent non-uniform heating. This led to drastically different sample dry-down rates (depending on their placement on the hot-plate) which increases the likelihood of samples being "overdried" and burned onto the vial bottom, interfering with the digestion efficiency. Completely dried down samples also tended to "flake-off" the bottom and re-mobilize, flying out of the sample vial due to static from gloves when grabbing the outside of the vials during handling.

Using the heating blocks also ensured appropriate spatial separation between the sample vials, reducing the likelihood of any potential cross-contamination, and improving the handling (during placement and removal) and of stability of the vials (from potentially tipping over). Most importantly, all samples dried down at the same rates regardless of their positioning on the hot-plate.

https://www.savillex.com/en/product/hotplates/hpx-200-hotplate-230-vac--550-200-230?pageid=19

Sample Vial Labeling:

Digestion Vials:

Regular permanent markers will not suffice for marking up the PFA vials and the ink will bead up. A "special" marker that is effective is the "PFA Marking Pen, Black or Red". They can be ordered from Savillex directly at: https://www.savillex.com/en/product/labeling/pfa-marking-pen-black--730-0400?pageid=19. I would recommend getting the "F" markers instead of the thinner "S" markers, as they are easier to marker and last a little longer. They do, however, come in a box of 10. If you prefer fewer markers, vendors can usually provide them to you. They are generally more expensive at websites like amazon.com, so I recommend ordering them through Savillex or one of their official vendors.

I recommend labeling each individual vial and respective cap with a unique number and/or letter combination and keeping them on. I have labeled all sample vials from "1 – 100" and CRM specific vials as "PACS-1 – PACS-9" or "BCR-1 – BCR-9" for Plankton CRMs. This way you are less likely to mix-up any caps while working with samples, and it is easier to identify problems with vials/caps (contamination or any defections).

Rediluted Sample Storage Vials:

When labeling the sample storage vials (e.g., 15 ml Centrifuge tubes) I recommend including the following information on each sample: (1) Cruise name; (2) Station and bottle No.; (3) Digest vial No.; (4) Digestion Batch Number; and (4) indicate the particulate fraction (e.g., L=Labile, R=Refractory, D=Total Digest only). Include the date of digestion on at least one of the samples per station. Also, label each sample pTM fraction with a different color (For example, leached samples labeled in blue, and **refractory samples in black**); this will prevent confusion in case of forgetting to include particulate fraction information (L or R) on the label.

2ml Centrifuge Vials:

When filling the 2ml centrifuge tubes before spinning in the centrifuge, I recommend not filling up to the maximum capacity of 2ml. This will cause the flip-lid to come in contact with the solution in the vial, and upon re-opening, it will tend to flick out the liquid trapped underneath the cap if not done carefully. This will cause a very small loss of sample and potentially contaminate any surrounding items.

I have found that filling the 2ml Centrifuge tubes with 1.8ml of the leachate solution before centrifuging them makes them easy to work with, then transferring 1.5ml out of the supernatant solution, after centrifuging, and into the separate vial used to process the leachate for the Labile particulate fraction (e.g., 7 ml Savillex digest vial).

Rhenium (Re) Spike Standard in Digest Reagent:

The Re spike serves as a way to monitor the recovery of the digested samples. Re is not expected to be present in the samples in any detectable quantity, so it can reliably be used to spike a known quantity of Re to each sample without having to worry about other sources or contamination of Re.

Another utility realized with having the Re spike is that it helps during the data calculations of samples after analysis as an additional 'fail-safe'. It provides a simple approach to notice any potential calculation errors by checking the recovered Re content [ng], with the expected content of 10 ng. For example, if the calculated total Re recovery is at ~0.1 or ~100ng, this reflects an error that likely lies with the dilution factor used in the calculations made. So checking to make sure all of the refractory samples have a recovery of ~10ng Re (± acceptable margin of error) makes potential calculation errors easier to spot.

Re Standard used: https://www.inorganicventures.com/10-000ug-ml-rhenium-125ml

Hydroxylamine Hydrochloride:

I used TM-Grade Hydroxylamine Hydrochloride when preparing my stock [2M] Hydroxylamine Hydrochloride and have found it to have reasonable blanks. I was unable to find a purer form in the market at the time of processing my samples.

This is the product that I used supplied by Sigma-Aldrich:
50g Hydroxylamine hydrochloride (99.999% trace metals basis)
Product Code:[431362-50G]
Can be found at: https://www.sigmaaldrich.com/catalog/product/aldrich/431362?lang=de&region=DE

Tweezers used for handling filters:

After trying out various different types of plastic tweezers to handle the samples, I have found that several that are either too flimsy and do not securely grip the filters or are too bulky when handling or

manipulating the filter in the narrow opening of the vial. Specifically, I have found PTFE tweezers to be too soft, and PP type tweezers too flimsy.

I have been very pleased with a set of CTFE type tweezers that were very suitable for working with the filters; they are rigid enough to keep a secure hold of the filters, and narrow enough to work comfortably within the narrow vials. They are also very chemical resistant, so they should be suitable for use with strong reagents.

The tweezers that I recommend can be found at:
https://www.carlroth.com/de/en/Labware/Laboratory-Glass%2C-Vessels%2C-Consumables/Forceps/Plastic-forceps/p/0000000000003ac100040023_en?text=C321.1

I recommend having at least 2 sets of these tweezer and storing them in an HCl bath when not in use to keep them clean.

Hot-Plate Set-up Recommended:

HPX-200 Savillex Heat Plate [w/temperature control] (550-23-17) -Savillex

8-Position Heating block (550-31-08) - Savillex

17-Position Heating Block (550-23-17) - Savillex

30ml PFA Vial, Rounded Interior (200-030-20) – Savillex

33mm PFA closures - (600-033-01) – Savillex

Vial Tray w/10x openings (730-2002) – Savillex

7ml PFA Vial, Rounded Interior (200-007-20) – Savillex

24mm PFA Closures (600-024-01) – Savillex

Vial Tray, 21mm Openings (730-2001) – Savillex

Other reagents and apparatus:

Here is a list of some of the supplies used during sample processing and where they can found:

15 ml Centrifuge Tubes (For storing redissolved samples after leach/digestion):

https://www.carlroth.com/de/en/centrifuge-tubes/centrifuge-tubes-metal-free/p/xx96.1

I recommend ordering the vials with a rack (which is made out of cardboard) which makes storage of samples easier, more convenient, and 'spatially' efficient.

Hydrogen Peroxide (Ultratrace grade - Sigma Aldrich):

https://www.sigmaaldrich.com/DE/de/product/sial/16911

You can send a request to order it to Deorders@sial.com asking for 250ml Ultra-Pure Hydrogen Peroxide, SKU no. 16911-250ML-F.

Leach + Digest Data Sheet Template (Front):

Date: ___/___/____

Particulate TEIs Digestions Data Sheet

Leach+Refractory Data

Samples Photographed: [ ] **Redilution Volume: _____ml**

Leaching Reagent Prep. Date: __/__/____ Reagent pH: _____

27.5 ml	Acetic Acid
1.1 ml	[2M] Hydroxylamine Hydrochloride
82.4 ml	MQ Water

Leach Reagent: _____ml / Sample

50% HNO3/ 15% H2O2 **#1 (Leach)**: ___ml / Sample

10 ml	HNO3
3 ml	H2O2
7 ml	MQ Water

Digest Reagent Prep. Date: __/__/____

50 ml	HNO3
10 ml	Hydrofluoric Acid
39 ml	MQ Water
1 ml	[400ppb] Re Spike

Digest Reagent: _____ml / Sample

50% HNO3/ 15% H2O2 **#2 (Refractory)**: ___ml / Sample

25 ml	HNO3
7.5 ml	H2O2
17.5 ml	MQ Water

Digest Vial ID	Sample ID	Leach Vial ID	LR Trans [ml]	Leach Drying	Drying Before Digest	Drying After Digest	Remarks

** **LR** = Leaching Reagent; **ND** = Near Dryness; **TD** = Total Dryness*

Leach + Digest Data Sheet Template (Back):

Particulate TEIs Digestions Data Sheet

Remarks & Observations

	Temp [°C]	Duration
Leach		
Digest		

References

Berger, C. J. M., Lippiatt, S. M., Lawrence, M. G., & Bruland, K. W. (2008). Application of a chemical leach technique for estimating labile particulate aluminum, iron, and manganese in the Columbia River plume and coastal waters off Oregon and Washington. *Journal of Geophysical Research*, *113*, 1–16. https://doi.org/10.1029/2007JC004703

Chester, R. ; Hughes, M. J. (1967). Chemical Geology - Elsevier Publishing Company Amsterdam Printed in the Netherlands A chemical technique for the separation of ferr-manganese mineral, carbonate minerals and adsorbed trace elements from pelagic sediments. R . Chester and M . J . *Chemical Geology*, *2*, 249–262.

Cullen, J.T., Field, M.P., Sherrell, R.M., 2001. Determination of trace elements in filtered suspended marine particulate material by sector field HR-ICP-MS. R. Soc. Chem. 16, 1307–1312. https://doi.org/10.1039/b104398f

Cullen, J. T., & Sherrell, R. M. (1999). Techniques for determination of trace metals in small samples of size-fractionated particulate matter: phytoplankton metals off central California. *Marine Chemistry*, *67*, 233–247. Retrieved from http://www.whoi.edu/science/MCG/people/jcullen/CullenandSherrell1999MarChem.pdf

Cutter, G.A., Andersson, P.S., Codispoti, L., Croot, P.L., Francois, R., Lohan, M.C., Obata, H., Rutgers van der Loeff, M.M., 2014. Sampling and sample-handling protocols for GEOTRACES cruises 1–238. https://doi.org/http://www.geotraces.org/science/intercalibration/222-sampling-and-sample-handling-protocols-for-geotraces-cruises

Cutter, G. A., Casciotti, K., Croot, P. L., Geibert, W., Heimbürger, L.-E., Lohan, M. C., Planquette, H., & van de Flierdt, T. (2017). Sampling and Sample-handling Protocols for GEOTRACES Cruises. Version 3, August 2017. *GEOTRACES Community Practices*, *August*, 139pp. & Appendices. http://www.geotraces.org/images/stories/documents/intercalibration/Cookbook.pdf

Chapter 3: Particulate Trace Metal Sources, Cycling, and Distributions on the Southwest African Shelf

Ali A. Al-Hashem[1,2], Aaron J. Beck[1], Stephan Krisch[1,3], Jan-Lukas Menzel Barraqueta[1,4], Tim Steffens[1], Eric P. Achterberg[1,2]

[1]GEOMAR Helmholtz Centre for Ocean Research Kiel, Kiel 24148, Germany.

[2]Christian-Albrechts-University of Kiel, Christian-Albrechts-Platz 4, 24118 Kiel, Germany.

[3]Now at: Bundesanstalt für Gewässerkunde, Am Mainzer Tor 1, 56068 Koblenz, Germany.

[4]Now at: European Ecological Consulting S.L. (EECO), Amorebieta 48340, Spain.

Published in *AGU* Global Biogeochemical Cycles

Al-Hashem, A.A., Beck, A.J., Krisch, S., Barraqueta, J.-L.M., Steffens, T., Achterberg, E.P., 2022. Particulate Trace Metal Sources, Cycling, and Distributions on the Southwest African Shelf. Global Biogeochem. Cycles e2022GB007453. https://doi.org/10.1029/2022GB007453

Key Points

(1) Different oxidation kinetics lead to decoupled Fe and Mn oxide redox cycling within oxygen-depleted waters on the Benguela Shelf.

(2) Lower lability of particulate phosphorus (~41%) indicate potential refractory biogenic source on Benguela shelf.

(3) Benthic nepheloid particles formed important sources of Fe & Mn oxides that adsorb TMs, and serve as TM sources from shelf to open ocean.

Abstract

We present labile (L-pTM) and refractory (R-pTM) particulate trace metal distributions of Fe, Mn, Al, Ti, Co, Zn, Cd, Ni, Pb, Cu, and P for a transect along the southwest African shelf and an off-shore section at 3°S of the GEOTRACES GA08 section cruise. Particle sources and biogeochemical cycling processes are inferred using particle-type proxies and elemental ratios. Enhanced concentrations of bio-essential L-pTMs (Zn, Cu, Ni, Cd, Co, and P) were observed in the Benguela upwelling region, attributed to enhanced primary production. Bio-essential pTM stoichiometric ratios (normalized to pP) were consistent with phytoplankton biomass across the transect, except for Fe and Mn, which included adsorbed and labile oxide phases. Low pP lability (~41%) suggests a potential refractory biogenic source on the Benguela shelf. Variable labilities observed between stations along the transect indicated potentially different biogenic pP labilities among different plankton groups. Benthic resuspension was prevalent in (near-)bottom waters along the transect and formed an important source of Fe and Mn oxides. Lithogenic particles along the entire shelf were Mn deficient and particles on the Benguela shelf were enriched in Fe, consistent with regional sediment compositions. Enhanced available-Fe (dissolved + labile particulate Fe) concentrations (up to 39.6 nM) were observed in oxygen-deficient (near-)bottom waters of the Benguela shelf coinciding with low L-pMn. This was attributed to the faster oxidation kinetics of Fe, allowing Fe-oxide precipitation and retention on the shelf, while Mn oxidation was slower. Enhanced L-pFe in the Congo River plume, which comprised as much as 93% of the available-Fe pool, was attributed to increased scavenging and formation of Fe oxides. Increased scavenging of other particle-reactive trace metals (TMs) (Mn,

Al, and Pb) was also apparent in Congo-influenced waters. However, particles did not play a significant role in transporting TMs off-shelf within Congo plume waters.

Plain Language Summary

Trace metals (TMs) are important to the functioning of marine ecosystems, with a range of TMs required as micronutrients by phytoplankton, while some are contaminants, and others may serve as tracers of water masses. Marine particles are key to the biogeochemical cycling of most TMs as sources, sinks, and essential transport vectors in the ocean. The transport and fate of TMs are often multi-faceted and rely upon a multitude of inter-related factors including particle sources/types, and environmental conditions, many of which are directly evident on continental shelves. Continental shelves thus are important conduits through which TMs are transferred from land to the ocean. Despite their importance, shelves are still understudied with respect to trace metal cycling. Here we present data from the longest continental shelf transect for TMs to date, which traversed through several key biogeochemical regimes, including an oxygen depleted zone, upwelling region, and a river plume, providing unique gradients under which particles from various sources and internal cycling processes were studied. A chemical leach was applied to marine particles to differentiate between particle types and phases. Utilizing the contrasting marine environments and particle types encountered along the transect, we highlight the major biogeochemical cycling dynamics controlling trace metal distributions, which provide valuable regional insights which may be extended to other regions of the global ocean.

Keywords: GEOTRACES; trace elements; marine particles; continental shelf; OMZ; nepheloid layers.

3.1 Introduction

Trace metals (TMs) are important to the functioning of marine ecosystems, with a range of TMs required as micronutrients by phytoplankton and serving as essential cofactors in metalloenzymes (Sunda, 1989, 2012). Iron (Fe), cobalt (Co), and manganese (Mn) are potentially (co-)limiting oceanic primary production (Browning et al., 2017, 2021; Martin et al., 1989; Moore et al., 2013) and, therefore their supply, removal and retention processes in the water column are important controls on phytoplankton growth. Marine particles play a vital role in the marine biogeochemical cycling of TMs as essential transport vectors (Jeandel et al., 2015), acting as sources and sinks of dissolved TMs (dTMs) through adsorption (e.g., Fe, Mn, Co, lead (Pb), copper (Cu), and aluminum (Al)), precipitation/dissolution (e.g., Fe and Mn), and/or bio-assimilation and remineralization (e.g., Fe, Mn, Zn, Cu, nickel (Ni), Co, cadmium (Cd)) (Boyd et al., 2017; Bruland et al., 2014; Bruland & Lohan, 2003; Goldberg, 1954; Morel & Price, 2003; Turekian, 1977). The interactions and exchanges between solid and dissolved TM phases are multi-faceted, relying upon interrelated biogeochemical mechanisms controlled by particle sources (types), characteristics, and environmental conditions (Anderson, 2020; Boyd et al., 2017; Bruland et al., 2014; Bruland & Lohan, 2003; Jeandel et al., 2015) many of which are evident on continental shelves (Elrod et al., 2004). Continental shelves form an important conduit for transfer between land and ocean of marine particles, yet remain understudied across large ocean basins (Charette et al., 2016; Henderson & Marchal, 2015).

The TM composition of marine particles reflects both particle source and biogeochemical cycling processes in the water column. Additional information about readily exchangeable or potentially soluble particulate TM (pTM) fractions can be gained by separating labile (L-pTM) from refractory particulate (R-pTM) phases. Elemental proxies are often employed as effective particle type indicators, namely particulate phosphorus (P) as a biogenic particle indicator, and an abundant lithogenic element (typically Al or Ti) for lithogenic particles (e.g., Lam et al., 2017, 2015a, 2015b; Lee et al., 2018; Liao and Ho, 2018; Martin et al., 1989; Ohnemus and Lam, 2015; Xiang and Lam, 2020). A chemical leaching application developed by Berger et al. (2008) (see section 2.2) to access the labile phase is now widely adopted for the study of marine particles (Cutter et al., 2017). The labile particulate phase reflects the

potentially bio-accessible, 'exchangeable' pTM pool, which includes readily reduceable, surface-bound (adsorbed/scavenged), and intra-cellular trace metals associated with biogenic particles, and authigenic particulate phases (i.e., Fe and Mn oxy-hydroxides) while leaving lithogenic and other refractory particle phases largely intact (Berger et al., 2008; Rauschenberg & Twining, 2015). Dissolved TM phases are often considered as the most reactive and bio-available to phytoplankton (Wells et al., 1995), but the L-pTM pool, particularly of Fe, comprises a significant fraction of the potentially available TM pool, and may buffer dissolved concentrations (for example, Achterberg et al., 2018; Berger et al., 2008; Hurst & Bruland, 2008; Lippiatt, Brown, et al., 2010; Milne et al., 2017). Hence, the "available" TM pool inferred in this study is the sum of the dTM and L-pTM pools, consistent with the definition adopted elsewhere (namely, Berger et al., 2008; Birchill et al., 2017; Hurst et al., 2010; Lippiatt et al., 2010; Milne et al., 2017; Twining et al., 2015).

The GEOTRACES GA08 section cruise, conducted in the southeast Atlantic Ocean, included the longest continental shelf transect sampled for TMs to date. The shelf transect traversed several major oceanographic features along the southwest African shelf, including the Benguela Upwelling System (BUS), an oxygen minimum zone (OMZ), and the Congo River plume. Regional particle sources included atmospheric deposition derived from surrounding deserts (Jickells, 2005; Prospero, 1996), riverine discharge (Vangriesheim et al., 2009), resuspended benthic sediment (Inthorn et al., 2006), and enhanced bio-assimilation of TMs into organic (biogenic) particles within the BUS (Carr, 2001; Shannon & Nelson, 1996). The combination of contrasting particle sources and oceanographic regimes that were sampled during the GA08 cruise offered unique gradients in pTM distributions under which TM biogeochemical cycling could be studied.

The primary goal of this study is to present, describe and interpret the pTM distributions and biogeochemical processes affecting pTMs along the southwest African shelf, and characterize dominant particle phases and sources of Fe, Zn, Cd, Mn, Co, Ni, Cu, Al, Ti, Pb, and P. The study was carried out utilizing chemically labile and refractory pTM phases, and elemental abundance ratios. We utilize dTM data and ancillary measurements from paired

samples. Insights from our data set offered valuable insights to regional TM cycling processes, which may be extended to other shelf regions of the global ocean.

3.2 Materials and Methods

3.2.1 Study Region

This study focuses on samples collected along a southwest African coastal transect of the GA08 GEOTRACES section cruise, between 28.8˚S and 3˚S (Figure 3.1), conducted during the austral summer of 2015 (22 November – 27 December) on *RV Meteor*. Regional water circulation includes the southward flowing Angola Current in the north bounded by the Tropical/Equatorial Eastern Atlantic Current, and the northward-flowing Benguela Current in the south bounded by the Agulhas current from the Indian Ocean (Peterson and Stramma, 1991; Shannon, 2001; Shannon et al., 1987; Shannon and Nelson, 1996). The two currents converge at the Angola-Benguela Front (ABF), north of Walvis Ridge, and are carried westward into the Angola Basin. The main water masses intersected along the transect are described below (see section 3.3.1).

The transect extended from southern Namibia at the southernmost point (28.7°S) and across to the shelf waters at Gabon at the northernmost station (3°S), where a longitudinal transect away from the shelf to 0° Meridian was sampled. The seafloor depths of the stations along the transect varied between 53 and 4501 m, including on-shelf and off-shelf stations. The cruise track traversed several oceanographic features along the shelf, including the Congo River outflow (stations [ST] 13-15; at 6.2˚S), BUS (ST 43-51, 1-4; between 18.6˚S and 28.8˚S), and an OMZ that extended throughout the transect (at a depth of ~50–600 m), with more pronounced oxygen-depletion on the Benguela shelf (see section 3.3.1). The Congo River provides a significant number of particles and organic matter to coastal waters (Vangriesheim et al., 2009), influencing TM cycling. Sampling nearest the Congo River outflow included a short (~100 km) transect of three stations (ST 13-15) at 6°S – 6.2°S, approximately 40-140 km away from the Congo River mouth. Anoxic and sulfidic shelf sediments are documented within 50 km of some stations on the Benguela shelf (e.g., ST 51) (Borchers et al., 2005; Inthorn et al., 2006). Phosphorite deposits are also widely documented on the Namibian shelf extending to Walvis

Ridge (Compton & Bergh, 2016). The Namib Desert is an important source of desert dust to the adjacent stations on the Benguela shelf compared to northern stations. The stations on the Benguela shelf are shallower and were sampled closer to the coast compared to the stations North of Walvis Ridge. The transect along the African shelf is hence sub-divided and described between the northern non-upwelling (NORTH; ST 6-20) and shallower Benguela upwelling regions (BENG; ST 43-51 & 1-5), separated by Walvis Ridge and Angola-Benguela Front (ABF) (Figure 3.1).

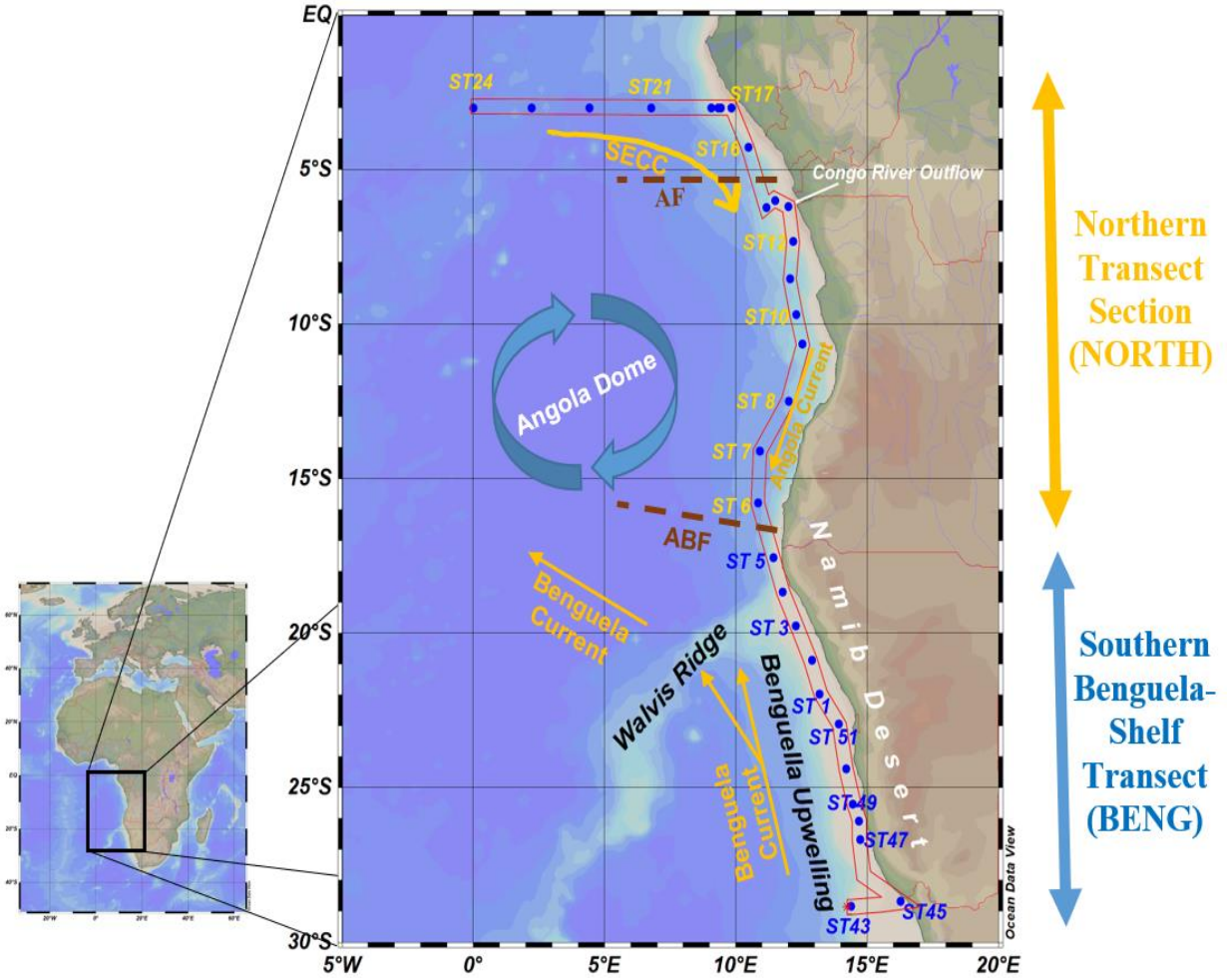

Figure 3.1. Map showing the large-scale circulation and oceanographic features that influence the Benguela ecosystem and Angola Basin, and part of the GA08 (M121) cruise track. Stations labeled in blue indicate the shallower stations above the Benguela shelf (BENG), and stations labeled in yellow indicate the Northern region stations (NORTH). ABF = Angola-Benguela Front; AF = Angola Front; SECC = South Equatorial Counter Current. Figure illustrations adapted from Shannon, (2001).

3.2.2 Sample Collection

Sampling was carried out following GEOTRACES protocols (Cutter et al., 2010) using a dedicated GEOTRACES trace metal clean CTD rosette (Seabird), equipped with 24 Go-Flo bottles (12 Liter; Ocean Test Equipment) to collect full water-column depth profiles. After each cast, the Go-Flo bottles were transferred to a containerized clean-room for subsampling seawater for dTM, pTM, and other parameters. A few failed bottle closures from CTD casts resulted in no samples being collected from the respective bottles, particularly in surface waters between stations 6 – 8, North of Walvis Ridge. Marine particle samples were collected by filtering typically 4 liters (range 0.38-6.8 L) of seawater through 0.2 µm pore-size acid cleaned polyethersulfone (PES) membrane filters (25 mm diameter, Sartorius). After filtration, samples were lightly misted with ultra-pure water (Milli-Q, Millipore) to remove salts, then transferred to acid-cleaned Petri-dishes, sealed with Parafilm, and stored frozen at -20°C until analysis in land-based facilities. The dTM samples were filtered through cartridge filters (0.2/0.8 µm Acropak-500, Pall) into acid-cleaned low-density polyethylene (LDPE) bottles, acidified to pH <2 using hydrochloric acid (UpA grade, Romil), and stored for later analysis.

In addition, surface seawater samples (~3-4 m) were collected for dTM analysis using a trace-metal clean tow-fish and a Teflon-diaphragm pump with acid-washed braided PVC tube while the ship was steaming; the waters were directly transferred into the containerized clean-room (Achterberg et al., 2001). Seawater was in-line filtered through a 0.8/0.2 µm cartridge filter (AcroPak1000, Pall) and collected into acid-cleaned 125 ml LDPE bottles, and subsequently processed identically as the samples from the trace metal clean CTD. No particulate trace metal samples were collected from the tow-fish.

3.2.3 Analytical Methods

Particulate samples were processed sequentially by leaching the filters following the protocol of Berger et al. (2008), followed by a strong acid digestion of the residual refractory material to determine L-pTM and R-pTM fractions using a method adapted from Cullen and Sherrell (1999). Briefly, the samples were processed in perfluoroalkoxy (PFA) digestion vessels (Savillex), and first leached in 2.5 – 3 ml of leaching reagent consisting of a weak acid (25%

acetic acid, Optima grade, Fisher Scientific) and a mild reducing agent (0.02 M hydroxylamine hydrochloride, Sigma TM grade) for a total leach time of 2 hrs, including a short heating step (90°C-95°C) of 10 mins. Subsequently, the leachate was centrifuged, sub-sampled, and processed separately from the residual (refractory) particles. The residual leachate remaining following sub-sampling from the centrifuged samples (0.1-0.2 ml) was transferred and processed with the refractory particles, with any contributions of TMs in the transferred leachate removed from the refractory particle fraction.

The filters with residual particles were adhered to the inner wall of the digestion vessel and reflux-digested at 150˚C for 15 hrs in 2.5 ml of a strong acid digestion solution (50% HNO_3/10% HF v/v %; Optima grade, Fisher Scientific). The digestion solution was prepared with a 10 ng rhenium (Re) standard spike (Inorganic Ventures) to monitor sample loss.

Following each leach-digestion step, the respective fractions were heated to near dryness, and 0.5 – 1 ml of 50% HNO_3/15% H_2O_2 (v/v%) solution was added before being heated to near dryness a second time. The final residual drops (< 50 µL) were re-diluted using 4.5 ml of 1 M nitric acid solution with an internal indium standard spike (1 µg/L), used as an analytical drift monitor, and stored in acid-cleaned 15 ml polypropylene tubes (MetalFree™, Labcon). The digested samples were analyzed using a high resolution inductively coupled mass spectrometer (HR-ICP-MS; Element XR, ThermoFisher) and quantified using external multi-element calibration with standards (Inorganic Ventures) prepared in a sample-matched matrix (Cullen et al., 2001).

The total particulate concentrations (T-pTM) reported are the sum of sample L-pTM and R-pTM concentrations. Blank PES filters were dipped in ultra-pure water and treated identically to sample filters, with at least two processed in each digestion batch as procedural blanks (total *n*= 30). The mean procedural blank values for each respective digestion batch were used to correct and determine sample concentrations. At least two replicates of certified reference material (BCR-414 freshwater plankton; 16.2-24.5 mg) were processed alongside the particulate samples in each digestion batch to monitor leach consistencies and total recoveries across all digestion batches. The efficacy of the digestion procedure on the lithogenic matrix was tested by employing the refractory digestion steps, without the chemical leach, using sediment

reference material (PACS-3; 17.5-34.8 mg). The procedural blank values, limits of detection, and reference material recoveries for the particulate analysis are summarized in Table S3.1.

Dissolved TM samples were measured following the procedure of (Rapp et al., 2017) using HR-ICP-MS (Element XR, ThermoFisher) after offline pre-concentration of dTMs using an automated pre-concentration system (SeaFAST – Elemental Scientific) and quantified using isotope dilution (Fe, Cu, Zn, and Ni) or standard addition (Mn, Co and Pb). Dissolved TM measurements were validated using GEOTRACES GSC reference seawater (measured values 1.60 ± 0.16 nM dFe; 1.85 ± 0.34 nM dMn; 1.29 ± 0.12 nM dCu; 1.31 ± 0.15 nM dZn; 4.27 ± 0.30 nM dNi; 0.038 ± 0.04 nM dPb; *n*=8), which were within ranges reported by Wuttig et al. (2019) (Except dCo which was slightly higher 0.117 ± 0.007 nM dCo). Dissolved aluminum was measured following the batch lumogallium method (Hydes and Liss, 1976) and validated measuring GS reference seawater (27.8 ± 0.2 nM; *n*=4; Consensus value 27.5 ± 0.2 nM, Menzel Barraqueta et al., 2019).

Macronutrient samples (NO_2^-, NO_3^-, PO_4^{3-}, and $Si(OH)_4$) were collected from each Go-Flo bottle and measured on-board using segmented flow injection analysis (QuAAtro - Seal Analytical). The hydrographic parameters, including dissolved oxygen (Seabird), fluorescence (Turner Designs), turbidity (Seapoint), and beam attenuation (BAT) (WETLabs) were measured using sensors mounted on the CTD frame (Seabird SBE 9plus - Seabird). The dissolved oxygen sensor data was calibrated using discrete samples measured using the Winkler titration method (Hansen, 2007; Winkler, 1888).

Statistical analysis to determine the bivariate Pearson's correlations and principal component analysis (PCA) was carried out using OriginPro (2021) (Version 9.80) and a Microsoft Excel statistical analysis add-in software (Analyse-it for Microsoft Excel, Version 5.66) on log-transformed datasets, which showed normal data distributions (Figure S3.1 in Supporting Information). Water column sections, station profiles, and scatterplots were prepared using Ocean Data View (Schlitzer, 2018).

3.2.4 Particle Type Indicator Elements

We used refractory particulate Al (R-pAl) as a lithogenic proxy since adsorbed Al is presumed to be removed by the labile leach, whereas lithogenic particles remain largely intact (Berger et al., 2008; Rauschenberg & Twining, 2015). Moreover, Al is more abundant and shows relatively lower variation among reported continental crust reference types than Ti (Rudnick & Gao, 2013; Taylor & McLennan, 1995). Sample R-pAl, R-pTi, and R-pFe elemental ratios were used to distinguish among lithogenic sources by comparing them to available regional lithogenic references (Table S3.2).

The labile particulate pool includes amorphous and readily reducible Mn bio-oxyhydroxides (hereafter *Mn oxides)* and Fe oxy-hydroxides (hereafter *Fe oxides*), adsorbed TMs, and intracellular biogenic pTMs, which are dissolved by the chemical leach (Berger et al., 2008; Rauschenberg & Twining, 2015; Twining et al., 2015). These particulate phases are referred to within the L-pTM fraction.

Phosphorus is primarily associated with organic (biogenic) particles, and hence total particulate phosphorus (pP) was selected as an indicator of biogenic particles. Biominerals, such as biogenic silica and calcium carbonate, and particulate organic carbon (POC) were not analyzed.

3.3 Results and Discussions

3.3.1 Hydrographic Features

The main water masses along the transect were defined using isopycnal densities calculated using salinity and potential temperature measurements (Rahlf, 2020). The section of the water column north of Walvis Ridge comprised of Tropical Surface Water (TSW) in the top 20 m and Subtropical Underwater (STUW) in the subsurface mixed layer (20 – 50 m), which was underlain by South Atlantic Central Water (SACW) between 50 and 500 m. The deeper water masses in the Angola Basin included Antarctic Intermediate Water (AAIW) between ~500 and 1,200 m, Upper Circumpolar Deep Water (UCDW) between ~1,200 and 2,000 m, and North Atlantic Deep Water (NADW) between 2,000 and 4,500 m (Figure 3.2A). Upwelling of colder

(15-18°C) and less saline (~35) SACW was observed between 15.8˚S – 28.7˚S at the southern Benguela shelf stations (ST 45-51 & 1-5), including the Lüderitz cell (ST 49-51; 23-25.5˚S) (Rahlf, 2020; Rahlf et al., 2020, 2021), which is the most intense wind-driven upwelling cell in the world's ocean (Lutjeharms & Meeuwis, 1987). Enhanced primary production supported by upwelled nutrient-rich waters was evident by increased fluorescence (Figure 3.2D). The Congo River plume signal was confined primarily within the TSW layer (< 20 m), which persisted as far south as station 8 and northwest as far as station 22 (up to 1000 km from the Congo River mouth), evident in the salinity, radium and dAl distributions (Vieira et al., 2020; Menzel Barraqueta et al., 2019).

An OMZ (<50 µM oxygen) persisted along the transect extending from the Benguela shelf into the northern open ocean transect (Figure 3.2B). Oxygen concentrations decreased with depth (~25 – 200 m) on the Benguela shelf (BENG) extending to (near-)bottom waters (≤ 50 m from bottom), and the lowest oxygen concentrations (<4 µM) were recorded within the Lüderitz cell (ST 49-51; 23-25.5˚S). The sediments underlying the BENG upwelling stations are reported to be anoxic, with several stations near locations where sulfidic sediments were also reported (e.g., ST 49-51 <50 km away) (Böning et al., 2020; Borchers et al., 2005; Govin et al., 2012). A less intense oxygen minimum layer (< 100 µM oxygen) persisted at the NORTH latitudinal coastal transect stations (ST 6-16) primarily within SACW between ~50 and 600 m with concentrations down to 20 µM. The oxygen minimum layer extended off the shelf and into the open ocean (3˚S; ST 17-24) between ~200 and 500 m, with dissolved oxygen as low as 40.5 µM.

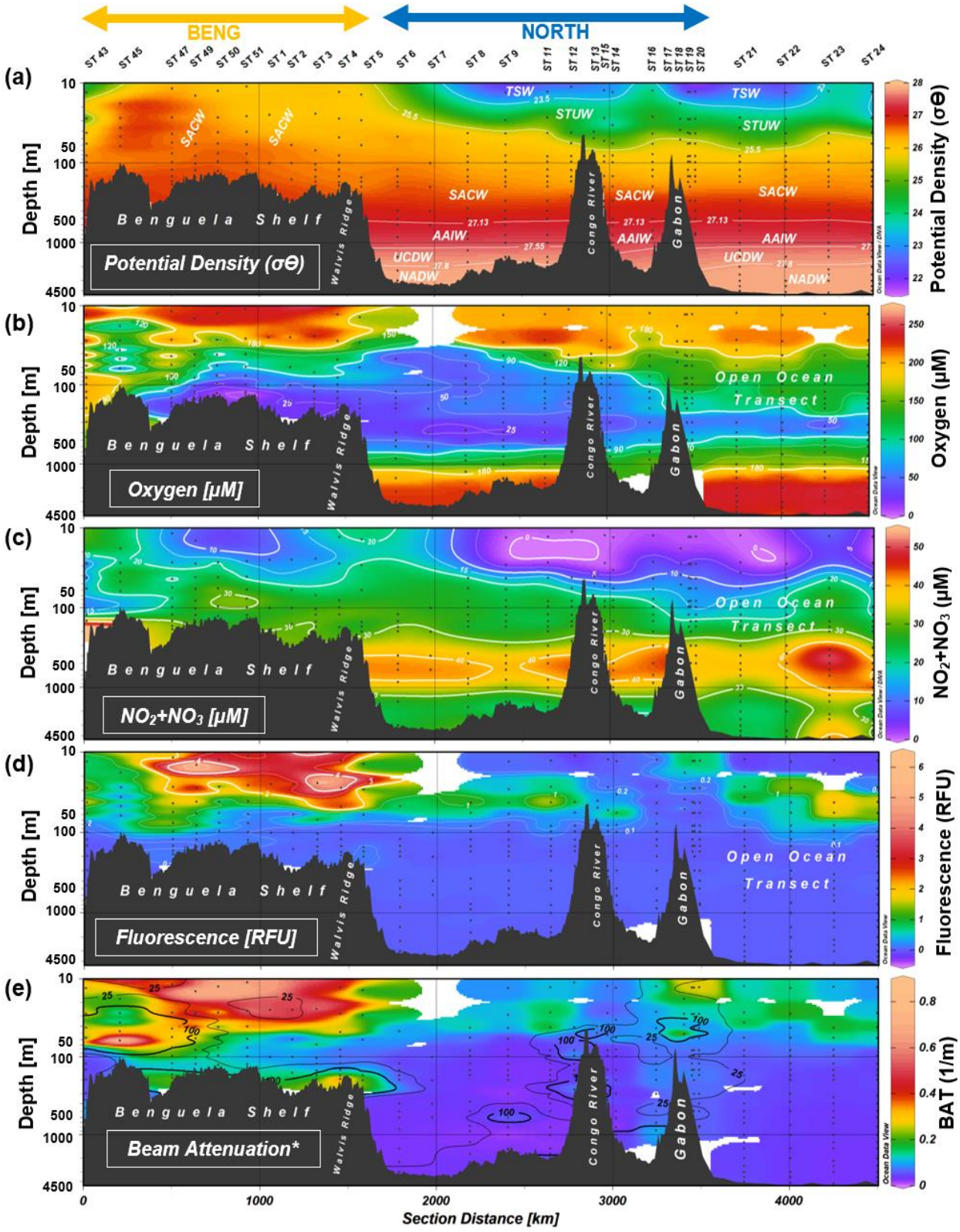

Figure 3.2. Main hydrographic features along the GA08 transect. Sections of (a) potential density of seawater with main water masses in the study region; TSW = Tropical Surface Water;

STUW = Subtropical Underwater; SACW = South Atlantic Central Water; AAIW = Antarctic Intermediate Waters; UCDW = Upper Circumpolar Deep Water; NADW = North Atlantic Deep Water. (b) dissolved oxygen concentrations. (c) nitrate + nitrite concentrations. (d) Fluorescence in Relative Fluorescence Units (RFU). (e) Beam Attenuation (BAT) in fractional attenuance per meter. Contour lines represent measurement intervals of each respective analyte, except (e), which are of refractory particulate Al (R-pAl) concentrations (nM). Note the logarithmic depth scales. Vertical labels used for stations 11-20 are to help distinguish between the stations that were close together and do not signify a categorical difference between stations.

3.3.2 Particulate Trace Metal Distribution Patterns

The T-pTM concentrations varied over orders of magnitude between 10^{-2} to 10^{7} pM, with mean concentrations decreasing in the order Al-P > Fe > Ti-Mn > Zn > Cu-Ni > Co > Cd-Pb (Figure S3.3 and S3.4). Most of the maximum concentrations of pTMs occurred in the bottom waters of the shallow coastal station 45 with concentrations reaching up to 5.11 µM pAl, 1.70 µM pFe, 138 nM pTi, 10.0 nM pMn, 3.19 nM pZn, 1.58 nM pNi, 438 pM pCo, 204 pM pPb, and 129 pM pCd (Figure S3.4). The highest concentration of pP was 253 nM at station 6 (11 m), and pCu was 1.33 nM at station 3 (69 m) (Figure S3.4). The T-pTM (pP, pCo, pFe, and pMn) concentrations at stations 6 and 7 were similar to values from a nearby station reported by Noble et al. (2012) collected in 2007 during the same season (Gac01-ST 19 – Figure S3.5). The pTM ranges were also comparable to other shelf and slope regions in the Pacific, Arctic, North and South Atlantic Oceans (Table S3.3). Sections of L-pTMs and R-pTMs are shown in Figures 3.3 and 3.4, respectively.

The mean labile fractions of T-pTMs were greater than 80% for Mn, Cd, Zn, and Pb, between 53 and 59% for Co, Ni, and Cu, around 41% for P, 25% for Fe, 19% for Al, and 1% for Ti (Figure 3.5). These observations are consistent with ranges reported elsewhere using the same chemical leach (e.g., Milne et al., 2017; Rauschenberg and Twining, 2015; Twining et al., 2019) (Table S3.4). An exception was pP, which was comparatively less labile in the current study compared with previous work, and R-pP was attributed primarily to residual (refractory) biogenic particles (see section 3.3.3). The labile pTM fractions generally decreased where the lithogenic particle abundance (R-pAl concentrations) increased, and refractory pTMs (primarily

lithogenic particles) dominated the pTM pool (van der Merwe et al., 2019), particularly for pAl, pPb, pCo, pCu, and pNi across the transect, and for pMn only below the photic zone on the Benguela shelf (Figure 3.5).

In the deeper NORTH stations (ST 6-11) and along the open ocean transect (ST 21-24), enhanced L-pAl/T-pAl fractions (up to 79.8%) were apparent only in (sub-)surface waters (≤350 m), with no enhanced L-pAl/T-pAl fractions below 2,000 m (Figure 3.5). The vertical concentration profiles of pCu, however, exhibited increasing labile fractions (52-78% L-pCu) and concentrations (13-47 pM L-pCu) at depths >2,000 m (Figures 3.3 and 3.5), where lithogenic particle concentrations were also relatively low (9.87 ± 12.8 nM R-pAl; n=23). The enhanced L-pCu fractions coincided with increases in dCu concentrations (up to 2.95 nM), indicating scavenging onto particulate phases (Bruland, 1980; Little et al., 2013, 2018), specifically within NADW (> 27.8 kg m^{-3} σ_Θ).

A principal component analysis (PCA) was conducted on log-transformed data for each particulate fraction for which full elemental and ancillary data were available (Figure S3.6). PC1 explained 50.1%, 36.8%, and 40.4% of the total variance of T-pTM, L-pTM, and R-pTM, respectively, and is associated with lithogenic particles, capturing 71 – 86 % of the individual variance of R-pAl. PC2 explained 16.7%, 22%, 18.2% of total variance of T-pTM, L-pTM and R-pTM, respectively, and is associated with biogenic particles, capturing 70 – 77% and 63 – 74% individual variance of fluorescence and T-pP, respectively. Despite their association to biogenic particles, only minor variances of several bio-essential L-pTMs (Zn, Cu, Ni, Cd, and Co; which are largely solubilized by the leach) were captured by PC2, with almost none for L-pCu and L-pZn (see section 3.3.3 below). This may be due to the variances of these L-pTMs being more closely associated with other abiogenic, non-lithogenic particulate phases, such as a scavenged phase, and by spatial (regional) contrasts in their concentrations (see section 3.3.2.1). PC4, PC5, and PC6 only captured relatively large variances for individual elements, specifically L-pZn, L-pCu, and L-pCd (81.4%, 69.4%, and 26.5% combined individual variances, respectively), likely reflecting variances arising from regional differences, with significant individual variance also captured for R-pTMs Ni (PC4: 60.7%), Cu (PC5: 54.5%), and Mn (PC6: 31.8%). PC variances that were largely exclusive to pCu are also reported for pTM datasets from the North Atlantic

(Ohnemus & Lam, 2015). PC3 (8.6 – 10.2% total variance) captured the greatest individual variance for oxygen (48-71%), with only significant associations with L-pCo (35%), R-pCd (30%), T-pMn (15%), and R-pZn (15%). No variance of the Mn oxide proxy, L-pMn, was captured within the third principal component of the L-pTM dataset analysis. However, relatively high variances for dFe (29-35%) were captured by PC3 in all pTM datasets.

The distributions of labile and refractory pTMs showed distinct regional and biogeochemical variations along the transect, including: (a) A contrasting biogenic particle abundance between BENG (upwelling) and NORTH (non-upwelling) stations; (b) Contrasting refractory (lithogenic) particle compositions on the Benguela Shelf and stations north of Walvis Ridge; (c) Distinct Fe and Mn cycling within the oxygen-depleted waters on the Benguela Shelf (d) Increased adsorption of TMs onto particles in the Congo River plume. The regional and biogeochemical variations will be discussed in the following sections.

3.3.2.1 Bio-Essential Particulate Trace Metals

Concentrations of bio-essential TMs (Zn, Cu, Ni, Cd, Co, and also P) in the L-pTM and R-pTM fractions were higher in the BENG region compared to the NORTH (T-Test; p <0.01 and <0.05, respectively; except R-pCo) (Table S3.5). This was attributed to the enhanced primary production (i.e., increased (bio-) assimilation of essential TMs) within BUS where concentrations of the biogenic particle indicator pP were up to 5-fold higher in the BENG region (ST 43-51 and 1-5) compared to NORTH (ST 6-20), reaching 253 nM T-pP (147 nM L-pP). Maximum bio-essential L-pTM concentrations in the BENG and (NORTH, in brackets) regions were 2.61 nM (0.81 nM) L-pZn, 228 pM (87.4 pM) L-pNi, 193 pM (155 pM) L-pCu, 74.3 pM (26.4 pM) L-pCd, and 35.3 pM (16.7 pM) L-pCo (Figure 3.3), excluding station 45. The vertical distributions of bio-essential L-pTMs (Zn, Cu, Ni, Cd, Co, and also P) and R-pP showed highest concentrations in surface waters and decreased with depth along the transect (Figure 3.3), coinciding with enhanced fluorescence (Figure 3.2D), implying phytoplankton sources.

Bio-essential R-pTMs (and also Pb; discussed in section 3.3.3) were co-distributed with R-pAl with good correlations (r = 0.56 – 0.97; p <0.01; Table S3.6), implying a lithogenic source. Moreover, bio-essential R-pTMs in the top 100 m showed higher correlations with R-pAl (r =

0.925 – 0.996) than with R-pP (r = 0.172-0.395) (Figure S3.7). The exceptions were R-pP and R-pCd, which showed lower correlations with R-pAl (r = 0.18 and 0.42, respectively; Table S3.6) but correlated well with each other (r = 0.73; p <0.001; Table S3.6) and were associated with refractory (residual) biogenic particles (see section 3.3.3).

3.3.2.2 Lithogenic Particulate Trace Metals

Concentrations of particulate lithogenic elements (Al, Ti, and Fe) showed no statistical difference among regions (Table S3.5). Lithogenic pTMs concentrations were generally lower in surface waters (<20 nM R-pAl; ≤50 m), except in the Congo plume (ST 16 – 20; 12.2 – 443 nM R-pAl), at some BENG stations (ST 47, 1, and 2; 30.9-85.3 nM R-pAl), and at shallow stations 13 (59 m) and 45 (68 m) (295 nM and 3.19 µM R-pAl, respectively) (Figure 3.4). Concentrations of lithogenic particles (i.e., R-pAl) were primarily enhanced in (near-)bottom waters, consistent with benthic resuspension and nepheloid layer distribution patterns. Elevated lithogenic particle concentrations were observed within 100 m from the seafloor at stations 9 and 11 (up to 97 nM and 227 nM R-pAl, respectively), and at shallower shelf stations 12 (289 m) and 17 (53 m) (up to 469 nM and 628 nM R-pAl, respectively). The highest lithogenic pTM concentrations were at the shallow coastal station 45, with 4.96 µM R-pAl (145 nM L-pAl), 1.38 µM R-pFe (314 nM L-pFe), and 138 nM R-pTi (138 pM L-pTi), and the lowest concentrations were in deep waters between Walvis Ridge and the Congo River shelf (ST 6 – 11), and in the open ocean (ST 22 – 24 ; <5 nM R-pAl) (Figures 3.3 and 3.4). Labile particulate Pb, Al, Ti, Mn, and Fe concentrations were also enhanced where R-pAl concentrations were high, as reflected by their close correlations with R-pAl (r = 0.61 – 0.91; p <0.001) (Table S3.6), implying common (benthic) sources.

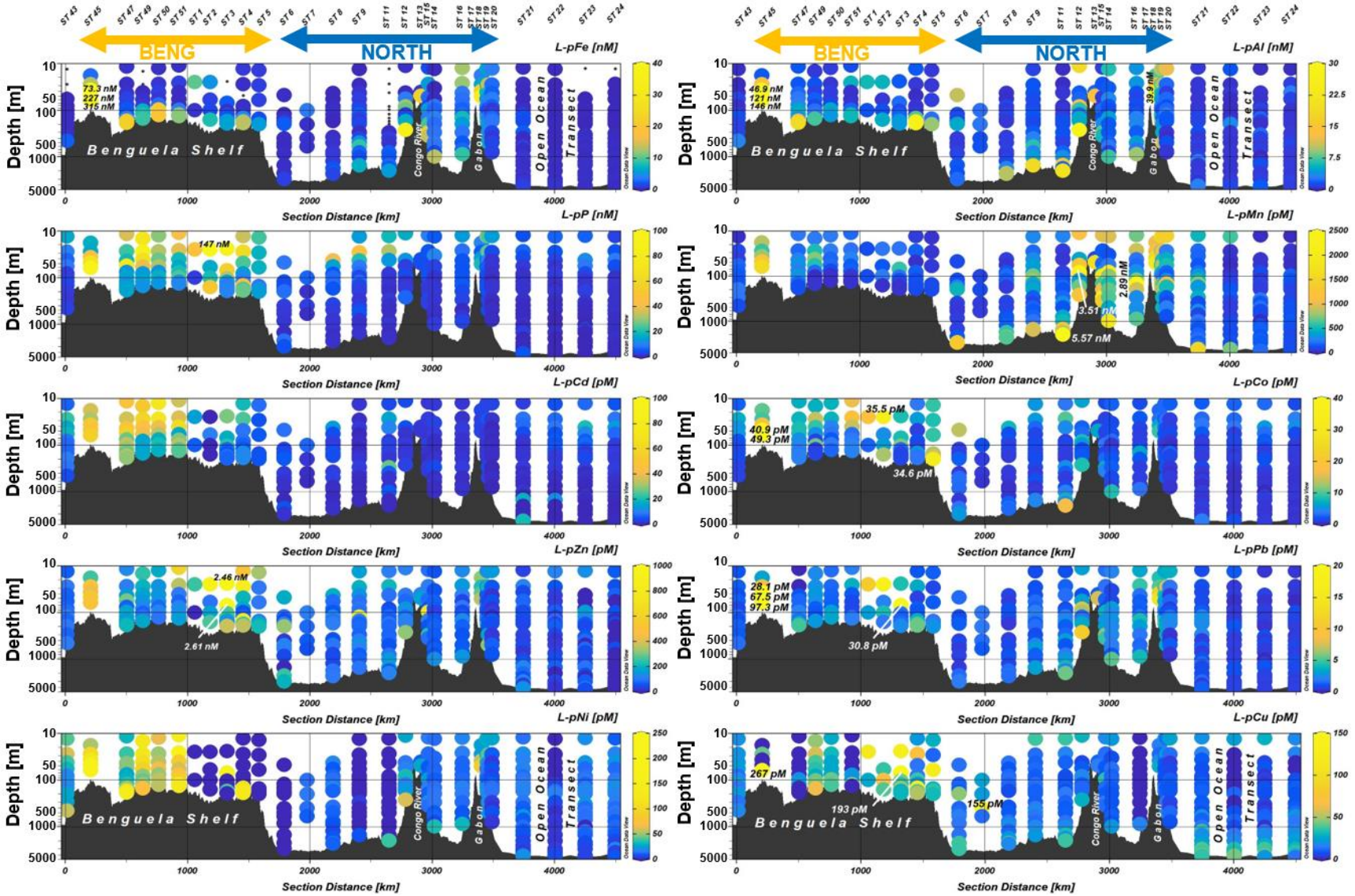

Figure 3.3. Distribution of labile particulate trace metals (L-pTMs) across the GA08 transect. Note the logarithmic depth scales. One anomalously high measurement was excluded a priori (>7.1 nM L-pCu; ST 2; 25 m). Concentrations have been annotated where values exceeded the color-bar scale (z-axis).

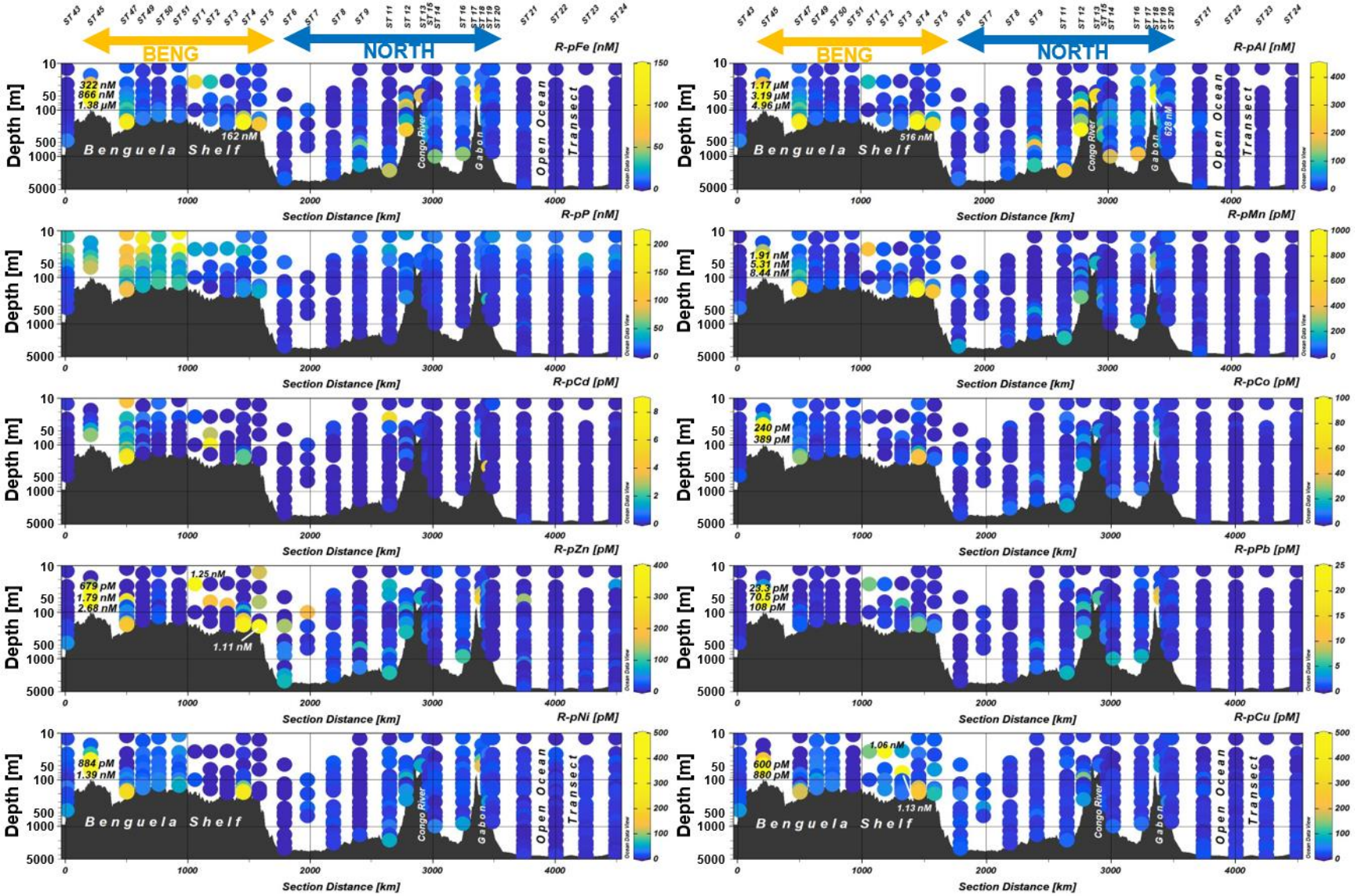

Figure 3.4. Distribution of refractory particulate trace metals (R-pTMs) across the GA08 transect. Note the logarithmic depth scales. One anomalously high measurement was excluded a priori (>1 nM R-pPb; ST 6; 196 m). Concentrations have been annotated where values exceeded the color-bar scale (z-axis).

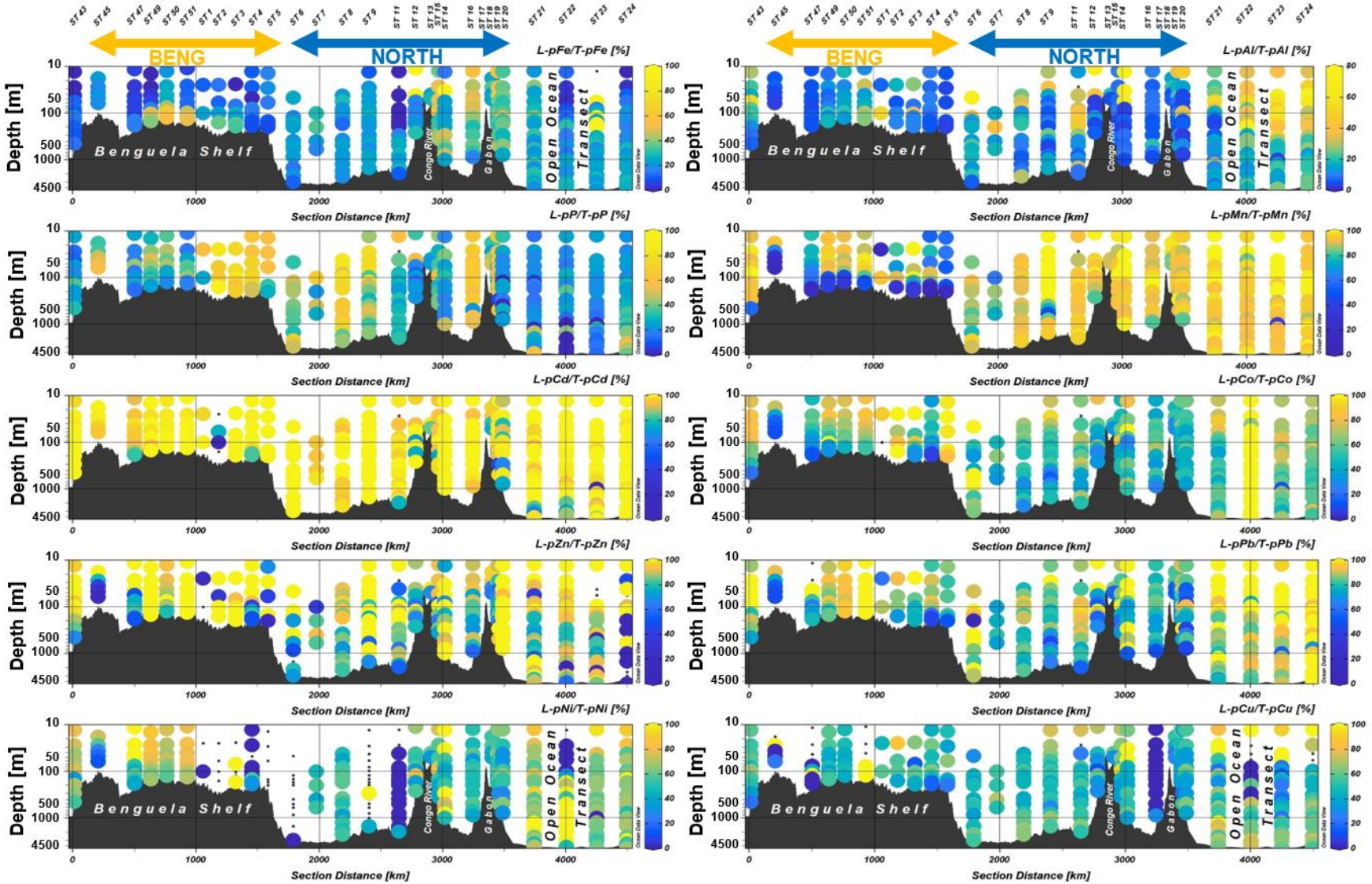

Figure 3.5. Distribution of labile particulate fraction (%) of total particulate trace metals across the GA08 transect. Contour lines indicate where refractory particulate Al (R-pAl) is ≥25 nM (thin) or ≥100 nM (thick). Note the logarithmic depth and different color scales for each element.

3.3.3 Biogenic Particles

Beam attenuation (BAT) and turbidity, used as a proxy for particulate matter, were enhanced primarily in surface waters and highest in the Benguela upwelling region (Figure 3.2E and S3.8), and strongly correlated with the biogenic particle indicator, T-pP (r=0.868 and 0.774, respectively; Figure S3.9a and S3.9c) and with fluorescence in the surface waters (r= 0.770, <100 m). T-pP in surface samples showed slightly higher correlations with BAT (r= 0.868; < 100 m; Figure S3.9a), compared to turbidity (r= 0.774; < 100 m), and enhanced BAT measurements were more pronounced in surface samples compared to turbidity (Figures S3.9e). This observation is consistent with other studies that reported enhanced BAT largely resulting from enhanced particulate organic matter concentrations (e.g., Bishop et al., 2004; Lam & Bishop, 2008; Noble et al., 2012; Ohnemus et al., 2018).

Particulate P concentrations, in all fractions, were highest in the euphotic zone (<50 m) and sharply decreased with depth along the transect, generally following the same vertical profiles as fluorescence (Figure S3.2 and S3.4). Higher L-pP and R-pP concentrations persisted deeper into the BENG water column compared to the NORTH (Figure 3.3 and 3.4), reflecting longer remineralization length scales due to increased biogenic particle production, oxygen deficiency with lower remineralization rates (Weber & Bianchi, 2020), increased particle ballasting with enhanced sinking rates (Armstrong et al., 2001; Klaas & Archer, 2002), or a combination thereof. Significant contributors of ballast to particle aggregates within the BENG upwelling stations likely include dust from the nearby Namib Desert and settling biominerals associated with the increase in primary production.

The mean L-pP/T-pP fractions in (sub-)surface waters (<200 m) were 39.7% ± 20.7% (n = 206) along the entire transect, which were notably lower than labile fractions from other regions reporting average L-pP/T-pP fractions of ~70-80% (e.g., Rauschenberg & Twining, 2015; Twining et al., 2015). L-pP/T-pP fractions varied (spatially) between stations, with some stations exhibiting higher L-pP/T-pP fractions (up to 84.8%) that were more consistent with labile fractions reported from other areas, such as between stations 1-9 (67±14%; ≤100 m; n=25).

Increasing biogenic or lithogenic particle loads did not affect the percentage leached from biogenic particles, as indicated by the weak correlations of L-pP fractions (%) with T-pP and R-pAl concentrations over several orders of magnitude (r= 0.04 and 0.06, respectively; top 300 m) (Figure S3.10). While it may be argued that the lower L-pP/T-pP fractions may reflect the inclusion of refractory inorganic pP phases, areas where inorganic pP would possibly be higher such as in (near-)bottom samples of the Benguela shelf where phosphorite deposits are documented (Compton & Bergh, 2016), did not show a significant contribution to the pP pool. This was indicated by the low co-occurring levels of lithogenic elements (R-pAl and R-pTi), which were also low where R-pP was highest (i.e., in surface waters; Figure 3.4). Furthermore, phosphorites included in particulate samples are potentially chemically labile (Jian-rui & Jie, 2016; Porto et al., 2018). Therefore, the R-pP pool through the transect was ascribed primarily to residual (more refractory) biogenic particle phases. Notable exceptions were at station 45 (1.17 – 4.96 µM R-pAl), and in the bottom waters of stations 4 and 5 (58.5-516 nM R-pAl), where lithogenic element concentrations were particularly high.

Bio-essential pTMs (Cd, Ni, Co, Cu, and Zn) correlated well with pP in both labile (r= 0.63 – 0.79) and total particulate (r= 0.52 – 0.79; except T-pZn) fractions in the top 100 m (Figure S3.11). Additionally, sample T-pTM:T-pP ratios (upper and lower quartile value ranges) and linear regression slopes of surface samples (<100 m) were consistent with ranges of reported plankton stoichiometries (Table 3.1 and Figure S3.11). This supports the assumption that T-pP was primarily associated with biogenic sources, and therefore a suitable biogenic particle indicator along this transect, also implying that these bio-essential pTMs were primarily associated with biogenic materials. Interestingly, however, the sample L-pTM:L-pP ratios (upper and lower quartile values, and linear regression slope values) of the bio-essential elements were comparatively higher than their respective T-pTM:T-pP ratios, which were at the upper limit of or slightly exceeded reported plankton values from other regions (Table 3.1). This suggested that the pTMs associated with biogenic particles were either comparatively more labile than biogenic pP, or that biogenic pP was (variably) more resistant to the applied leach, with the latter case providing an explanation for the persistence of R-pP in surface waters and biogenic particle-like vertical profiles through the water column.

The spatial fluctuations in L-pP/T-pP fractions are suspected to have varied as dominant taxa in bulk phytoplankton communities shifted between stations, reflecting differential lability of pP among different (dominant) phytoplankton groups. This was inferred using phytoplankton taxa assemblage data from this cruise which were reported by Browning et al. (2017) (*n*=5 stations along the transect of this study). In regions influenced by upwelling, diatoms dominated the bulk plankton assemblages (fraction of total chlorophyll-a) and generally coincided with elevated L-pP fractions, particularly in surface waters between stations 2-5 (58-84% L-pP fraction of total pP). Increased L-pP fractions continued to persist where diatoms comprised an important fraction of the bulk plankton assemblages (about one-third) in between stations 8-9 (up to 84.5% L-pP/T-pP) and stations 16-20 (up to 69% L-pP/T-pP). In contrast, where haptophytes dominated the plankton assemblage, away from upwelling regions, lower L-pP fractions were generally observed, such as in the southernmost coastal region on the Benguela shelf (11.9-56.5% L-pP of total pP; ST 45-50 <100 m). The lowest L-pP fractions that were generally observed in surface waters between stations 21-24 (14.8-28.4% L-pP of total pP; <100 m), where haptophytes and *Prochlorococcus* equally comprised about one-third, each, of the community assemblage, with almost no diatoms present.

Differential remineralization length scales of bio-essential elements through the water column, attributed to variable lability of respectively associated (intra-)cellular components, have been described using synchrotron x-ray fluorescence mapping by Twining et al. (2014), focused on diatoms. Given the similarity of bio-essential T-pTM:T-pP ratios to plankton reference sources in surface waters along the transect (Table 3.1), but variable L-pP/T-pP fractions (Figure 3.5), we postulate that it is plausible that the lability of biogenic pP is also variable between different phytoplankton taxa. This assumption is based on indirect evidence, further exploration of pP (and pTM) lability of different phytoplankton taxa is warranted in future studies to confirm and expand on this hypothesis.

Nonetheless, refractory particulate phases represent the particulate fraction that will persist in the water column on longer timescales, compared to the L-pTM fractions, as they settle or are laterally transported away from their sources. This also implicates pP cycling, particularly over the Benguela shelf, as it would directly imply that (biogenic) R-pP from settling

particles are a potentially significant source of refractory pP to the underlying seafloor, contributing to the enriched pP documented on the Benguela shelf (Compton & Bergh, 2016).

Samples from the NORTH stations (ST 6-20) exhibited higher labile and total bio-essential pTMs:pP ratios in the top 100 m compared to the BENG stations, except for pCd, which was higher in the BENG region (Table 3.1 and Figure S3.13). This is possibly due to the partial inclusion of other abiotic L-pTM phases (i.e., adsorbed, and precipitated phases) into the L-pTM pool and/or higher intracellular TM:P quotas associated with the above described, differing bulk plankton community structures along the transect. Some TMs released in solution following the remineralization of biogenic particles are susceptible to (re-)adsorption onto particle surfaces, such as Cu (Boyle et al., 1977; Bruland, 1980; Bruland et al., 2014; Little et al., 2013, 2018; Richon & Tagliabue, 2019), and Ni, Co, and Zn (Archer et al., 2020; Weber et al., 2018; Zheng et al., 2021). Therefore, increased adsorption of these TMs onto particles is more likely to occur where dTM concentrations were high, as in the river-influenced stations in the NORTH region (see section 3.3.6), and where higher concentrations of labile authigenic phases were present (i.e., Fe and Mn oxides), where enhanced biogenic L-pTM:L-pP ratios were observed (Figure S3.13).

The pCo:pP ratios in waters <50 m were very similar in the BENG (0.09-0.24 and 0.14-0.55 mmol:mol T-pCo:T-pP and L-pCo:L-pP, respectively; lower and upper quartile values; *n*=25) and NORTH (0.13-0.24 and 0.20-0.53 mmol:mol T-pCo:T-pP and L-pCo:L-pP, respectively; lower and upper quartile values; *n*=40) regions (Figure S3.13b and g), where biogenic particle abundance was highest. Also, the pCo:pP ratios were within the same order of magnitude of reported plankton ranges (Table 3.1). This suggests that the pCo pool was most likely associated with biogenic particles, and that abiotic phases (i.e., Co adsorbed onto particles) were not a major fraction of the L-pCo pool in surface waters (≤50 m). However, waters at depths between 50-100 m exhibited higher pCo:pP ratios (0.19-0.38 and 0.29-0.79 mmol:mol T-pCo:T-pP and L-pCo:L-pP, respectively; lower and upper quartile values; *n*=41), and showed close correlations between L-pCo and L-pMn (r=0.827; ST 6 – 24; *n*=41), implying that L-pCo and L-pMn were largely associated with the same labile particulate phases (i.e., Mn oxides), which is consistent

with co-precipitation of Co and Mn, during Mn (bio-)oxidation (Cowen & Bruland, 1985; Moffett & Ho, 1996; Tebo et al., 2004, 2005).

Particulate Fe and Mn, in labile and total particulate fractions, showed weak correlations with pP (r <0.1; ≤100 m; Figure S3.12), with much higher individual sample labile and total pTM:pP ratios compared to reported plankton stoichiometry ranges (Table 3.1). This is likely due to an increased fraction of co-occurring labile abiogenic pTM phases (such as adsorbed Fe and Mn, and labile Fe and Mn oxides) as part of the labile particulate fraction, masking the biogenic L-pTM pool, which were enhanced with lithogenic (benthic) sources, as implied through their closer correlations with R-pAl (r=0.64-0.82; Figure S3.12) (see sections 3.3.4 – 3.3.6).

The enhanced labile fractions of pAl observed in the top 350 m of the water column at the NORTH and open ocean stations (up to 74%; ST 6-24; Figure 3.5) were associated with increased adsorption of Al, possibly onto biogenic silica (i.e., opal) or other particles, and/or the inclusion of other labile L-pAl phases, such as aluminum oxyhydroxides (Berger et al., 2008). Samples that were deeper showed much lower L-pAl fractions (14.8% ± 7.4%; Max 33.1%; ≥350 m; n= 92), as biogenic particle (opal) fractions tend to decrease with depth due to dissolution (Lam et al., 2017; Lam, Ohnemus, et al., 2015; Xiang & Lam, 2020). While biogenic silica was not measured in samples of this study, other studies across the Atlantic, Indian, and Southern oceans, as well as in mesocosm experiments have shown preferential Al adsorption onto biogenic silica (Barrett et al., 2018; Menzel Barraqueta et al., 2018; Middag et al., 2015; Moran & Moore, 1988; Orians & Bruland, 1986). Diatom abundances were apparently low in open ocean stations (ST 21-24), as inferred above, we can only speculate that enhanced L-pAl/T-pAl fractions in these samples (Figure 3.5) may reflect the inclusion of a relatively higher fraction of labile aluminum oxyhydroxides, adsorption onto other particles, or inclusion of other L-pAl phases.

At first glance, the significant L-pPb variance (57%; Figure S3.6) captured by PC2 of the L-pTM dataset (associated with biogenic particles) suggests enhanced Pb adsorption onto biogenic particles. However, correlations between L-pPb and R-pAl (lithogenic proxy) (r= 0.95;

n= 132) were stronger in the top 100 m, where biogenic particle abundances were highest, compared to L-pP (*r* = 0.44; *n*=132) (Figure S3.14). L-pPb also exhibited better correlations with L-pFe and L-pMn (*r*= 0.81 and *r*= 0.66, respectively, Table S3.6). The closer correlations of L-pPb with the other particle proxies suggested that the affinity for Pb adsorption was higher onto other co-occurring (abiogenic) particles, such as lithogenic particles (Chen, Boyle, et al., 2016; Rutgers Van Der Loeff & Boudreau, 1997), and/or Fe and Mn oxides (Allen et al., 1990; Boyle et al., 2005; Fernex et al., 1992; Ohnemus & Lam, 2015; Rapp et al., 2019; Rusiecka et al., 2018; Sherrell & Boyle, 1992). However, Pb adsorption onto biogenic particles cannot be discounted and has been implicated in observations in the North Atlantic and Southern Ocean (Cochran et al., 1990; Schlosser & Garbe-Schönberg, 2019), North Pacific (Cochran et al., 1990; Nozaki et al., 1976), and in laboratory studies (Chuang et al., 2014; Yang et al., 2015).

Table 3.1. Compiled Plankton Reference Trace Metal Stoichiometries Compared to Samples From the Top 100 m of the GA08 transect. *Note:*Concentration ranges referenced from this study are the upper and lower quartile values of individual sample labile particulate trace metal (L-pTM) : labile particulate phosphorus (L-pP) ratios (mmol:mol) and total particulate TM (T-pTM) : T-pP ratios. GA08 values reported in brackets are linear regression slope values, shown for elements where *r* is ≥0.5, and **bold** values represent the T-pTM:T-pP fractions, while unformatted values represent L-pTM:L-pP fractions. Table adapted from Twining & Baines (2013).

Reference Source	TM:P ratio (mmol:mol)						
	Fe	Mn	Zn	Ni	Cu	Cd	Co
North Atlantic Ocean (Trichodesmium) (Nuester et al., 2012; Tovar-Sanchez et al., 2006)	5-31	1-5	0.2-13	1-8	0.4-2.1	0.02-0.31	0.01-0.15
Equatorial Pacific Ocean (Phytoplankton) (Twining et al., 2011)	1.9-8.4	0.49-0.58	-	1.0-1.2	-	-	0.06-0.07
Culture (Average Eukaryotic Phytoplankton-15 species) (Ho et al., 2003)	7.5	3.8	0.8	-	0.38	0.21	0.19
Southern Ocean (Large Diatoms) (Cullen et al., 2003)	-	1.7	11.1	-	1.44	1.29	0.15
North Atlantic Ocean (mostly Flagellated cells) (Kuss & Kremling, 1999)	4.6	1.6	1.9	1.4	0.37	0.51	0.19
Equatorial Pacific Ocean (mostly Zooplankton) (Collier & Edmond, 1984)	4.9	0.35	3.2	0.97	0.48	0.56	-
Southern Ocean (Large Diatoms) (Collier & Edmond, 1984)	-	-	13.3	0.68	2	0.07	-
Northeast Atlantic Spring Bloom (picoplankton and coccolithophores) (Klein et al., 2013)	9.1-9.8	-	-	-	0.27-0.52	0.06-0.07	0.04-0.06
Eastern Tropical South Pacific (near Peruvian Coast) (Ohnemus et al., 2017)	39.7	1.0	1.0 ± 0.88	0.54 ±0.39	0.40 ± 0.37	0.54 ± 0.24	0.08 ± 0.05
GA08 (All ≤100 m) (*n*=131) (This Study) **T-pTM:T-pP** L-pTM:L-pP	**(-)** (-)	**(-)** (-)	**(-)** (8.7)	**(0.46)** (1.6)	**(0.50)** (0.96)	**(0.27)** (0.57)	**(0.10)** (0.21)
GA08 (BENG - ST 43-51 & 1-5 ≤100 m) (*n*=46) (This Study) **T-pTM:T-pP** L-pTM:L-pP	***36.5-214*** *14.5-146*	***1.8-8.1*** *4.5-14.6*	**1.6-8.7** 4.9-11	**0.66-1.7** 1.9-3.8	**0.69-2.11** 0.86-2.6	**0.24-0.51** 0.59-2.1	**0.09-0.23** 0.13-0.47
GA08 (NORTH - ST 6-24 ≤100 m) (*n*=85) (This Study) **T-pTM:T-pP** L-pTM:L-pP	***42.2-953*** *33.0-916*	***7.1-49.6*** *21.6-134*	**4.3-9.2** 9.1-27.7	**0.96-2.8** 2.2-4.5	**0.97-2.1** 1.3-3.7	**0.10-0.31** 0.26-0.96	**0.15-0.32** 0.25-0.62

3.3.4 Lithogenic Particles

Turbidity and BAT were enhanced in (near-)bottom waters (Figures 3.2E and S3.8) where very high concentrations of the lithogenic proxy, R-pAl, were observed. Increased lithogenic particle (R-pAl) concentrations exhibited higher correlations with turbidity measurements (r = 0.703; >100 m; Figure S3.9d) than BAT (r = 0.677; >100 m; Figure S3.9b), and enhancements in the turbidity signals were more pronounced in samples below the surface (>100 m), compared to BAT (Figures S3.9e). This suggests that lithogenic particles exhibited a higher influence on turbidity signals compared to BAT.

Refractory particles from the BENG region were distinctly enriched in R-pFe (Figure 3.6b and Table S3.2), showing higher R-pFe:R-pAl and R-pFe:R-pTi ratios (0.276 and 9.90 mol:mol, respectively; linear regression slope values), compared to samples from the NORTH region (0.186 and 7.66 mol:mol, respectively; linear regression slope values) (t-test p <0.05; Table S3.7) and upper continental crust (UCC) reference sources (0.232 and 8.77 mol:mol, respectively; Rudnick and Gao, 2013). The higher R-pFe abundances in BENG region samples are partially attributed to local sources of sediment resuspension (Böning et al., 2020; Borchers et al., 2005; Govin et al., 2012) and the Namib dust (Annegarn et al., 1983; Eltayeb et al., 1993), which are enriched in Fe (Table S3.2). The presence of Fe sulfides and biotite in resuspended sediment particles, as reported for the Benguela shelf (Böning et al., 2020; Bremner & Willis, 1993), can contribute to R-pFe enrichment relative to R-pAl and R-pTi. Additionally, Fe-sulfide precipitation within microenvironments of organic-rich particle aggregates within the oxygen-deficient waters of the BENG region (Bianchi et al., 2018) may possibly contribute to the increased R-pFe (Bianchi et al., 2018). Indeed, elevated R-pFe:R-pAl ratios (0.43 – 0.72, mol:mol) in (near-)bottom water samples of the most oxygen-depleted waters on the Benguela shelf (<10 µM oxygen; ST 49-51) were consistent with the inclusion of benthic particles (0.90 Fe:Al was reported in sediment at a nearby location at 14.4°E, 25.0°S; (Böning et al., 2020)).

Another regional contrast showing higher R-pMn:R-pAl and R-pMn:R-pTi abundance in particles from the BENG region (1.88 and 62.1 mmol:mol, respectively; linear regression slope values), compared to NORTH (0.530 and 21.2 mmol:mol; linear regression slope values) was

also apparent (Figure 3.6c), although the R-pMn abundances were deficient compared to average canonical UCC reference sources (4.67 and 176 mmol:mol, respectively; Rudnick and Gao, 2013) (Table S3.2). This feature was consistent with Mn deficiencies in Benguela sediment sources as reported by Böning et al. (2020).

In (near-)bottom waters of NORTH stations, the distributions of elevated lithogenic R-pTMs (Al, Ti, and Fe) were also largely consistent with benthic resuspension (Figure 3.4), with some evidence for lateral transport of benthic (nepheloid) particles off-shelf (Figure 3.6). Samples at intermediate depths with elevated R-pAl concentrations, observed at station 9 (400 – 800 m; 70-204 nM R-pAl), and between stations 17-19 (100 – 300 m; 20.5 – 25.2 nM R-pAl) (Figure 3.4), exhibited relatively consistent R-pFe:R-pAl and R-pAl:R-pTi ratios (Figure 3.6), reflecting nepheloid particles from the same respective (lithogenic) sources. The latter nepheloid layer source (100-300 m; ST 17-19) appeared to persist laterally off-shelf into the open ocean through stations 20 and 21 within isopycnal densities of the SACW (~26.3-26.9 kg m^{-3} σ_Θ), over 300 km away from the African shelf, as suggested by the relatively consistent sample R-pFe:R-pAl ratios (Figure 3.6). This illustrated the role of shelf particles as potential vectors onto which TMs may be carried off-shelf and into the Angola Dome, facilitated via adsorption directly onto lithogenic particles, or concomitantly with other co-occurring particle phases, such as (re-)precipitated Fe and Mn oxides (Burdige, 1993). Additionally, high particle concentrations, such as those in nepheloid layers, but also in river plume particles (ST 16-20), may facilitate enhanced scavenging (Honeyman et al., 1988; Rutgers Van Der Loeff & Boudreau, 1997), increasing the L-pTM pools of essential elements, such as Fe, subsequently buffering dTM pools (Achterberg et al., 2018; Milne et al., 2017). The role of advected particles in supplementing available Fe pools was described in the North Atlantic (Achterberg et al., 2018; Milne et al., 2017), Southern (van der Merwe et al., 2015) and Pacific (Lam et al., 2006; Lam & Bishop, 2008) Oceans and, hence, may also be an important source to the Angola Dome. L-pFe and R-pAl were closely correlated (r = 0.91; p < 0.001; Table S3.6), indicating that benthic particles could play an important role in sustaining the available Fe pool required by phytoplankton through L-pFe phases. This is relevant for Fe (Beghoura et al., 2019; Burdige & Komada, 2020), which is often limiting to primary production (Boyd & Ellwood, 2010; Moore et

al., 2013), but was not in waters on and immediately off the shelf of the Angola Dome (as determined through field incubations conducted between approximately at ST 10 and 21) (Browning et al., 2017).

Particles collected nearest the Congo River outflow (ST 13-15), exhibited R-pTM:R-pAl linear regression slope values of 0.202 Fe:Al, 8.08 Fe:Ti, and 39.1 Al:Ti (Figure S3.15a-c), which are comparable to UCC reference ranges (0.232, 8.77, and 37.7 (mol:mol), respectively) (Rudnick & Gao, 2013). However, particles were also deficient in R-pMn (0.641 R-pMn:R-pAl and 24.0 R-pMn:R-pTi (mmol:mol); Figure S3.15d and e) by about an order of magnitude compared to UCC reference values (4.67 R-pMn:R-pAl and 176 R-pMn:R-pTi, mmol:mol). No literature values reporting TM concentrations were available for Congo River particles to compare with our results at the time of this study. Particles in (sub-)surface waters with high lithogenic R-pTM in the river plume also exhibited increases in scavenging, particularly between stations 16-20, associated with high dTMs delivered by the river (Section 3.3.6).

Elevated L-pPb concentrations in benthic resuspended particles (R-pAl) were likely associated with anthropogenic Pb accumulated in sediments, which was released and subsequently (re-)adsorbed onto benthic particles following resuspension (Rusiecka et al., 2018). Re-adsorption of dissolved Pb may have occurred onto Fe and/or Mn oxides, or lithogenic particles (Chen, Goodkin, et al., 2016; Rusiecka et al., 2018; Rutgers Van Der Loeff & Boudreau, 1997), which is difficult to discern, as discussed in Section 3.3.3. However, the mechanism of Pb transport via resuspended benthic particles may be important for overall transfer of anthropogenic Pb from coastal to deeper ocean sediment inventories.

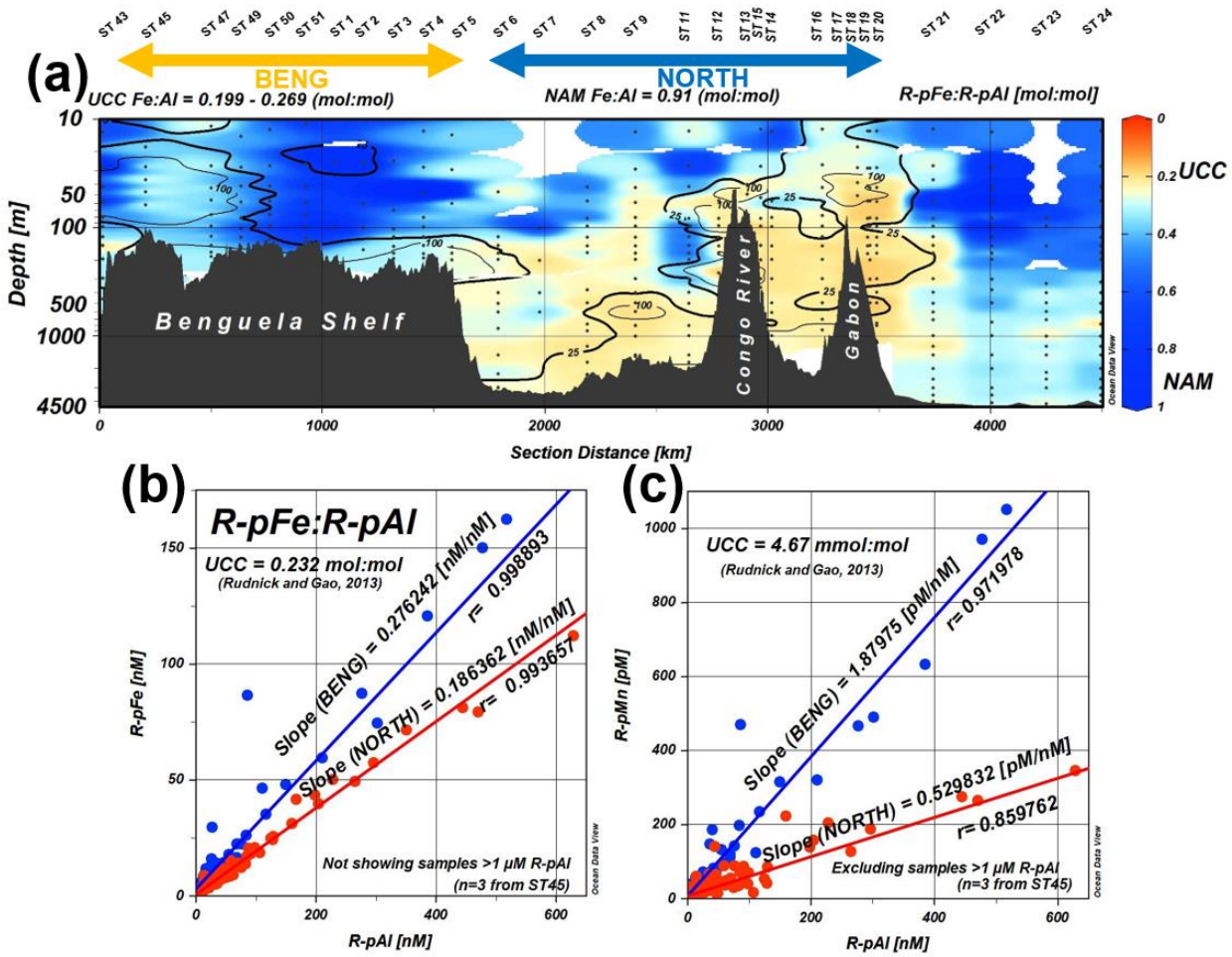

Figure 3.6. Spatial distribution of sample elemental ratios of refractory particulate iron (R-pFe) and aluminum (R-pAl) (a); and scatter plots illustrating regional contrasts in refractory particle compositions showing (b) enriched R-pFe abundance in BENG region (ST 43-51; and 1-5) compared to the NORTH (ST 6-24); and (c) refractory particulate Mn (R-pMn) abundance between BENG and NORTH regions. Note the logarithmic depth scale on (a). Reference elemental ratio ranges for Namibian desert dust (NAM) (Eltayeb et al. 1993; Annegarn et al. 1983) and Upper Continental Crust (UCC) (Rudnick and Gao, 2013) are shown above the section plot and annotated on *z*-axis color bar scale (a), and within each respective scatter plot (b) and (c). Annotated contour lines indicate R-pAl concentrations >25 nM and >100 nM. The blue and red sample points and regression lines represent samples from the BENG and NORTH regions, respectively. Three samples were not shown on scatter plots (ST 45; 1.2 – 4.9 µM R-pAl) that stretched the scales and decreased resolution.

3.3.5 Iron and Manganese Cycling on the Benguela Shelf

The upwelling stations on the Benguela shelf were characterized by a more intense OMZ (<4 µM oxygen), compared to the Northern non-upwelling stations (> 20 µM), and were underlain by anoxic and sulfidic sediments (Böning et al., 2020; Borchers et al., 2005; Inthorn et al., 2006). Stations 49 – 51 featured the most oxygen-deficient subsurface waters along the transect (< 10 µM; 96-150 m; Figure 3.2b and 3.7e) and were located within the Lüderitz Cell.

In (near-)bottom waters at the NORTH stations with oxygen levels > 20 µM (ST 6-20), L-pFe and L-pMn concentrations were enhanced, reaching up to 35.3 nM and 5.57 nM, respectively (Figure 3.3), coinciding with high lithogenic particle abundance (up to 469 nM R-pAl; Figure 3.4). The oxygen-depleted waters (<4 µM oxygen) on the Benguela shelf exhibited high L-pFe concentrations (up to 22.5 nM; ST 47-51 and 1-5), while L-pMn was comparatively low (18 – 357 pM; > 75 m) (Figure 3.3). Vertical profiles for stations 49-51 featured increasing concentrations of L-pFe (6.9 – 20.8 nM; Figure 3.7f) and dFe (11.8 – 27 nM; Figure 3.7c) below the oxycline toward the seafloor, where L-pFe comprised 39 – 65% of the T-pFe pool (Figure 3.7g). In contrast, vertical L-pMn profiles showed decreasing concentrations (18.2 – 44.9 pM; Figure 3.7h) and L-pMn/T-pMn fractions with depth below the oxycline (34 – 82% L-pMn/T-pMn; Figure 3.7i). Dissolved Fe and Mn concentrations (not shown) were enhanced in (near-)bottom waters where their labile particulate fractions were high, whilst dFe was particularly high on the Benguela Shelf (up to 27.4 nM; excluding ST 45, which was up to 46.3 nM) and dMn only slightly increasing with depth (1.27 – 2.25 nM Figure 3.7d). These differences in behavior of Fe and Mn were attributed to rapid oxidation kinetics of sediment derived Fe(II) and removal by precipitation (Elrod et al., 2004; Millero et al., 1987) and comparatively slower oxidation and further transport of Mn (Heggie & Lewis, 1984; Jensen et al., 2020; Klinkhammer, 1980; Luther et al., 2018; Tebo et al., 2004, 2005; von Langen et al., 1997).

The enhanced available Fe pools were associated with benthic supplies of reduced dFe(II) that rapidly precipitated as authigenic Fe oxides following oxidation by oxygen or nitrate, as observed in the oxycline of the Peruvian OMZ (Heller et al., 2017; Schlosser et al., 2018; Scholz et al., 2016) with subsequent accumulation in bottom waters and surface sediments.

Nanoparticulate (colloidal [0.02-0.2 µm]) Fe oxides that may have precipitated (Raiswell & Canfield, 2012) are included in the operationally defined dFe pool (<0.2 µm), thus contributed to the enhanced dFe concentrations. Organically complexed Fe (van den Berg, 1995; Gledhill & Buck, 2012; Hopwood et al., 2020; Hunter & Boyd, 2007; Rue & Bruland, 1995), and non-reductive dissolution of lithogenic particles, as colloids (Homoky et al., 2013, 2021), may also supplement the dFe pool. The subsequent exchange of the colloidal Fe pool between the dissolved and particulate pools (i.e., through (dis-)aggregation) may explain the concomitant increase in both dFe and L-pFe fractions observed on the Benguela shelf (Boyd & Ellwood, 2010; Bruland et al., 2014; Bruland & Lohan, 2003) (Figure 3.7c and 3.7f).

The slight increase in dMn below the oxycline indicates a benthic source of reduced dMn (Burdige, 1993). The primarily microbially-mediated (bio-)oxidation of Mn (Moffett and Ho, 1996; Tebo et al., 2005, 2004; von Langen et al., 1997), was retarded in the oxygen-deficient environment, resulting in low L-pMn concentrations. Subsequent off-shelf transport of dMn in bottom seawater away from the shelf led to the relative depletion of Mn oxides within underlying sediment, consistent with regional sediment compositions reporting Mn depletion (Böning et al., 2020; Borchers et al., 2005).

However, poor correlations between L-pMn and L-pCo were observed in samples deeper than 50 m on the Benguela shelf (r=0.041; ST 47-51 and 1-5; >50 m; Figure S3.16), with increases in L-pCo concentrations, relative to L-pMn, below the oxycline, indicating an additional source for L-pCo. This was ascribed to biogenic particles, driven by the increased production and longer remineralization length scales within the upwelling stations (Section 3.3.3). Also, pCo: pP ratios were relatively consistent (0.214±0.186 and 0.243±0.187 mmol:mol T-pCo:T-pP and L-pCo:L-pP, respectively; ST47-51 and 1-5) and generally in agreement with reported plankton stoichiometry ranges (Table 3.1).

Overall, the relative deficiency in Mn oxide production on the shelf, an important dCo sink (Hawco et al., 2018), may have been an important factor allowing enhanced dCo signals to be carried further off-shore within the OMZ and into the South Atlantic Ocean. This would provide an explanation for the dCo plume that was detected within the OMZ of the South

Atlantic on the CoFeMUG (GAc01) transect (Noble et al., 2012, 2017), as the existence of an off-shore plume of dCo downstream within the open-ocean OMZ of the eastern tropical Pacific also relied on low concentrations of Mn oxides (Lam et al., 2018; Landing & Bruland, 1987; Lee et al., 2018; and Vedamati et al., 2015).

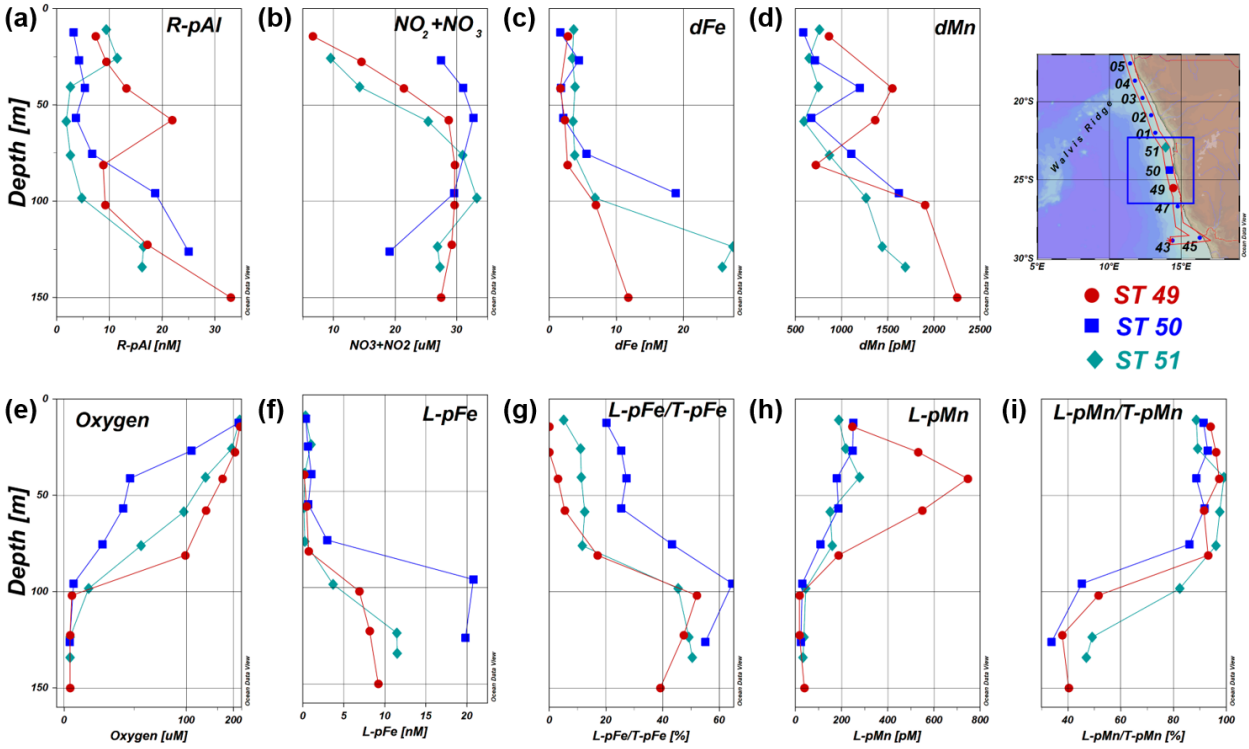

Figure 3.7. Water column profiles within the oxygen-depleted waters of the Lüderitz cell between stations 49-51 of (a) Refractory particulate aluminum (R-pAl); (b) Nitrate + Nitrite; (c) Dissolved Iron (dFe); (d) Dissolved Mn (dMn); (e) Dissolved Oxygen; (f) Labile particulate Fe (L-pFe); (g) Labile particulate Fe fraction (%); (h) Labile particulate Mn (L-pMn); (i) Labile particulate Mn fraction (%). Note the stretched scale for oxygen concentration.

3.3.6 Congo River Plume

Samples collected in the Congo River plume (ST 13-20) exhibited patterns of enhanced TM adsorption that were associated with a high supply of dTMs by the river, combined with high particle abundance providing sites for adsorption. This was evident through increased L-pTM concentrations (Figure 3.3) and L-pTM/T-pTM fractions (Figure 3.5) coinciding with relatively high concentrations of R-pAl (57.6 ± 95.8 nM; ST 13-20) and T-pP at the surface (up to

47.0 nM; <100 m; ST 13-20). Enhanced dTM concentrations were measured in surface waters of the plume (~5 m, towed-fish samples), reaching up to 1.24 µM dFe, 784 nM dAl, 125 nM dMn, 1.04 nM dCo, 84 nM dPb, 8.13 nM dCu, 2.72 nM dZn, and 7.08 nM dNi (Figure S3.17; only dFe shown; other TMs will be presented elsewhere). The enhanced supply of TMs by the Congo River is likely related to the presence of ore bodies and copper-cobalt mining in the Congo catchment (Prasad, 1989). Enhanced particle-reactive L-pTM (notably Fe, Mn, Al, and Pb) concentrations and L-pTM/T-pTM ratios were observed at the coastal plume stations (ST 12-20), reaching up to 22.6 nM (64.8 %) L-pFe, 2.3 nM (99.4 %) L-pMn, 21.6 nM (77.5 %) L-pAl, and 14.3 pM (93.2 %) L-pPb (Figures 3.3 and 3.5). Dissolved Fe was particularly enhanced within TSW (up to 8.75 nM; <20 m) and persisted north of the river mouth and westward into the open ocean through to station 22 (3.69 nM at ST 22) (not shown). However, enhanced L-pFe concentrations (up to 34.9 nM) were mostly confined to the coastal plume stations (ST 13-20) and were relatively low within TSW off-shelf (mean 0.136 ± 0.125 nM L-pFe at ST 21-22; ≤100 m; *n*=12). Similarly, L-pAl and L-pPb concentrations were enhanced in surface waters of the coastal plume stations (up to 21.6 nM and 11.3 pM, respectively; ST 12-20; < 50 m; Figure 3.3) and did not persist off-shelf. In contrast, enhanced L-pMn concentrations (up to 3.51 nM; ST 12-20) were relatively persistent off-shelf within TSW (617 pM L-pMn at ST 22) and coincided with elevated dMn (up to 6.47 nM at ST 13; and 4.87 nM dMn at ST 22) in river plume stations. Elevated dMn concentrations also persisted within STUW south of the Congo River mouth (3.21 ± 0.93 nM dMn; ST 8-11; <50 m; *n*=7; not shown) and coincided with low L-pMn concentrations (177 ± 118 pM; ST 8-11; <50 m; *n*=7) (Figure 3.3).

In agreement with the dissolved and labile particulate TM observations, available Fe, Mn, and Al at the coastal plume stations (ST 13-20) were enhanced with concentrations up to 41.3 nM, 7.23 nM, and 104 nM, respectively (Figure S3.18e – S3.18g). The available Pb concentrations were not enhanced and were higher on the Benguela shelf. Enhanced available Mn and Al concentrations that were associated with the river plume persisted off-shelf within TSW as far west as ST 22, and possibly southward as well for Mn (ST 8 -11) (Figure S3.18f and S3.18g). Available Fe and Pb, did not persist off-shelf (Figure S3.18e and S3.18h). The enhanced available Al pool in plume samples was dominated by dAl, which were high (up to 85 nM dAl,

and 98% of available Al), while L-pAl was relatively low off-shelf (Figure S3.18g). In contrast, L-pFe comprised most of the available Fe pool in coastal plume stations (up to 93%) but was also low off-shelf. The low L-pFe and L-pAl concentrations off-shelf implied that particles played a decreasing role in sustaining elevated dFe and dAl concentrations off-shelf, which were instead sustained through other mechanisms. Dissolved Fe is likely kept in solution by complexation with organic ligands (van den Berg, 1995; Buck et al., 2015; Gledhill & Buck, 2012; Hopwood et al., 2020; Hunter & Boyd, 2007) and also photo- and/or non-reductive dissolution processes from lithogenic particles (Homoky et al., 2021, 2013). The latter case may also support the explanation of the persistently elevated dAl signal within the plume.

Increased L-pTM/dTM fractions of Fe, Mn and Pb were evident in the coastal plume (sub-)surface waters, consistent with increased adsorption and/or precipitation of labile Fe and Mn oxides (Figure S3.18a, S3.18b, and S3.18d), compared to non-plume stations. Lithogenic particle concentrations were also enhanced, particularly between stations 16-20 (up to 628 nM R-pAl). Increases in L-pTM/dTM partitioning of Pb, Fe and Mn were co-distributed with R-pAl, suggesting that lithogenic particles were important sites for adsorption, including Fe and Mn oxides. Closer correlations of L-pPb and L-pAl with L-pFe (r=0.919 and 0.691, respectively; Figure S3.19a and 3.19b) over L-pMn (r=0.787 and 0.529, respectively; Figure S3.19c and 3.19d) may suggest a slight preferential affinity for Al and Pb with Fe oxides, or that they shared preferential affinities to same particle surfaces as Fe. Although, the closer correlations to L-pFe may be due to a comparatively higher abundance of labile Fe oxides, compared to Mn oxides, and corresponding binding sites for adsorption.

Elevated L-pMn, persisted in photic surface waters, within the TSW (<25 m), away from the shelf (to ST 22), in contrast to L-pFe and L-pPb. This suggested that either Mn had an increased affinity for particles at the surface (i.e., biogenic particles) or that Fe and Pb had a steeper removal gradient than Mn towards off-shelf waters. T-pMn:T-pP (17 and 26 mmol:mol; ST 21 and 22, respectively; n=2) and L-pMn:L-pP (116 and 97 mmol:mol; ST 21 and 22, respectively; n=2) ratios were higher than reported biogenic particle stoichiometries (Table 3.1), and Mn oxides abundance in surface waters are decreased due to photo-reductive dissolution (Sunda & Huntsman, 1988, 1994). This left biogenic particles as the dominant

particulate phases in offshore surface waters (ST21-22; <25 m) onto which dissolved Mn may adsorb onto, although this assumption is based on only a few datapoints.

The adsorptive processes occurring within the plume indicated that adsorbed pFe (i.e., L-pFe) likely played an important role in maintaining elevated dFe concentrations in coastal plume stations (ST 13-20) through reversible adsorption (Achterberg et al., 2018, 2021; Milne et al., 2017), with a lower influence in off-shelf plume waters (within TSW in ST 21 and 22). However, it was also apparent that reversible-scavenging was either not in equilibrium and/or that variable supplies of dFe may have occurred in the shelf waters, as L-pFe and dFe showed a weak correlation (r= 0.2718; ST 13-20; n=70).

3.4. Conclusions

Overall, this work provides important insights to the biogeochemical cycling processes and the influences of different environments controlling pTM distributions in the southwest African shelf and the Angola basin region. Our results complement regional studies of shelf sediments by providing a snapshot of processes occurring in the overlying water column and illustrate a decoupled redox cycling of Fe and Mn on the Benguela shelf, with Fe retention and Mn transport off-shelf. Additionally, we illustrate several advantages of how separating the labile from refractory particulate fractions may be utilized to enhance the interpretations of pTM cycling, though also highlight some cautions and potential considerations for future work as well.

The decoupled distributions of Fe oxide enrichment and Mn oxide deficiency in the oxygen-depleted waters on the Benguela shelf could have broader implications on TM cycling and export in other upwelling regions of the ocean. Iron oxides precipitated and accumulated in bottom waters are a potential source of Fe following subsequent transport. In cases where seasonal oxygen depletion occurs, subsequent advection of bottom waters may supply a source of available Fe (and associated scavenged TMs) downstream that may potentially support or enhance primary production. Manganese oxide deficiency under sub-oxic conditions could enhance the shuttling of typically associated TMs, such as Co away from the shelf. Indeed, the

transport of Co to the South Atlantic Ocean appears to be facilitated by enhanced supply from benthic sources on the oxygen-depleted Benguela shelf.

The Congo River plume formed a significant source of available TMs to the shelf, mainly through enhanced scavenging, reflected in labile pTM fractions, with subsequent buffering of dTM concentrations in shelf and off-shelf waters. However, the role of plume particles in sustaining dTM concentrations off-shelf did not appear to be dominant. Transport of available Fe within the river plume was instead sustained within the dissolved fraction, likely following the photo-reductive release of Fe(II) from lithogenic particles and/or ligand-bound dFe. However, dissolved Mn removal from the water column through scavenging appeared less efficient than dFe, allowing it to persist off-shelf.

Bio-essential pTM:pP ratios (Zn, Ni, Cd, Co, and Cu) of labile and total particulate fractions in surface waters were comparable to reported plankton stoichiometries, implying the predominant association of their pTM pools with biogenic particles. However, labile particulate Fe and Mn pools in surface waters included a significant fraction of L-pTM phases attributed to adsorption onto cell surfaces and also the possible inclusion of labile Fe and Mn oxides. Additionally, the variability in labile biogenic particle fractions, in particular for pP, highlighted the need to exercise caution when interpreting labile fractions, importantly when comparing pTM datasets between ocean basins and across seasons.

The relatively high refractory biogenic refractory pP fractions observed across several stations raises some uncertainties that require further investigation in future work, specifically into the chemical lability of major phytoplankton taxa groups when applying chemical leaches. With the increased adoption of the Berger et al. (2008) leach, as its use is recommended in GEOTRACES standard protocols (i.e., the GEOTRACES “Cookbook”; Cutter et al., 2017), further improvement of biogenic particle characterization will improve inter-comparison of pTM cycling in other regions, enhancing pTM cycling components in biogeochemical modelling, and providing relevant insights for palaeoceanographic and benthic interpretations as well.

The observations and conclusions in this work contribute to a growing body of literature (e.g., Lee et al., 2018; Lippiatt, Brown, et al., 2010; Milne et al., 2017; Twining et al., 2019; Xiang

& Lam, 2020) demonstrating the importance of particles for TM cycling and transport within the ocean and emphasize the importance of selective leach procedures for understanding TM cycling by particles.

Acknowledgments

We thank the captain and crew of the RV Meteor M121 cruise/GEOTRACES GA08 section; S. Koesling, P. Lodeiro, J. Pampín Baro, J. C. Yong and C. Schlosser for cruise support and assistance in sample collection and P. Streu and Bernhard Wenzel for technical laboratory assistance. Detailed comments by an anonymous reviewer improved the manuscript who is gratefully acknowledged. The PhD fellowships to A. Al-Hashem and S. Krisch were funded by the Kuwait Institute for Scientific Research, Kuwait, and the Deutsche Forschungsgemeinschaft (AC 217/1-1 granted to Eric P. Achterberg), respectively. The cruise was funded by the Deutsche Forschungsgemeinschaft (DFG). The open-access publishing charges for this publication were covered by the Helmholtz Research Centre/Association. The GEOTRACES 2021 Intermediate Data Product (IDP2021) represents an international collaboration and is endorsed by the Scientific Committee on Oceanic Research (SCOR). The many researchers and funding agencies responsible for the collection of data and quality control are thanked for their contributions to the IDP2021.

Author Contributions: A.A.A.: investigation, methodology and analysis, data curation, visualization, writing—original draft. A.J.B.: validation, writing—review and editing. S.K.: formal analysis (dTMs). J.M.B.: formal analysis (dAl). T.S.: formal analysis (TM analysis on HR-ICP-MS). E.P.A.: conceptualization, funding acquisition, resources, supervision, writing—review and editing.

Conflict of Interest

The authors declare that they have no conflicts of interest.

Data Availability

The full datasets for labile (L-pTM), refractory (R-pTM), and total (T-pTM) particulate trace metal concentrations of Iron (Fe), Aluminum (Al), Titanium (Ti), Manganese (Mn), Cobalt (Co), Zinc (Zn), Nickel (Ni), Copper (Cu), Cadmium (Cd), and Lead (Pb), and particulate Phosphorus (P) for the presented sections of the GA08 (M121) cruise transect are available at https://doi.pangaea.de/10.1594/PANGAEA.945498. The full dataset for dissolved TM (dTM) concentrations of Fe, Co, Mn, Ni, Cd, Cu, Pb and Zn, Fe(II), and macronutrients (phosphate, nitrate + nitrite, and silicic acid) concentrations are available at https://doi.org/10.1594/PANGAEA.947275. The dataset for the presented sections of the GA08 (M121) cruise transect are also provided as a Source Data file.

References

Achterberg, E. P., Holland, T. W., Bowie, A. R., Mantoura, R. F. C., & Worsfold, P. J. (2001). Determination of iron in seawater. *Analytica Chimica Acta*, *442*(1), 1–14. https://doi.org/10.1016/S0003-2670(01)01091-1

Achterberg, E. P., Steigenberger, S., Marsay, C. M., Lemoigne, F. A. C., Painter, S. C., Baker, A. R., et al. (2018). Iron Biogeochemistry in the High Latitude North Atlantic Ocean. *Scientific Reports*, *8*(1). https://doi.org/10.1038/s41598-018-19472-1

Achterberg, E. P., Steigenberger, S., Klar, J. K., Browning, T. J., Marsay, C. M., Painter, S. C., et al. (2021). Trace Element Biogeochemistry in the High-Latitude North Atlantic Ocean: Seasonal Variations and Volcanic Inputs. *Global Biogeochemical Cycles*, *35*(3). https://doi.org/10.1029/2020GB006674

Al-Hashem, Ali A; Beck, Aaron; Achterberg, Eric Pieter (2022): Labile, Refractory, and Total Particulate Trace Metal Concentrations from the GEOTRACES GA08 Shelf section and 3-degree Latitudinal transect. PANGAEA, https://doi.org/10.1594/PANGAEA.945498

Allen, J. R. L., Rae, J. E., & Zanin, P. E. (1990). Metal speciation (Cu, Zn, Pb) and organic matter in an oxic salt marsh, Severn Estuary, southwest Britain. *Marine Pollution Bulletin*, *21*(12), 574–580. https://doi.org/10.1016/0025-326X(90)90606-9

Anderson, R. F. (2020). GEOTRACES: Accelerating Research on the Marine Biogeochemical Cycles of Trace Elements and Their Isotopes. *Annual Review of Marine Science*, *12*, 49–85. https://doi.org/10.1146/annurev-marine-010318-095123

Annegarn, H. J., van Grieken, R. E., Bibby, D. M., & von Blottnitz, F. (1983). Background aerosol composition in the namib desert, South West Africa (Namibia). *Atmospheric Environment (1967)*, *17*(10), 2045–2053. https://doi.org/10.1016/0004-6981(83)90361-X

Archer, C., Vance, D., Milne, A., & Lohan, M. C. (2020). The oceanic biogeochemistry of nickel and its isotopes: New data from the South Atlantic and the Southern Ocean biogeochemical divide. *Earth and Planetary Science Letters*, *535*, 116118. https://doi.org/10.1016/j.epsl.2020.116118

Armstrong, R. A., Lee, C., Hedges, J. I., Honjo, S., & Wakeham, S. G. (2001). A new, mechanistic model for organic carbon fluxes in the ocean based on the quantitative association of POC with ballast minerals. *Deep-Sea Research Part II: Topical Studies in Oceanography*, *49*(1–3), 219–236. https://doi.org/10.1016/S0967-0645(01)00101-1

Barrett, P. M., Resing, J. A., Grand, M. M., Measures, C. I., & Landing, W. M. (2018). Trace element composition of suspended particulate matter along three meridional CLIVAR

sections in the Indian and Southern Oceans: Impact of scavenging on Al distributions. *Chemical Geology*, *502*, 15–28. https://doi.org/10.1016/j.chemgeo.2018.06.015

Beghoura, H., Gorgues, T., Aumont, O., Planquette, H., Tagliabue, A., & Auger, P. A. (2019). Impact of Inorganic Particles of Sedimentary Origin on Global Dissolved Iron and Phytoplankton Distribution. *Journal of Geophysical Research: Oceans*, *124*(12), 8626–8646. https://doi.org/10.1029/2019JC015119

van den Berg, C. M. G. (1995). Evidence for organic complexation of iron in seawater. *Marine Chemistry*, *50*(1–4), 139–157. https://doi.org/10.1016/0304-4203(95)00032-M

Berger, C. J. M., Lippiatt, S. M., Lawrence, M. G., & Bruland, K. W. (2008). Application of a chemical leach technique for estimating labile particulate aluminum, iron, and manganese in the Columbia River plume and coastal waters off Oregon and Washington. *Journal of Geophysical Research*, *113*, 1–16. https://doi.org/10.1029/2007JC004703

Bianchi, D., Weber, T. S., Kiko, R., & Deutsch, C. (2018). Global niche of marine anaerobic metabolisms expanded by particle microenvironments. *Nature Geoscience*, *11*(4), 263–268. https://doi.org/10.1038/s41561-018-0081-0

Birchill, A. J., Milne, A., Woodward, E. M. S., Harris, C., Annett, A. L., Rusiecka, D., et al. (2017). Seasonal iron depletion in temperate shelf seas. *Geophysical Research Letters*, *44*(17), 8987–8996. https://doi.org/10.1002/2017GL073881

Bishop, J. K. B., Wood, T. J., Davis, R. E., & Sherman, J. T. (2004). Robotic Observations of Enhanced Carbon Biomass and Export at 55°S during SOFeX. *Science*, *304*(5669), 417–420. https://doi.org/10.1126/science.1087717

Böning, P., Schnetger, B., Belz, L., Ferdelman, T. G., Brumsack, H. J., & Pahnke, K. (2020). Sedimentary iron cycling in the Benguela upwelling system off Namibia. *Earth and Planetary Science Letters*, *538*, 116212. https://doi.org/10.1016/j.epsl.2020.116212

Borchers, S. L., Schnetger, B., Böning, P., & Brumsack, H. J. (2005). Geochemical signatures of the Namibian diatom belt: Perennial upwelling and intermittent anoxia. *Geochemistry, Geophysics, Geosystems*, *6*(6). https://doi.org/10.1029/2004GC000886

Boyd, P. W., & Ellwood, M. J. (2010). The biogeochemical cycle of iron in the ocean. *Nature Geoscience*, *3*(10), 675–682. https://doi.org/10.1038/ngeo964

Boyd, P. W., Ellwood, M. J., Tagliabue, A., & Twining, B. S. (2017). Biotic and abiotic retention, recycling and remineralization of metals in the ocean. *Nature Geoscience*. https://doi.org/10.1038/ngeo2876

Boyle, E. A., Sclater, F. R., & Edmond, J. M. (1977). The distribution of dissolved copper in the Pacific. *Earth and Planetary Science Letters*, *37*(1), 38–54. https://doi.org/10.1016/0012-821X(77)90144-3

Boyle, Edward A., Bergquist, B. A., Kayser, R. A., & Mahowald, N. M. (2005). Iron, manganese, and lead at Hawaii Ocean Time-series station ALOHA: Temporal variability and an intermediate water hydrothermal plume. *Geochimica et Cosmochimica Acta*, *69*(4), 933–952. https://doi.org/10.1016/J.GCA.2004.07.034

Bremner, J. M., & Willis, J. P. (1993). Mineralogy and geochemistry of the clay fraction of sediments from the Namibian continental margin and the adjacent hinterland. *Marine Geology*, *115*(1–2), 85–116. https://doi.org/10.1016/0025-3227(93)90076-8

Browning, T. J., Achterberg, E. P., Rapp, I., Engel, A., Bertrand, E. M., Tagliabue, A., & Moore, C. M. (2017). Nutrient co-limitation at the boundary of an oceanic gyre. *Nature*, *551*(7679), 242–246. https://doi.org/10.1038/nature24063

Browning, T. J., Achterberg, E. P., Engel, A., & Mawji, E. (2021). Manganese co-limitation of phytoplankton growth and major nutrient drawdown in the Southern Ocean. *Nature Communications*, *12*(1), 1–9. https://doi.org/10.1038/s41467-021-21122-6

Bruland, K. W. (1980). Oceanographic distributions of cadmium, zinc, nickel, and copper in the North Pacific. *Earth and Planetary Science Letters*, *47*(2), 176–198. https://doi.org/10.1016/0012-821X(80)90035-7

Bruland, K. W., & Lohan, M. C. (2003). Controls of trace metals in Seawater. *The Oceans and Marine Geochemistry*, *6*, 23–47.

Bruland, K. W., Middag, R., & Lohan, M. C. (2014). *Controls of Trace Metals in Seawater*. *Treatise on Geochemistry: Second Edition* (2nd ed., Vol. 8). Elsevier Ltd. https://doi.org/10.1016/B978-0-08-095975-7.00602-1

Buck, K. N., Sohst, B., & Sedwick, P. N. (2015). The organic complexation of dissolved iron along the U.S. GEOTRACES (GA03) North Atlantic Section. *Deep-Sea Research Part II: Topical Studies in Oceanography*. https://doi.org/10.1016/j.dsr2.2014.11.016

Burdige, D. J. (1993). The biogeochemistry of manganese and iron reduction in marine sediments. *Earth Science Reviews*, *35*(3), 249–284. https://doi.org/10.1016/0012-8252(93)90040-E

Burdige, D. J., & Komada, T. (2020). Iron redox cycling, sediment resuspension and the role of sediments in low oxygen environments as sources of iron to the water column. *Marine Chemistry*, *223*(September 2019), 103793. https://doi.org/10.1016/j.marchem.2020.103793

Carr, M. E. (2001). Estimation of potential productivity in Eastern Boundary Currents using remote sensing. *Deep Sea Research Part II: Topical Studies in Oceanography*, *49*(1–3), 59–80. https://doi.org/10.1016/S0967-0645(01)00094-7

Charette, M. A., Lam, P. J., Lohan, M. C., Kwon, E. Y., Hatje, V., Jeandel, C., et al. (2016). Coastal ocean and shelf-sea biogeochemical cycling of trace elements and isotopes: Lessons learned from GEOTRACES. *Philosophical Transactions of the Royal Society A: Mathematical, Physical and Engineering Sciences*, *374*(2081). https://doi.org/10.1098/rsta.2016.0076

Chen, M., Goodkin, N. F., Boyle, E. A., Switzer, A. D., & Bolton, A. (2016). Lead in the western South China Sea: Evidence of atmospheric deposition and upwelling. *Geophysical Research Letters*, *43*(9), 4490–4499. https://doi.org/10.1002/2016GL068697

Chen, M., Boyle, E. A., Lee, J. M., Nurhati, I., Zurbrick, C., Switzer, A. D., & Carrasco, G. (2016). Lead isotope exchange between dissolved and fluvial particulate matter: A laboratory study from the Johor River estuary. *Philosophical Transactions of the Royal Society A: Mathematical, Physical and Engineering Sciences*, *374*(2081). https://doi.org/10.1098/rsta.2016.0054

Chuang, C. Y., Santschi, P. H., Jiang, Y., Ho, Y. F., Quigg, A., Guo, L., et al. (2014). Important role of biomolecules from diatoms in the scavenging of particle-reactive radionuclides of thorium, protactinium, lead, polonium, and beryllium in the ocean: A case study with Phaeodactylum tricornutum. *Limnology and Oceanography*, *59*(4), 1256–1266. https://doi.org/10.4319/LO.2014.59.4.1256

Cochran, J. K., McKibbin-Vaughan, T., Dornblaser, M. M., Hirschberg, D., Livingston, H. D., & Buesseler, K. O. (1990). 210Pb scavenging in the North Atlantic and North Pacific Oceans. *Earth and Planetary Science Letters*, *97*(3–4), 332–352. https://doi.org/10.1016/0012-821X(90)90050-8

Collier, R., & Edmond, J. (1984). The trace element geochemistry of marine biogenic particulate matter. *Progress in Oceanography*, *13*(2), 113–199. https://doi.org/10.1016/0079-6611(84)90008-9

Compton, J. S., & Bergh, E. W. (2016). Phosphorite deposits on the Namibian shelf. *Marine Geology*, *380*, 290–314. https://doi.org/10.1016/j.margeo.2016.04.006

Cowen, J. P., & Bruland, K. W. (1985). Metal deposits associated with bacteria: implications for Fe and Mn marine biogeochemistry. *Deep Sea Research Part A. Oceanographic Research Papers*, *32*(3), 253–272. https://doi.org/10.1016/0198-0149(85)90078-0

Cullen, J. T., & Sherrell, R. M. (1999). Techniques for determination of trace metals in small samples of size-fractionated particulate matter: phytoplankton metals off central California. *Marine Chemistry*, *67*, 233–247. Retrieved from http://www.whoi.edu/science/MCG/people/jcullen/CullenandSherrell1999MarChem.pdf

Cullen, J. T., Field, M. P., & Sherrell, R. M. (2001). Determination of trace elements in filtered suspended marine particulate material by sector field HR-ICP-MS. *The Royal Society of Chemistry*, *16*, 1307–1312. https://doi.org/10.1039/b104398f

Cullen, J. T., Chase, Z., Coale, K. H., Fitzwater, S. E., & Sherrell, R. M. (2003). Effect of iron limitation on the cadmium to phosphorus ratio of natural phytoplankton assemblages from the Southern Ocean. *Limnology and Oceanography*, *48*(3), 1079–1087. https://doi.org/10.4319/LO.2003.48.3.1079

Cutter, G. A., Andersson, P. S., Codispoti, L., Croot, P. L., Francois, R., Lohan, M. C., et al. (2010). Sampling and sample-handling protocols for GEOTRACES cruises, (December), 1–238. https://doi.org/http://www.geotraces.org/science/intercalibration/222-sampling-and-sample-handling-protocols-for-geotraces-cruises

Cutter, G. A., Casciotti, K., Croot, P. L., Geibert, W., Heimbürger, L.-E., Lohan, M. C., et al. (2017). Sampling and Sample-handling Protocols for GEOTRACES Cruises. Version 3, August 2017. *GEOTRACES Community Practices*, (August), 139pp. & Appendices. Retrieved from http://www.geotraces.org/images/stories/documents/intercalibration/Cookbook.pdf

Elrod, V. A., Berelson, W. M., Coale, K. H., & Johnson, K. S. (2004). The flux of iron from continental shelf sediments: A missing source for global budgets. *Geophys. Res. Lett.*, *31*(12), L12307. https://doi.org/10.1029/2004gl020216

Eltayeb, M. A. H., van Grieken, R. E., Maenhaut, W., & Annegarn, H. J. (1993). Aerosol-soil fractionation for Namib Desert samples. *Atmospheric Environment Part A, General Topics*, *27*(5), 669–678. https://doi.org/10.1016/0960-1686(93)90185-2

Fernex, F., Février, G., Bénaïm, J., & Arnoux, A. (1992). Copper, lead and zinc trapping in Mediterranean deep-sea sediments: probable coprecipitation with Mn and Fe. *Chemical Geology*, *98*(3–4), 293–306. https://doi.org/10.1016/0009-2541(92)90190-G

Gledhill, M., & Buck, K. N. (2012). The organic complexation of iron in the marine environment: A review. *Frontiers in Microbiology*, *3*(FEB), 1–17. https://doi.org/10.3389/fmicb.2012.00069

Goldberg, E. D. (1954). Chemical Scavengers of the Sea. *The Journal of Geology*, *62*(3), 249–265.

Govin, A., Holzwarth, U., Heslop, D., Ford Keeling, L., Zabel, M., Mulitza, S., et al. (2012). Distribution of major elements in Atlantic surface sediments (36°N-49°S): Imprint of terrigenous input and continental weathering. *Geochemistry, Geophysics, Geosystems*, *13*(1), 1–23. https://doi.org/10.1029/2011GC003785

Hansen, H. P. (2007). Determination of oxygen. *Methods of Seawater Analysis: Third, Completely Revised and Extended Edition*, 75–89. https://doi.org/10.1002/9783527613984.CH4

Hawco, N. J., Lam, P. J., Lee, J. M., Ohnemus, D. C., Noble, A. E., Wyatt, N. J., et al. (2018). Cobalt scavenging in the mesopelagic ocean and its influence on global mass balance: Synthesizing water column and sedimentary fluxes. *Marine Chemistry*, *201*, 151–166. https://doi.org/10.1016/j.marchem.2017.09.001

Heggie, D., & Lewis, T. (1984). Cobalt in pore waters of marine sediments. *Nature*, *311*(5985), 453–455. https://doi.org/10.1038/311453a0

Heller, M. I., Lam, P. J., Moffett, J. W., Till, C. P., Lee, J.-M., Toner, B. M., & Marcus, M. A. (2017). Accumulation of Fe oxyhydroxides in the Peruvian oxygen deficient zone implies non-oxygen dependent Fe oxidation. *Geochimica et Cosmochimica Acta*, *211*, 174–193. https://doi.org/10.1016/j.gca.2017.05.019

Henderson, G. M., & Marchal, O. (2015). Recommendations for future measurement and modelling of particles in GEOTRACES and other ocean biogeochemistry programmes. *Progress in Oceanography*, *133*, 73–78. https://doi.org/10.1016/j.pocean.2015.01.015

Ho, T.-Y., Finkel, Z. v, Milligan, A. J., Wyman, K., Falkowski, P. G., & Morel, F. M. M. (2003). The elemental composition of some marine phytoplankton. *Journal of Phycology*, *39*, 1145–1159.

Homoky, W. B., John, S. G., Conway, T. M., & Mills, R. A. (2013). Distinct iron isotopic signatures and supply from marine sediment dissolution. *Nature Communications*, *4*, 1–2. https://doi.org/10.1038/ncomms3143

Homoky, W. B., Conway, T. M., John, S. G., König, D., Deng, F. F., Tagliabue, A., & Mills, R. A. (2021). Iron colloids dominate sedimentary supply to the ocean interior. *Proceedings of the National Academy of Sciences of the United States of America*, *118*(13). https://doi.org/10.1073/PNAS.2016078118

Honeyman, B. D., Balistrieri, L. S., & Murray, J. W. (1988). Oceanic trace metal scavenging: the importance of particle concentration. *Deep Sea Research Part A, Oceanographic Research Papers*, *35*(2), 227–246. https://doi.org/10.1016/0198-0149(88)90038-6

Hopwood, M. J., Santana-González, C., Gallego-Urrea, J., Sanchez, N., Achterberg, E. P., Ardelan, M. v., et al. (2020). Fe(II) stability in coastal seawater during experiments in Patagonia, Svalbard, and Gran Canaria. *Biogeosciences*, *17*(5), 1327–1342. https://doi.org/10.5194/bg-17-1327-2020

Hunter, K. A., & Boyd, P. W. (2007). Iron-binding ligands and their role in the ocean biogeochemistry of iron. *Environmental Chemistry*, *4*(4), 221–232. https://doi.org/10.1071/EN07012

Hurst, M. P., & Bruland, K. W. (2008). The effects of the San Francisco Bay plume on trace metal and nutrient distributions in the Gulf of the Farallones. *Geochimica et Cosmochimica Acta*. https://doi.org/10.1016/j.gca.2007.11.005

Hurst, M. P., Aguliar-Islas, A., & Bruland, K. W. (2010). Iron in the southeastern Bering Sea: Elevated leachable particulate Fe in shelf bottom waters as an important source for surface waters. *Continental Shelf Research*. https://doi.org/10.1016/j.csr.2010.01.001

Inthorn, M., Mohrholz, V., & Zabel, M. (2006). Nepheloid layer distribution in the Benguela upwelling area offshore Namibia. *Deep-Sea Research Part I: Oceanographic Research Papers*, *53*(8), 1423–1438. https://doi.org/10.1016/j.dsr.2006.06.004

Jeandel, C., Rutgers van der Loeff, M., Lam, P. J., Roy-Barman, M., Sherrell, R. M., Kretschmer, S., et al. (2015). What did we learn about ocean particle dynamics in the GEOSECS-JGOFS era? *Progress in Oceanography*, *133*, 6–16. https://doi.org/10.1016/j.pocean.2014.12.018

Jensen, L. T., Morton, P. L., Twining, B. S., Heller, M. I., Hatta, M., Measures, C. I., et al. (2020). A comparison of marine Fe and Mn cycling: U.S. GEOTRACES GN01 Western Arctic case study. *Geochimica et Cosmochimica Acta*, *288*, 138–160. https://doi.org/10.1016/j.gca.2020.08.006

Jian-rui, W., & Jie, Z. (2016). Study on the selective leaching of low-grade phosphate ore for beneficiation of phosphorus and rare earths using citric acid as leaching agent. *Russian Journal of Applied Chemistry 2016 89:7*, *89*(7), 1196–1205. https://doi.org/10.1134/S1070427216070211

Jickells, T. D. (2005). Global Iron Connections Between Desert Dust, Ocean Biogeochemistry, and Climate. *Science*, *308*(5718), 67–71. https://doi.org/10.1126/science.1105959

Klaas, C., & Archer, D. E. (2002). Association of sinking organic matter with various types of mineral ballast in the deep sea: Implications for the rain ratio. *Global Biogeochemical Cycles*, *16*(4), 63-1-63–14. https://doi.org/10.1029/2001gb001765

Klein, N. J., Beck, A. J., Hutchins, D. A., & Sañudo-Wilhelmy, S. A. (2013). Regression modeling of the North East Atlantic Spring Bloom suggests previously unrecognized biological roles for V and Mo. *Frontiers in Microbiology*, *4*(MAR), 1–12. https://doi.org/10.3389/fmicb.2013.00045

Klinkhammer, G. P. (1980). Observations of the distribution of manganese over the East Pacific Rise. *Chemical Geology*, *29*(1–4), 211–226. https://doi.org/10.1016/0009-2541(80)90021-2

Kuss, J., & Kremling, K. (1999). Spatial variability of particle associated trace elements in near-surface waters of the North Atlantic (30°N/60°W to 60°N/2°W), derived by large volume sampling. *Marine Chemistry*, *68*(1–2), 71–86. https://doi.org/10.1016/S0304-4203(99)00066-3

Lam, P. J., & Bishop, J. K. B. (2008). The continental margin is a key source of iron to the HNLC North Pacific Ocean. *Geophysical Research Letters*, *35*(7), 1–5. https://doi.org/10.1029/2008GL033294

Lam, P. J., Bishop, J. K. B., Henning, C. C., Marcus, M. A., Waychunas, G. A., & Fung, I. Y. (2006). Wintertime phytoplankton bloom in the subarctic Pacific supported by continental margin iron. *Global Biogeochemical Cycles*, *20*(1), 1–12. https://doi.org/10.1029/2005GB002557

Lam, P. J., Twining, B. S., Jeandel, C., Roychoudhury, A., Resing, J. A., Santschi, P. H., & Anderson, R. F. (2015). Methods for analyzing the concentration and speciation of major and trace elements in marine particles. *Progress in Oceanography*, *133*, 32–42. https://doi.org/10.1016/j.pocean.2015.01.005

Lam, P. J., Ohnemus, D. C., & Auro, M. E. (2015). Size-fractionated major particle composition and concentrations from the US GEOTRACES North Atlantic Zonal Transect. *Deep-Sea Research Part II: Topical Studies in Oceanography*, *116*, 303–320. https://doi.org/10.1016/j.dsr2.2014.11.020

Lam, P. J., Lee, J.-M., Heller, M. I., Mehic, S., Xiang, Y., & Bates, N. R. (2017). Size-fractionated distributions of suspended particle concentration and major phase composition from the U.S. GEOTRACES Eastern Pacific Zonal Transect (GP16). *Marine Chemistry*. https://doi.org/10.1016/

Lam, P. J., Lee, J. M., Heller, M. I., Mehic, S., Xiang, Y., & Bates, N. R. (2018). Size-fractionated distributions of suspended particle concentration and major phase composition from the U.S. GEOTRACES Eastern Pacific Zonal Transect (GP16). *Marine Chemistry*, *201*(August), 90–107. https://doi.org/10.1016/j.marchem.2017.08.013

Landing, W. M., & Bruland, K. W. (1987). The contrasting biogeochemistry of iron and manganese in the Pacific Ocean. *Geochimica et Cosmochimica Acta*, *51*(1), 29–43. https://doi.org/10.1016/0016-7037(87)90004-4

von Langen, P. J., Johnson, K. S., Coale, K. H., & Elrod, V. A. (1997a). Oxidation kinetics of manganese (II) in sea water at nanomolar concentrations. *Geochimica et Cosmochimica Acta*, *61*(23), 4945–4954. https://doi.org/10.1016/S0016-7037(97)00355-4

Lee, J. M., Heller, M. I., & Lam, P. J. (2018). Size distribution of particulate trace elements in the U.S. GEOTRACES Eastern Pacific Zonal Transect (GP16). *Marine Chemistry*, *201*(September), 108–123. https://doi.org/10.1016/j.marchem.2017.09.006

Liao, W.-H., & Ho, T.-Y. (2018). Particulate Trace Metal Composition and Sources in the Kuroshio Adjacent to the East China Sea: The Importance of Aerosol Deposition. *Journal of Geophysical Research: Oceans*, *123*(9), 6207–6223. https://doi.org/10.1029/2018JC014113

Lippiatt, S. M., Brown, M. T., Lohan, M. C., Berger, C. J. M., & Bruland, K. W. (2010). Leachable particulate iron in the Columbia River, estuary, and near-field plume. *Estuarine, Coastal and Shelf Science*, *87*(1), 33–42. https://doi.org/10.1016/j.ecss.2009.12.009

Lippiatt, S. M., Lohan, M. C., & Bruland, K. W. (2010). The distribution of reactive iron in northern Gulf of Alaska coastal waters. *Marine Chemistry*, *121*(1–4), 187–199. https://doi.org/10.1016/j.marchem.2010.04.007

Little, S. H., Vance, D., Siddall, M., & Gasson, E. (2013). A modeling assessment of the role of reversible scavenging in controlling oceanic dissolved Cu and Zn distributions. *Global Biogeochemical Cycles*, *27*(3), 780–791. https://doi.org/10.1002/gbc.20073

Little, S. H., Archer, C., Milne, A., Schlosser, C., Achterberg, E. P., Lohan, M. C., & Vance, D. (2018). Paired dissolved and particulate phase Cu isotope distributions in the South Atlantic. *Chemical Geology*, *502*(June), 29–43. https://doi.org/10.1016/j.chemgeo.2018.07.022

Liu, Te; Krisch, Stephan; Hopwood, Mark J; Achterberg, Eric Pieter; Mutzberg, André (2022): Trace metal data from water samples during METEOR cruise M121. *PANGAEA*, https://doi.pangaea.de/10.1594/PANGAEA.947275

Luther, G. W., Thibault de Chanvalon, A., Oldham, V. E., Estes, E. R., Tebo, B. M., & Madison, A. S. (2018). Reduction of Manganese Oxides: Thermodynamic, Kinetic and Mechanistic Considerations for One- Versus Two-Electron Transfer Steps. *Aquatic Geochemistry*, *24*(4), 257–277. https://doi.org/10.1007/s10498-018-9342-1

Lutjeharms, J. R. E., & Meeuwis, J. M. (1987). The extent and variability of South-East Atlantic upwelling. *South African Journal of Marine Science*, *5*(1), 51–62. https://doi.org/10.2989/025776187784522621

Martin, J. H., Gordon, R. M., Fitzwater, S., & Broenkow, W. W. (1989). Vertex: phytoplankton/iron studies in the Gulf of Alaska. *Deep Sea Research Part A, Oceanographic Research Papers*, *36*(5), 649–680. https://doi.org/10.1016/0198-0149(89)90144-1

Menzel Barraqueta, J.-L., Christian, S., Hélène, P., Arthur, G., Marie, C., Julia, B., et al. (2018). Aluminium in the North Atlantic Ocean and the Labrador Sea (GEOTRACES GA01 section): roles of continental inputs and biogenic particle removal. https://doi.org/10.5194/bg-2018-39

van der Merwe, P., Bowie, A. R., Quéroué, F., Armand, L., Blain, S., Chever, F., et al. (2015). Sourcing the iron in the naturally fertilised bloom around the Kerguelen Plateau: Particulate trace metal dynamics. *Biogeosciences*, *12*(3), 739–755. https://doi.org/10.5194/bg-12-739-2015

van der Merwe, P., Wuttig, K., Holmes, T. M., Trull, T. W., Chase, Z., Townsend, A. T., et al. (2019). High lability Fe particles sourced from glacial erosion can meet previously unaccounted biological demand: Heard Island, Southern Ocean. *Frontiers in Marine Science*, *6*(JUN), 1–20. https://doi.org/10.3389/fmars.2019.00332

Middag, R., van Hulten, M., van Aken, H. M., Rijkenberg, M. J. A., Gerringa, L. J. A., Laan, P., & de Baar, H. J. (2015). Dissolved aluminium in the ocean conveyor of the West Atlantic Ocean: Effects of the biological cycle, scavenging, sediment resuspension and hydrography. *Marine Chemistry*, *177*. https://doi.org/10.1016/j.marchem.2015.02.015

Millero, F. J., Sotolongo, S., & Izaguirre, M. (1987). The oxidation kinetics of Fe(II) in seawater. *Geochimica et Cosmochimica Acta*, *51*(4), 793–801. https://doi.org/10.1016/0016-7037(87)90093-7

Milne, A., Schlosser, C., Wake, B. D., Achterberg, E. P., Chance, R., Baker, A. R., et al. (2017). Particulate phases are key in controlling dissolved iron concentrations in the (sub)tropical North Atlantic. *Geophysical Research Letters*, *44*(5), 2377–2387. https://doi.org/10.1002/2016GL072314

Moffett, J. W., & Ho, J. (1996). Oxidation of cobalt and manganese in seawater via a common microbially catalyzed pathway. *Geochimica et Cosmochimica Acta*, *60*(18), 3415–3424. https://doi.org/10.1016/0016-7037(96)00176-7

Moore, C. M., Mills, M. M., Arrigo, K. R., Berman-Frank, I., Bopp, L., Boyd, P. W., et al. (2013). Processes and patterns of oceanic nutrient limitation. *Nature Geoscience*, *6*(9), 701–710. https://doi.org/10.1038/ngeo1765

Moran, S. B., & Moore, R. M. (1988). Evidence from mesocosm studies for biological removal of dissolved aluminium from sea water. *Nature 1988 335:6192*, *335*(6192), 706–708. https://doi.org/10.1038/335706a0

Morel, F. M. M., & Price, N. M. (2003). The biogeochemical cycles of trace metals in the oceans. *Science*, *300*(5621), 944–947. https://doi.org/10.1126/science.1083545

Noble, A. E., Lamborg, C. H., Ohnemus, D. C., Lam, P. J., Goepfert, T. J., Measures, C. I., et al. (2012). Basin-scale inputs of cobalt, iron, and manganese from the Benguela-Angola front to the South Atlantic Ocean. *Limnology and Oceanography*, *57*(4), 989–1010. https://doi.org/10.4319/lo.2012.57.4.0989

Noble, A. E., Ohnemus, D. C., Hawco, N. J., Lam, P. J., & Saito, M. A. (2017). Coastal sources, sinks and strong organic complexation of dissolved cobalt within the US North Atlantic GEOTRACES transect GA03. *Biogeosciences*, *14*(11), 2715–2739. https://doi.org/10.5194/bg-14-2715-2017

Nozaki, Y., Thomson, J., & Turekian, K. K. (1976). The distribution of 210Pb and 210Po in the surface waters of the Pacific Ocean. *Earth and Planetary Science Letters*, *32*(2), 304–312. https://doi.org/10.1016/0012-821X(76)90070-4

Nuester, J., Vogt, S., Newville, M., Kustka, A. B., & Twining, B. S. (2012). The unique biogeochemical signature of the marine diazotroph trichodesmium. *Frontiers in Microbiology*, *3*(APR). https://doi.org/10.3389/FMICB.2012.00150

Ohnemus, D. C., & Lam, P. J. (2015). Cycling of lithogenic marine particles in the US GEOTRACES North Atlantic transect. *Deep-Sea Research Part II: Topical Studies in Oceanography*, *116*, 283–302. https://doi.org/10.1016/j.dsr2.2014.11.019

Ohnemus, D. C., Rauschenberg, S., Cutter, G. A., Fitzsimmons, J. N., Sherrell, R. M., & Twining, B. S. (2017). Elevated trace metal content of prokaryotic communities associated with marine oxygen deficient zones. *Limnology and Oceanography*, *62*(1), 3–25. https://doi.org/10.1002/LNO.10363

Ohnemus, D. C., Lam, P. J., & Twining, B. S. (2018). Optical observation of particles and responses to particle composition in the GEOTRACES GP16 section. *Marine Chemistry*, *201*, 124–136. https://doi.org/10.1016/J.MARCHEM.2017.09.004

Orians, K. J., & Bruland, K. W. (1986). The biogeochemistry of aluminum in the Pacific Ocean. *Earth and Planetary Science Letters Elsevier Science Publishers B.V*, *78*, 397–410.

Peterson, R. G., & Stramma, L. (1991). Upper-level circulation in the South Atlantic Ocean. *Progress in Oceanography*, *26*(1), 1–73. https://doi.org/10.1016/0079-6611(91)90006-8

Porto, F. G. M., Neto, M. C. A., & Finzer, J. R. D. (2018). Solubility of Phosphate Rocks in citric Acid. *World Scientific Research*, *5*(1), 32–36. https://doi.org/10.20448/journal.510.2018.51.32.36

Prasad, M. S. (1989). Production of copper and cobalt at Gecamines, Zaire. *Minerals Engineering*, *2*(4), 521–541. https://doi.org/10.1016/0892-6875(89)90087-3

Rahlf, P. (2020). Tracing water masses and terrestrial inputs with radiogenic neodymium and hafnium isotopes and rare earth elements in the southeastern Atlantic Ocean (thesis). Retrieved from https://macau.uni-kiel.de/receive/macau_mods_00001033?lang=de

Rahlf, P., Hathorne, E., Laukert, G., Gutjahr, M., Weldeab, S., & Frank, M. (2020). Tracing water mass mixing and continental inputs in the southeastern Atlantic Ocean with dissolved neodymium isotopes. *Earth and Planetary Science Letters*, *530*, 115944. https://doi.org/10.1016/J.EPSL.2019.115944

Rahlf, P., Laukert, G., Hathorne, E. C., Vieira, L. H., & Frank, M. (2021). Dissolved neodymium and hafnium isotopes and rare earth elements in the Congo River Plume: Tracing and

quantifying continental inputs into the southeast Atlantic. *Geochimica et Cosmochimica Acta*, *294*, 192–214. https://doi.org/10.1016/J.GCA.2020.11.017

Raiswell, R., & Canfield, D. E. (2012). The iron biogeochemical cycle past and present. *Geochemical Perspectives*, *1*(1), 1–232. https://doi.org/10.7185/geochempersp.1.1

Rapp, I., Schlosser, C., Rusiecka, D., Gledhill, M., & Achterberg, E. P. (2017). Automated preconcentration of Fe, Zn, Cu, Ni, Cd, Pb, Co, and Mn in seawater with analysis using high-resolution sector field inductively-coupled plasma mass spectrometry. *Analytica Chimica Acta*, *976*. https://doi.org/10.1016/j.aca.2017.05.008

Rapp, I., Schlosser, C., Menzel Barraqueta, J.-L., Wenzel, B., Lüdke, J., Scholten, J., et al. (2019). Controls on redox-sensitive trace metals in the Mauritanian oxygen minimum zone. *Biogeosciences*, *16*(21), 4157–4182. https://doi.org/10.5194/bg-16-4157-2019

Rauschenberg, S., & Twining, B. S. (2015). Evaluation of approaches to estimate biogenic particulate trace metals in the ocean. *Marine Chemistry*, *171*, 67–77. https://doi.org/10.1016/j.marchem.2015.01.004

Richon, C., & Tagliabue, A. (2019). Insights Into the Major Processes Driving the Global Distribution of Copper in the Ocean From a Global Model. *Global Biogeochemical Cycles*, *33*(12), 1594–1610. https://doi.org/10.1029/2019GB006280

Rudnick, R. L., & Gao, S. (2013). *Composition of the Continental Crust*. *Treatise on Geochemistry: Second Edition* (2nd ed., Vol. 4). Elsevier Ltd. https://doi.org/10.1016/B978-0-08-095975-7.00301-6

Rue, E. L., & Bruland, K. W. (1995). Complexation of iron(III) by natural organic ligands in the Central North Pacific as determined by a new competitive ligand equilibration/adsorptive cathodic stripping voltammetric method. *Marine Chemistry*, *50*(1–4), 117–138. https://doi.org/10.1016/0304-4203(95)00031-L

Rusiecka, D., Gledhill, M., Milne, A., Achterberg, E. P., Annett, A. L., Atkinson, S., et al. (2018). Anthropogenic Signatures of Lead in the Northeast Atlantic. *Geophysical Research Letters*, *45*(6), 2734–2743. https://doi.org/10.1002/2017GL076825

Rutgers Van Der Loeff, M. M., & Boudreau, B. P. (1997). The effect of resuspension on chemical exchanges at the sediment-water interface in the deep sea — A modelling and natural radiotracer approach. *Journal of Marine Systems*, *11*(3–4), 305–342. https://doi.org/10.1016/S0924-7963(96)00128-5

Schlitzer, R., Ocean Data View, https://odv.awi.de, 2018.

Schlosser, C., & Garbe-Schönberg, D. (2019). Mechanisms of Pb supply and removal in two remote (sub-)polar ocean regions. *Marine Pollution Bulletin*, *149*, 110659. https://doi.org/10.1016/J.MARPOLBUL.2019.110659

Schlosser, C., Streu, P., Frank, M., Lavik, G., Croot, P. L., Dengler, M., & Achterberg, E. P. (2018). H2S events in the Peruvian oxygen minimum zone facilitate enhanced dissolved Fe concentrations. *Scientific Reports*, *8*(1). https://doi.org/10.1038/s41598-018-30580-w

Scholz, F., Löscher, C. R., Fiskal, A., Sommer, S., Hensen, C., Lomnitz, U., et al. (2016). Nitrate-dependent iron oxidation limits iron transport in anoxic ocean regions. *Earth and Planetary Science Letters*, *454*, 272–281. https://doi.org/10.1016/j.epsl.2016.09.025

Shannon, L. v., & Nelson, G. (1996). The Benguela: Large Scale Features and Processes and System Variability. *The South Atlantic*, 163–210. https://doi.org/10.1007/978-3-642-80353-6_9

Shannon, L. v., Agenbag, J. J., & Buys, M. E. L. (1987). Large- and mesoscale features of the Angola-Benguela front. *South African Journal of Marine Science*, *5*(1), 11–34. https://doi.org/10.2989/025776187784522261

Shannon, LV. (2001). Benguela current. In *Encyclopedia of Ocean Sciences* (1st ed., pp. 225–267).

Sherrell, R. M., & Boyle, E. A. (1992). The trace metal composition of suspended particles in the oceanic water column near Bermuda. *Earth and Planetary Science Letters*, *111*, 155–174. Retrieved from http://ac.els-cdn.com/0012821X9290176V/1-s2.0-0012821X9290176V-main.pdf?_tid=362fe70c-971c-11e7-bb75-00000aab0f01&acdnat=1505153488_611fb430616d3fdcd9d26f5cfb2f3853

Sunda, W. G. (1989). Trace Metal Interactions with Marine Phytoplankton. *Biological Oceanography*, *6*, 411–442. Retrieved from https://www.tandfonline.com/doi/pdf/10.1080/01965581.1988.10749543?needAccess=true

Sunda, W. G. (2012). Feedback interactions between trace metal nutrients and phytoplankton in the ocean. *Frontiers in Microbiology*, *3*(JUN), 1–22. https://doi.org/10.3389/fmicb.2012.00204

Sunda, W. G., & Huntsman, S. A. (1988). Effect of sunlight on redox cycles of manganese in the southwestern Sargasso Sea. *Deep Sea Research Part A, Oceanographic Research Papers*, *35*(8), 1297–1317. https://doi.org/10.1016/0198-0149(88)90084-2

Sunda, W. G., & Huntsman, S. A. (1994). Photoreduction of manganese oxides in seawater. *Marine Chemistry*, *46*(1–2), 133–152. https://doi.org/10.1016/0304-4203(94)90051-5

Taylor, S. R., & McLennan, S. M. (1995). The geochemical evolution of the continental crust. *Reviews of Geophysics*, *33*(2), 241–265. https://doi.org/10.1029/95RG00262

Tebo, B. M., Bargar, J. R., Clement, B. G., Dick, G. J., Murray, K. J., Parker, D., et al. (2004). Biogenic manganese oxides: Properties and mechanisms of formation. *Annual Review of*

Earth and Planetary Sciences, *32*(Goldberg 1954), 287–328. https://doi.org/10.1146/annurev.earth.32.101802.120213

Tebo, B. M., Johnson, H. A., McCarthy, J. K., & Templeton, A. S. (2005). Geomicrobiology of manganese(II) oxidation. *Trends in Microbiology*, *13*(9), 421–428. https://doi.org/10.1016/j.tim.2005.07.009

Tovar-Sanchez, A., Sañudo-Wilhelmy, S. A., Kustka, A. B., Agustí, S., Dachs, J., Hutchins, D. A., et al. (2006). Effects of dust deposition and river discharges on trace metal composition of Trichodesmium spp. in the tropical and subtropical North Atlantic Ocean. *Limnology and Oceanography*, *51*(4), 1755–1761. https://doi.org/10.4319/LO.2006.51.4.1755

Turekian, K. K. (1977). The fate of metals in the oceans. *Geochimica et Cosmochimica Acta*. https://doi.org/10.1016/0016-7037(77)90109-0

Twining, B. S., & Baines, S. B. (2013). The Trace Metal Composition of Marine Phytoplankton. *Annu. Rev. Mar. Sci*, *5*, 191–215. https://doi.org/10.1146/annurev-marine-121211-172322

Twining, B. S., Baines, S. B., Bozard, J. B., Vogt, S., Walker, E. A., & Nelson, D. M. (2011). Metal quotas of plankton in the equatorial Pacific Ocean. *Deep-Sea Research Part II: Topical Studies in Oceanography*, *58*(3–4), 325–341. https://doi.org/10.1016/j.dsr2.2010.08.018

Twining, B. S., Rauschenberg, S., Morton, P. L., & Vogt, S. (2015). Metal contents of phytoplankton and labile particulate material in the North Atlantic Ocean. *Progress in Oceanography*, *137*, 261–283. https://doi.org/10.1016/j.pocean.2015.07.001

Twining, B. S., Rauschenberg, S., Baer, S. E., Lomas, M. W., Martiny, A. C., & Antipova, O. (2019a). A nutrient limitation mosaic in the eastern tropical Indian Ocean. *Deep-Sea Research Part II: Topical Studies in Oceanography*, *166*, 125–140. https://doi.org/10.1016/j.dsr2.2019.05.001

Vangriesheim, A., Pierre, C., Aminot, A., Metzl, N., Baurand, F., & Caprais, J. C. (2009). The influence of Congo River discharges in the surface and deep layers of the Gulf of Guinea. *Deep-Sea Research Part II: Topical Studies in Oceanography*, *56*(23), 2183–2196. https://doi.org/10.1016/j.dsr2.2009.04.002

Vedamati, J., Chan, C., & Moffett, J. W. (2015). Distribution of dissolved manganese in the Peruvian Upwelling and Oxygen Minimum Zone. *Geochimica et Cosmochimica Acta*, *156*, 222–240. https://doi.org/10.1016/j.gca.2014.10.026

Vieira, L. H., Krisch, S., Hopwood, M. J., Beck, A. J., Scholten, J., Liebetrau, V., & Achterberg, E. P. (2020). Unprecedented Fe delivery from the Congo River margin to the South Atlantic Gyre. *Nature Communications*, *11*(1), 1–8. https://doi.org/10.1038/s41467-019-14255-2

Weber, T. S., & Bianchi, D. (2020). Efficient Particle Transfer to Depth in Oxygen Minimum Zones of the Pacific and Indian Oceans. *Frontiers in Earth Science*, *8*(September), 1–11. https://doi.org/10.3389/feart.2020.00376

Weber, T. S., John, S., Tagliabue, A., & DeVries, T. (2018). Biological uptake and reversible scavenging of zinc in the global ocean. *Science*, *361*(6397), 72–76. https://doi.org/10.1126/science.aap8532

Wells, M. L., Price, N. M., & Bruland, K. W. (1995). Iron chemistry in seawater and its relationship to phytoplankton: a workshop report. *Marine Chemistry*, *48*, 157–182. Retrieved from http://ac.els-cdn.com/030442039400055I/1-s2.0-030442039400055I-main.pdf?_tid=74580e62-83b5-11e7-ba88-00000aab0f6c&acdnat=1503020282_080c7a8a96fccd3ab908da4e60287d39

Winkler, L. W. (1888). The determination of dissolved oxygen in water. *Berlin DeutChem Gas*, *21*, 2843–2855. Retrieved from https://ci.nii.ac.jp/naid/20001681874

Wuttig, K., Townsend, A. T., van der Merwe, P., Gault-Ringold, M., Holmes, T., Schallenberg, C., et al. (2019). Critical evaluation of a seaFAST system for the analysis of trace metals in marine samples. *Talanta*, *197*(November 2018), 653–668. https://doi.org/10.1016/j.talanta.2019.01.047

Xiang, Y., & Lam, P. J. (2020). Size-Fractionated Compositions of Marine Suspended Particles in the Western Arctic Ocean: Lateral and Vertical Sources. *Journal of Geophysical Research: Oceans*, *125*(8), 1–33. https://doi.org/10.1029/2020JC016144

Yang, W., Guo, L., Chuang, C. Y., Santschi, P. H., Schumann, D., & Ayranov, M. (2015). Influence of organic matter on the adsorption of 210Pb, 210Po and 7Be and their fractionation on nanoparticles in seawater. *Earth and Planetary Science Letters*, *423*, 193–201. https://doi.org/10.1016/j.epsl.2015.05.007

Zheng, L., Minami, T., Takano, S., Ho, T.-Y., & Sohrin, Y. (2021). Sectional Distribution Patterns of Cd, Ni, Zn, and Cu in the North Pacific Ocean: Relationships to Nutrients and Importance of Scavenging. *Global Biogeochemical Cycles*, *35*(7). https://doi.org/10.1029/2020GB006558

Supporting Information for

Particulate Trace Metal Sources, Cycling, and Distributions on the Southwest African Shelf

Ali A. Al-Hashem[1,2*], Aaron J. Beck[1], Stephan Krisch[1,3], Jan-Lukas Menzel Barraqueta[1,4], Tim Steffens[1], Eric P. Achterberg[1,2]

[1]GEOMAR Helmholtz Centre for Ocean Research Kiel, Kiel 24148, Germany.
[2]Christian-Albrechts-University of Kiel, Christian-Albrechts-Platz 4, 24118 Kiel, Germany.
[3]Now at: Bundesanstalt für Gewässerkunde, Am Mainzer Tor 1, 56068 Koblenz, Germany.
[4]Now at: European Ecological Consulting S.L. (EECO), Amorebieta 48340, Spain.

Corresponding author: Ali A. Al-Hashem (aalhashem@geomar.de)

Contents of this section

Introduction

The supplementary information includes a range of different tables with further details that are relevant for the presentation of the analytical method, comparisons of our data with reference sources and other study sites, as well as a summary of statistical analysis (i.e., *t*-tests, correlations, and principal component analysis). In addition, figures include plots used to compute statistics which are referenced in the main article, as well as additional illustrations (scatter, station, section, and isosurface plots) that help reinforce the narrative of the discussions in the main article

Table S3.1. Sample procedural blanks, limits of detection, measurement relative standard deviation (RSD%) and proportion of samples below the detection limit (BDL) of labile (L-pTM) and refractory (R-pTM) particulate fractions between 13 different particle leach-digestion batches. Detection Limits were determined as 3x the standard deviation (SD) of procedural blanks. Certified Reference Material (CRM) recoveries were determined using certified values and consensus values acquired from the GeoReM database at the time of publication (Jochum et al., 2005). BENG refers to the Benguela shelf stations (ST 43-51; and 1-5) and NORTH refers to the rest of the stations North of Walvis Ridge (ST 6-24).

	n	Al	Fe	Ti	P	Mn	Zn	Cu	Ni	Co	Cd	Pb
Average Process Blank L-pTM (pM/filter ± 1 SD)	***30***	**116 ± 117**	**119 ± 128**	**0.9 ± 1.6**	**415 ± 973**	**2.7 ± 1.8**	**46 ± 40**	**19 ± 36**	**14 ± 16**	**0.36 ± 0.28**	**0.01 ± 0.03**	**0.41 ± 0.71**
Median Process Blank L-pTM (pM/filter)		103	103	0.2	44	2.3	40	6.1	12	0.31	0	0.1
L-pTM Detection Limit (pM/filter)		351	384	4.9	2920	5.4	120	108	49	0.85	0.09	2.1
Percent Samples BDL (BENG%/NORTH%)		1%/0%	10%/5%	57%/16%	0%/4%	0%/0%	1%/10%	22%/10%	30%/21%	0%/0%	13%/5%	0%/0%
Average (L-pTM) Sample RSD (%) (1 SD)		3%	2%	8%	7%	2%	4%	5%	7%	3%	6%	8%
Average Process Blank R-pTM (pM/filter ± 1 SD)	***30***	**130 ± 125**	**165 ± 616**	**115 ± 148**	**128 ± 198**	**1.1 ± 2.6**	**22 ± 51**	**3.4 ± 5.4**	**1.6 ± 3.1**	**0.37 ± 0.58**	**0 ± 0.01**	**0.08 ± 0.11**
Median Process Blank R-pTM (pM/filter)		120	68	79	91	0.37	8.4	1.7	0.99	0.28	0	0.05
R-pTM Detection Limit (pM/filter)		376	1849	445	595	7.9	154	16	9.3	1.7	0.04	0.34
% Samples BDL (BENG/NORTH)		0%/0%	0%/4%	1%/1%	0%/0%	4%/16%	53%/33%	20%/6%	30%/21%	5%/10%	59%/52%	0%/0%
Average (R-pTM) Sample RSD (%) (1 SD)		5%	4%	10%	19%	5%	12%	12%	17%	8%	21%	22%

	n	Al	Fe	Ti	P	Mn	Zn	Cu	Ni	Co	Cd	Pb
BCR-414 Certified/Ref. Values (ng/mg ± 1 SD)		*2673 ± 96*	1850 ± 190	*126 ± 4*	*13400 ± 3200*	**299 ± 13**	**111.6 ± 2.5**	**29.5 ± 1.3**	**18.8 ± 0.8**	1.43 ± 0.06	**0.383 ± 0.014**	**3.97 ± 0.19**
BCR-414 Recovery (Labile, % ± 1 SD)	***25***	1.9 ± 3.7	18.7 ± 10.9	0.2 ± 3.2	104 ± 25	85.1 ± 8.1	92.8 ± 10.5	84.6 ± 12	18.2 ± 8.1	52 ± 7.2	85.6 ± 15.6	76.2 ± 19.9
BCR-414 Recovery (Total, % ± 1 SD)	***25***	108.6 ± 7.8	103.6 ± 14	109.4 ± 8.9	113.1 ± 20.7	92.5 ± 8.3	99.3 ± 11.1	105 ± 13.8	81.2 ± 18.9	102.1 ± 10.2	90.3 ± 18.2	96.8 ± 24
PACS-3 Certified/Ref. Values (ng/mg ± 1 SD)		***65800 ± 1200***	**41060 ± 640**	**4420 ± 180**	**937 ± 44**	**432 ± 16**	**376 ± 12**	**326 ± 10**	**39.5 ± 2.2**	*12.1*	**2.23 ± 0.16**	**188 ± 7.4**
PACS-3 Recovery (Total, % ± 1 SD)	***3***	84.9 ± 1.8	84.6 ± 2.2	95.4 ± 4.4	112.1 ± 7.5	96.7 ± 2.2	86.9 ± 1.3	90.4 ± 2.9	79.7 ± 5.3	*110.8 ± 2.1*	113.7 ± 11.6	95.6 ± 1.5

Table S3.2. Elemental abundance ratios of regional lithogenic sources, average Upper Continental Crust (UCC) values, and GA08 samples (this study). GA08 Sample ratios presented are of the refractory particulate (R-pTM) fraction.

Region	Fe:Al (mol:mol)	Fe:Ti (mol:mol)	Al:Ti (mol:mol)	Al:Mn (mol:mol)	Ti:Mn (mol:mol)
UCC (Rudnick & Gao, 2013)	*0.232 (0.199-0.269)*	*8.77 (6.99-11.11)*	*37.7 (31.65-45.45)*	*208 (166-250)*	*5.90 (4.39-7.41)*
NAM Namibian Atmos. Aerosol (Annegarn et al., 1983)	-	*11.1*	-	-	-
NAM Namib Dust ***(from soil, 0.3-2.6 µm)*** (Eltayeb et al., 1993)	*0.91*	*12.5*	*13.7*	*52.6*	*5*
This study (R-pTM ratios)	**R-pFe:R-pAl (mol:mol)**	**R-pFe:R-pTi (mol:mol)**	**R-pAl:R-pTi (mol:mol)**	**R-pAl:R-pMn (mol:mol)**	**R-pTi:R-pMn (mol:mol)**
BENG stations (ST 43-51;1-5)	*0.276*	*9.90*	*35.9*	*591*	*16.5*
NORTH stations (ST 6-24)	*0.185*	*7.66*	*41.2*	*1391*	*33.3*

Figure S3.1. Normality distributions of the entire Log transformed pTM dataset (Top); and results of distribution fit parameter estimates (below) executed on OriginPro (Version 9.8.5).

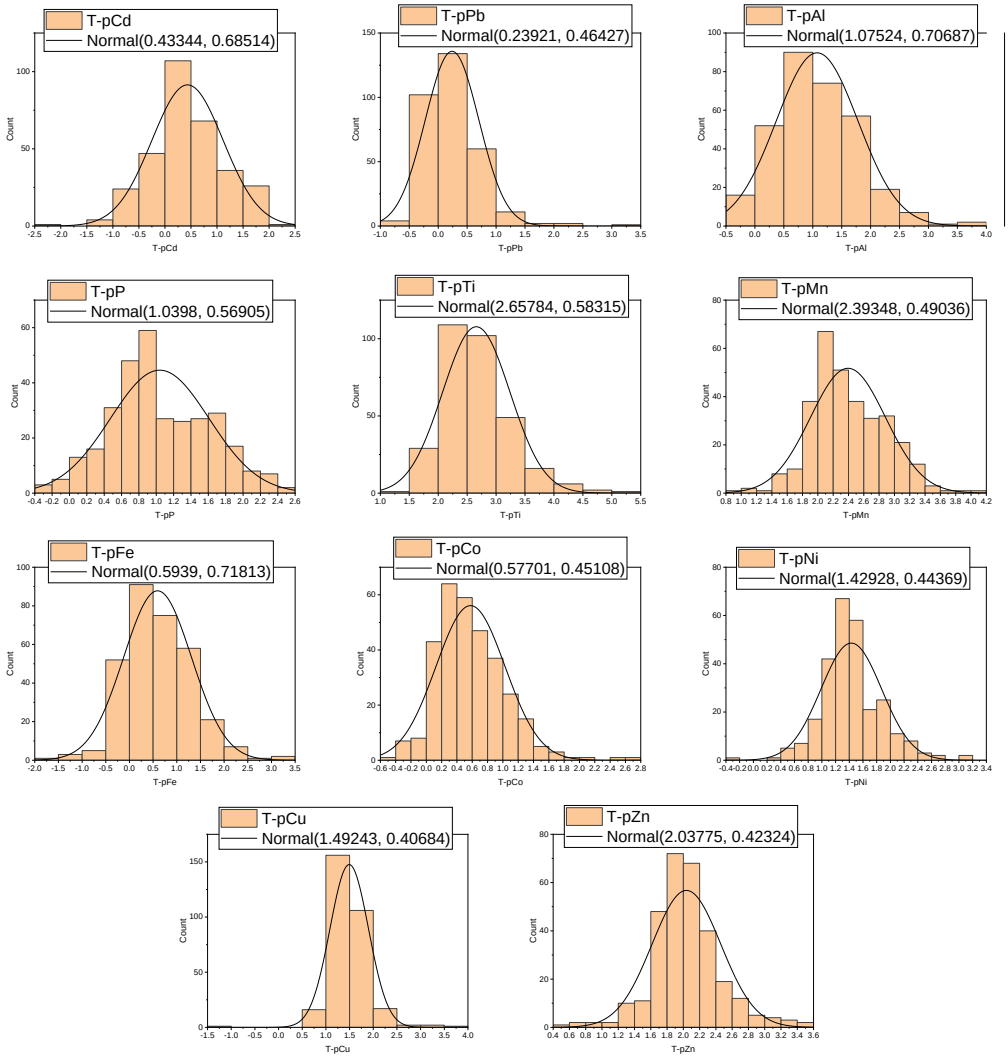

	Distribution	Parameter	Estimate	Lower 95%	Upper 95%
T-pCd	Normal	Location mu	0.43344	0.35766	0.50922
		Scale sigma	0.68514	0.63348	0.74101
T-pPb	Normal	Location mu	0.23921	0.18802	0.2904
		Scale sigma	0.46427	0.42937	0.50201
T-pAl	Normal	Location mu	1.07524	0.99755	1.15293
		Scale sigma	0.70687	0.65389	0.76413
T-pP	Normal	Location mu	1.0398	0.97726	1.10235
		Scale sigma	0.56905	0.5264	0.61515
T-pTi	Normal	Location mu	2.65784	2.59344	2.72224
		Scale sigma	0.58315	0.53925	0.63063
T-pMn	Normal	Location mu	2.39348	2.33958	2.44737
		Scale sigma	0.49036	0.45361	0.53009
T-pFe	Normal	Location mu	0.5939	0.51472	0.67308
		Scale sigma	0.71813	0.66415	0.77651
T-pCo	Normal	Location mu	0.57701	0.52735	0.62666
		Scale sigma	0.45108	0.41723	0.48769
T-pNi	Normal	Location mu	1.42928	1.37636	1.48221
		Scale sigma	0.44369	0.40771	0.48285
T-pCu	Normal	Location mu	1.49243	1.44647	1.53839
		Scale sigma	0.40684	0.37553	0.44076
T-pZn	Normal	Location mu	2.03775	1.98994	2.08557
		Scale sigma	0.42324	0.39067	0.45853

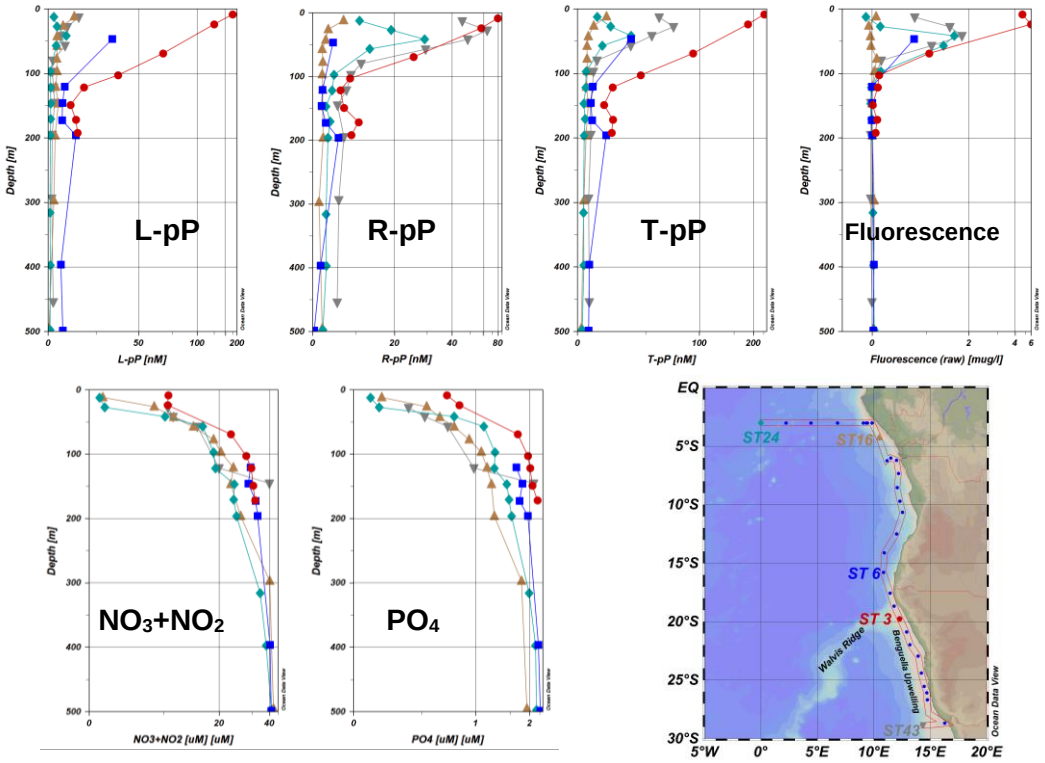

Figure S3.2. Water column profiles of the different pP fractions, Fluorescence, nitrate + nitrite, and phosphate in Stations 43 (grey), 3 (red), 6 (blue), 16 (brown), and 24 (green). Note the stretched scales on the horizontal axis.

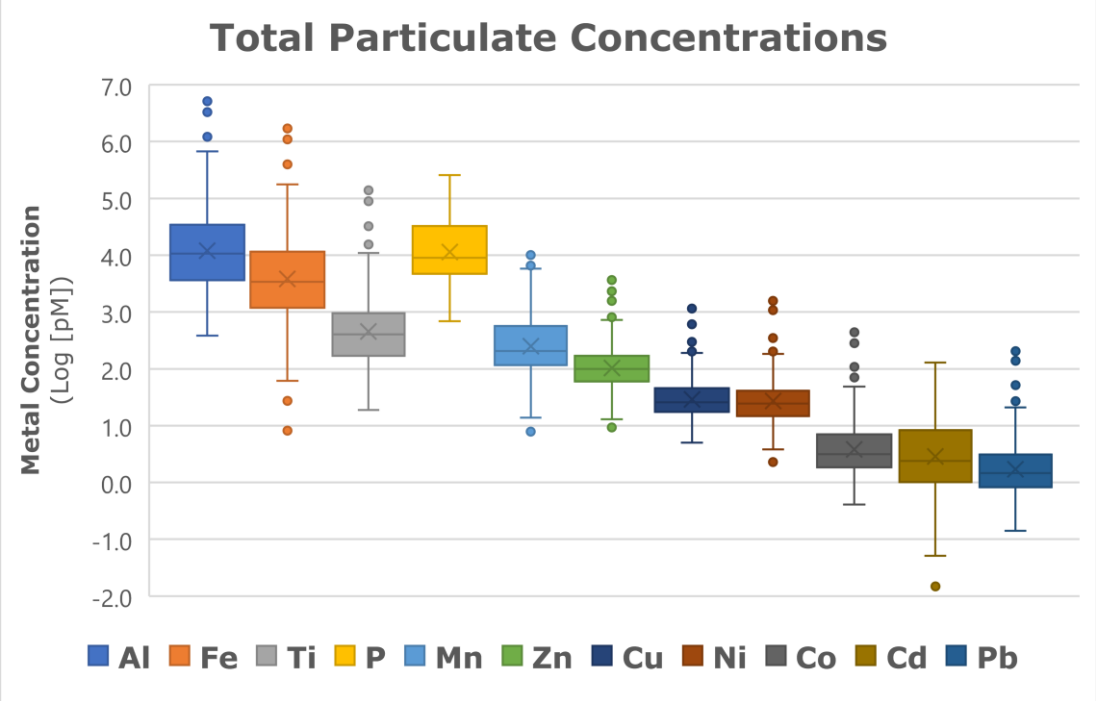

Figure S3.3. Total particulate trace metal (T-pTM) concentration ranges in samples across the GA08 transect. Note the logarithmic concentration scale (pM). The ends of boxes and whiskers represent the 25th and 75th percentiles and the 5th and 95th percentiles, respectively. The points beyond the whiskers represent outliers. The horizontal line and "X" within each box represent the median and average, respectively. Total particulate concentrations shown are the sum of the sample labile and refractory particulate concentrations.

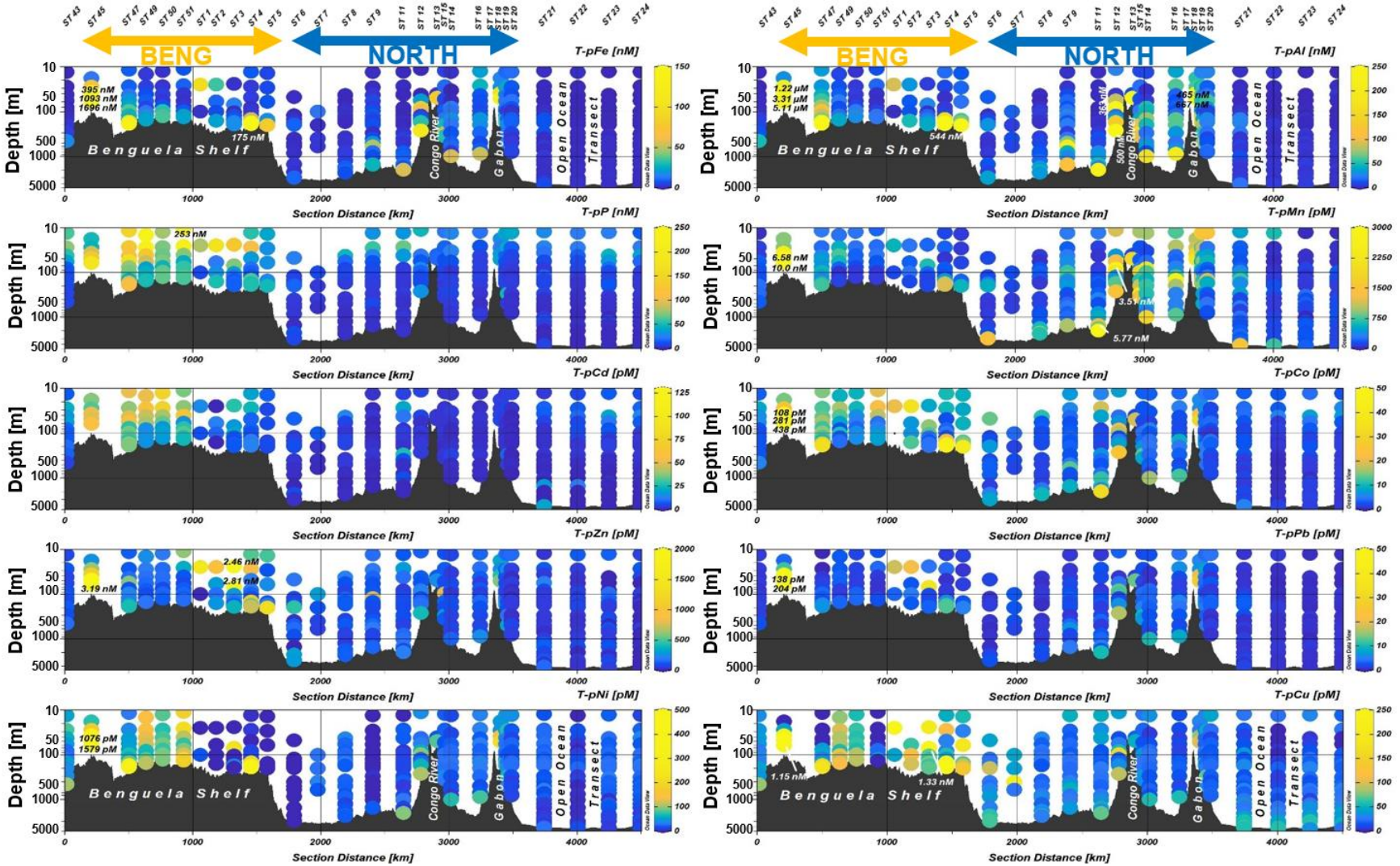

Figure S3.4. Distribution of total particulate trace metal (pTM) concentrations along the GA08 transect. Note the logarithmic depth scales. Excluded 2 anomalously high measurements (8.2 nM T-pCu and 1.1 nM T-pPb).

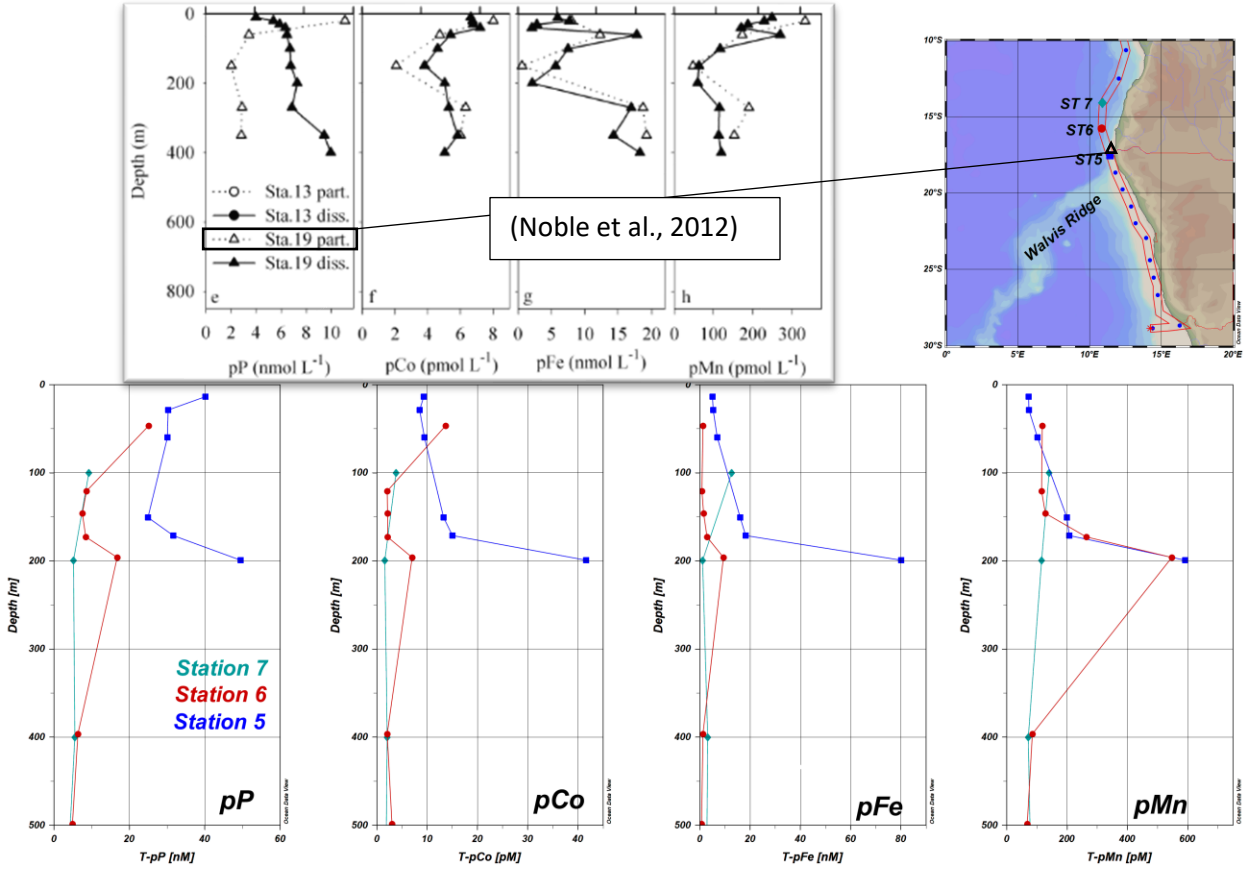

Figure S3.5. Comparison of particulate phosphorus (pP), cobalt (pCo), iron (pFe), and manganese (pMn) concentrations reported by Noble et al., (2012) (Top) with values from nearby stations within our transect (Bottom). The values by Noble et al., (2012) were from in GAc01-ST19, sampled at 14.75°S, 12.2°E roughly in between stations 6 and 7 of this study (illustrated on map, top-right).

Table S3.3. Total particulate trace metal (pTM) concentrations of samples from our study area (GA08) compared to other reported shelf and slope regions (< 1,000 m bottom depth). The ranges reported are of the upper and lower quartile values of all particulate samples within the respective stations referenced. Reference values were compiled from the GEOTRACES IDP2021.

		pAl [nM]	pFe [nM]	pTi [nM]	pP [nM]	pMn [pM]	pZn [pM]	pCu [pM]	pNi [pM]	pCo [pM]	pCd [pM]	pPb [pM]	Remarks
This Study	**1st-3rd Quart**	**7.04 - 54.3**	**2.56 - 180**	**0.292 - 1.48**	**6.77 - 46.4**	**140 - 738**	**82.7 - 224**	**19.4 - 55.8**	**9.44 - 53.6**	**2.55 - 9.61**	**1.23 - 15.0**	**1.24 - 3.77**	GA06 (ST 4+5)
	MAX conc.	**5111**	**1697**	**138**	**253**	**10024**	**3189**	**1326**	**1579**	**439**	**129**	**205**	
Peruvian Shelf	**1st-3rd Quart**	3.01 - 7.47	3.52 - 9.68	0.07 - 0.12	27.4 - 79.5	20.6 - 76	75.1 - 152	76.7 - 123	90.1 - 149	3.02 - 8.73	8.54 - 50.7	1.2 - 1.70	GP16 (ST 2-4)
	MAX conc.	162	159	2.96	983	712	1216	949	705	36.5	355	51.7	
South Africa	**1st-3rd Quart**	2.28 - 26.2	0.1 - 6.60	0.14 - 0.65	8.1 - 47.4	72.4 - 163	41.0 - 145	22.9 - 58.0	28.5 - 159	10.4 - 16.2	1.52 - 7.67	1.00 - 2.10	GA10
	MAX conc.	131	37.8	3.61	131	360	1132	92.7	490	47.9	13.8	3.51	(ST 8)
Uruguay	**1st-3rd Quart**	50.1 - 501	10.8 - 144	1.66 - 18.1	54.8 - 75.4	874 - 8000	100 - 497	83.2 - 153	124 - 225	45.6 - 80.7	18.1 - 21.1	5.69 - 21.0	GA10
	MAX conc.	1005	280	23.8	81.7	10160	589	186	252	95.3	25.5	27.4	(ST 24)
Portugal	**1st-3rd Quart**	7.88 - 50.8	2.01 - 10.0	0.13 - 0.87	2.05 - 16.4	173 - 273	-	15.4 - 21.3	-	2.05 - 4.55	0.42 - 1.81	1.91 - 4.63	GA01
	MAX conc.	1544	304	21.5	34.2	2510	-	221	-	76.8	4.64	68.9	(ST 2+4)
Greenland	**1st-3rd Quart**	21.9 - 58.8	4.37 - 16.5	0.55 - 1.79	17.7 - 47.3	143 - 509	-	47.0 - 59.8	-	3.44 - 7.93	4.17 - 14.1	1.43 - 2.66	GA01
	MAX conc.	75.3	22.1	2.39	161	781	-	145	-	16.0	33.8	3.49	(ST 53+56)
Senegal	**1st-3rd Quart**	366 - 595	75.9 - 114	11 - 19.2	56.3 - 78	869 - 1038	294 - 529	64.1 - 78.8	167 - 228	38.6 - 49.5	12.5 - 15.6	12.5 - 19.4	GA06
	MAX conc.	779	134	26.1	83.6	1368	863	127	265	59.7	18.5	23.2	(ST 4+5)
Bering Sea	**1st-3rd Quart**	2.75 - 454	1.15 - 213	0.29 - 20.1	12.7 - 83.6	200 - 4425	-	50.8 - 188	-	2.93 - 67.6	6.45 - 17.0	1.84 - 24.9	GN01
	MAX conc.	5213	2246	262	308	30350	-	1135	-	639	39.8	82.3	(ST1-3)
Chukchi Sea	**1st-3rd Quart**	89.4 - 1759	23.4 - 500	2.38 - 52.7	27.0 - 173	3620 - 12300	-	64.1 - 456	-	14.5 - 196	3.56 -16.0	4.72 - 43.7	GN01
	MAX conc.	6170	2262	207	336	118450	-	1051	-	617	84.9	199	(ST4-6;8;10;61;66)
Newfoundland	**1st-3rd Quart**	25.1 - 248	8.14 - 75.8	0.77 - 7.44	17.3 - 32.8	255 - 1034	-	53.4 - 88.8	-	7.54 - 25.1	6.53 - 9.33	1.70 - 11.9	GA01
	MAX conc.	559	168	16.7	96.8	1998	-	154	-	52.0	22.5	24.6	(ST 78)

Table S3.4. Labile particulate trace metal fractions (L-pTM/T-pTM, [%]) (upper and lower quartile values) of samples from our study area compared to other study regions.

Sample Labile pTM (%)	LpCd/TpCd (%)	LpPb/TpPb (%)	LpAl/TpAl (%)	LpP/TpP (%)	LpTi/TpTi (%)	LpMn/TpMn (%)	LpFe/TpFe (%)	LpCo/TpCo (%)	LpNi/TpNi (%)	LpCu/TpCu (%)	LpZn/TpZn (%)	Remarks
This Study	94.9 - 99.9	77.2 - 95.2	6.7 - 25.1	21.1 - 55.8	0.1 - 1.5	89.2 - 96.8	15.9 - 29.9	45.5 - 71.7	49.8 - 68.1	41.3 - 64.5	75 - 93.9	Upper and Lower Quartile values
Twining et al., (2015)	>70	-	<20	~ 80	<20	88 - 95	16 - 31	76 - 84	57 - 81	54 - 78	78 - 94	North Atlantic Ocean
Milne et al., (2017)	-	-	-	-	-	-	13-52	-	-	-	-	North Atlantic Ocean; AVG= 24%
Berger et al., (2008)	-	-	7 - 13	-	-	68 - 98	22-37	-	-	-	-	Columbia River Plume
Twining et al., (2019)	-	79 ± 12	16.9 ± 11.7	-	-	82 ± 2	29 ± 7	16.9 ± 11.7	-	-	75 ± 18	Indian Ocean
Rauschenberg & Twining, (2015)	-	-	-	68 - 78	1 - 22	-	-	-	-	-	-	North Atlantic Ocean
Little et al., (2018)	-	-	-	-	-	-	-	-	-	56 ± 11	-	South Atlantic Ocean
Rusiecka et al., (2018)	-	78 ± 10	-	-	-	-	-	-	-	-	-	Northeast Atlantic Ocean

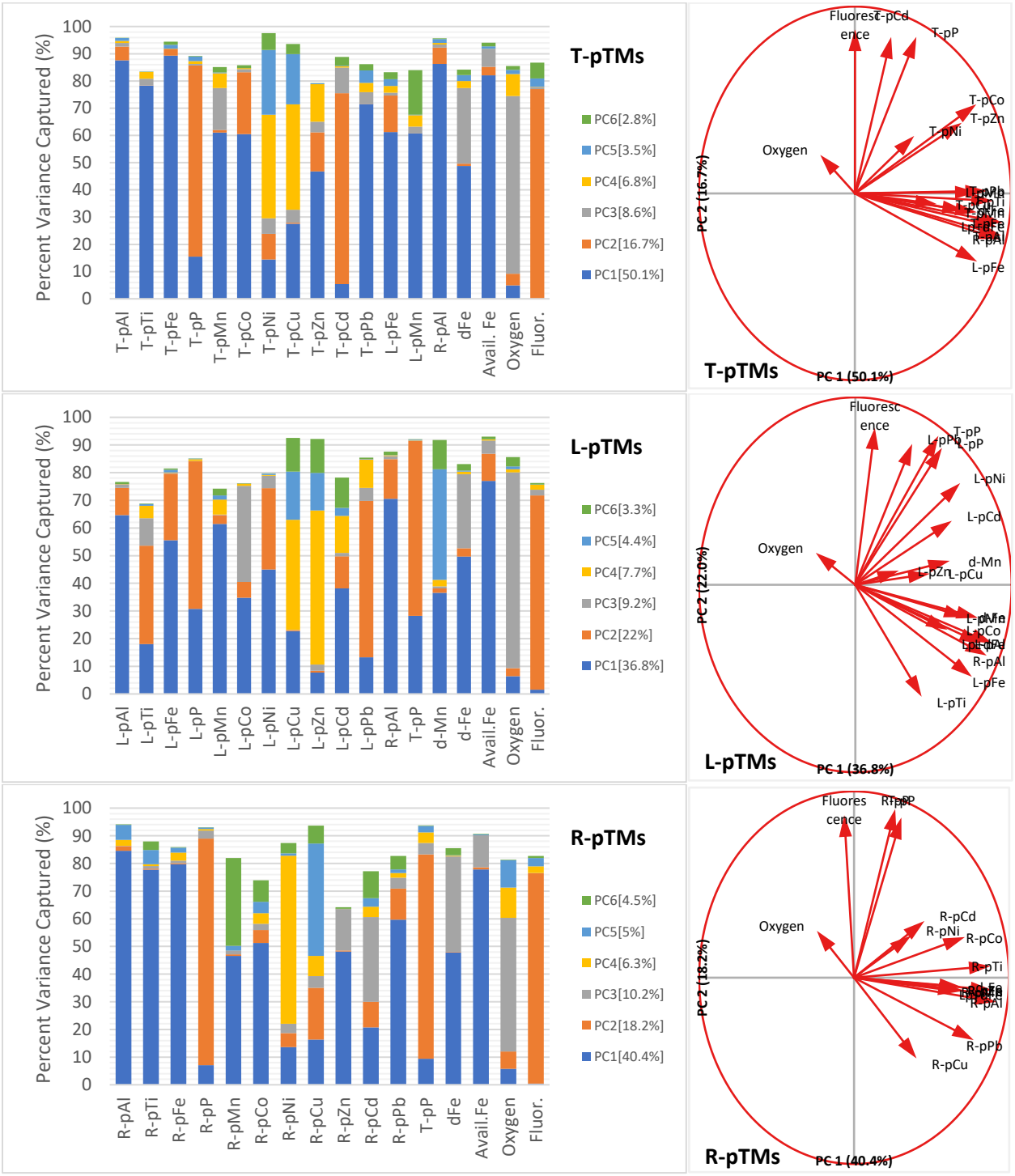

Figure S3.6. A summary of the Principal Component Analysis (PCA) results. (Left) Cumulative variance explained in a 6 PC Model shown for total particulate trace metals (T-pTMs) (Top); Labile particulate trace metals (L-pTMs) (Middle); and Refractory particulate trace metals (R-pTMs) (Bottom). The total variance captured by each component is indicated in the legend embedded in each chart. (Right panel) Biplots showing the vectors of each variable against the first and second PCs of T-pTMs (top); L-pTMs (middle); and R-pTMs (bottom).

Table S3.5. Summarized results of two-sample unequal variance (homoscedastic) *t*-test between samples from BENG stations (ST 43-51 and 1-5) and NORTH stations (ST 6-20) for each element in the labile particulate trace metal (L-pTM) and Refractory particulate trace metal (R-pTM) fractions. **Bold** values correspond to *p*-values < 0.05.

	T-Test Results (*p*-values) (2 Sample Unequal Variance)	
	L-pTM	**R-pTM**
Al	0.3192	0.1421
Fe	0.1515	0.0650
Ti	0.7273	0.1088
P	**0.0000**	**0.0000**
Mn	0.0699	**0.0460**
Zn	**0.0030**	**0.0375**
Cu	**0.0011**	**0.0052**
Ni	**0.0000**	**0.0330**
Co	**0.0001**	0.0616
Cd	**0.0000**	**0.0310**
Pb	0.1139	0.1707

Table S3.6. Bivariate Pearson's correlation matrix of Log-transformed dataset for Labile (L-pTM) and Refractory (R-pTM) particulate trace metals with ancillary measurements and indicators for the GA08 transect along SW African coast and northern open ocean transect. Pearson correlation coefficient values (*r*) are shown in the white-cells, and the intensity of the colored boxes depict the strength of correlations with asterisks signifying different p-value thresholds, respectively. Latitude is the only parameter that was not Log-transformed. Samples with values below detection limit were excluded (pairwise) from the correlation matrix.

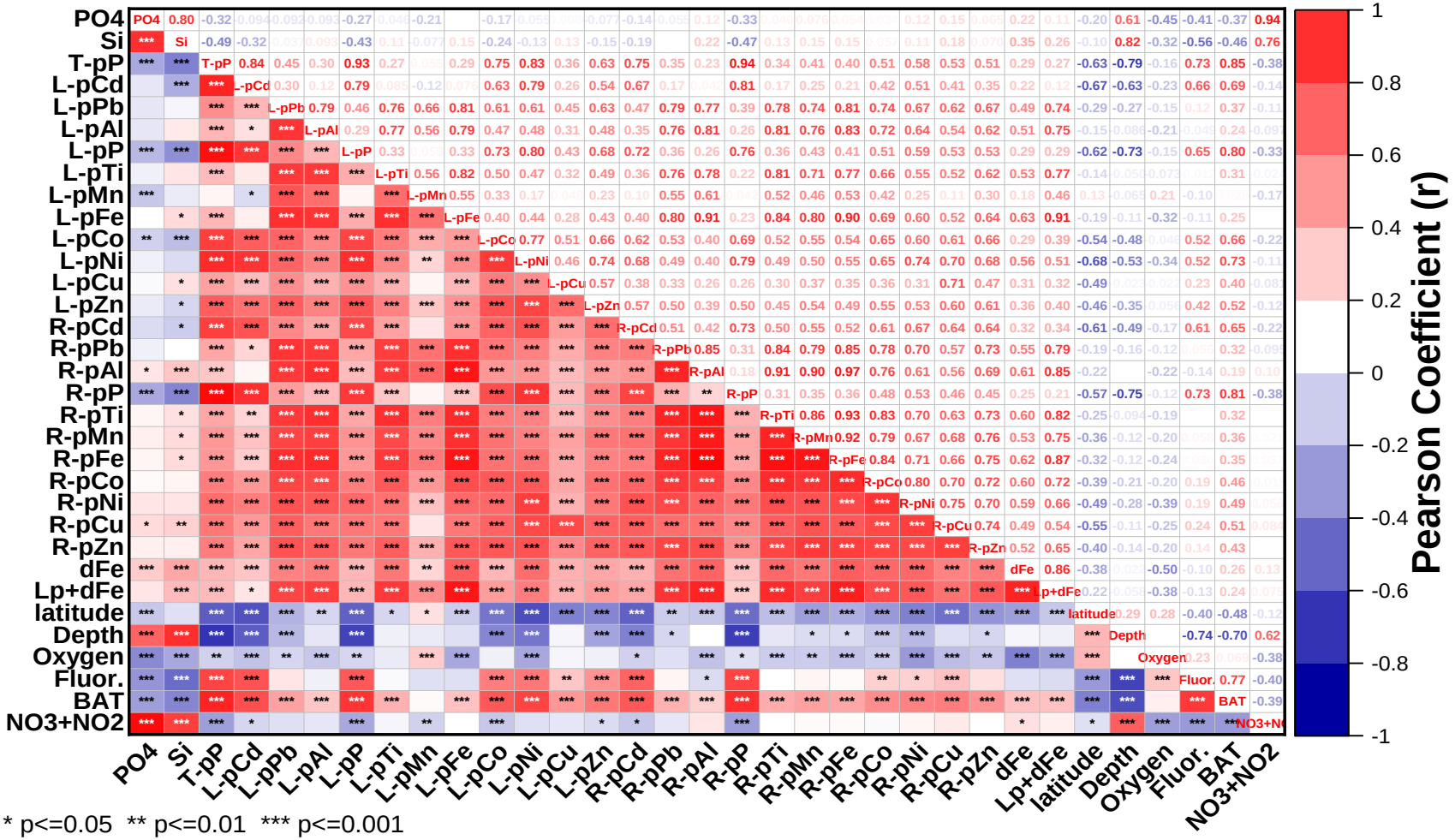

* p<=0.05 ** p<=0.01 *** p<=0.001

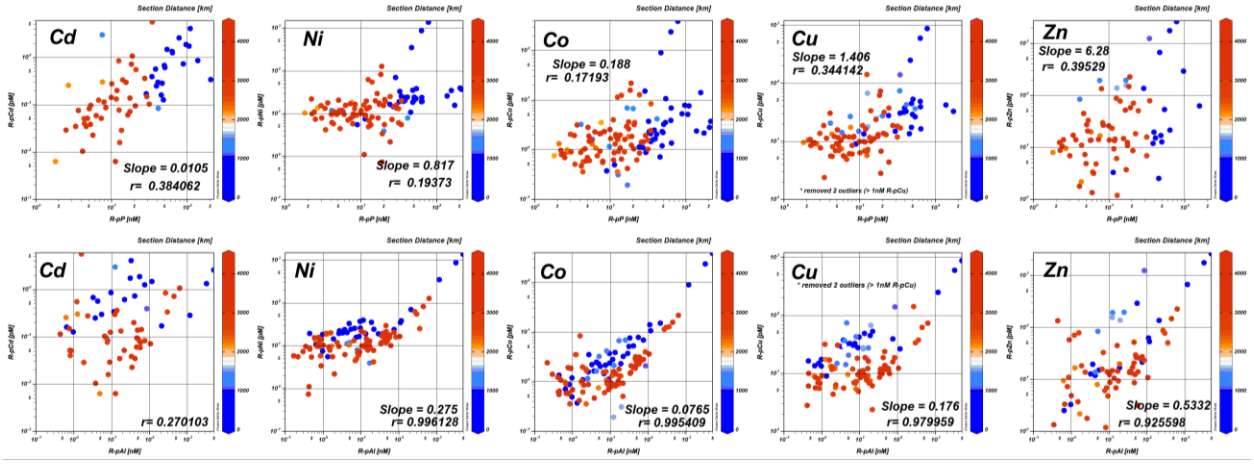

Figure S3.7. (Top Panel) Correlations of bioessential refractory particulate trace metals (R-pTMs) vs. refractory particulate phosphorus (R-pP) for top 100 m of water column through entire transect; and (Bottom Panel) correlations of bioessential RpTMs vs. Refractory pAl (R-pAl) for samples from top 100 m of water column through entire transect. The blue and red sample points indicate samples from BENG and NORTH stations, respectively. Note the logarithmic scales.

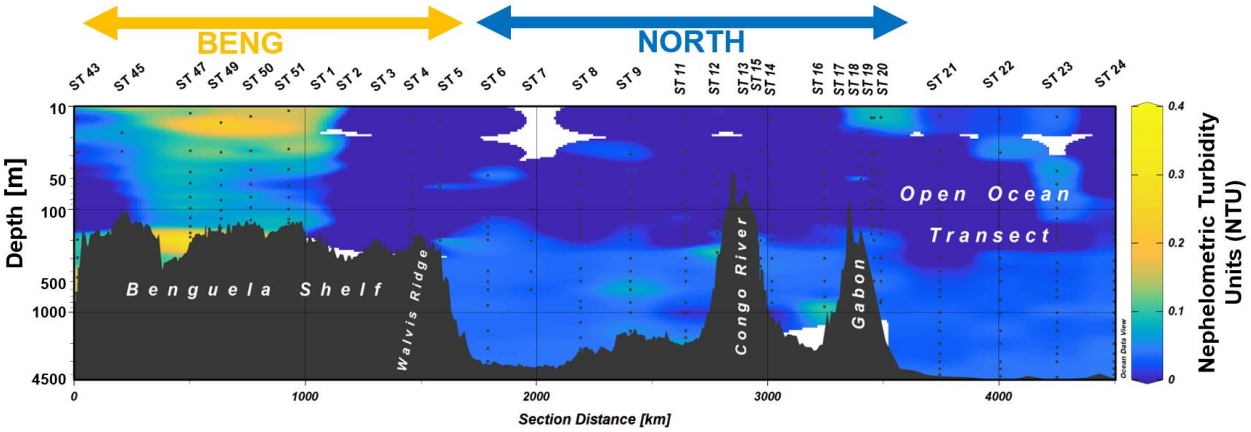

Figure S3.8. The distribution of turbidity measurements (nephelometric turbidity units [NTU]) from nephelometer mounted on CTD along the transect. Excluded samples with >1 µM R-pAl (*n*=3) from station 45. No data is available between stations 1-3 because the CTD was not deployed, due to poor weather conditions, and samples were instead collected using single Go-Flo bottle deployments on the aramid line.

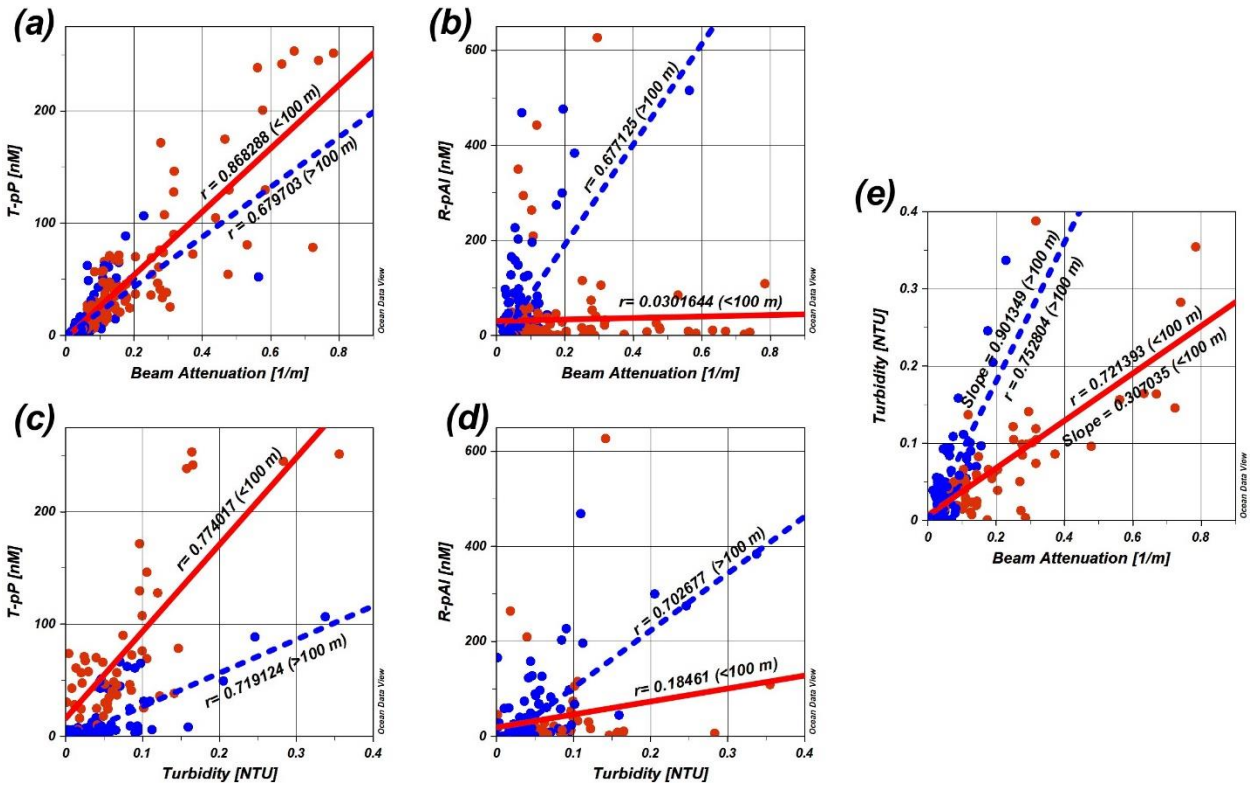

Figure S3.9. Scatterplots illustrating the correlations between (a) total particulate phosphorus (T-pP) and Beam Attenuation (BAT); (b) Refractory particulate aluminum (R-pAl) and BAT; (c) T-pP and Turbidity; and (d) R-pAl and Turbidity. Correlations between Turbidity and BAT are shown on (e). Red solid regression lines are calculated for surface samples (<100 m), and blue dotted regression lines are for samples > 100m. Samples with R-pAl > 1 µM were excluded (*n*=3).

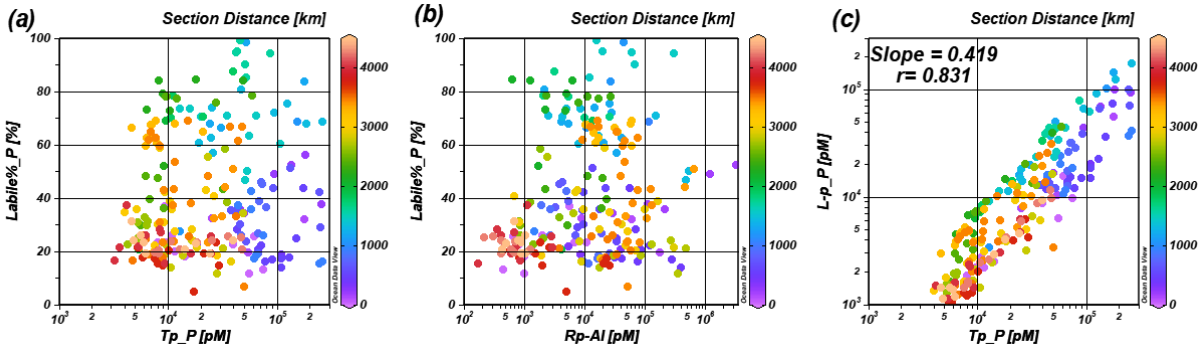

Figure S3.10. Scatterplots illustrating the variable chemical solubility of particulate phosphorus (pP) in the top 300 m across the transect. No significant influences on pP solubilities were apparent by the particle load sizes of (a) biogenic particles (T-pP), or (b) lithogenic particles (R-pAl). Labile fractions remained relatively consistent across the transect (c). Note the Logarithmic scales on scatterplot (c). Section distance (km) was plotted in the *z*-axis (color scale) to illustrate sample (station) locations through the transect.

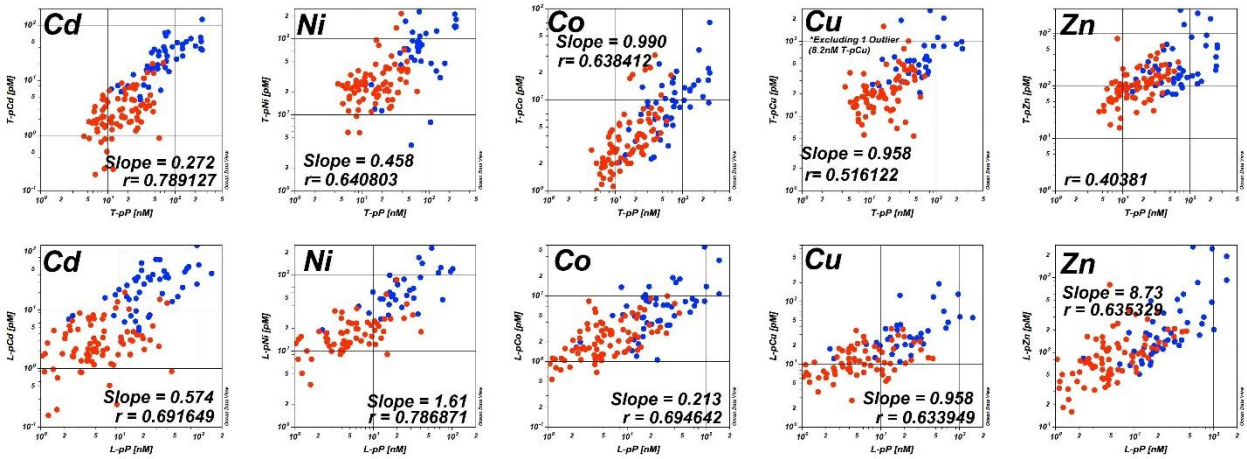

Figure S3.11. Scatterplots showing the correlations of bioessential particulate trace metals (Cadmium [Cd], Nickel [Ni], Cobalt [Co], Copper [Cu], and Zinc [Zn]) with particulate phosphorus concentrations in the total (T-pTM; top panel) and labile particulate (L-pTM; bottom panel) fractions, respectively, in samples within the top 100 m of the water column through the entire GA08 transect. The blue and red sample points indicate samples from BENG (ST43-51 and 1-5) and NORTH (ST6-24) stations, respectively. Note the logarithmic concentration scales. Linear regression slope values are annotataed onto respective plots where *r* >0.5. Refer to Table 3.1 in the main article for a summary of the pTM:pP values within each region and comparison to other plankton stoichiometric reference values.

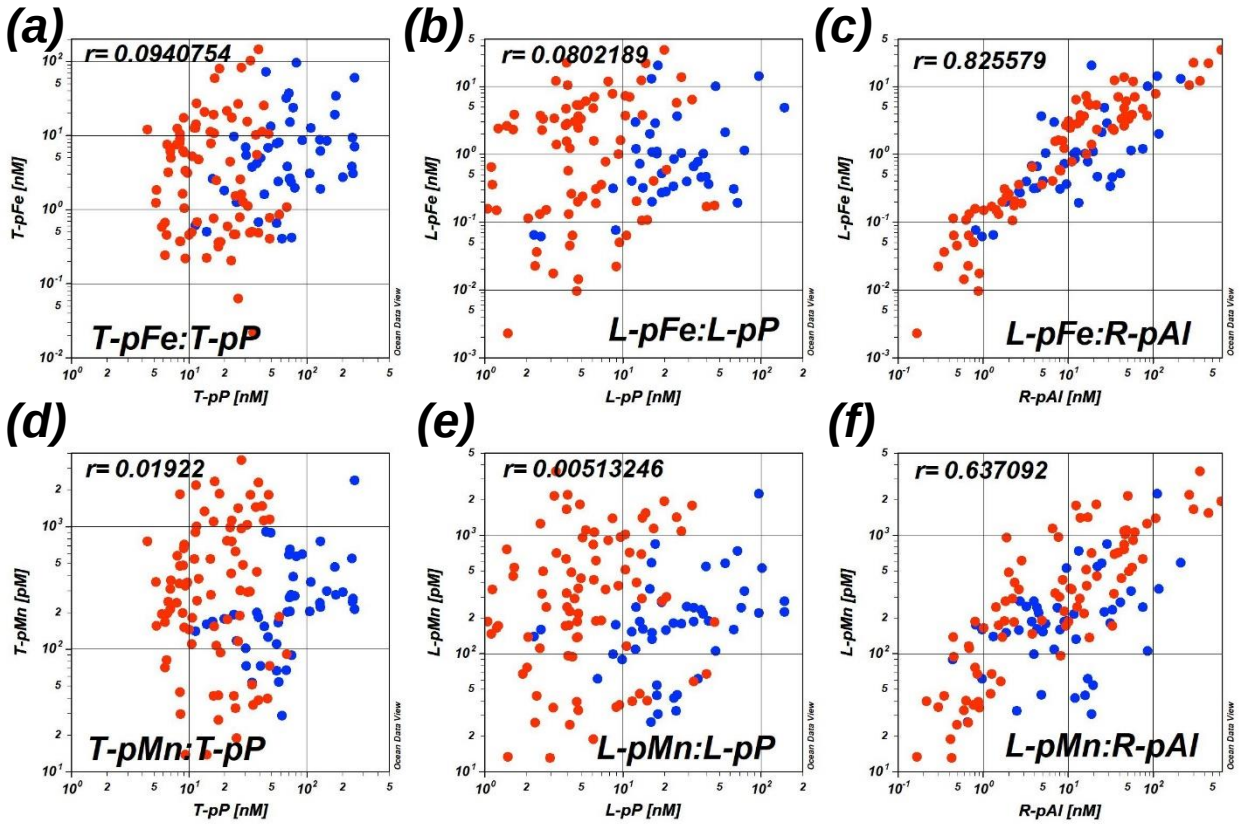

Figure S3.12. Scatterplots showing the correlations of total (T-pFe) and labile particulate iron (L-pFe) with total (T-pP) and labile particulate phosphorus (L-pP), (a and b), respectively; L-pFe with refractory particulate aluminum (R-pAl) (c); total (T-pMn) and labile particulate manganese (L-pMn) with T-pP and L-pP (d and e), respectively; and L-pMn and R-pAl (f), for samples in top 100 m across the transect. The blue and red sample points indicate samples from BENG and NORTH stations, respectively. Scatterplots excluded samples with > 1 µM (*n*=3, from station 45 bottom samples). Note the logarithmic concentration scales.

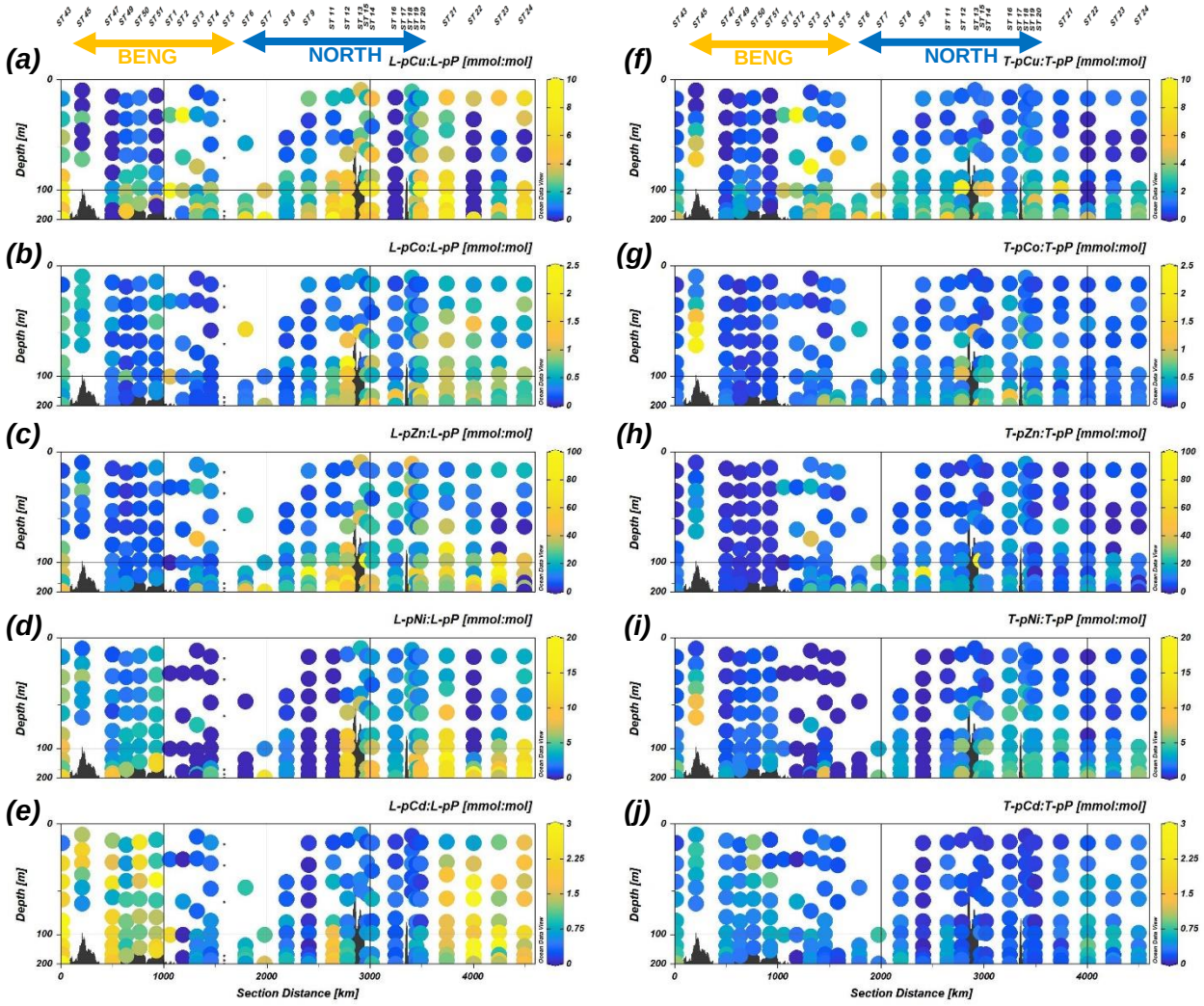

Figure S3.13. Distribution of ratios of labile particulate (L-pTM) and total particulate (T-pTM) bio-essential trace metals (Copper (Cu), Cobalt (Co), Zinc (Zn), Nickel (Ni), and Cadmium (Cd)) normalized to labile (L-pP) (a-e) and total particulate phosphorus (T-pP) (f-j), respectively, for samples in the top 200 m of the water column along the SW African coast and Northern open-ocean transect. Note the stretched depth scales. Refer to Table 3.1 in the main article for a summary of the labile and total pTM:pP values within each region and comparison to other plankton stoichiometric reference values.

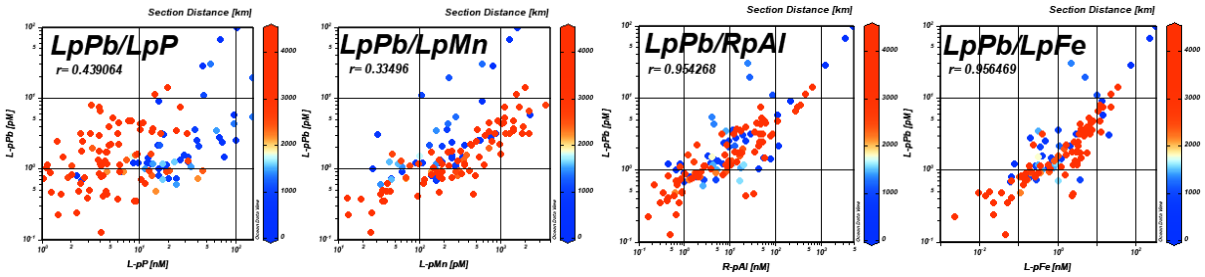

Figure S3.14. (Left-to-Right) Scatterplots of labile particulate lead (L-pPb) against particle-type proxies labile particulate phosphorus (L-pP), labile particulate manganese (L-pMn), refractory particulate aluminum (R-pAl), and labile particulate iron (L-pFe) from samples in the top 100 m across the transect. Note the logarithmic scales. The blue and red sample points indicate samples from BENG and NORTH stations, respectively.

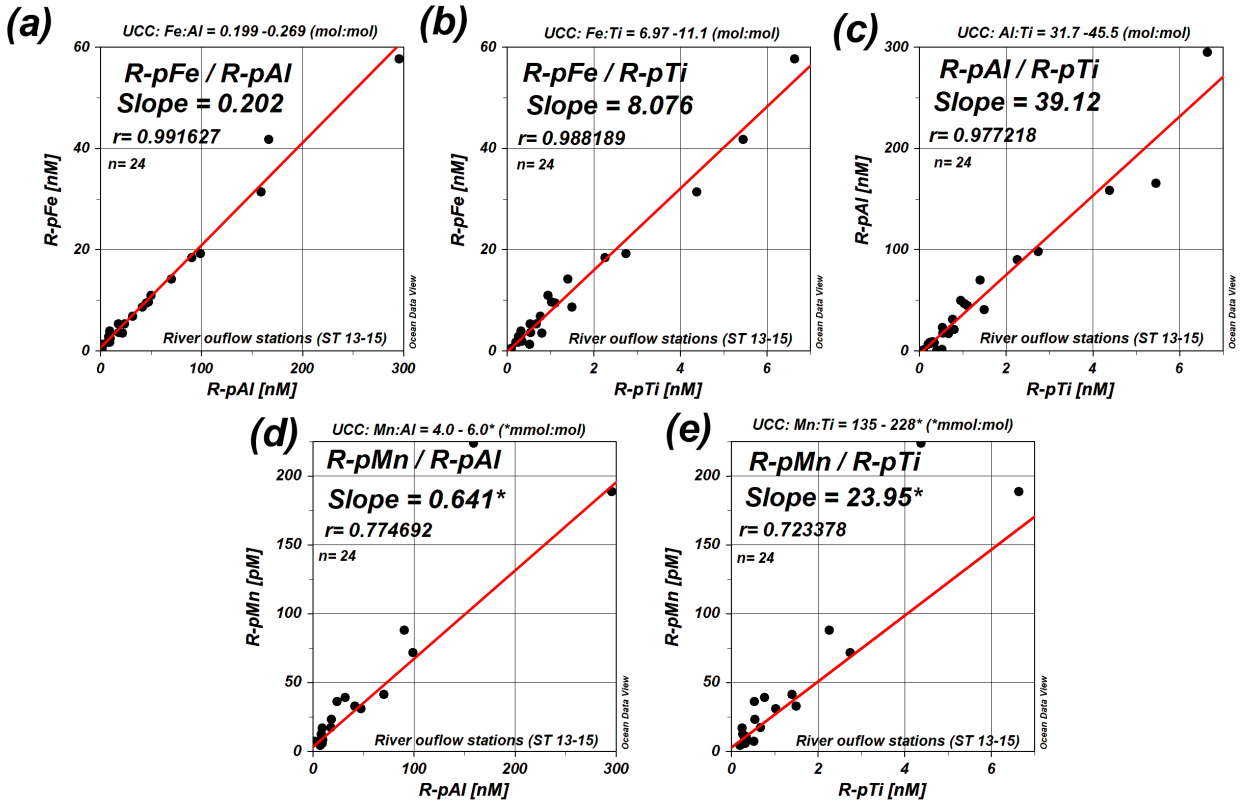

Figure S3.15. Scatterplots of samples from river outflow stations (ST 13-15) showing elemental abundance ratios of refractory particulate trace metals (R-pTM) for (a) R-pFe:R-pAl; (b) R-pFe:R-pTi; (c) R-pAl:R-pTi; (d) R-pMn:R-pAl; and (e) R-pMn:R-pTi. The slope values reported in (a-c) are in mol:mol; and (d-e) are in mmol:mol. The upper continental crust reference values are noted above each respective plot and are also included on Table S3.1.

Table S3.7. *t*-test results (2-sample equal variance) demonstrating regional contrast in refractory particle composition (R-pTMs) between BENG and NORTH shelf regions.

	BENG-Fe:Al	NORTH-Fe:Al	BENG-Fe:Ti	NORTH-Fe:Ti	BENG-Al:Ti	NORTH-Al:Ti
Mean	**0.338**	**0.254**	**8.79**	**7.61**	**29.7**	**32.2**
Mean Diff.	0.084		1.178		-2.57	
Median	0.267		8.40		31.7	
StDev	0.206	0.107	4.39	2.564	11.5	11.3
RSD	0.6	0.4	0.5	0.3	0.4	0.3
	n=	357	*n*=	350	*n*=	348
	Deg. Freedom	355		348		346
***t*-test**	**Fe:Al**		**Fe:Ti**		**Al:Ti**	
2-sample eq. Var.	0.0000		0.0050		0.0422	
2-sample uneq. Var.	0.0000		0.0017		0.0412	

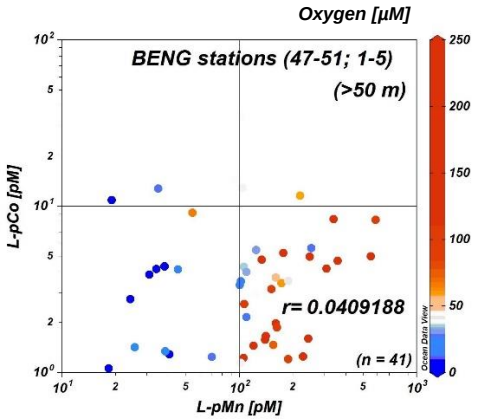

Figure S3.16. Scatterplot showing the correlation between labile particulate Mn (L-pMn) and labile particulate Co (L-pCo) in samples below 50 m over the Benguela shelf. Note the logarithmic concentration scales.

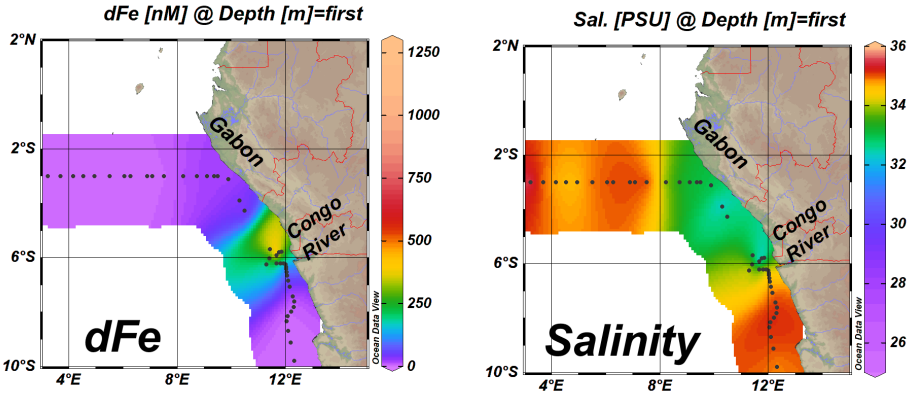

Figure S3.17. Dissolved iron (dFe) concentrations and salinity in surface waters (~5 m) of seawater collected near the Congo River using a towed trace metal clean sampler.

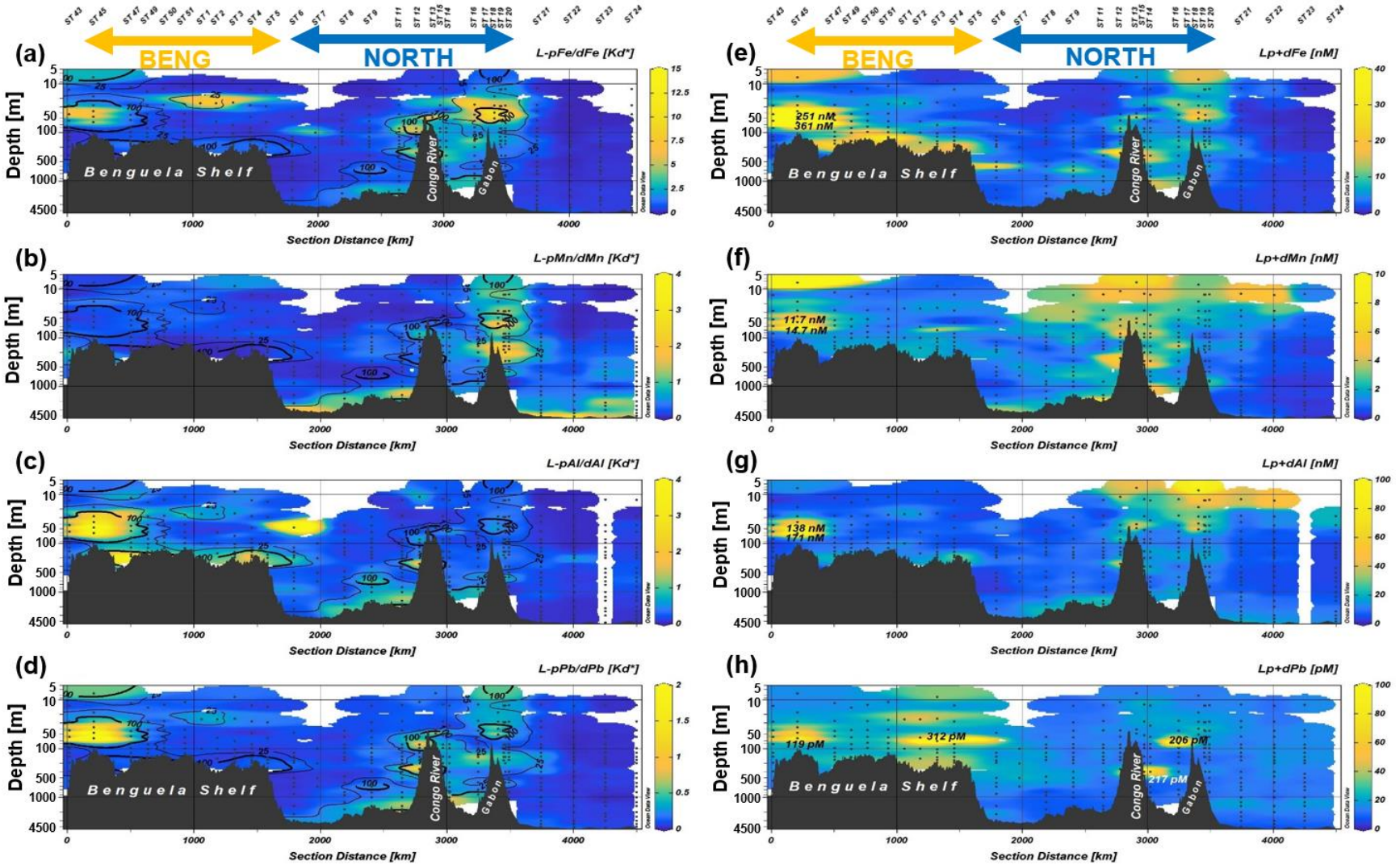

Figure S3.18. Sections illustrating the labile particulate/dissolved trace metal (L-pTM/dTM) partitioning of (a) iron (Fe); (b) manganese (Mn); (c) aluminum (Al); and (d) lead (Pb); and the available TM (L-pTM + dTM) concentration distributions of (e) Fe; (f) Mn; (g) Al; and (h) Pb. Contour lines on plots (a-d) depict the concentrations of the lithogenic particle proxy, refractory particulate Al (R-pAl). Concentrations have been annotated where values exceeded the color-bar scale (*z*-axis).

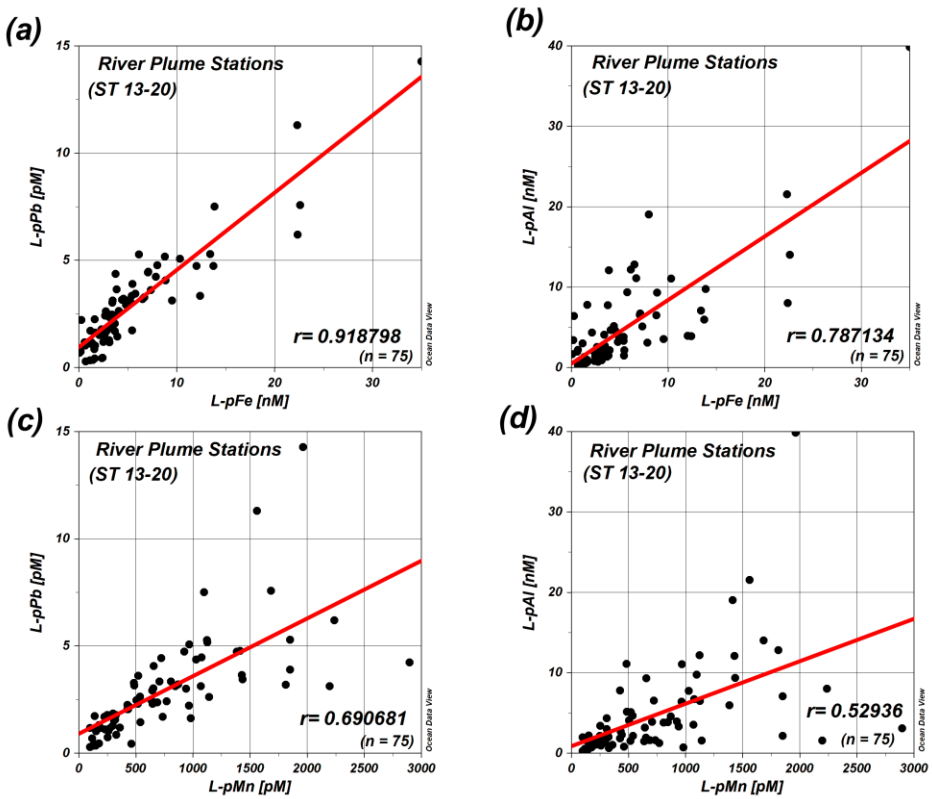

Figure S3.19. Scatter plots showing the correlations between (a) labile particulate lead and iron (L-pPb/L-pFe); (b) L-pPb/labile particulate manganese (L-pMn); (c) labile particulate aluminum (L-pAl)/L-pFe; and (d) L-pAl/L-pMn. Samples shown are from the coastal Congo River plume stations 13-20.

References:

Al-Hashem, Ali A; Beck, Aaron; Achterberg, Eric Pieter (2022): Labile, Refractory, and Total Particulate Trace Metal Concentrations from the GEOTRACES GA08 Shelf section and 3-degree Latitudinal transect. PANGAEA, https://doi.org/10.1594/PANGAEA.945498

Annegarn, H. J., van Grieken, R. E., Bibby, D. M., & von Blottnitz, F. (1983). Background aerosol composition in the namib desert, South West Africa (Namibia). *Atmospheric Environment (1967)*, *17*(10), 2045–2053. https://doi.org/10.1016/0004-6981(83)90361-X

Berger, C. J. M., Lippiatt, S. M., Lawrence, M. G., & Bruland, K. W. (2008). Application of a chemical leach technique for estimating labile particulate aluminum, iron, and manganese in the Columbia River plume and coastal waters off Oregon and Washington. *Journal of Geophysical Research*, *113*, 1–16. https://doi.org/10.1029/2007JC004703

Eltayeb, M. A. H., van Grieken, R. E., Maenhaut, W., & Annegarn, H. J. (1993). Aerosol-soil fractionation for Namib Desert samples. *Atmospheric Environment Part A, General Topics*, *27*(5), 669–678. https://doi.org/10.1016/0960-1686(93)90185-2

Jochum, K. P., Nohl, U., Herwig, K., Lammel, E., Stoll, B., & Hofmann, A. W. (2005). GeoReM: A new geochemical database for reference materials and isotopic standards. *Geostandards and Geoanalytical Research*, *29*(3), 333–338. https://doi.org/10.1111/j.1751-908x.2005.tb00904.x

Little, S. H., Archer, C., Milne, A., Schlosser, C., Achterberg, E. P., Lohan, M. C., & Vance, D. (2018). Paired dissolved and particulate phase Cu isotope distributions in the South Atlantic. *Chemical Geology*, *502*(June), 29–43. https://doi.org/10.1016/j.chemgeo.2018.07.022

Liu, Te; Krisch, Stephan; Hopwood, Mark J; Achterberg, Eric Pieter; Mutzberg, André (2022): Trace metal data from water samples during METEOR cruise M121. *PANGAEA*, https://doi.pangaea.de/10.1594/PANGAEA.947275

Milne, A., Schlosser, C., Wake, B. D., Achterberg, E. P., Chance, R., Baker, A. R., et al. (2017). Particulate phases are key in controlling dissolved iron concentrations in the (sub)tropical North Atlantic. *Geophysical Research Letters*, *44*(5), 2377–2387. https://doi.org/10.1002/2016GL072314

Noble, A. E., Lamborg, C. H., Ohnemus, D. C., Lam, P. J., Goepfert, T. J., Measures, C. I., et al. (2012). Basin-scale inputs of cobalt, iron, and manganese from the Benguela-Angola front to the South Atlantic Ocean. *Limnology and Oceanography*, *57*(4), 989–1010. https://doi.org/10.4319/lo.2012.57.4.0989

Rauschenberg, S., & Twining, B. S. (2015). Evaluation of approaches to estimate biogenic particulate trace metals in the ocean. *Marine Chemistry*, *171*, 67–77. https://doi.org/10.1016/j.marchem.2015.01.004

Rudnick, R. L., & Gao, S. (2013). *Composition of the Continental Crust*. *Treatise on Geochemistry: Second Edition* (2nd ed., Vol. 4). Elsevier Ltd. https://doi.org/10.1016/B978-0-08-095975-7.00301-6

Rusiecka, D., Gledhill, M., Milne, A., Achterberg, E. P., Annett, A. L., Atkinson, S., et al. (2018). Anthropogenic Signatures of Lead in the Northeast Atlantic. *Geophysical Research Letters*, *45*(6), 2734–2743. https://doi.org/10.1002/2017GL076825

Schlitzer, R., Ocean Data View, https://odv.awi.de, 2018.

Twining, B. S., Rauschenberg, S., Morton, P. L., & Vogt, S. (2015). Metal contents of phytoplankton and labile particulate material in the North Atlantic Ocean. *Progress in Oceanography*, *137*, 261–283. https://doi.org/10.1016/j.pocean.2015.07.001

Twining, B. S., Rauschenberg, S., Baer, S. E., Lomas, M. W., Martiny, A. C., & Antipova, O. (2019). A nutrient limitation mosaic in the eastern tropical Indian Ocean. *Deep-Sea Research Part II: Topical Studies in Oceanography*, *166*(November 2018), 0–1. https://doi.org/10.1016/j.dsr2.2019.05.001

Chapter 4: Marine Biogeochemical Cycling of Particulate Trace Metals on the Peruvian Shelf

Ali A. Al-Hashem[1,2], Aaron J. Beck[1], Insa Rapp[1], Mark J. Hopwood[1,3], Eric P. Achterberg[1,2]

[1]GEOMAR Helmholtz Centre for Ocean Research Kiel, Kiel 24148, Germany.

[2]Christian-Albrechts-University of Kiel, Christian-Albrechts-Platz 4, 24118 Kiel, Germany.

[3]Now at: Southern University of Science and Technology, Shenzhen, China.

The research presented in this chapter is being prepared for submission to *Biogeochemistry.*

Abstract

Trace metal (TM) export from continental shelves form an important source to the open ocean. The TM concentrations are typically enhanced on shelves associated with eastern boundary upwelling systems (EBUS) and oxygen minimum zones (OMZs), although the mechanisms controlling the fate of TMs in the water column are not fully constrained. Untangling the intricate mechanisms governing TM inventories and their (bio-)availability in the water column requires identification of the principal carrier phases and solubility of particulate TMs. Here we present the chemically labile and refractory particulate TM (pTM) distributions of Fe, Mn, Co, Al, Cu, Ni, Zn, Cd, Pb, Ti, V, and P along four transects traversing the Peruvian shelf. We characterize the principal carrier phases associated with the pTMs using particle-type indicators and use elemental ratios to interpret biogeochemical processes governing their distributions. Particulate Mn, Cd, Co, Zn, Cu, Ni, V, and P were mostly labile (>64%) in surface waters across all stations, and elemental stoichiometries similar to plankton sources suggested biogenic origin. Benthic particles contributed to the enhanced labile pTM inventories of Fe, Al, Ti, Mn, V and Pb at shelf stations, with enhanced adsorption of Fe, V, Pb, Al, and Cu. Manganese oxides were generally deficient along the transects, attributed to slow oxidation kinetics of Mn within the OMZ. In contrast, Fe oxides were high in the OMZ, with labile pFe as high as 9.85 nM in the offshore OMZ. A strong association between labile pFe and dissolved Fe (dFe) persisted in offshore waters and suggested that dynamic solid-solution exchange sustained high corresponding dFe concentrations (as high as 4.64 nM). This potentially has consequences for other TMs which are co-transported with Fe oxides via adsorption, particularly V, and thereby facilitates their offshore transfer from continental shelves or out of the OMZ into the underlying sediment reservoir.

4.1 Introduction

Eastern boundary upwelling systems (EBUS) form important regions of enhanced primary production supported by upwelling of macronutrient-rich (nitrogen (N), phosphorus (P), and silicon (Si)) subsurface waters. Extensive oxygen minimum zones (OMZs) are associated with the EBUS as organic matter debris sinks from the euphotic zone to subsurface waters, where it is remineralized, thereby depleting dissolved oxygen concentrations (Helly and Levin, 2004; Karstensen et al., 2008). In addition to macronutrients, marine organisms require a suite of trace metals (TMs) as micronutrients for their growth and functioning, and in some cases a low micronutrient supply may (co-)limit primary production (e.g., Browning et al., 2021, 2018, 2017; Moore et al., 2013). Examples of key metalloenzymes that contain micronutrients include, superoxide dismutase (may require iron (Fe), manganese (Mn), nickel (Ni), copper (Cu) and zinc (Zn)) (Morel and Price, 2003; Twining and Baines, 2013), carbonic anhydrase (Zn, cadmium (Cd), cobalt (Co)) (Morel et al., 1994), amino acid oxidase (Cu) (Ensign et al., 1993), and nitrogenase (Fe and vanadium(V)) (Winter and Moore, 2009), among many others. The Peruvian margin lies within an EBUS of the Eastern Tropical South Pacific Ocean (ETSP) and is among the most productive regions in the global ocean (Bakun and Weeks, 2008; Chavez et al., 2008).

Upwelled waters in the ETSP are often deficient in Fe relative to macronutrients, when considering phytoplankton requirements (Bruland et al., 2005; Moore et al., 2013; Rapp et al., 2020). Therefore, phytoplankton growth can be limited by Fe in surface waters during off shelf transport, resulting in decreases in primary production, with the onset of co-limiting conditions in the open ocean (Browning et al., 2018; Hutchins et al., 2002; Moore et al., 2013). Therefore, it is crucial to constrain the variables that affect the supply of Fe, and other TMs, in eastern boundary currents to predict the biogeochemical response to physical and chemical perturbations in these systems (Capone and Hutchins, 2013).

Marine particles play a key role in the cycling of TMs and form vital transport vectors by which TMs may be carried from shelf regions to the open ocean. The interactions between particles and TMs in seawater are multi-faceted and determined by biogeochemical factors, such as particle types (i.e., substrate), bio-assimilation and remineralization, (non-)reductive

dissolution and (bio-)oxidative (i.e., authigenic) precipitation, (dis-)aggregation, and reversible-adsorption (also referred to as scavenging) (Anderson, 2020; Boyd et al., 2017; Close et al., 2021; Jeandel et al., 2015; Jeandel and Oelkers, 2015; Lam and Anderson, 2018). Dynamic exchanges or transformations between solid and solution phases through these processes assign particles vital roles as reservoirs of exchangeable TMs and/or bio-accessible TM inventories, either directly or through buffering of the dissolved TM (dTM) pool (Achterberg et al., 2018; Fitzsimmons et al., 2017; Lippiatt et al., 2010; Milne et al., 2017; Rusiecka et al., 2018). Despite their important roles in TM biogeochemical cycles, particulate TMs are understudied, particularly within shelf regions of the ocean.

The ETSP's principal source of TMs from shelf and slope sediments is amplified within the OMZ (Chever et al., 2015; Dale et al., 2015), making the OMZ an important conduit for shuttling of Fe, and possibly other TMs, from the coastal margin to the adjacent open ocean (Vedamati et al., 2014). Enhanced fluxes of Fe and other redox-sensitive TMs have been observed on the Peruvian shelf where the sediments intersect with the OMZ, between ~50-500 m, (Noffke et al., 2012; Scholz et al., 2014) and were attributed to the release of reductively dissolved TMs from benthic sources (Lam et al., 2020). However, the extent to which TMs are exported away from the shelf is ultimately governed by stabilization and removal mechanisms. Sediments in the OMZ release substantial dissolved Fe (II) into the water column, which is then quickly oxidized by oxygen or nitrate and removed via precipitation and settling of Fe oxides (Heller et al., 2017; Millero et al., 1987; Schlosser et al., 2018; Scholz et al., 2016). In contrast, dFe released from organic rich sediment overlain by oxygenated seawater is largely stabilized by complexing ligands before being released into the water column enabling further transport away from the benthic sources (Lam et al., 2020). Although, during episodic oxygenation events, such as those occurring during El Nino seasons in the ETSP, water column inventories of redox-sensitive dTM (i.e., Fe, Mn, and Co) decreased, limiting their transport to the open ocean (Rapp et al., 2020). This highlights the complexity of Fe and other TM cycling within dynamic shelf regions, and how different factors such as buffering, supply pathways, and carrier phases influence TM export from shelf sources to the Fe limited ETSP (Browning et al., 2018; Bruland et al., 2005).

Identifying the main pTM carrier phases and their labile fractions is critical to understand how biogeochemical processes in EBUS and OMZs control dissolved TMs. The degree to which TMs are exchangeable between solid and solution phases in the water column impacts their overall stability, and hence the extent of their vertical and lateral transport. Here we apply a widely adopted chemical leach method (Berger et al., 2008) to marine particles from the Peruvian shelf and slope regions, and compare the labile and refractory pTM content with lithogenic and biogenic indicators to determine the principal carrier phases of Fe, Mn, Co, aluminum (Al), Cu, Ni, Zn, Cd, lead (Pb), titanium(Ti), and V. Combined with other ancillary parameters, we infer the biogeochemical processes governing their distributions and discuss the potential implications for seasonal/episodic changes on TM availability and export from the shelf, which may be applicable to other OMZ and EBUS regions.

4.2 Methods

4.2.1 Sample Collection

Seawater samples were collected along four cross-shelf transects off the Peruvian coast between 9 – 16°S aboard the German RV Sonne during the ASTRA-OMZ SO243 cruise between 8th – 19th October 2015 (Figure 4.1). Samples were collected using Go-Flo bottles (General Oceanics) deployed on a Kevlar wire following GEOTRACES protocols (Cutter et al., 2010). Once on deck, the Go-Flo bottles were transferred to a class-100 clean container where they were sub-sampled for TM and iodine samples.

Particulate samples were collected by filtering 0.8 – 5.4 liters (median 3.4 liters) of seawater through 0.2 µm polyethersulfone (PES) membrane filters (25 mm diameter, Sartorius) using overpressure of nitrogen gas (0.2 bar) on each Go-Flo bottle. The filters were then stored frozen at -20°C for later analysis at GEOMAR. Dissolved trace metal (dTM) samples were filtered through a 0.2 µm pore filter (Acropak-500 cartridge filter, Pall) into acid-cleaned 125 ml low density polyethylene (LDPE) bottles (Nalgene), acidified (pH ~1.9) using HCl (OPTIMA grade – Fischer Scientific), and stored for later analysis at GEOMAR. Iodine (iodate and iodide) samples were filtered (0.2 µm Acropak-500 cartridge filter, Pall) and collected in 100 ml opaque high-

density polyethylene (HDPE) bottles (Nalgene), kept at -20°C until later analysis. Unfiltered seawater was sub-sampled from the CTD bottles to determine Fe (II) and was analyzed as soon as possible while on-board (Hopwood et al., 2017). Macronutrient samples were collected using Niskin bottles (General Oceanics) mounted on a stainless-steel CTD rosette (Seabird).

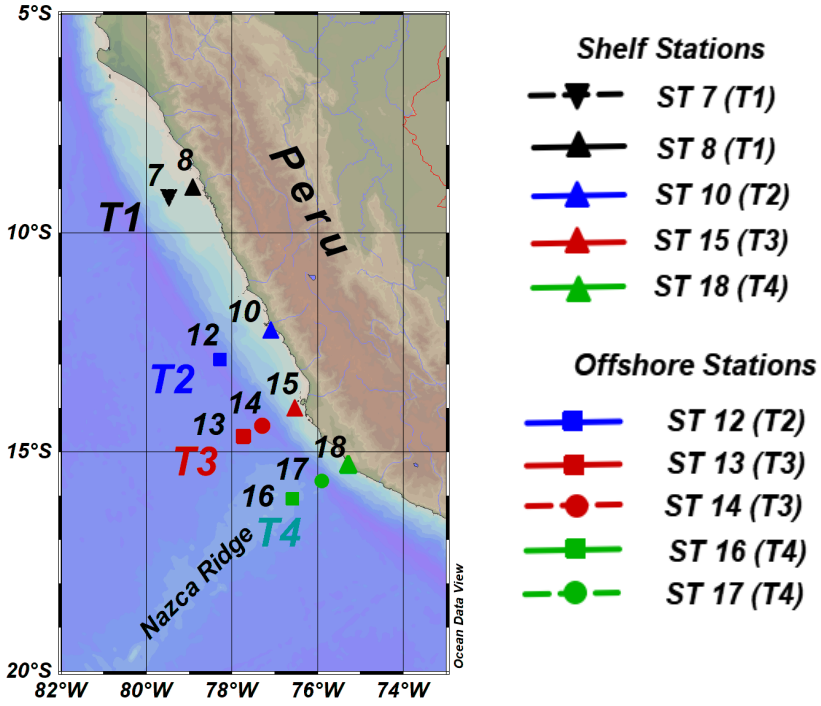

Figure 4.1 - Regional map showing the SO243 stations where samples were collected from the water column. Triangles depict shallow (<300 m) shelf stations. The cross-shelf transects (T1 – T4) are labelled in the same color of their respective stations symbol colors.

4.2.2 Sample Analysis

Particulate trace metal samples were subjected to a sequential chemical leach followed by refractory digestion carried out in perfluoroalkoxy alkane (PFA) digestion vials (Savillex). The labile particulate (L-pTM) fraction was distinguished from refractory particulate (R-pTM) phases, using the method described by Berger et al., (2008). Briefly, the sample L-pTM fraction was solubilized using a solution of 0.02 M hydroxylamine hydrochloride (TM Grade, Sigma-Aldrich) in 25 % Acetic Acid (UpA, Romil), for 2 hours, including a 10 minute heating step at 90°C. The sample leachate was then centrifuged, sub-sampled, and processed separately from the remaining

refractory particles. The remaining leachate (~5-10%) was heated to near-dryness prior to subsequent digestion along with the refractory particles. The filter with remaining refractory particles was adhered to the inner wall of the digestion vial and refluxed for 15 hours at 150˚C using a strong acid mixture (50 % HNO_3/10 % HF v/v%; Optima grade, Fisher Scientific) with a rhenium (Re) spike (Inorganic Ventures) added as an internal standard to monitor for sample loss (10 ng Re per sample), following a method modified from Cullen and Sherrell (1999). Afterwards, the sub-sampled leachate and digested refractory samples, were separately heated to near-dryness and further oxidized using 15% H_2O_2 / 50% HNO_3 (volume %). Following the oxidation step, the samples were again heated to near dryness before the final residual drops (< 50 µL) were re-dissolved using 1 M nitric acid with 1 $\mu g \cdot L^{-1}$ indium (Inorganic Ventures).

Blank acid-cleaned PES filters were prepared using ultra-pure water (Milli-Q, Millipore) and processed identically as the samples and included in each digestion batch as procedural blanks (n=10). At least two replicate samples of plankton certified reference material (BCR-414 – European Commission – Joint Research Centre; 16.7-24.6 mg; n=9) were processed alongside the samples to monitor sample recoveries and reproducibility across digestion batches.

The efficacy of the digestion method on the lithogenic matrix was tested in a separate digestion batch (PACS-3; 17.5-34.8 mg; n=3). TM recoveries were generally within the reference value ranges and summarized in Table S1. Total particulate (T-pTM) concentrations are reported as the sum of the L-pTM and R-pTM concentrations.

Digested pTM samples were measured using high resolution inductively coupled plasma mass spectrometry (HR-ICP-MS, Element XR, Thermo Scientific), and concentrations were determined using external standard calibration curves prepared in the same sample matrix using multi-element standards (71A and 71B, Inorganic Ventures) (Cullen et al., 2001). Analytical drift was monitored and corrected using the added indium. Dissolved TM samples were analyzed using HR-ICP-MS following offline preconcentration using an automated system (Sea-FAST) and were quantified using isotope dilution (Fe, Cu, Cd, Zn, Co, Pb, and Ni) or standard addition (Mn) following the procedure described by Rapp et al. (2017). Fe (II) in seawater was analyzed in the

field within 2 hours of sampling using luminol chemiluminescence flow-injection-analysis (FIA) method as described by (Hopwood et al., 2017).

Macronutrients (NO_2^-, NO_3^-, PO_4^{3-}, and $Si(OH)_4$) were analyzed spectrophotometrically on-board using a QuAAtro autoanalyzer (Seal Analytical) following Becker et al. (2020). Temperature, conductivity, and oxygen were measured by double sensors mounted on the CTD frames. The oxygen sensors were calibrated by Winkler titration on discrete seawater samples (Hansen, 2007; Winkler, 1888).

Principal component analysis (PCA) and bivariate Pearson's correlations were carried out on log-transformed datasets using a Microsoft Excel statistical analysis add-in software (Analyse-it for Microsoft Excel, Version 5.92) and statistical analysis software, OriginPro 2022b (Version 9.95), respectively. Principal component analysis was conducted using data for which full TM and ancillary data were available. Water column sections, station profiles, and scatterplots were prepared using Ocean Data View (Schlitzer, 2019).

Refractory particulate Al and total particulate P were used as lithogenic and biogenic particle indicators, respectively. Particulate Al is used to estimate the lithogenic particulate fraction of other TMs using canonical upper continental crustal abundance ratios (Rudnick and Gao, 2013; Taylor and McLennan, 1995). Phosphorus is an essential macronutrient and stoichiometric TM:P ratios in marine plankton are available from previous field and laboratory studies (compiled in Table 1). Although the applied leach accesses the biogenic pP pool, a relatively large fraction of biogenic pP is thought to be leach-resistant and is likely included in the R-pP pool (Al-Hashem et al., 2022). The chemical leach solubilizes absorbed TM fractions from particles while keeping lithogenic particles largely intact in the refractory fraction (Berger et al., 2008; Rauschenberg and Twining, 2015). Readily reducible Fe and Mn (oxy-)hydroxides (hereafter Fe and Mn oxides) are also solubilized by the chemical leach (Berger et al., 2008; Birchill et al., 2017; Rauschenberg and Twining, 2015).

4.3 Results and Discussion

4.3.1 Hydrographic Features

Samples were collected along four cross-shelf longitudinal transects traversing the Peruvian shelf between 9-16°S (Figure 4.1), which included shelf stations (≤300 m bottom depth; Stations (ST) 7,8,10,15, and 18; *n*=26) and deeper offshore stations (> 300 m bottom depth; ST 12-14,16 and 17; *n*=58) but with a maximum sampling depth of 982 m. The transects featured a southward decrease in shelf width, with increasingly steep shelf slopes.

The main water masses within the study region were Subtropical Water (STW; <25.8 σ_Θ), Equatorial Subsurface Water (ESSW; 25.8 – 27.34 σ_Θ), and a mixture of Antarctic Intermediate Water (AAIW) and Pacific Deep water (PDW) (Silva et al., 2009). The maximum potential density in the water column from which the samples were collected did not exceed 27.4 σ_Θ. Coastal upwelling over the Peruvian shelf is driven by the equatorward Peru coastal current and the poleward flowing Peru undercurrent (Fiedler and Talley, 2006; Pennington et al., 2006; Strub et al., 1998), and increases in intensity southwards (Stramma et al., 2016).

Samples were collected during the strong 2015/2016 El Niño event during which reduced upwelling induced an atypical presence of warmer and more oxygenated waters in the surface mixed layer compared to non-El Niño conditions (Stramma et al., 2016). This effect was most pronounced at the northern shelf stations of Transect 1 (ST 7 and 8; 9.0-9.2°S), with the lowest oxygen concentrations at stations 7 and 8 of 47.6 and 23.7 µM, respectively (Figure 4.2d). Oxygen concentrations at all other shelf and offshore stations reached levels below the sensor detection limit (~2-3 µM oxygen). The onset of oxygen minimum conditions (<20 µM oxygen) occurred below 50 m at shelf stations and extended to bottom water, except at transect 1 (ST 7 and 8) (Figure 4.2d). The OMZ at offshore stations occurred between the isopycnal densities of ~26.0 – 27.1 σ_Θ (~100-500 m; <20 µM) (Figures 4.2c and 4.2d, respectively), with gradually increasing oxygen concentrations in deeper waters (>27.1 σ_Θ).

Iodide (I^-) and iodate (IO_3^-) were measured as an indicator of the water column oxidation state under sub-oxic conditions, whereby iodate is reduced to iodide following oxygen depletion (Cutter et al., 2018). The I^-/inorganic iodine (I^-+IO_3^-) fractions (%) of the shelf stations

along transects 1-3 (9-14°S) ranged between 15-47 %, while more reducing conditions were observed in the southernmost shelf station at transect 4 (61-74% I^-/IO_3^-) (Figure 4.2i). All offshore stations exhibited higher reduced iodine fractions, with near complete reduction (≥90% I^-/IO_3^-) occurring between ~200-400 m at transects 2 and 3, and 150-400 m at transect 4.

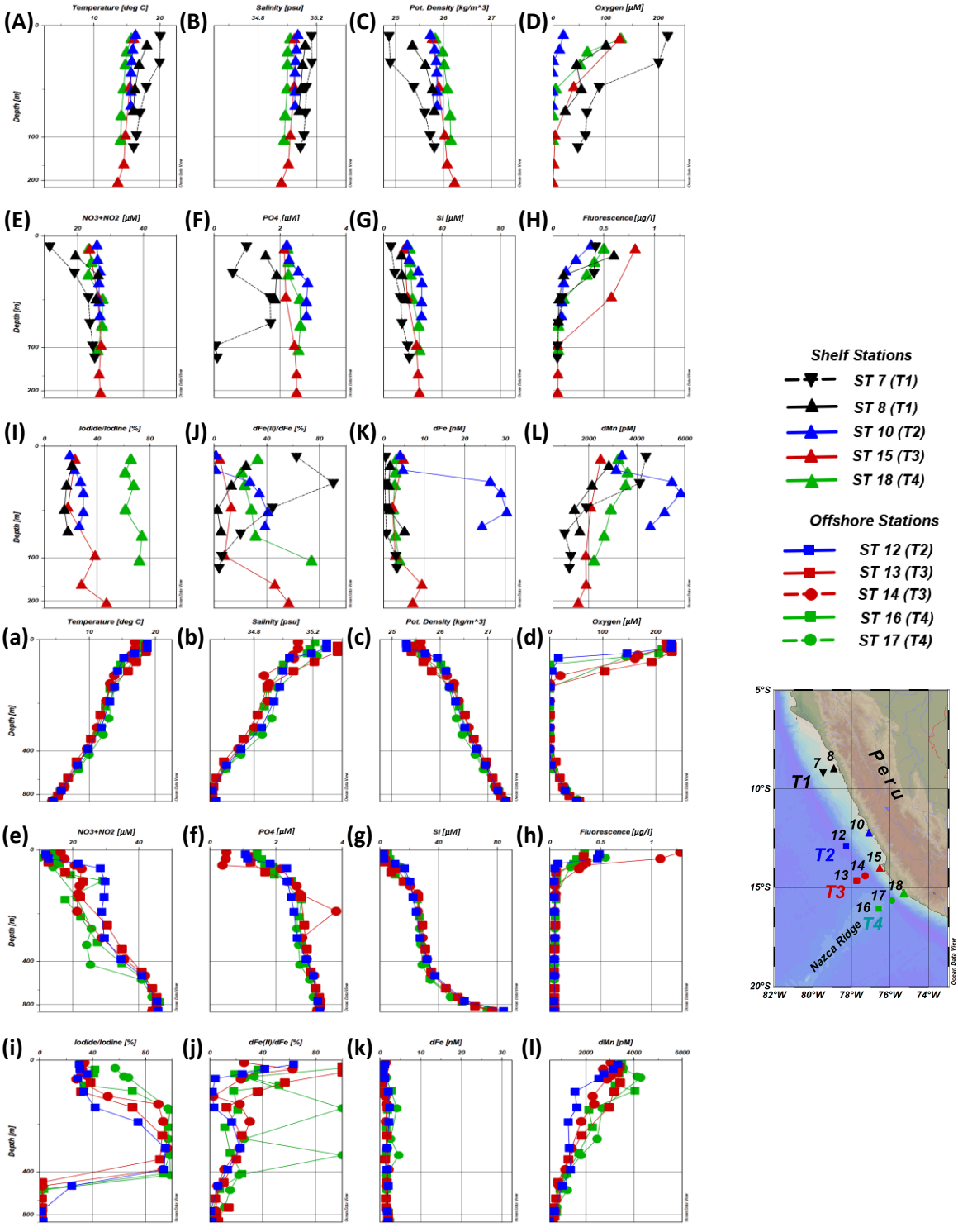

Figure 4.2 – Depth profiles of (A-a) Temperature; (B-b) Salinity; (C-c) Potential Density; (D-d) Oxygen; (E-e) Nitrate + Nitrite; (F-f) Phosphate; (G-g) Silicic acid; (H-h) Fluorescence; (I-i) Iodide/Iodate; (J-j) Dissolved Fe(II) fraction of total dFe (dFe(II)/dFe); (K-k) Total dFe concentrations; and (L-l) Dissolved manganese (dMn) concentrations for SO243 stations (ST) traversing the Peruvian shelf. Shelf stations (Top, A-L) are depicted using triangle symbols, and Offshore stations (Bottom, a-l) are depicted using square and circle symbols. The vertical line and symbol colors represent stations that part of the Transect 1 (T1; Black), Transect 2 (T2; Blue); Transect 3 (T3; Red); Transect 4 (T4; Green). Note the stretched depth scales.

4.3.2 Particulate Trace Metal Distribution Patterns

Total pTM (and pP) concentrations varied by orders of magnitude between the elements, ranging from 10^{-1} to 10^{5} pM (Total samples *n*=84), with average concentrations decreasing in the order P > Al-Fe > Ti > Mn > Zn > Cu-V-Ni > Pb-Cd > Co (Figures 4.3 and S4.1). Particulate TM concentrations in all fractions were higher at shelf stations (ST 7, 8, 10, 15, 18), compared to offshore stations (ST 12-14 and 16-17), except for T-pP, T-pCd, T-pV, and T-pCo, which were higher at the offshore station 14 (Figure 4.3). The maximum T-pTM concentrations measured across all stations were 216 nM pAl, 115 nM pFe, 5.3 nM pTi, 1.04 nM pMn, 1.26 nM pZn, 517 pM pCu, 449 pM pV, 434 pM pNi, 198 pM pPb, 157 pM pCd, and 30.8 pM pCo, and 379 nM for pP. The lowest pTM concentrations were generally observed in the deeper offshore waters and below the oxycline (Figures 4.2d and 4.3). The T-pTM concentration ranges observed at transect 2 (ST 10 and 12; 12.3-12.9°S) were comparable to ranges reported for the shelf stations of a nearby GEOTRACES section cruise (GP16; ST 2-5; 12°S) (GEOTRACES IDP2021; Lee et al., 2018) (Figure S4.2).

Labile pTMs were generally enhanced in surface waters (<50 m), particularly for bio-essential type TMs (Mn, Cd, Co, Zn, Cu, Ni, and V), and at shelf stations where lithogenic particles concentrations were high (*n*=19 of 26 shelf samples were >25 nM R-pAl), compared to offshore stations (*n*=1 of 58 was >25 nM R-pAl) (Figure 4.4). All maximum L-pTM concentrations were measured within the top 50 m of the water column, reaching as high as 88.8 nM L-pFe, 34.1 nM L-pAl, 523 pM L-pTi, 505 pM L-pZn, 447 pM L-pCu, 434 pM L-pNi, and 188 pM L-pPb at shelf stations, and 683 pM L-pMn, 422 pM L-pV, 156 pM L-pCd, and 24.2 pM L-pCo at offshore stations. Labile-pTMs have been associated with multiple particle types (i.e., biogenic, lithogenic, and authigenic particles), often co-occurring in high concentrations on the shelf. The principal carrier phases of each of the L-pTMs are explored in subsequent sub-sections (4.3.3.1-4.3.3.3).

The L-pTM fraction reported in this study differed from the 'reactive particulate fraction' (total dissolvable – dissolved TMs) for Fe, Mn, and Co reported by *Rapp et al.* (2020), with L-pTM concentrations mostly lower (Figure S4.3). This was likely due to the partial solubilization of refractory (lithogenic) particles in the acidified (pH ~1.9) unfiltered seawater samples during the

relatively long storage period (>6 months) of the operationally defined total dissolvable metals (e.g., Birchill et al., 2017).

Refractory pTM concentrations generally showed similar trends to lithogenic particles (R-pAl) (r> 0.64) (see section 4.3.3.3), whilst bio-essential type R-pTMs were also enhanced in the surface layer (<50 m) coinciding with elevated R-pP concentrations (up to 64.4 nM) (see section 4.3.3.1). The majority of R-pTM concentrations (Fe, Al, Ti, Pb, V, Mn, Co, Cu, and Zn) were higher at the shallow shelf stations, coinciding with enhanced lithogenic particles (R-pAl), and where maximum R-pTM concentrations were measured (except for R-pPb, and R-pP; Figure 4.5) reaching up to 207 nM R-pAl, 49.7 nM R-pFe, 5.26 nM R-pTi, 727 pM R-pMn, 138 pM R-pV, 13.0 pM R-pCo, 106 pM R-pNi, 82.5 R-pCu, 228 pM R-pZn, 2.39 pM R-pCd, and 11.9 pM R-pPb.

The average labile particulate fractions (L-pTM/T-pTM x 100) were >90% for Cd, 70-76% for Zn, Ni, V, P, and Pb, 56-60% for Mn, Co, Cu, 35% for Fe, 11% for Al, and 3.7% for Ti (Figure 4.6), which were comparable with average labile particulate fractions reported in the North Atlantic (Milne et al., 2017; Rauschenberg and Twining, 2015; Rusiecka et al., 2018; Twining et al., 2015), South Atlantic (Little et al., 2018), North Pacific (Berger et al., 2008), and Indian (Twining et al., 2019) Oceans, from studies that applied the same chemical leach (Table S4.2). Average L-pMn fractions were slightly lower in our samples (59.7 ± 27.9% L-pMn/T-pMn; n=84), which can be attributed to Mn oxide deficiency in oxygen deficient waters (<20 µM oxygen; n= 40 of 84 samples; see section 4.3.3.2), which reduces the relative proportion of L-pMn/T-pMn phases. However, the low L-pMn/T-pMn fractions in the current study are similar to those observed in the Benguela OMZ (48.5±14.9%; Al-Hashem et al., 2022).

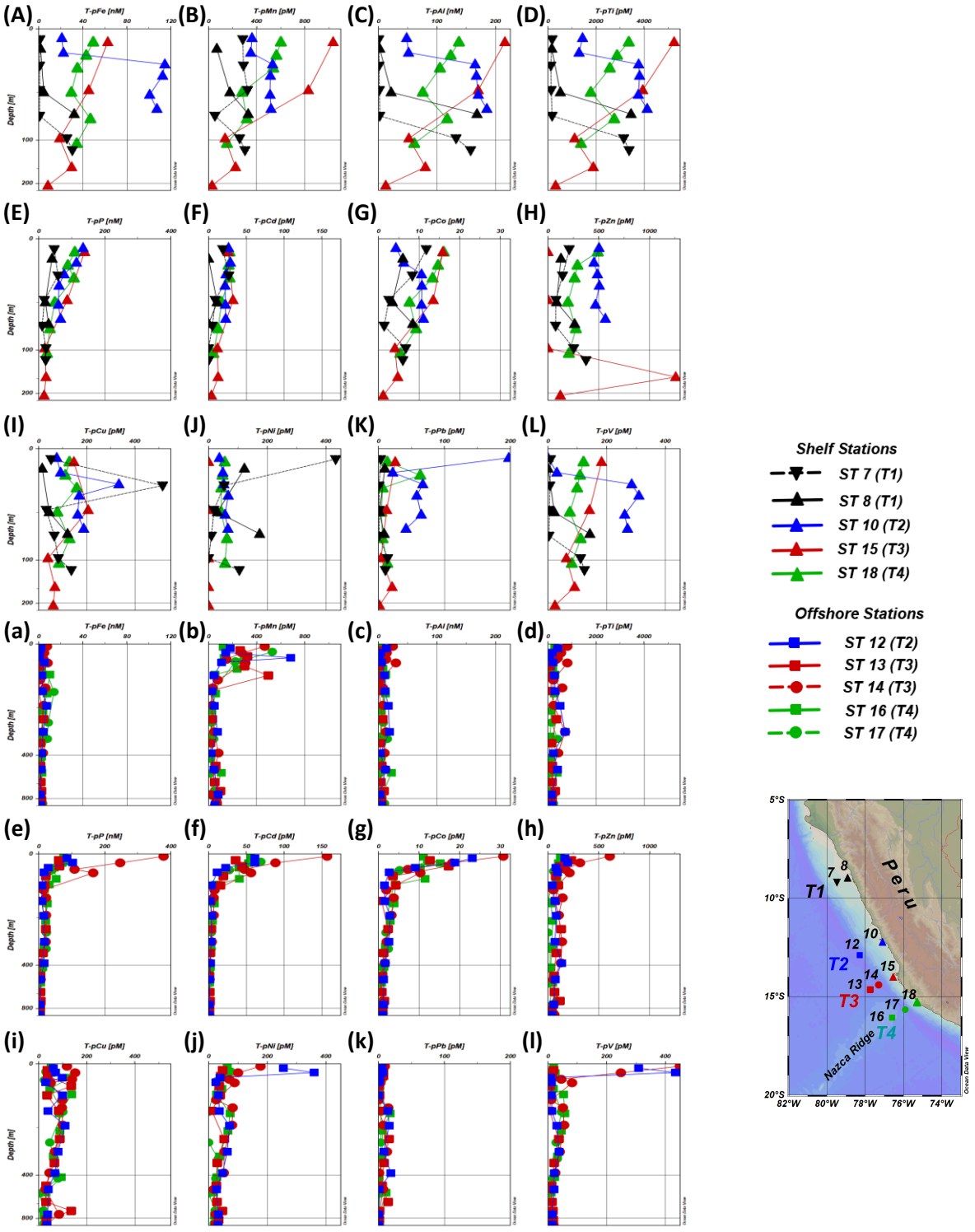

Figure 4.3 – Vertical profiles of total particulate (T-pTM) concentrations for (A-a) Iron (Fe); (B-b) Manganese (Mn); (C-c) Aluminum (Al); (D-d) Titanium (Ti); (E-e) Phosphorus (P); (F-f) Cadmium (Cd); (G-g) Cobalt (Co); (H-h) Zinc (Zn); (I-i) Copper (Cu); (J-j) Nickel (Ni); (K-k) Lead (Pb); and (L-l) Vanadium (V) for SO243 stations off the Peruvian shelf. Station (ST) and transect (T) symbols and colors are exactly as on Figure 4.2. Note the stretched depth scales.

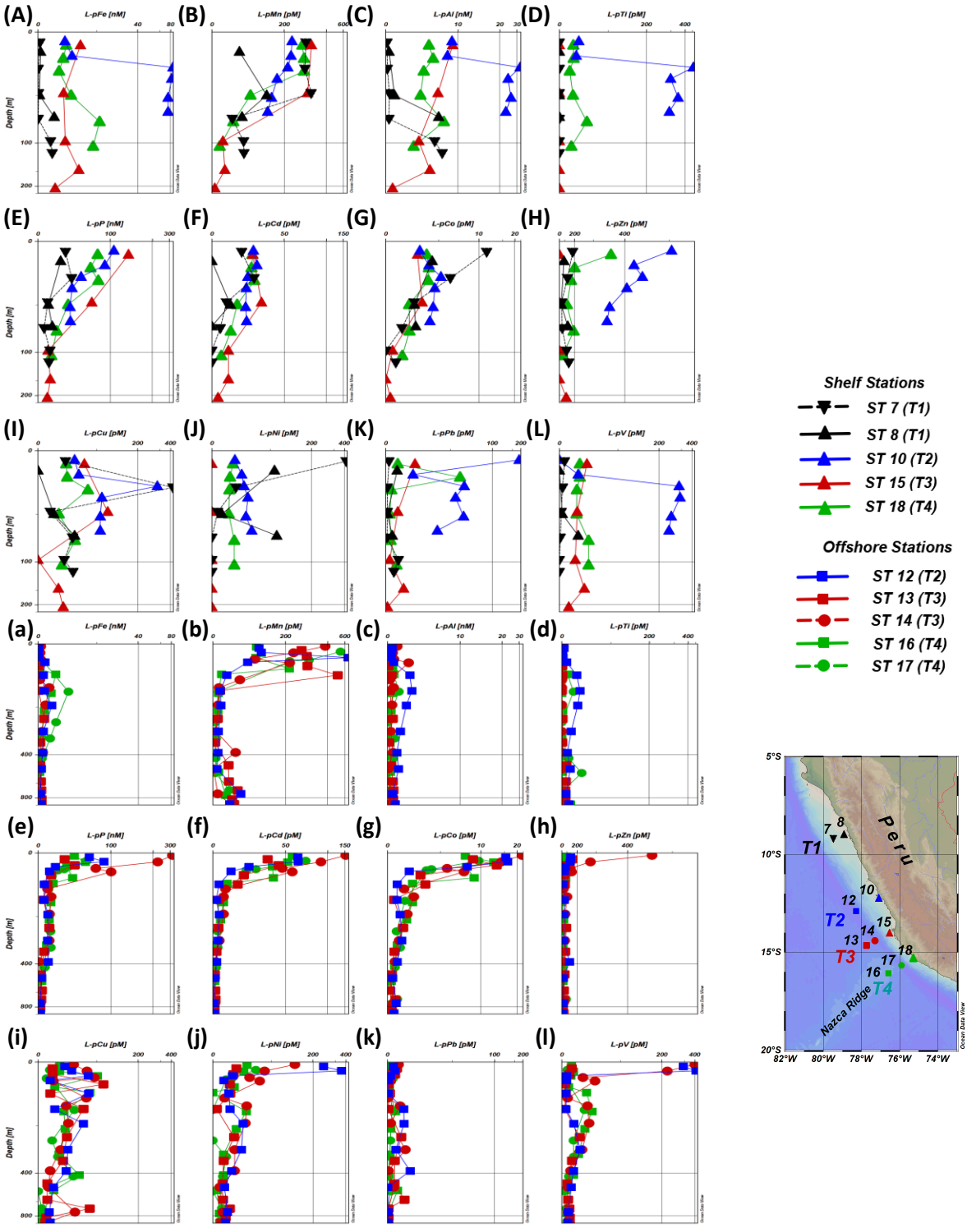

Figure 4.4 – Vertical profiles of labile particulate trace metal (L-pTM) concentrations for (A-a) Iron (Fe); (B-b) Manganese (Mn); (C-c) Aluminum (Al); (D-d) Titanium (Ti); (E-e) Phosphorus (P); (F-f) Cadmium (Cd); (G-g) Cobalt (Co); (H-h) Zinc (Zn); (I-i) Copper (Cu); (J-j) Nickel (Ni); (K-k) Lead (Pb); and (L-l) Vanadium (V) for SO243 stations off the Peruvian shelf. Station (ST) and transect (T) symbols and colors are exactly as on Figure 4.2. Note the stretched depth scales.

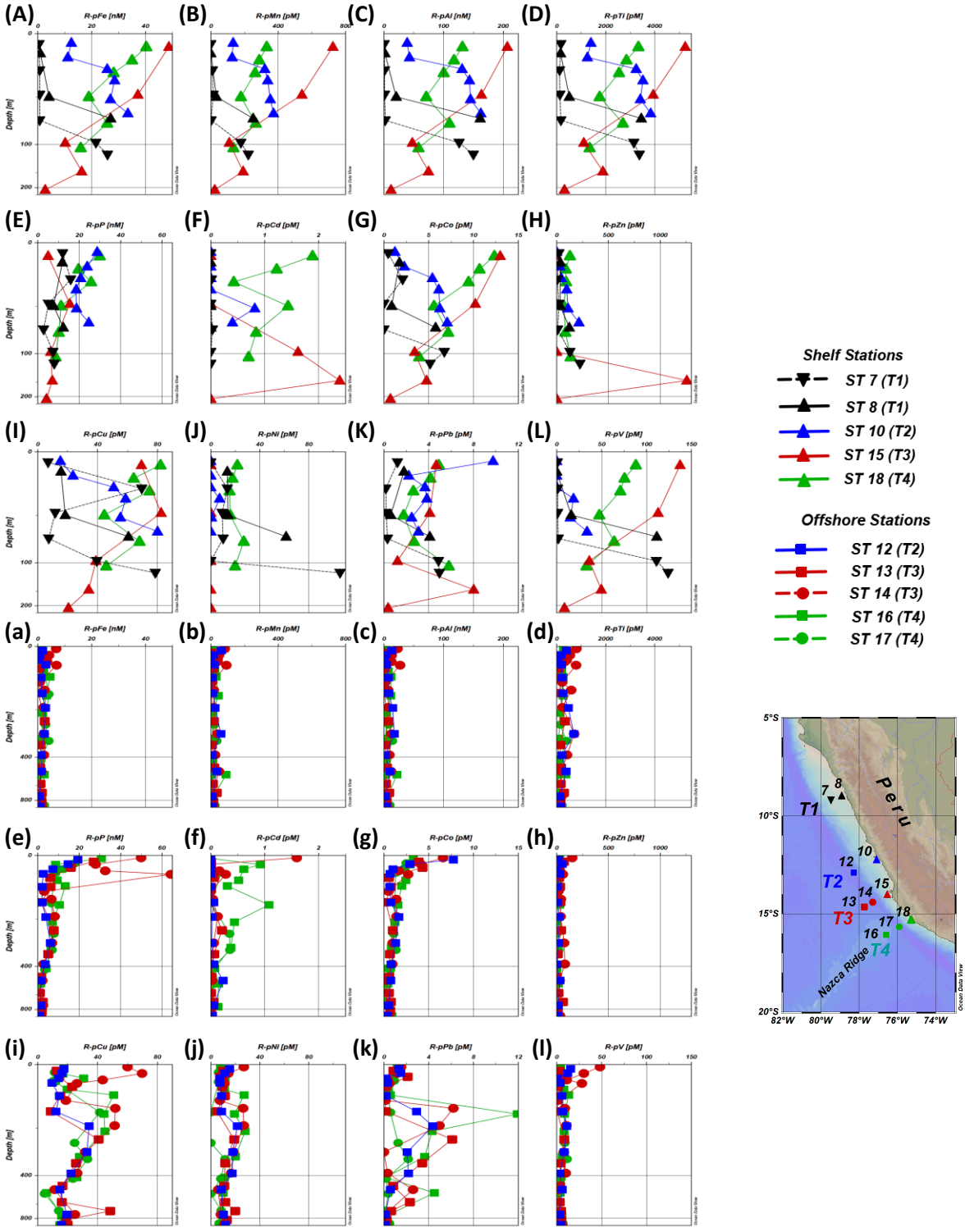

Figure 4.5 – Vertical profiles of refractory particulate trace metal (R-pTM) concentrations for (A-a) Iron (Fe); (B-b) Manganese (Mn); (C-c) Aluminum (Al); (D-d) Titanium (Ti); (E-e) Phosphorus (P); (F-f) Cadmium (Cd); (G-g) Cobalt (Co); (H-h) Zinc (Zn); (I-i) Copper (Cu); (J-j) Nickel (Ni); (K-k) Lead (Pb); and (L-l) Vanadium (V) for SO243 stations off the Peruvian shelf. Station (ST) and transect (T) symbols and colors are exactly as on Figure 4.2. Note the stretched depth scales.

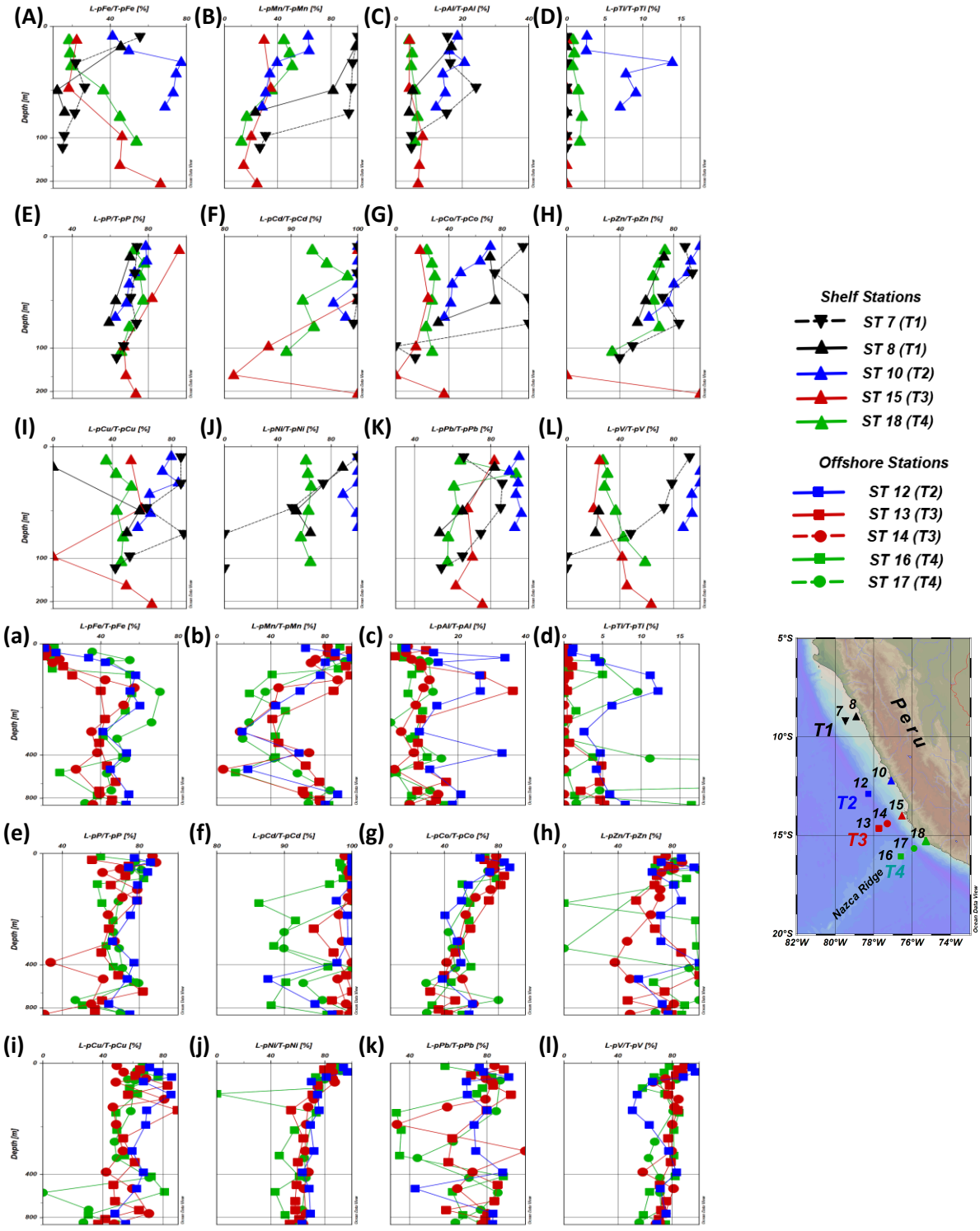

Figure 4.6 – Vertical profiles of labile particulate fractions of total particulate concentrations (L-pTM/T-pTM, %) for (A-a) Iron (Fe); (B-b) Manganese (Mn); (C-c) Aluminum (Al); (D-d) Titanium (Ti); (E-e) Phosphorus (P); (F-f) Cadmium (Cd); (G-g) Cobalt (Co); (H-h) Zinc (Zn); (I-i) Copper (Cu); (J-j) Nickel (Ni); (K-k) Lead (Pb); and (L-l) Vanadium (V) for SO243 stations off the Peruvian shelf. Station (ST) and transect (T) symbols and colors are exactly as on Figure 4.2. Note the stretched depth scales.

4.3.2.1 Bivariate Correlations and Principal Component Analysis (PCA)

Bivariate correlations were carried out on log-transformed datasets for T-pTMs, and L-pTMs and R-pTMs, to prevent skewing from outliers, and are summarized in supplementary Tables S4.3a and S4.3b, respectively. The log-transformed T-pTM concentrations showed normal data distributions (Figure S4.4). Most of the T-pTMs correlated relatively well with each other, with an average Pearson's coefficient (*r*) of 0.571, reflecting shared particle sources (Table S4.3a). We focus on examining the correlations of the different elements against different particle type indicators and geochemical/redox proxies to help determine the primary biogeochemical mechanisms influencing the general pTM distribution patterns.

The highest correlations of T-pTMs to the lithogenic particle indicator R-pAl were with T-pAl > T-pFe > T-pTi (*r*=0.91-1.0; *p*<0.001), and T-pV, T-pPb, and T-pZn (*r*= 0.78, 0.60, and 0.58, respectively, *p*<0.001), with *r*<0.5 for all other T-pTMs. The biogenic particle indicator (T-pP) correlated best with T-pCd > T-pCo > T-pZn > T-pMn >T-pNi > T-pV > T-pCu (*r*= 0.94, 0.92, 0.70, 0.67, 0.62, 0.61, and 0.54; *p*<0.001), and strongly correlated with fluorescence (*r*=0.82; *p*<0.001). T-pPb and T-pTi also correlated well with T-pP (*r*=0.53 and 0.52, respectively; *p*<0.001). L-pFe correlated best with lithogenic type elements T-pAl, T-pTi and T-pFe (*r*= 0.74-0.94), and with T-pV and T-pPb (*r*=0.64 and 0.59, respectively, *p*<0.001). T-pMn correlated best with bio-essential T-pTMs, Co, Cd and Zn (*r*=0.69-0.79; *p*<0.001), with R-pP and fluorescence (*r*=0.67 and 0.63, respectively; *p*<0.001), and also correlated relatively well with lithogenic elements, T-pTi and R-pAl (*r*=0.61 and 0.46, respectively) and oxygen (*r*=0.56; *p*<0.001).

Within the labile particulate fractions, L-pP strongly correlated with fluorescence (*r*=0.82; *p*<0.001), and negatively correlated with nitrate+nitrite and silicic acid (*r*= -0.75 and -0.77, respectively; *p*<0.001) and depth (*r*= -0.89; *p*<0.001). Bio-essential type L-pTMs (Cd > Co > Zn > Ni > Mn > V > Cu) correlated well with L-pP (*r*=0.54-0.93; *p*<0.001; Table S4.3b) and with fluorescence (Cd > Co > Mn > Ni > Zn, *r*=0.61-0.83; and V > Cu, *r*=0.40 and 0.31, respectively; *p*<0.001; Table S4.3b). The strongest L-pTM correlations with R-pAl were with Al > Fe > Ti > V > Pb > Zn (*r*=0.52-0.87; *p*<0.001; Table S4.3b). Notably, L-pV correlated similarly with R-pAl and L-pP (*r*=0.61 and 0.57, respectively; *p*<0.001), indicating strong associations with both biogenic and

lithogenic sources. The strongest correlations with oxygen were with L-pMn > L-pFe > L-pCd=L-pCu (r=0.70, -0.39, 0.38, respectively; p<0.001; Table S4.3b), while the highest correlations to the I^-/IO_3^- ratio were to bio-essential elements L-pP > L-pCd=L-pCu > L-pCo > L-pZn > L-pNi and L-pV (r=0.31-0.56).

Most refractory particulate elements correlated relatively well with each other, except R-pNi (average r=0.637 for all R-pTMs and R-pP, excluding R-pNi), implying common particle sources, primarily as lithogenic and residual (refractory) biogenic sources (see sections 4.3.3.1 and 4.3.3.3). However, all R-pTMs showed higher correlations with R-pAl than with R-pP (average r=0.69 and 0.46, respectively), including bio-essential R-pTMs. Excellent correlations of R-pAl were observed with R-pFe, R-pMn, R-pV, and R-pTi (r=0.91-0.96; p<0.001), and all other R-pTMs also correlated very well (r=0.59-0.69; p<0.001), except R-pNi (r=0.29). The strongest R-pTM correlations with fluorescence were with R-pP, R-pCo and R-pCd (r=0.72, 0.48 and 0.42, respectively). The highest correlations with R-pNi were with R-pV and R-pCu (r=0.51 and 0.49, respectively; p<0.001).

Principal component analysis was conducted on log-transformed datasets for the T-pTM, L-pTM and R-pTM datasets and included ancillary data, where full elemental and ancillary data was available (Figure 4.7).

For the T-pTM dataset, a model with five principal components captured 91% of total variance. PC1 (51% of total variance; Figure 4.7a) captured >29% of the individual variances of all T-pTMs, and was indicative of biogenic particles, capturing the highest individual variance (91.3%) of the biogenic particle indicator T-pP. Most of the individual variances of bio-essential type elements T-pCo (90.7%), T-pCd (83.8), T-pZn (69.1%), T-pNi (54.7%), T-pMn (54.2%), and T-pV (56.9%), and depth (83.5%) fluorescence (64.5%), silicic acid (54.8%) and nitrate+nitrate (50.9%) were also captured by PC1. Significant individual variance of the lithogenic indicator, R-pAl (29.8%) was captured by PC1, with relatively little variance captured for L-pFe (11.5%), compared to T-pFe (31.9%), while almost no variance was captured for oxygen (<1%). This highlights that most of the covariance of pFe with the biogenic particle indicator, T-pP, is associated more closely with the refractory pFe phases (i.e., lithogenic particles), rather than with labile biogenic particle phases. PC2 (25.2% of total variance; Figure 4.7a) was associated with

lithogenic particle sources, capturing individual variances of 56.5% for R-pAl and 62.2%, 58.6%, 39.4%, and 20.6% for T-pFe, T-pAl, T-pTi, and T-pPb, respectively, with less than 17% for all other T-pTMs. Notably, PC2 captured 76.9% and 41.7% variance for L-pFe and oxygen, respectively, although oxygen, fluorescence and T-pCd negatively covaried with all parameters where individual variance captured was >5%. This indicated that L-pFe covariance was largely associated with lithogenic (i.e., benthic) sources and enhanced where oxygen concentrations were low. PC3 (8.1% of total variance; Figure 4.7a) reflected variance partially associated with reductive or remineralization processes within the OMZ. Significant individual variances were only captured for oxygen (47.8%) and T-pMn (23.4%), which negatively covaried with the ratio I^-/IO_3^- (55.9%) and T-pCu (10.6%). PC4 and 5 explained only <4% of the total variance (Figure 4.7a), but were important for T-pNi (28.4%) and to a lesser extent T-pV (19.6%) and T-pMn (9.7%) in PC4, likely representing a refractory biogenic particle fraction, while variance in PC5 was exclusive to T-pPb (26.1%) and T-pCu (23.7%), which negatively covaried with each other.

For the L-pTM dataset, 5 principal components captured 89.3% of the total variance (Figure 4.7b). PC1 (53.1% of total variance; Figure 4.7b) was strongly indicative of biogenic particles, capturing individual variances of 95%, 93.1%, and 72.1% for T-pP, L-pP, and fluorescence, respectively, and 73.3% and 71.4% of silicic acid and nitrate+nitrite, respectively, which negatively covaried with all L-pTMs. Significant variances of bio-essential L-pTMs were also captured by PC1, decreasing from L-pCd (94.4%) > L-pCo (90.6%) > L-pZn (67.2%) > L-pNi (63.5%) > L-pMn (43.4%) > L-pV (39.8%) > L-pCu (29.6%), with very little variance captured for R-pAl (11.3%), L-pFe (2.4%), oxygen (3.3%), and L-Al (5.1%) (Figure 4.7b). dFe(II) covariance (33.5%) was higher in PC1 than dFe(III) (7.4%), with dFe(III) negatively co-varying against all L-pTMs. PC2 (22% of total variance; Figure 4.7b) was associated with benthic sources and the oxygen depletion, capturing most of the individual variances for L-pFe (85.1%), L-pAl (76.7%), dFe(III) (66.4%), and R-pAl (58.4%), and significant variance for oxygen (47.7%), L-pPb (32.7%), L-pV (26%), and dFe(II) (27.1%). Fluorescence, oxygen, L-pCd, L-pMn, and L-pCo all negatively covaried with all other L-pTMs within PC2. PC3 (7.2% of total variance; Figure 4.7b) captured variance mostly associated with Mn oxide (24.9% L-pMn variance) and iodate reduction (47.9% I^-/IO_3^- variance), with oxygen (38.6%) negatively covarying with I^-/IO_3^-. PC4 and PC5 (4% and 3% of total variance, respectively;

Figure 4.7b) captured variances that were specific to few L-pTMs, with the highest variance for L-pV (25.5%) L-pNi (19.3%), and for L-pMn (12.9%) in PC4, and L-pCu (26.7%) and L-pPb (17.5%) negatively covarying within PC5.

For the R-pTM dataset, 5 principal components captured 89.8% of the total variance (Figure 4.7c). R-pCd was excluded from the R-pTM dataset PC analysis, as many samples were below the detection limit (34 of 84 samples), and including R-pCd in the analysis would have omitted a relatively high proportion of samples from the PC analysis. PC1 (48.8% of the total variance) captured most of variance associated with residual (refractory) biogenic particles, with 81.6%, 80.4%, 58.7% of the variance for T-pP, R-pP, and fluorescence, respectively. PC1 was also associated with lithogenic particles, but only to a slightly lower extent, capturing 48.2-60.5% of the variance for R-pAl, R-pTi and R-pFe. Individual variances of 88.8% for R-pCo, 63.9% for R-pV, 51.8% for R-pMn, and 46% and 41.6% for R-pCu and R-pZn, respectively was captured by PC1, and macronutrients (NO_3+NO_2, PO_4, and SiO_3) and depth (31.4-67.7 % individual variances) negatively covaried with all R-pTMs. PC2 (22.7% of total variance; Figure 4.7c) was primarily indicative of lithogenic particles, but also captured coinciding variance associated with biogenic particle remineralization. Individual variances of 40.6%, 31.6%, and 24.6% was captured for lithogenic elements R-pAl, R-pFe, and R-pTi, respectively, and 31.6% for R-pMn. Significant variances were captured for oxygen (34.4%), fluorescence (24.3%), and to a lesser extent, T-pP (13.1%), and R-pP (8.2%), which negatively covaried with all R-pTMs, macronutrients (NO_3+NO_2, PO_4, and SiO_3; 43.5-53% variance within PC2), and depth (22.2% variance within PC2). PC3 (9.4% of total variance; Figure 4.7c) was associated with iodate reduction, capturing with 48.3% of I^- /IO_3^- variance, and coincided only with relatively minor of covariance with R-pNi and R-pPb (18.1% and 16.6% individual variance, respectively), while oxygen negatively covaried with 47.7% variance captured within PC3. PC4 and PC5 (5.7% and 3.2% of total variance, respectively; Figure 4.7c) only captured significant variances largely exclusive to R-pNi (65.3% individual variance) in PC4, and R-pZn (35.1% individual variance) in PC5.

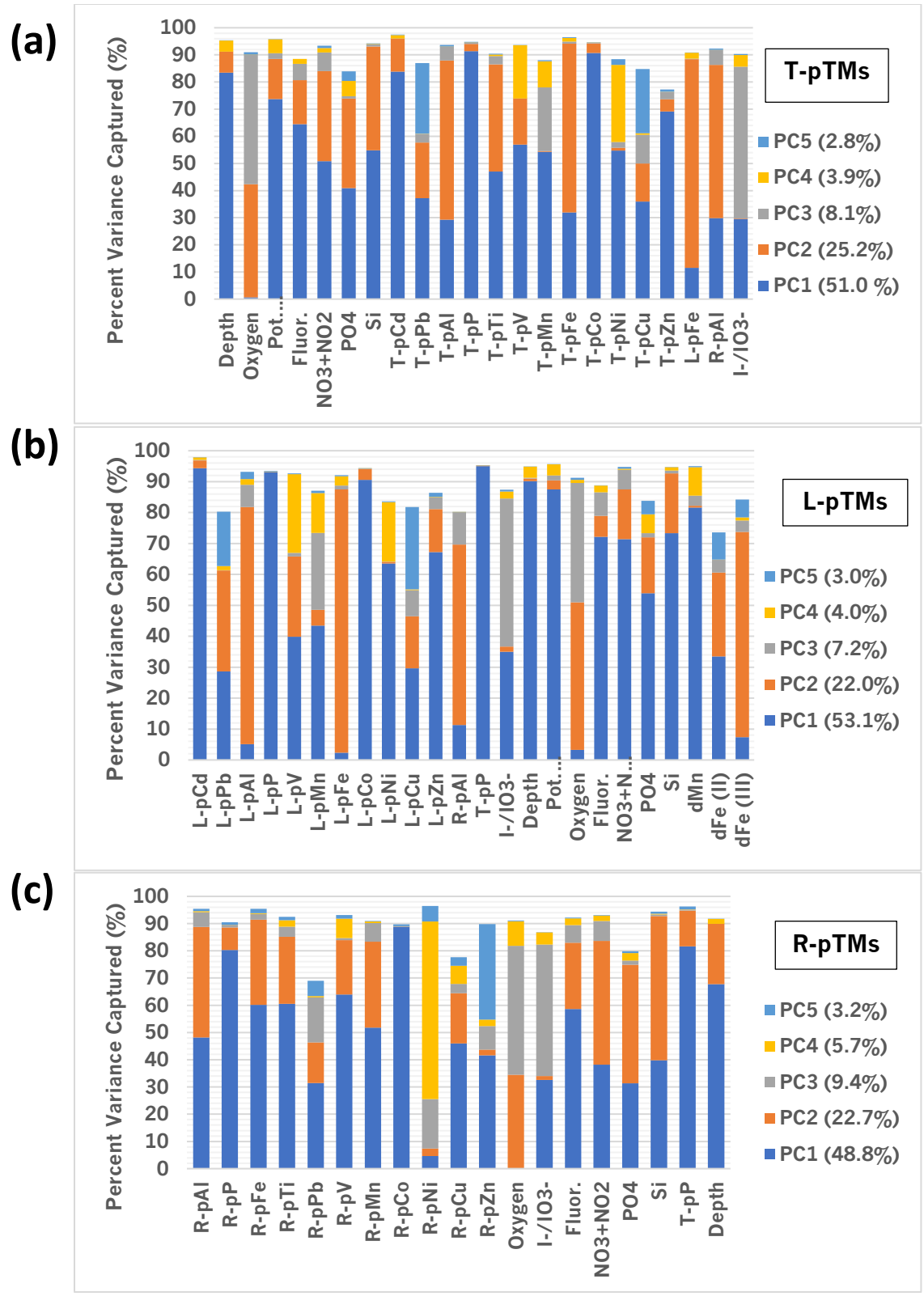

Figure 4.7 - Summary of the Principal Component Analysis (PCA) results illustrating the cumulative variance in a 5 PC model for (a) total particulate trace metals (T-pTMs); (b) labile particulate trace metals (L-pTMs); and (c) refractory particulate trace metals (R-pTMs). The total variance captured by each component is indicated in the legend embedded in each chart.

4.3.3 Definition of Regions

Several distinct pTM distribution patterns were apparent and TM distributions and cycling is described accordingly between different defined regions, including the: (1) surface waters (<50 m; n=28); (2) OMZ (<20 µM oxygen; n=40); and (3) nepheloid layer (>25 nM R-pAl; n=20), with some intersections of samples between the defined regions. These descriptors were chosen in a manner that is consistent with other studies that used the same terminology (for example, Lee et al., 2018; Marsay et al., 2018; Noffke et al., 2012).

4.3.3.1 pTM Distributions and Cycling in Surface Waters

Biogenic particle concentrations were highest at the offshore station 14 (Transect 3) with up to 379 nM T-pP, which was over 5-fold higher than the average T-pP concentration in surface waters of all other stations (72.5 ± 33.1 nM; 1 S.D.; <50 m). Station 14 also exhibited the highest L-pP (329 nM), R-pP (64.4 nM), and fluorescence (Figure 4.2h). The average L-pP fractions in surface samples (76 ± 8.7 % L-pP/T-pP; <50 m; *n*=28) did not differ significantly from the average across all samples (70 ± 10.7 % L-pP/T-pP; *n*=84) (Figure 4.6). Labile pP fractions did not appear to be considerably influenced by biogenic (T-pP) or lithogenic (R-pAl) particle loads, remaining relatively constant over concentration ranges of the indicator elements covering orders of magnitude (Figure S4.5). Shelf stations of transects 2-4 exhibited high lithogenic particle concentrations within the surface layer (115 ± 52.9 nM R-pAl; *n*=10) (i.e., resuspended particles) and are mainly discussed in section 4.3.3.3.

Bio-essential L-pTMs (Mn, Cd, Co, Zn, Cu, Ni, and V) generally followed biogenic particle-type distribution patterns, showing enhanced concentrations in surface waters across all stations and sharply decreasing with depth in the top 100 m (Figure 4.4). This feature was particularly apparent at offshore stations, where bio-essential L-pTMs were generally higher and coincided with higher pP concentrations (107 ± 97.8 nM T-pP; and 86.2 ± 88.3 nM L-pP; <50 m; *n*= 13), and with relatively low co-occurring lithogenic particle concentrations (7.24 ± 6.80 nM R-pAl; <50 m; Offshore). Average bio-essential L-pTM concentrations in surface waters were

244 ± 133 pM L-pMn, 38.8 ± 30.3 pM L-pCd, 7.54 ± 5.30 pM L-pCo, 181 ± 147 pM L-pZn, 76.5 ± 90.1 pM L-pCu, 77.0 ± 102 pM L-pNi, and 82.1 ± 131 pM L-pV across all stations.

Linear regression slope values of total and labile particulate Cd, Co, Zn, and Ni, normalized to T-pP and L-pP, respectively, were comparable to documented plankton stoichiometry ranges across all surface samples (Table 4.1; Figures S4.6 and S4.7). The values were also largely consistent with previously reported values from the surface mixed layer from the same region (Ohnemus et al., 2017), which were primarily attributed to biogenic particles.

The linear regression slope values of particulate Mn, Cu, and V (normalized to T-pP) were typically at the upper limit of, or slightly exceeded documented plankton stoichiometric values, but were often within the same order of magnitude as documented plankton stoichiometric values (Table 4.1). This suggested either increased intracellular TM:P quotas of these elements in bulk biogenic particles within the sampled transects, or the inclusion of other abiogenic particulate phases associated with these metals, likely as scavenged phases. A biochemical role for vanadium has been reported, such as in V-haloperoxidases in cyanobacteria and diatoms (Hill and Manley, 2009; Johnson et al., 2011; Nuester et al., 2012; Tovar-Sanchez and Sañudo-Wilhelmy, 2011), but datasets documenting intracellular stoichiometries of V in plankton are sparse. Enhanced uptake of V as an analogue of phosphate is possible during P-limitation (Nuester et al., 2012), but phosphate was not limiting during the period of sampling (0.39 µM minimum phosphate concentration). Excluding nepheloid particle samples (>25 nM R-pAl), our results show that pV: pP were relatively consistent throughout surface waters at 0.796 ± 1.18 T-pV:T-pP mmol:mol (0.856 ± 1.39 L-pV:L-pP mmol:mol) (n=18), and were comparable to values reported in the North East Atlantic by Klein et al. (2013) (0.2-0.39 pV:pP mmol:mol; Table 4.1).

Adsorption of several TMs onto biominerals, Fe oxides, or particulate organic matter is possible at offshore stations (Boyd et al., 2017; Feely et al., 1989; German et al., 1991; Richon and Tagliabue, 2019; Tagliabue et al., 2017; Weber et al., 2018), while increased scavenging onto benthic resuspended particles at shelf stations may contribute to the increase in L-pTM concentrations (see section 4.3.3.3). Elevated T-pTM stoichiometric ratios (normalized to R-pAl)

observed in surface waters for T-pMn, T-pV, and T-pCu were higher than lithogenic reference sources (Figure S4.8) and were also mostly labile (44.3-95.6% upper and lower quartile values; <50 m), indicating adsorption of these TMs. Manganese oxide precipitation may contribute to the L-pMn pool within oxygenated waters below the photic layer, formed by oxidation of remineralized Mn from benthic resuspension or remineralization of organic particles (Cowen and Bruland, 1985; Tebo et al., 2005, 2004).

Average L-pFe concentrations in shelf surface waters (16.9 ± 28.6 nM; max 88.8 nM; <50 m; *n*=15) were about an order of magnitude higher than at offshore stations (0.41 ± 0.29 nM L-pFe; max 9.9 nM; <50 m; *n*=13) (Figure 4.4). The L-pFe fraction associated with biogenic particles in shelf waters was presumably small, as shown by the poor correlations of L-pFe with L-pP and T-pP (*r*=0.0124 and 0.0526, respectively; <50 m), and since total and labile pFe:pP ratios were 1-2 orders of magnitude higher than reported intracellular plankton stoichiometries. Instead, L-pFe concentrations on the shelf correlated more closely with lithogenic particles (R-pAl) (*r*= 0.461; <50 m), indicating a stronger association with benthic sources, likely as Fe oxides from resuspended sediment particles following oxidation and precipitation of reduced dFe form benthic sources (see section 4.3.3.3). Additionally, Fe scavenged onto available particle surfaces at shelf stations is also likely to increase L-pFe concentrations. This strongly suggested that benthic particles were significant sources of enhanced labile pFe over the Peruvian shelf. The exception was at transect 1 shelf stations (24.8 ± 14.8 mmol:mol L-pFe:L-pP; ST 7 and 8; <50 m), where lithogenic particle abundance was relatively low. The L-pFe pool in offshore surface waters, however, was primarily associated with biogenic particles, indicated by the pFe:pP stoichiometric ratios which were largely consistent with plankton reference sources (in both T-pTM and L-pTM fractions, Table 4.1 and Figure S4.7).

Refractory TMs were associated with biogenic particles in surface samples where R-pP was relatively enhanced (19.7 ± 10.3 nM; <50 m; max 49.9 nM; n= 28; Figure 4.7), correlated well with fluorescence (*r*=0.72; p<0.001; Table S4.3), and exhibited vertical profiles typical of biogenic particles. Some bio-essential type R-pTM concentrations (Cd, Co, Zn, Cu, and V) in surface waters were more strongly associated with residual biogenic particles in offshore

stations where biogenic particle concentrations (T-pP) were higher and lithogenic particles (R-pAl) were lower compared to shelf stations (Figure 4.5). However, bio-essential R-pTM concentrations were lower than their respective L-pTM concentrations.

Good correlations between R-pCo, R-pNi, R-pCu, R-pZn, R-pV, and R-pMn with R-pP were found at offshore stations (r= 0.518-0.819; <50 m; Figure S4.9), with linear regression slope values similar to plankton reference values (Figure S4.8 and Table 4.1), suggesting that the R-pTM pools were primarily associated with refractory biogenic particles. Substantial refractory biogenic fractions have been reported from particulate samples in the Southeast Atlantic that were analyzed following the same chemical leach (39.7±20.7% L-pP/T-pP; Al-Hashem et al., 2022), although particulate P in our study region was comparatively more labile (L-pP/T-pP 76.1±8.7%; <50m; n=28) (Figure 4.6). By extension, the relatively high lability of pP implied that the biogenic pTMs are remineralized on shorter timescales, thereby retaining P in the photic surface layer for extended periods of time before sinking (Lemaitre et al., 2020).

Bio-essential R-pTMs (Co, Cu, Ni, and V) correlated poorly with R-pP at shelf stations (r≤0.304), where lithogenic particle concentrations were high, except for R-pZn (r=0.459) (Figure S4.9). All bio-essential R-pTMs except R-pZn showed closer correlations with R-pAl (r=0.69-0.90; Figure S4.9) than with R-pP, indicating that most of the R-pTM pool in shelf stations were associated with lithogenic particles.

R-pCo, R-pV, and R-pCu correlated well with R-pAl (r=0.90, 0.80, and 0.76, respectively; Figure S4.9) and linear regression slopes R-pCo:R-pAl and R-pV:R-pAl were consistent with canonical upper continental crust (UCC) values (Rudnick and Gao, 2013; Taylor and McLennan, 1995) (Figures S4.8 and S4.9), while R-pCu:R-pAl was only slightly higher (0.31 R-pCu:R-pAl mmol:mol, compared to 0.15-0.21 Cu:Al mmol:mol in UCC), indicating their primary associations with lithogenic sources over the shelf. At offshore stations, bio-essential R-pTMs all correlated relatively well with R-pAl (r=0.65-0.89; Figure S4.9), but linear regression slopes were steeper than UCC reference values (within about an order of magnitude; Figures S4.8 and S4.9) likely due to the inclusion of residual biogenic particle fractions. Refractory biogenic pTM fractions likely comprise the organic pTM fraction which settles and accumulates on the

seafloor and are returned to the water column over longer timescales (Hansen and Blackburn, 1991; Henrichs and Reeburgh, 1987; Martens and Val Klump, 1984).

R-pFe and R-pMn correlated strongly with R-pAl in surface waters of shelf and offshore stations (*r*=0.92-0.98; Figure S4.9) and exhibited linear regression slope values that were consistent with UCC reference sources (Figures S4.8 and S4.9), indicating a dominant lithogenic particle source. However, relatively close correlations of R-pMn and R-pFe with R-pP in offshore stations (*r*=0.64 and 0.79, respectively; Figure S4.9) with linear regression slopes that were also consistent (1.38 R-pMn:R-pP, mmol:mol) or within an order of magnitude of biogenic particle references sources (120 R-pFe:R-pP, mmol:mol; Table 4.1), and implied the inclusion of a greater proportion of biogenic R-pTM fractions (Table 4.1). However, this may be due to aggregation of biogenic and lithogenic particles associated with the enhanced primary production at offshore stations.

Lithogenic particles are possibly included in biological aggregates, as indicated by the shared close correlations and co-variance between T-pP and R-pAl, with lithogenic and bio-essential type pTMs (see section 4.3.2.1). Also, T-pP and R-pAl correlated more closely in surface waters at offshore stations (*r*=0.831; Figure S4.10), where biogenic particles concentrations were higher than shelf stations (*r*= 0.581; Figure S4.10). While R-pAl concentrations were higher at shelf stations, the lithogenic particle sources on the shelf were primarily from benthic resuspended nepheloid particles at the bottom of the shallow water column. In contrast, a higher proportion of lithogenic particles in offshore stations were probably from aerosol sources in surface waters, albeit at low concentrations (Jickells, 2005; Mahowald et al., 2005). Biotic aggregation of lithogenic particles has previously been shown during dust deposition events, with residence times of fine lithogenic particle on the order of days to weeks (Boyd et al., 2017; Dammshäuser and Croot, 2012; Ohnemus and Lam, 2015). Additionally, the applied leach may not dissolve biogenic pTM in chemically resistant cell components such as diatom frustule fractions, whereas P is associated with organic fractions of the plankton cells (Twining et al., 2014).

Particulate and labile Pb was highest in surface waters at station 10 (86.4±76.8 pM T-pPb; 81.6±73.5 pM L-pPb; and 93.2 ± 2.36% L-pPb/T-pPb), the shallowest nearshore station, coinciding with high lithogenic particle concentrations. Particulate Pb was lower and slightly less labile at the other stations (8.73 ± 12.9 pM T-pPb; 7.07 ± 11.9 pM L-pPb; and 76.6% L-pPb/T-pPb <50 m; Excluding ST10). This may have been due to anthropogenic Pb in sediment close to the coast at station 10, or the higher exchangeability of Pb phases from resuspended benthic particles (Rusiecka et al., 2018). Dissolved Pb (dPb) was also higher at station 10 (133 ± 73.9 pM dPb; ST10) compared to the rest of the stations (86.3 ± 82.3 pM dPb). Additional Pb may have also been adsorbed onto biogenic particle surfaces, as has been suggested to occur in the North Pacific, North Atlantic, and Southern Oceans (Cochran et al., 1990; Nozaki et al., 1976; Schlosser and Garbe-Schönberg, 2019).

Biogenic particles were therefore the primary carrier phases for bio-essential L-pTMs, Mn, Cd, Co, Zn, Cu, Ni, and V in surface waters at all stations. Additional L-pTM carrier phases were associated with lithogenic particles (Fe, Ti, Mn, V, Pb), authigenic (mainly Fe oxides), and adsorbed phases (V, Pb, Al, Cu) where resuspended benthic particles and sources of reduced Fe susceptible to precipitation are present, particularly in shelf stations.

Table 4.1. Compiled plankton reference trace metal stoichiometries compared to samples from the top 50m of the SO243 stations. Concentration ranges referenced from this study are the upper and lower quartile values of individual sample particulate TM : particulate phosphorus (T-pTM:T-pP and L-pTM:L-pP) ratios (mmol:mol). Slope values of linear regression lines were only reported where r>0.5. *Values reported for Fe regression slopes excluded shelf stations. Table adapted from Twining & Baines, (2013).

Reference Source	TM:P ratio (mM):(M)							
	Fe	**Mn**	**Zn**	**Ni**	**Cu**	**Cd**	**Co**	**V**
North Atlantic Ocean (Trichodesmium) (Nuester et al., 2012; Tovar-Sanchez et al., 2006)	5-31	1-5	0.2-13	1-8	0.4-2.1	0.02-0.31	0.01-0.15	13-63
Equatorial Pacific Ocean (Phytoplankton) (Twining et al., 2011)	1.9-8.4	0.49-0.58	-	1.0-1.2	-	-	0.06-0.07	-
Culture (Eukaryotic Phytoplankton-15 species) (Ho et al., 2003)	7.5	3.8	0.8	-	0.38	0.21	0.19	-
Southern Ocean (Large Diatoms) (Cullen et al., 2003)	-	1.7	11.1	-	1.44	1.29	0.15	-
North Atlantic Ocean (mostly Flagellated cells) (Kuss and Kremling, 1999)	4.6	1.6	1.9	1.4	0.37	0.51	0.19	-
Equatorial Pacific Ocean (mostly Zooplankton) (Collier and Edmond, 1984)	4.9	0.35	3.2	0.97	0.48	0.56	-	-
Southern Ocean (Large Diatoms) (Collier and Edmond, 1984)	-	-	13.3	0.68	2	0.07	-	-
Northeast Atlantic Spring Bloom (picoplankton and coccolithophores) (Klein et al., 2013)	9.1-9.8	-	-	-	0.27-0.52	0.06-0.07	0.04-0.06	0.2-0.39
Eastern Tropical South Pacific (near Peruvian Coast) (Ohnemus et al., 2017)	39.7	1.0	1.0 ± 0.88	0.54 ± 0.39	0.40 ± 0.37	0.54 ± 0.24	0.08 ± 0.05	0.17 ± 0.16
SO243 All stations (≤50 m) T-pTMs:T-pP (Individual sample Average ± 1 S.D.)	**252 ± 442**	**5.7 ± 5.0**	**2.9 ± 1.8**	**1.28 ± 1.77**	**1.6 ± 1.7**	**0.47 ± 0.23**	**0.16 ± 0.07**	**1.1 ± 1.4**
SO243 All stations (≤50 m) T-pTMs:T-pP Regression Slope (Figure S6)	*19.3	-	1.3	0.31	-	0.35	0.06	1.1
SO243 All stations (≤50 m) L-pTMs:L-pP Regression Slope (Figure S6)	*1.8	-	-	0.196	-	0.38	0.048	1.1

4.3.3.2 TM Distributions and Cycling within the Oxygen Minimum Zone

Shelf samples within the OMZ intersected with nepheloid layer particle samples, which had high lithogenic particle concentrations (90.9 ± 49.9 nM R-pAl; n=11). As a result, we focus on the offshore OMZ samples and discuss the TM cycling of the corresponding shelf samples in section 4.3.3.3.

Labile particulate Fe concentrations were enhanced within the offshore OMZ (2.23 ± 2.13 nM), particularly in the upper oxycline (<26.5 σ_Θ; approximately 100-300 m) and were primarily associated with labile Fe oxides. The highest L-pFe concentrations were found at transect 4 near the Nazca Ridge (up to 9.85 nM L-pFe). Labile pFe/T-pFe fractions were higher in the upper oxycline (52.1 ± 13.4%; <26.5 σ_Θ), compared to the bottom of the OMZ (41.3 ± 9.3 %; >26.5 σ_Θ) and surface waters (20.4 ± 13.2 L-pFe/T-pFe%; <50 m offshore). Also, the ratios of T-pFe:R-pAl, T-pFe:T-pP, and L-pFe:L-pP (0.623 ± 0.321 mol:mol, 280 ± 132 mmol:mol, and 195 ± 126 mmol:mol, respectively) were higher than those of canonical UCC (Rudnick and Gao, 2013; Taylor and McLennan, 1995; Figure S4.8) and plankton reference sources (Table 4.1), indicating the presence of additional particulate phases.

Enhanced dFe concentrations (up to 4.64 nM; <0.2 µm) correlated well with L-pFe in the OMZ (*r*=0.721; Figure S4.11), suggesting tight coupling through buffering between the solid-solution phases either through reversible scavenging (Achterberg et al., 2021, 2018; Hurst and Bruland, 2008; Lippiatt et al., 2010; Milne et al., 2017) or (dis-)aggregation of colloidal (0.02-0.2 µm) nano-particulate Fe oxides between the operational defined dissolved and solid phases (Raiswell, 2011; Raiswell and Canfield, 2012). Since the upper offshore OMZ (<26.5 σ_Θ) had relatively low concentrations of biogenic (22.1 ± 11.2 nM T-pP) and lithogenic (8.5 ± 3.9 nM R-pAl) particles, authigenic Fe oxides probably accounted for a substantial percentage of the L-pFe pool. This explanation is consistent with other studies in the region documenting similar pFe enrichments in the upper OMZ (Cutter et al., 2018; Lam et al., 2020; Lee et al., 2018). This pFe was mostly labile, isotopically light (Marsay et al., 2018), and composed of Fe(III) oxyhydroxides near the Peruvian shelf (Heller et al., 2017).

Low concentrations of L-pMn within the OMZ (25.9±40.4 pM; Offshore OMZ), including at shelf stations (68.7±59.5 pM; Shelf OMZ), reflected the low abundance of Mn oxides. Instead, the L-pMn pool was largely associated with biogenic particles within the OMZ, which showed elevated L-pMn concentrations in surface waters quickly decreasing below 100 m (from up to 214 pM L-pMn; <100 m). Furthermore, L-pMn:L-pP abundance ratios (2.42±2.27 mmol:mol, excluding one outlier; n=39) throughout the OMZ and shelf stations were within the ranges of phytoplankton reference sources (Table 4.1). L-pMn concentrations were low throughout the OMZ, with the lowest L-pMn concentrations coinciding with highest iodide/iodine ratios (13.7 pM L-pMn; >80% I^-/IO_3^-; n=16). As oxygen concentrations increased and iodide reduction decreased (< 40% I^-/IO_3^-), L-pMn only marginally increased at the lower part and below the oxycline, but remained relatively low (maximum 81.7 pM L-pMn; 100-982 m). The deficiency of Mn oxides within the OMZ is due to the low redox potential of the anoxic water column (Cutter et al., 2018), as well as the slow oxidation kinetics of Mn (Jensen et al., 2020; Luther et al., 2018; Tebo et al., 2005, 2004; von Langen et al., 1997).

Labile pTMs Cd and Co, and L-pP concentrations were elevated in the upper oxycline and corresponded with elevated labile pTM fractions that declined in the top 300 m (Figures 4.4 and 4.6), consistent with biogenic particles sinking from the surface into the OMZ. As the proportion of the biogenic fraction of pTMs decreased through the water column as organic particles underwent remineralization, L-pCd and L-pCo concentrations, and L-pP fractions, which were evidently predominantly comprised of biogenic pTM phases, decreased as a result. Other bio-essential pTMs (i.e., Cu, Zn, Ni, and V) that were elevated in surface waters did not exhibit the same pronounced exponential decrease in L-pTM concentrations in the upper oxycline. This could be due to the different remineralization rates of TM containing cellular components, whereby for example Ni and Zn from biogenic particles may be released relatively quickly (Twining et al., 2014), or because there were other abiogenic phases present, including adsorbed phases (Archer et al., 2020; Boyle et al., 1977; Little et al., 2013; Zheng et al., 2021).

Average T-pTM:T-pP and L-pTM:L-pP ratios for Cd, Co and Zn (and L-pMn:L-pP) within the offshore OMZ were consistent with reported ratios in phytoplankton (Table 4.1). While T-pFe:T-pP and L-pFe:L-pP were higher by about 1-2 orders of magnitude, T-pTM:T-pP and L-

pTM:L-pP ratios for V, Mn, Cu, and Ni were at the upper limits of plankton reference values, or exceeded them by a factor of about 2, suggesting the influence of additional abiogenic phases. Furthermore, T-pTM:R-pAl ratios of V, Mn, Cu, Ni were also higher than UCC reference sources by about a factor of 2 for Mn, an order of magnitude for V and Ni, and about 2 orders of magnitude for Cu and Zn. Biogenic associated Cu can be adsorbed onto particle surfaces following particle remineralization (Boyle et al., 1977; Bruland, 1980; Bruland et al., 2014; Little et al., 2018, 2013; Richon and Tagliabue, 2019). V adsorption onto organic particles and Fe oxides is enhanced under anoxic conditions, following the reduction of vanadate (VO^{3-}) to the more particle-reactive vanadyl (IV) speciation (Borchers et al., 2005; Breit and Wanty, 1991; Edmonds and German, 2004; Ho et al., 2018; Trefry and Metz, 1989; Wehrli and Stumm, 1989). Indeed, L-pV concentrations were enhanced within oxygen depleted waters corresponding with enhanced iodine/iodate ratios (Figure S4.13), implying enhanced V adsorption within anoxic waters (Scholz et al., 2011).

Longer remineralization length scales through the OMZ (Devol and Hartnett, 2001; Keil et al., 2016; Weber and Bianchi, 2020), along with decreased disaggregation of particles, (Alldredge et al., 1993; Engel, 2000; Lee et al., 2018) partly due to decreased presence of grazers in OMZs, means that larger biogenic particle aggregates may persist further into deeper waters. This persistence of larger biogenic particles is supported by closer correlations of bio-essential refractory pTMs (Co, Ni, Cu, and V) with R-pP (r=0.534-0.810; Figure S4.13a-e), compared to R-pAl ($r \leq 0.48$; Figure S4.13f-j) with elemental ratios that were consistent with plankton reference values (Table 4.1). The inclusion of refractory biogenic pTM fractions and the concomitant low lithogenic particle abundance resulted in average bio-essential R-pTM:R-pAl abundance ratios that were higher by an average of 1-2 orders of magnitude than lithogenic UCC reference sources (Zn, Cu, Ni, V, and P). There were two exceptions: R-pFe:R-pAl and R-pMn:R-pAl (0.31±0.14 mol:mol, and 3.04±0.86 mmol:mol, respectively), which were primarily within the UCC reference ranges (Figure S4.8) and suggested that lithogenic particles were the predominant refractory particulate carrier phases. R-pZn poorly correlated with both R-pP and R-pAl (r= 0.06 and 0.28, respectively; Figure S4.13) which may be attributable to the varied solubility of phytoplankton cell components included within biotically aggregated particles.

4.3.3.3 Nepheloid Layer Particles

Lithogenic pTM concentrations increased towards the seafloor (Figure 4.3), and high lithogenic particle concentrations were mainly observed at shelf stations (n=19 of 26; R-pAl >25 nM) likely due to resuspended benthic particles. As most of these samples were collected in relatively shallow waters (average depth 56.9±39.6 m; max 147 m), high concentrations of biogenic particles (average 71.9±45.0 nM T-pP and 53.5±36.4 nM L-pP) were also included in samples from the nepheloid layer. L-pTM concentrations of Fe, Al, Ti, Pb, Cu and Zn in the nepheloid samples were enhanced, while higher concentrations of bio-essential Cd, Co, Ni, V, and Mn all indicated strong associations with benthic and biogenic sources, respectively, including surface samples collected from the shelf.

Benthic mineralization releases bio-essential TMs and simultaneously depletes the water column of important electron acceptors (i.e., oxygen, nitrate). TMs that have been remineralized may be stabilized after binding to organic ligands (Beckler et al., 2015; Bundy et al., 2016; Klar et al., 2017; Velasquez et al., 2016). Under sulfidic conditions, TMs may be retained in the sediment inventory as sulfides (such as Fe, Cd, Zn, Cu) (Borchers et al., 2005; Jacobs et al., 1985). Following their release from anoxic/euxinic sediment porewater, reduced TMs are either advected away, or subject to (co-)precipitation following re-oxidation (particularly for Fe)(Beckler et al., 2016, 2015), bio-assimilation, or (re-)adsorption onto particle surfaces (Archer et al., 2020; Boyle et al., 1977; Little et al., 2013; Weber et al., 2018; Zheng et al., 2021).

The average T-pFe:R-pAl (0.445±0.194 mol:mol) and T-pFe:T-pP (800±620 mmol:mol) ratios in nepheloid particle samples were higher than those in UCC and plankton reference sources (Figure S4.7 and Table 4.1, respectively), indicating a high abundance of abiogenic and non-lithogenic pFe phases. Average particulate T-pFe and L-pFe concentrations were high in nepheloid samples (48.7±33.3 nM and 23.8±29.4 nM, respectively; Figures 4.3 and 4.4) and particularly enhanced in samples within the OMZ (61.9±41.3 nM and 40.5±34.6 nM, respectively; <20 µM; *n*=10). Additionally, L-pFe fractions in OMZ samples (55.7±15.0 %; ≤20 µM oxygen; n=11) were markedly higher compared to non-OMZ samples (17.8±2.4 %; >20 µM

oxygen; n=9) (Figure S4.14). High corresponding dFe concentrations within the OMZ (13.7±12.2 nM; Figure 4.2), and enhanced L-pFe/T-pFe fractions (57.1±15.0% and up to 77.5%; Figure 4.6) suggest exchange between operationally defined solid and solution phases, possibly through (dis-)aggregation of colloidal Fe (0.02-0.2 µm) (Raiswell, 2011; Raiswell and Canfield, 2012). We attribute the enhanced L-pFe and dFe pools within the OMZ predominantly to an increased abundance of (nano-)particulate Fe oxides in the water column, rather than increased Fe scavenging typical of nepheloid layers (Honeyman et al., 1988; Rutgers Van Der Loeff and Boudreau, 1997). The Peruvian shelf may thus be similar to the Santa Monica Basin, where Fe oxides in surficial sediment underlying low oxygen bottom water conditions (<10 µM oxygen) are a source of reactive Fe oxides to the water column (Burdige and Komada, 2020).

The oxidation and subsequent precipitation of benthic (reduced) dFe released from the anoxic sediment, which is amplified within the OMZ, may have contributed to the observed rise in (labile) Fe oxides (Noffke et al., 2012; Scholz et al., 2011). Reduced Fe can be oxidized by nitrate and precipitate as nano-particulate Fe oxides when oxygen levels are low (Heller et al., 2017; Millero et al., 1987; Scholz et al., 2016). This mechanism can account for the simultaneous increases in dFe and L-pFe pools near to the seafloor (Figures 4.2 and 4.4), similar to the Benguela shelf (Al-Hashem et al., 2022). The highest L-pFe concentrations (up to 88.8 nM), fractions (up to 77.5%), and dFe (II) and dFe (III) concentrations (12.4 and 19.1 nM, respectively) were detected at station 10, where these patterns were most pronounced. Fe oxides from resuspended benthic particles are likely to comprise less soluble minerals (e.g., goethite, hematite, magnetite) and contribute sparingly to the L-pFe pool (Burdige and Komada, 2020; Cornell and Schwertmann, 2006; Dale et al., 2015; Poulton and Canfield, 2005).

No labile Mn oxides were found within the nepheloid layer, likely due to reductive dissolution of Mn oxides within the OMZ (see section 4.3.3.2)(Cutter et al., 2018; Lam et al., 2015; Lee et al., 2018), consistent with previous observations in the Peruvian OMZ (Cutter et al., 2018; Lam et al., 2015; Lee et al., 2018), and with regional surface sediment composition reporting Mn deficiency (Böning et al., 2004). The strongest concentration gradients observed for L-pMn were coupled to T-pP and L-pP (r= 0.957 and 0.962, respectively), with poor

correlations with R-pAl in nepheloid samples (r=0.224), even in non-OMZ waters (r= -0.012). This further indicates that L-pMn phases are associated with biogenic particles.

4.4 Conclusions

This study investigated the principal carrier phases and relative lability of particulate trace metals over the Peruvian shelf. The inventory of pTMs in surface water was dominated by biogenic particles for Mn, Cd, Co, Zn, Cu, Ni, V, and P. These TMs were mostly labile (>68% L-pTM/T-pTM), thus likely to be recycled on short timescales, extending their residence time in surface waters. Future work should investigate whether seasonal changes and shifting phytoplankton community structures affect biogenic particle lability.

Benthic particles were important sources of lithogenic material at shelf stations, and less so off the Peruvian shelf. Resuspended particles included authigenic Fe oxides which persisted at offshore stations, particularly in the upper part of the OMZ. Reduced Fe from anoxic shelf sediments was likely stabilized in the water column following oxidation as insoluble (nano-)particulate Fe oxides. Labile Fe oxides appears to play an important role with sustaining elevated dFe concentrations, as enhanced L-pFe and dFe concentrations were closely coupled and persisted offshore. This supports a buffering effect of exchangeable particulate Fe on the dissolved Fe inventories. This has broader implications for the transport of TMs adsorbed on Fe oxides, which may be shuttled away from the shelf or out of the OMZ into the underlying sediment via advection or settling, respectively. One such TM is V, which consistently exhibited patterns suggesting a high affinity with labile Fe oxides. In contrast, Mn oxide abundance was low over the Peruvian shelf, consistent with previous reports.

Acknowledgements

We thank the captain, crew, and the chief scientists of the RV Sonne SO243 cruise, C.A. Marandino, T. Steinhoff, and D. Grundle; C. Schlosser for help with sample collection; and P. Streu for technical laboratory assistance. The PhD fellowships to A. Al-Hashem was funded by the Kuwait institute for Scientific Research, Kuwait, and I. Rapp by the Deutsche Forschungsgemeinschaft as part of the Sonderforschungsbereich (SFB) 754: "Climate-Biogeochemistry Interactions in the Tropical Ocean". The cruise was funded by the Bundesministrerium fur Bildung und Forschung (03G0243A).

Author Contributions: A.A.A.: investigation, methodology and analysis, data curation, visualization, writing—original draft. A.J.B.: writing—review and editing. I.R.: formal analysis (dTMs). M.J.H.: formal analysis (dFe). E.P.A.: conceptualization, funding acquisition, resources, supervision, writing—review and editing.

Data Availability

Dissolved trace metal and iodide/iodate data are freely accessible from https://doi.pangaea.de/10.1594/ PANGAEA.913798. Nutrient data are freely accessible from https://doi.pangaea.de/10.1594/ PANGAEA.861391. All Particulate trace metal data is included as a source file and will be submitted to the PANGAEA oceanographic data repository.

References

Achterberg, E.P., Steigenberger, S., Klar, J.K., Browning, T.J., Marsay, C.M., Painter, S.C., Vieira, L.H., Baker, A.R., Hamilton, D.S., Tanhua, T., Moore, C.M., 2021. Trace Element Biogeochemistry in the High-Latitude North Atlantic Ocean: Seasonal Variations and Volcanic Inputs. Global Biogeochem Cycles 35. https://doi.org/10.1029/2020GB006674

Achterberg, E.P., Steigenberger, S., Marsay, C.M., Lemoigne, F.A.C., Painter, S.C., Baker, A.R., Connelly, D.P., Moore, C.M., Tagliabue, A., Tanhua, T., 2018. Iron Biogeochemistry in the High Latitude North Atlantic Ocean. Sci Rep 8. https://doi.org/10.1038/s41598-018-19472-1

Al-Hashem, A.A., Beck, A.J., Krisch, S., Barraqueta, J.-L.M., Steffens, T., Achterberg, E.P., 2022. Particulate Trace Metal Sources, Cycling, and Distributions on the Southwest African Shelf. Global Biogeochem Cycles e2022GB007453. https://doi.org/10.1029/2022GB007453

Alldredge, A.L., Passow, U., Logan, B.E., 1993. The abundance and significance of a class of large, transparent organic particles in the ocean. Deep Sea Research Part I: Oceanographic Research Papers 40, 1131–1140. https://doi.org/10.1016/0967-0637(93)90129-Q

Anderson, R.F., 2020. GEOTRACES: Accelerating Research on the Marine Biogeochemical Cycles of Trace Elements and Their Isotopes. Ann Rev Mar Sci 12, 49–85. https://doi.org/10.1146/annurev-marine-010318-095123

Archer, C., Vance, D., Milne, A., Lohan, M.C., 2020. The oceanic biogeochemistry of nickel and its isotopes: New data from the South Atlantic and the Southern Ocean biogeochemical divide. Earth Planet Sci Lett 535, 116118. https://doi.org/10.1016/j.epsl.2020.116118

Bakun, A., Weeks, S.J., 2008. The marine ecosystem off Peru: What are the secrets of its fishery productivity and what might its future hold? Prog Oceanogr 79, 290–299. https://doi.org/10.1016/j.pocean.2008.10.027

Becker, S., Aoyama, M., Woodward, E.M.S., Bakker, K., Coverly, S., Mahaffey, C., Tanhua, T., 2020. GO-SHIP Repeat Hydrography Nutrient Manual: The Precise and Accurate Determination of Dissolved Inorganic Nutrients in Seawater, Using Continuous Flow Analysis Methods. Front Mar Sci 7, 908. https://doi.org/10.3389/FMARS.2020.581790/BIBTEX

Beckler, J.S., Jones, M.E., Taillefert, M., 2015. The origin, composition, and reactivity of dissolved iron(III) complexes in coastal organic- and iron-rich sediments. Geochim Cosmochim Acta 152, 72–88. https://doi.org/10.1016/J.GCA.2014.12.017

Beckler, J.S., Kiriazis, N., Rabouille, C., Stewart, F.J., Taillefert, M., 2016. Importance of microbial iron reduction in deep sediments of river-dominated continental-margins. Mar Chem 178, 22–34. https://doi.org/10.1016/J.MARCHEM.2015.12.003

Berger, C.J.M., Lippiatt, S.M., Lawrence, M.G., Bruland, K.W., 2008. Application of a chemical leach technique for estimating labile particulate aluminum, iron, and manganese in the Columbia River plume and coastal waters off Oregon and Washington. J Geophys Res 113, 1–16. https://doi.org/10.1029/2007JC004703

Birchill, A.J., Milne, A., Woodward, E.M.S., Harris, C., Annett, A.L., Rusiecka, D., Achterberg, E.P., Gledhill, M., Ussher, S.J., Worsfold, P.J., Geibert, W., Lohan, M.C., 2017. Seasonal iron depletion in temperate shelf seas. Geophys Res Lett 44, 8987–8996. https://doi.org/10.1002/2017GL073881

Böning, P., Brumsack, H.J., Böttcher, M.E., Schnetger, B., Kriete, C., Kallmeyer, J., Borchers, S.L., 2004. Geochemistry of Peruvian near-surface sediments. Geochim Cosmochim Acta 68, 4429–4451. https://doi.org/10.1016/J.GCA.2004.04.027

Borchers, S.L., Schnetger, B., Böning, P., Brumsack, H.J., 2005. Geochemical signatures of the Namibian diatom belt: Perennial upwelling and intermittent anoxia. Geochemistry, Geophysics, Geosystems 6. https://doi.org/10.1029/2004GC000886

Boyd, P.W., Ellwood, M.J., Tagliabue, A., Twining, B.S., 2017. Biotic and abiotic retention, recycling and remineralization of metals in the ocean. Nat Geosci. https://doi.org/10.1038/ngeo2876

Boyle, E.A., Sclater, F.R., Edmond, J.M., 1977. The distribution of dissolved copper in the Pacific. Earth Planet Sci Lett 37, 38–54. https://doi.org/10.1016/0012-821X(77)90144-3

Breit, G.N., Wanty, R.B., 1991. Vanadium accumulation in carbonaceous rocks: A review of geochemical controls during deposition and diagenesis. Chem Geol 91, 83–97. https://doi.org/10.1016/0009-2541(91)90083-4

Browning, T.J., Achterberg, E.P., Engel, A., Mawji, E., 2021. Manganese co-limitation of phytoplankton growth and major nutrient drawdown in the Southern Ocean. Nat Commun 12, 1–9. https://doi.org/10.1038/s41467-021-21122-6

Browning, T.J., Achterberg, E.P., Rapp, I., Engel, A., Bertrand, E.M., Tagliabue, A., Moore, C.M., 2017. Nutrient co-limitation at the boundary of an oceanic gyre. Nature 551, 242–246. https://doi.org/10.1038/nature24063

Browning, T.J., Rapp, I., Schlosser, C., Gledhill, M., Achterberg, E.P., Bracher, A., le Moigne, F.A.C., 2018. Influence of Iron, Cobalt, and Vitamin B12 Supply on Phytoplankton Growth in the Tropical East Pacific During the 2015 El Niño. Geophys Res Lett 45, 6150–6159. https://doi.org/10.1029/2018GL077972

Bruland, K.W., 1980. Oceanographic distributions of cadmium, zinc, nickel, and copper in the North Pacific. Earth Planet Sci Lett 47, 176–198. https://doi.org/10.1016/0012-821X(80)90035-7

Bruland, K.W., Middag, R., Lohan, M.C., 2014. Controls of Trace Metals in Seawater, 2nd ed, Treatise on Geochemistry: Second Edition. Elsevier Ltd. https://doi.org/10.1016/B978-0-08-095975-7.00602-1

Bruland, K.W., Rue, E.L., Smith, G.J., DiTullio, G.R., 2005. Iron, macronutrients and diatom blooms in the Peru upwelling regime: Brown and blue waters of Peru. Mar Chem 93, 81–103. https://doi.org/10.1016/j.marchem.2004.06.011

Bundy, R.M., Jiang, M., Carter, M., Barbeau, K.A., 2016. Iron-binding ligands in the Southern California current system: Mechanistic studies. Front Mar Sci 3, 27. https://doi.org/10.3389/FMARS.2016.00027/BIBTEX

Burdige, D.J., Komada, T., 2020. Iron redox cycling, sediment resuspension and the role of sediments in low oxygen environments as sources of iron to the water column. Mar Chem 223, 103793. https://doi.org/10.1016/j.marchem.2020.103793

Capone, D.G., Hutchins, D.A., 2013. Microbial biogeochemistry of coastal upwelling regimes in a changing ocean. Nat Geosci. https://doi.org/10.1038/ngeo1916

Chavez, F.P., Bertrand, A., Guevara-Carrasco, R., Soler, P., Csirke, J., 2008. The northern Humboldt Current System: Brief history, present status and a view towards the future. Prog Oceanogr 79, 95–105. https://doi.org/10.1016/j.pocean.2008.10.012

Chever, F., Rouxel, O.J., Croot, P.L., Ponzevera, E., Wuttig, K., Auro, M., 2015. Total dissolvable and dissolved iron isotopes in the water column of the Peru upwelling regime. Geochim Cosmochim Acta 162, 66–82. https://doi.org/10.1016/j.gca.2015.04.031

Close, H.G., Lam, P.J., Popp, B.N., 2021. Marine Particle Chemistry: Influence on Biogeochemical Cycles and Particle Export. ACS Earth Space Chem 5, 1210–1211. https://doi.org/10.1021/acsearthspacechem.1c00091

Cochran, J.K., McKibbin-Vaughan, T., Dornblaser, M.M., Hirschberg, D., Livingston, H.D., Buesseler, K.O., 1990. 210Pb scavenging in the North Atlantic and North Pacific Oceans. Earth Planet Sci Lett 97, 332–352. https://doi.org/10.1016/0012-821X(90)90050-8

Collier, R., Edmond, J., 1984. The trace element geochemistry of marine biogenic particulate matter. Prog Oceanogr 13, 113–199. https://doi.org/10.1016/0079-6611(84)90008-9

Cornell, R.M., Schwertmann, U., 2006. The Iron Oxides: Structure, Properties, Reactions, Occurrences and Uses 707.

Cowen, J.P., Bruland, K.W., 1985. Metal deposits associated with bacteria: implications for Fe and Mn marine biogeochemistry. Deep Sea Research Part A. Oceanographic Research Papers 32, 253–272. https://doi.org/10.1016/0198-0149(85)90078-0

Cullen, J.T., Chase, Z., Coale, K.H., Fitzwater, S.E., Sherrell, R.M., 2003. Effect of iron limitation on the cadmium to phosphorus ratio of natural phytoplankton assemblages from the Southern Ocean. Limnol Oceanogr 48, 1079–1087. https://doi.org/10.4319/LO.2003.48.3.1079

Cullen, J.T., Field, M.P., Sherrell, R.M., 2001. Determination of trace elements in filtered suspended marine particulate material by sector field HR-ICP-MS. The Royal Society of Chemistry 16, 1307–1312. https://doi.org/10.1039/b104398f

Cullen, J.T., Sherrell, R.M., 1999. Techniques for determination of trace metals in small samples of size-fractionated particulate matter: phytoplankton metals off central California. Mar Chem 67, 233–247.

Cutter, G.A., Andersson, P.S., Codispoti, L., Croot, P.L., Francois, R., Lohan, M.C., Obata, H., Rutgers van der Loeff, M.M., 2010. Sampling and sample-handling protocols for GEOTRACES cruises 1–238. https://doi.org/http://www.geotraces.org/science/intercalibration/222-sampling-and-sample-handling-protocols-for-geotraces-cruises

Cutter, G.A., Moffett, J.G., Nielsdóttir, M.C., Sanial, V., 2018. Multiple oxidation state trace elements in suboxic waters off Peru: In situ redox processes and advective/diffusive horizontal transport. Mar Chem 201, 77–89. https://doi.org/10.1016/j.marchem.2018.01.003

Dale, A.W., Nickelsen, L., Scholz, F., Hensen, C., Oschlies, A., Wallmann, K., 2015. A revised global estimate of dissolved iron fluxes from marine sediments. Global Biogeochem Cycles 29, 691–707. https://doi.org/10.1002/2014GB005017

Dammshäuser, A., Croot, P.L., 2012. Low colloidal associations of aluminium and titanium in surface waters of the tropical Atlantic. Geochim Cosmochim Acta 96, 304–318. https://doi.org/10.1016/J.GCA.2012.07.032

Devol, A.H., Hartnett, H.E., 2001. Role of the oxygen-deficient zone in transfer of organic carbon to the deep ocean. Limnol Oceanogr 46, 1684–1690. https://doi.org/10.4319/LO.2001.46.7.1684

Edmonds, H.N., German, C.R., 2004. Particle geochemistry in the Rainbow hydrothermal plume, Mid-Atlantic Ridge. Geochim Cosmochim Acta 68, 759–772. https://doi.org/10.1016/S0016-7037(03)00498-8

Engel, A., 2000. The role of transparent exopolymer particles (TEP) in the increase in apparent particle stickiness (α) during the decline of a diatom bloom. J Plankton Res 22, 485–497. https://doi.org/10.1093/PLANKT/22.3.485

Ensign, S.A., Hyman, M.R., Arp, D.J., 1993. In vitro activation of ammonia monooxygenase from Nitrosomonas europaea by copper. J Bacteriol 175, 1971–1980. https://doi.org/10.1128/JB.175.7.1971-1980.1993

Feely, R.A., Massoth, G., Trefry, J., 1989. The Role of Fe Oxhydroxides in Phosphorus, Vanadium and Arsenic Scavenging over the Mid Atlantic Ridge and Juan-De-Fuca Ridge Hydrothermal systems. Abstracts of Papers of the American Chemical Society 198, 102-GEOC.

Fiedler, P.C., Talley, L.D., 2006. Hydrography of the eastern tropical Pacific: A review. Prog Oceanogr 69, 143–180. https://doi.org/10.1016/j.pocean.2006.03.008

Fitzsimmons, J.N., John, S.G., Marsay, C.M., Hoffman, C.L., Nicholas, S.L., Toner, B.M., German, C.R., Sherrell, R.M., 2017. Iron persistence in a distal hydrothermal plume supported by dissolved–particulate exchange. Nat Geosci 10, 195–201. https://doi.org/10.1038/ngeo2900

GEOTRACES IDP2021 [WWW Document], n.d. URL https://www.bodc.ac.uk/data/published_data_library/catalogue/10.5285/cf2d9ba9-d51d-3b7c-e053-8486abc0f5fd/ (accessed 7.28.22a).

German, C.R., Campbell, A.C., Edmond, J.M., 1991. Hydrothermal scavenging at the Mid-Atlantic Ridge: Modification of trace element dissolved fluxes. Earth Planet Sci Lett 107, 101–114. https://doi.org/10.1016/0012-821X(91)90047-L

Hansen, H.P., 2007. Determination of oxygen. Methods of Seawater Analysis: Third, Completely Revised and Extended Edition 75–89. https://doi.org/10.1002/9783527613984.CH4

Hansen, L.S., Blackburn, T.H., 1991. Aerobic and anaerobic mineralization of organic material in marine sediment microcosms. Mar Ecol Prog Ser 75, 283–291. https://doi.org/10.3354/MEPS075283

Heller, M.I., Lam, P.J., Moffett, J.W., Till, C.P., Lee, J.M., Toner, B.M., Marcus, M.A., 2017. Accumulation of Fe oxyhydroxides in the Peruvian oxygen deficient zone implies non-oxygen dependent Fe oxidation. Geochim Cosmochim Acta 211, 174–193. https://doi.org/10.1016/j.gca.2017.05.019

Helly, J.J., Levin, L.A., 2004. Global distribution of naturally occurring marine hypoxia on continental margins. Deep Sea Research Part I: Oceanographic Research Papers 51, 1159–1168. https://doi.org/10.1016/J.DSR.2004.03.009

Henrichs, S.M., Reeburgh, W.S., 1987. Anaerobic mineralization of marine sediment organic matter: Rates and the role of anaerobic processes in the oceanic carbon economy. Geomicrobiol J 5, 191–237. https://doi.org/10.1080/01490458709385971

Hill, V.L., Manley, S.L., 2009. Release of reactive bromine and iodine from diatoms and its possible role in halogen transfer in polar and tropical oceans. Limnol Oceanogr 54, 812–822. https://doi.org/10.4319/LO.2009.54.3.0812

Ho, P., Lee, J.M., Heller, M.I., Lam, P.J., Shiller, A.M., 2018. The distribution of dissolved and particulate Mo and V along the U.S. GEOTRACES East Pacific Zonal Transect (GP16): The roles of oxides and biogenic particles in their distributions in the oxygen deficient zone and the hydrothermal plume. Mar Chem 201, 242–255. https://doi.org/10.1016/j.marchem.2017.12.003

Ho, T.-Y., Finkel, Z. v, Milligan, A.J., Wyman, K., Falkowski, P.G., Morel, F.M.M., 2003. The elemental composition of some marine phytoplankton. J Phycol 39, 1145–1159.

Honeyman, B.D., Balistrieri, L.S., Murray, J.W., 1988. Oceanic trace metal scavenging: the importance of particle concentration. Deep Sea Research Part A, Oceanographic Research Papers 35, 227–246. https://doi.org/10.1016/0198-0149(88)90038-6

Hopwood, M.J., Rapp, I., Schlosser, C., Achterberg, E.P., 2017. Hydrogen peroxide in deep waters from the Mediterranean Sea, South Atlantic and South Pacific Oceans. Sci Rep 7, 1–10. https://doi.org/10.1038/srep43436

Hurst, M.P., Bruland, K.W., 2008. The effects of the San Francisco Bay plume on trace metal and nutrient distributions in the Gulf of the Farallones. Geochim Cosmochim Acta. https://doi.org/10.1016/j.gca.2007.11.005

Hutchins, D.A., Hare, C.E., Weaver, R.S., Zhang, Y., Firme, G.F., DiTullio, G.R., Alm, M.B., Riseman, S.F., Maucher, J.M., Geesey, M.E., Trick, C.G., Smith, G.J., Rue, E.L., Conn, J., Bruland, K.W., 2002. Phytoplankton iron limitation in the Humboldt Current and Peru Upwelling. Limnol Oceanogr 47, 997–1011. https://doi.org/10.4319/LO.2002.47.4.0997

Jacobs, L., Emerson, S., Skei, J., 1985. Partitioning and transport of metals across the O2H2S interface in a permanently anoxic basin: Framvaren Fjord, Norway. Geochim Cosmochim Acta 49, 1433–1444. https://doi.org/10.1016/0016-7037(85)90293-5

Jeandel, C., Oelkers, E.H., 2015. The influence of terrigenous particulate material dissolution on ocean chemistry and global element cycles. Chem Geol 395, 50–66. https://doi.org/10.1016/j.chemgeo.2014.12.001

Jeandel, C., Rutgers van der Loeff, M., Lam, P.J., Roy-Barman, M., Sherrell, R.M., Kretschmer, S., German, C., Dehairs, F., 2015. What did we learn about ocean particle dynamics in the GEOSECS-JGOFS era? Prog Oceanogr 133, 6–16. https://doi.org/10.1016/j.pocean.2014.12.018

Jensen, L.T., Morton, P.L., Twining, B.S., Heller, M.I., Hatta, M., Measures, C.I., John, S.G., Zhang, R., Pinedo-Gonzalez, P., Sherrell, R.M., Fitzsimmons, J.N., 2020. A comparison of marine Fe and Mn cycling: U.S. GEOTRACES GN01 Western Arctic case study. Geochim Cosmochim Acta 288, 138–160. https://doi.org/10.1016/j.gca.2020.08.006

Jickells, T.D., 2005. Global Iron Connections Between Desert Dust, Ocean Biogeochemistry, and Climate. Science (1979) 308, 67–71. https://doi.org/10.1126/science.1105959

Jochum, K.P., Nohl, U., Herwig, K., Lammel, E., Stoll, B., Hofmann, A.W., 2005. GeoReM: A new geochemical database for reference materials and isotopic standards. Geostand Geoanal Res 29, 333–338. https://doi.org/10.1111/j.1751-908x.2005.tb00904.x

Johnson, T.L., Palenik, B., Brahamsha, B., 2011. CHARACTERIZATION OF A FUNCTIONAL VANADIUM-DEPENDENT BROMOPEROXIDASE IN THE MARINE CYANOBACTERIUM SYNECHOCOCCUS SP. CC9311(1). J Phycol 47, 792–801. https://doi.org/10.1111/J.1529-8817.2011.01007.X

Karstensen, J., Stramma, L., Visbeck, M., 2008. Oxygen minimum zones in the eastern tropical Atlantic and Pacific oceans. Prog Oceanogr 77, 331–350. https://doi.org/10.1016/J.POCEAN.2007.05.009

Keil, R.G., Neibauer, J.A., Biladeau, C., van der Elst, K., Devol, A.H., 2016. A multiproxy approach to understanding the “enhanced” flux of organic matter through the oxygen-deficient waters of the Arabian Sea. Biogeosciences 13, 2077–2092. https://doi.org/10.5194/BG-13-2077-2016

Klar, J.K., Homoky, W.B., Statham, P.J., Birchill, A.J., Harris, E.L., Woodward, E.M.S., Silburn, B., Cooper, M.J., James, R.H., Connelly, D.P., Chever, F., Lichtschlag, A., Graves, C., 2017. Stability of dissolved and soluble Fe(II) in shelf sediment pore waters and release to an oxic water column. Biogeochemistry 135, 49–67. https://doi.org/10.1007/S10533-017-0309-X/FIGURES/10

Klein, N.J., Beck, A.J., Hutchins, D.A., Sañudo-Wilhelmy, S.A., 2013. Regression modeling of the North East Atlantic Spring Bloom suggests previously unrecognized biological roles for V and Mo. Front Microbiol 4, 1–12. https://doi.org/10.3389/fmicb.2013.00045

Kuss, J., Kremling, K., 1999. Spatial variability of particle associated trace elements in near-surface waters of the North Atlantic (30°N/60°W to 60°N/2°W), derived by large volume sampling. Mar Chem 68, 71–86. https://doi.org/10.1016/S0304-4203(99)00066-3

Lam, P.J., Anderson, R.F., 2018. GEOTRACES: The Marine Biogeochemical Cycle of Trace Elements and Their Isotopes. Elements 14, 377–378. https://doi.org/10.2138/GSELEMENTS.14.6.377

Lam, P.J., Heller, M.I., Lerner, P.E., Moffett, J.W., Buck, K.N., 2020. Unexpected Source and Transport of Iron from the Deep Peru Margin. ACS Earth Space Chem 4, 977–992. https://doi.org/10.1021/acsearthspacechem.0c00066

Lam, P.J., Ohnemus, D.C., Auro, M.E., 2015. Size-fractionated major particle composition and concentrations from the US GEOTRACES North Atlantic Zonal Transect. Deep Sea Res 2 Top Stud Oceanogr 116, 303–320. https://doi.org/10.1016/j.dsr2.2014.11.020

Lee, J.M., Heller, M.I., Lam, P.J., 2018. Size distribution of particulate trace elements in the U.S. GEOTRACES Eastern Pacific Zonal Transect (GP16). Mar Chem 201, 108–123. https://doi.org/10.1016/j.marchem.2017.09.006

Lemaitre, N., Planquette, H., Dehairs, F., Planchon, F., Sarthou, G., Gallinari, M., Roig, S., Jeandel, C., Castrillejo, M., 2020. Particulate Trace Element Export in the North Atlantic (GEOTRACES GA01 Transect, GEOVIDE Cruise). ACS Earth Space Chem 4, 2185–2204. https://doi.org/10.1021/acsearthspacechem.0c00045

Lippiatt, S.M., Brown, M.T., Lohan, M.C., Berger, C.J.M., Bruland, K.W., 2010. Leachable particulate iron in the Columbia River, estuary, and near-field plume. Estuar Coast Shelf Sci 87, 33–42. https://doi.org/10.1016/j.ecss.2009.12.009

Little, S.H., Archer, C., Milne, A., Schlosser, C., Achterberg, E.P., Lohan, M.C., Vance, D., 2018. Paired dissolved and particulate phase Cu isotope distributions in the South Atlantic. Chem Geol 502, 29–43. https://doi.org/10.1016/j.chemgeo.2018.07.022

Little, S.H., Vance, D., Siddall, M., Gasson, E., 2013. A modeling assessment of the role of reversible scavenging in controlling oceanic dissolved Cu and Zn distributions. Global Biogeochem Cycles 27, 780–791. https://doi.org/10.1002/gbc.20073

Luther, G.W., Thibault de Chanvalon, A., Oldham, V.E., Estes, E.R., Tebo, B.M., Madison, A.S., 2018. Reduction of Manganese Oxides: Thermodynamic, Kinetic and Mechanistic Considerations for One- Versus Two-Electron Transfer Steps. Aquat Geochem 24, 257–277. https://doi.org/10.1007/s10498-018-9342-1

Mahowald, N.M., Baker, A.R., Bergametti, G., Brooks, N., Duce, R.A., Jickells, T.D., Kubilay, N., Prospero, J.M., Tegen, I., 2005. Atmospheric global dust cycle and iron inputs to the ocean. Global Biogeochem Cycles 19. https://doi.org/10.1029/2004GB002402

Marsay, C.M., Lam, P.J., Heller, M.I., Lee, J.M., John, S.G., 2018. Distribution and isotopic signature of ligand-leachable particulate iron along the GEOTRACES GP16 East Pacific Zonal Transect. Mar Chem 201, 198–211. https://doi.org/10.1016/j.marchem.2017.07.003

Martens, C.S., Val Klump, J., 1984. Biogeochemical cycling in an organic-rich coastal marine basin 4. An organic carbon budget for sediments dominated by sulfate reduction and

methanogenesis. Geochim Cosmochim Acta 48, 1987–2004. https://doi.org/10.1016/0016-7037(84)90380-6

Millero, F.J., Sotolongo, S., Izaguirre, M., 1987. The oxidation kinetics of Fe(II) in seawater. Geochim Cosmochim Acta 51, 793–801. https://doi.org/10.1016/0016-7037(87)90093-7

Milne, A., Schlosser, C., Wake, B.D., Achterberg, E.P., Chance, R., Baker, A.R., Forryan, A., Lohan, M.C., 2017. Particulate phases are key in controlling dissolved iron concentrations in the (sub)tropical North Atlantic: Particulate Phases Control dFe. Geophys Res Lett. https://doi.org/10.1002/2016GL072314

Moore, C.M., Mills, M.M., Arrigo, K.R., Berman-Frank, I., Bopp, L., Boyd, P.W., Galbraith, E.D., Geider, R.J., Guieu, C., Jaccard, S.L., Jickells, T.D., la Roche, J., Lenton, T.M., Mahowald, N.M., Marañón, E., Marinov, I., Moore, J.K., Nakatsuka, T., Oschlies, A., Saito, M.A., Thingstad, T.F., Tsuda, A., Ulloa, O., 2013. Processes and patterns of oceanic nutrient limitation. Nat Geosci 6, 701–710. https://doi.org/10.1038/ngeo1765

Morel, F.M.M., Price, N.M., 2003. The biogeochemical cycles of trace metals in the oceans. Science (1979) 300, 944–947. https://doi.org/10.1126/science.1083545

Morel, F.M.M., Reinfelder, J.R., Roberts, S.B., Chamberlain, C.P., Lee, J.G., Yee, D., 1994. Zinc and carbon co-limitation of marine phytoplankton. Nature 369, 740–742. https://doi.org/10.1038/369740a0

Noffke, A., Hensen, C., Sommer, S., Scholz, F., Bohlen, L., Mosch, T., Graco, M., Wallmann, K., 2012. Benthic iron and phosphorus fluxes across the Peruvian oxygen minimum zone. Limnol Oceanogr 57, 851–867. https://doi.org/10.4319/lo.2012.57.3.0851

Nozaki, Y., Thomson, J., Turekian, K.K., 1976. The distribution of 210Pb and 210Po in the surface waters of the Pacific Ocean. Earth Planet Sci Lett 32, 304–312. https://doi.org/10.1016/0012-821X(76)90070-4

Nuester, J., Vogt, S., Newville, M., Kustka, A.B., Twining, B.S., 2012a. The unique biogeochemical signature of the marine diazotroph Trichodesmium. Front Microbiol 3, 1–15. https://doi.org/10.3389/fmicb.2012.00150

Ohnemus, D.C., Lam, P.J., 2015. Cycling of lithogenic marine particles in the US GEOTRACES North Atlantic transect. Deep Sea Res 2 Top Stud Oceanogr 116, 283–302. https://doi.org/10.1016/j.dsr2.2014.11.019

Ohnemus, D.C., Rauschenberg, S., Cutter, G.A., Fitzsimmons, J.N., Sherrell, R.M., Twining, B.S., 2017. Elevated trace metal content of prokaryotic communities associated with marine oxygen deficient zones. Limnol Oceanogr 62, 3–25. https://doi.org/10.1002/LNO.10363

Pennington, J.T., Mahoney, K.L., Kuwahara, V.S., Kolber, D.D., Calienes, R., Chavez, F.P., 2006. Primary production in the eastern tropical Pacific: A review. Prog Oceanogr 69, 285–317. https://doi.org/10.1016/j.pocean.2006.03.012

Poulton, S.W., Canfield, D.E., 2005. Development of a sequential extraction procedure for iron: Implications for iron partitioning in continentally derived particulates. Chem Geol 214, 209–221. https://doi.org/10.1016/j.chemgeo.2004.09.003

Raiswell, R., 2011. Iceberg-hosted nanoparticulate Fe in the Southern Ocean: Mineralogy, origin, dissolution kinetics and source of bioavailable Fe. Deep Sea Res 2 Top Stud Oceanogr 58, 1364–1375. https://doi.org/10.1016/j.dsr2.2010.11.011

Raiswell, R., Canfield, D.E., 2012. The iron biogeochemical cycle past and present. Geochem Perspect 1, 1–232. https://doi.org/10.7185/geochempersp.1.1

Rapp, I., Schlosser, C., Browning, T.J., Wolf, F., le Moigne, F.A.C., Gledhill, M., Achterberg, E.P., 2020. El Niño-Driven Oxygenation Impacts Peruvian Shelf Iron Supply to the South Pacific Ocean. Geophys Res Lett 47. https://doi.org/10.1029/2019GL086631

Rapp, I., Schlosser, C., Rusiecka, D., Gledhill, M., Achterberg, E.P., 2017. Automated preconcentration of Fe, Zn, Cu, Ni, Cd, Pb, Co, and Mn in seawater with analysis using high-resolution sector field inductively-coupled plasma mass spectrometry. Anal Chim Acta 976. https://doi.org/10.1016/j.aca.2017.05.008

Rauschenberg, S., Twining, B.S., 2015. Evaluation of approaches to estimate biogenic particulate trace metals in the ocean. Mar Chem 171, 67–77. https://doi.org/10.1016/j.marchem.2015.01.004

Richon, C., Tagliabue, A., 2019. Insights Into the Major Processes Driving the Global Distribution of Copper in the Ocean From a Global Model. Global Biogeochem Cycles 33, 1594–1610. https://doi.org/10.1029/2019GB006280

Rudnick, R.L., Gao, S., 2013. Composition of the Continental Crust, 2nd ed, Treatise on Geochemistry: Second Edition. Elsevier Ltd. https://doi.org/10.1016/B978-0-08-095975-7.00301-6

Rusiecka, D., Gledhill, M., Milne, A., Achterberg, E.P., Annett, A.L., Atkinson, S., Birchill, A.J., Karstensen, J., Lohan, M.C., Mariez, C., Middag, R., Rolison, J.M., Tanhua, T., Ussher, S., Connelly, D., 2018. Anthropogenic Signatures of Lead in the Northeast Atlantic. Geophys Res Lett 45, 2734–2743. https://doi.org/10.1002/2017GL076825

Rutgers Van Der Loeff, M.M., Boudreau, B.P., 1997. The effect of resuspension on chemical exchanges at the sediment-water interface in the deep sea - A modelling and natural radiotracer approach. Journal of Marine Systems 11, 305–342. https://doi.org/10.1016/S0924-7963(96)00128-5

Schlitzer, R., Ocean Data View, https://odv.awu.de, 2019.

Schlosser, C., Garbe-Schönberg, D., 2019. Mechanisms of Pb supply and removal in two remote (sub-)polar ocean regions. Mar Pollut Bull 149, 110659. https://doi.org/10.1016/J.MARPOLBUL.2019.110659

Schlosser, C., Streu, P., Frank, M., Lavik, G., Croot, P.L., Dengler, M., Achterberg, E.P., 2018. H2S events in the Peruvian oxygen minimum zone facilitate enhanced dissolved Fe concentrations. Sci Rep 8. https://doi.org/10.1038/s41598-018-30580-w

Scholz, F., Hensen, C., Noffke, A., Rohde, A., Liebetrau, V., Wallmann, K., 2011. Early diagenesis of redox-sensitive trace metals in the Peru upwelling area - a response to ENSO-related oxygen fluctuations in the water column. Geochim Cosmochim Acta 75, 7257–7276. https://doi.org/10.1016/j.gca.2011.08.007

Scholz, F., Löscher, C.R., Fiskal, A., Sommer, S., Hensen, C., Lomnitz, U., Wuttig, K., Göttlicher, J., Kossel, E., Steininger, R., Canfield, D.E., 2016. Nitrate-dependent iron oxidation limits iron transport in anoxic ocean regions. Earth Planet Sci Lett 454, 272–281. https://doi.org/10.1016/j.epsl.2016.09.025

Scholz, F., McManus, J., Mix, A.C., Hensen, C., Schneider, R.R., 2014. The impact of ocean deoxygenation on iron release from continental margin sediments. Nat Geosci 7, 433–437. https://doi.org/10.1038/ngeo2162

Silva, N., Rojas, N., Fedele, A., 2009. Water masses in the Humboldt Current System: Properties, distribution, and the nitrate deficit as a chemical water mass tracer for Equatorial Subsurface Water off Chile. Deep Sea Res 2 Top Stud Oceanogr 56, 1004–1020. https://doi.org/10.1016/j.dsr2.2008.11.001

Stramma, L., Fischer, T., Grundle, D.S., Krahmann, G., Bange, H.W., Marandino, C.A., 2016. Observed El Niño conditions in the eastern tropical Pacific in October 2015. Ocean Science 12, 861–873. https://doi.org/10.5194/os-12-861-2016

Strub, P.T., Mesías, M.J., Montecino, V., Rutllant, J., Salinas, S., 1998. Coastal ocean circulation off western South America coastal segment. The Sea.

Tagliabue, A., Bowie, A.R., Boyd, P.W., Buck, K.N., Johnson, K.S., Saito, M.A., 2017. The integral role of iron in ocean biogeochemistry. Nature 543, 51–59. https://doi.org/10.1038/nature21058

Taylor, S.R., McLennan, S.M., 1995. The geochemical evolution of the continental crust. Reviews of Geophysics 33, 241–265. https://doi.org/10.1029/95RG00262

Tebo, B.M., Bargar, J.R., Clement, B.G., Dick, G.J., Murray, K.J., Parker, D., Verity, R., Webb, S.M., 2004. Biogenic manganese oxides: Properties and mechanisms of formation. Annu Rev Earth Planet Sci 32, 287–328. https://doi.org/10.1146/annurev.earth.32.101802.120213

Tebo, B.M., Johnson, H.A., McCarthy, J.K., Templeton, A.S., 2005. Geomicrobiology of manganese(II) oxidation. Trends Microbiol 13, 421–428. https://doi.org/10.1016/j.tim.2005.07.009

Tovar-Sanchez, A., Sañudo-Wilhelmy, S.A., 2011. Influence of the Amazon River on dissolved and intra-cellular metal concentrations in Trichodesmium colonies along the western boundary of the sub-tropical North Atlantic Ocean. Biogeosciences 8, 217–225. https://doi.org/10.5194/bg-8-217-2011

Tovar-Sanchez, A., Sañudo-Wilhelmy, S.A., Kustka, A.B., Agustí, S., Dachs, J., Hutchins, D.A., Capone, D.G., Duarte, C.M., 2006. Effects of dust deposition and river discharges on trace metal composition of Trichodesmium spp. in the tropical and subtropical North Atlantic Ocean. Limnol Oceanogr 51, 1755–1761. https://doi.org/10.4319/LO.2006.51.4.1755

Trefry, J.H., Metz, S., 1989. Role of hydrothermal precipitates in the geochemical cycling of vanadium. Nature 1989 342:6249 342, 531–533. https://doi.org/10.1038/342531a0

Twining, B.S., Baines, S.B., 2013. The Trace Metal Composition of Marine Phytoplankton. Annu. Rev. Mar. Sci 5, 191–215. https://doi.org/10.1146/annurev-marine-121211-172322

Twining, B.S., Baines, S.B., Bozard, J.B., Vogt, S., Walker, E.A., Nelson, D.M., 2011. Metal quotas of plankton in the equatorial Pacific Ocean. Deep Sea Res 2 Top Stud Oceanogr 58, 325–341. https://doi.org/10.1016/j.dsr2.2010.08.018

Twining, B.S., Nodder, S.D., King, A.L., Hutchins, D.A., Lecleir, G.R., Debruyn, J.M., Maas, E.W., Vogt, S., Wilhelm, S.W., Boyd, P.W., 2014. Differential remineralization of major and trace elements in sinking diatoms. Limnol Oceanogr 59, 689–704. https://doi.org/10.4319/lo.2014.59.3.0689

Twining, B.S., Rauschenberg, S., Baer, S.E., Lomas, M.W., Martiny, A.C., Antipova, O., 2019. A nutrient limitation mosaic in the eastern tropical Indian Ocean. Deep Sea Res 2 Top Stud Oceanogr 166, 0–1. https://doi.org/10.1016/j.dsr2.2019.05.001

Twining, B.S., Rauschenberg, S., Morton, P.L., Vogt, S., 2015. Metal contents of phytoplankton and labile particulate material in the North Atlantic Ocean. Prog Oceanogr 137, 261–283. https://doi.org/10.1016/j.pocean.2015.07.001

Vedamati, J., Goepfert, T., Moffett, J.W., 2014. Iron speciation in the eastern tropical south pacific oxygen minimum zone off peru. Limnol Oceanogr 59, 1945–1957. https://doi.org/10.4319/lo.2014.59.6.1945

Velasquez, I.B., Ibisanmi, E., Maas, E.W., Boyd, P.W., Nodder, S., Sander, S.G., 2016. Ferrioxamine siderophores detected amongst iron binding ligands produced during the remineralization of marine particles. Front Mar Sci 3, 172. https://doi.org/10.3389/FMARS.2016.00172/BIBTEX

von Langen, P.J., Johnson, K.S., Coale, K.H., Elrod, V.A., 1997. Oxidation kinetics of manganese (II) in seawater at nanomolar concentrations. Geochim Cosmochim Acta 61, 4945–4954. https://doi.org/10.1016/S0016-7037(97)00355-4

Weber, T.S., Bianchi, D., 2020. Efficient Particle Transfer to Depth in Oxygen Minimum Zones of the Pacific and Indian Oceans. Front Earth Sci (Lausanne) 8, 1–11. https://doi.org/10.3389/feart.2020.00376

Weber, T.S., John, S., Tagliabue, A., DeVries, T., 2018. Biological uptake and reversible scavenging of zinc in the global ocean. Science (1979) 361, 72–76. https://doi.org/10.1126/science.aap8532

Wehrli, B., Stumm, W., 1989. Vanadyl in natural waters: Adsorption and hydrolysis promote oxygenation. Geochim Cosmochim Acta 53, 69–77. https://doi.org/10.1016/0016-7037(89)90273-1

Winkler, L.W., 1888. The determination of dissolved oxygen in water. Berlin DeutChem Gas 21, 2843–2855.

Winter, J.M., Moore, B.S., 2009. Exploring the chemistry and biology of vanadium-dependent haloperoxidases. Journal of Biological Chemistry 284, 18577–18581. https://doi.org/10.1074/jbc.R109.001602

Zheng, L., Minami, T., Takano, S., Ho, T.-Y., Sohrin, Y., 2021. Sectional Distribution Patterns of Cd, Ni, Zn, and Cu in the North Pacific Ocean: Relationships to Nutrients and Importance of Scavenging. Global Biogeochem Cycles 35. https://doi.org/10.1029/2020GB006558

Supporting Information for

Marine Biogeochemical Cycling of Particulate Trace Metals on the Peruvian Shelf

Ali A. Al-Hashem[1,2*], Aaron J. Beck[1], Insa Rapp[1], Mark J. Hopwood[1,3], Eric P. Achterberg[1,2]

[1]GEOMAR Helmholtz Centre for Ocean Research Kiel, Kiel 24148, Germany.
[2]Christian-Albrechts-University of Kiel, Christian-Albrechts-Platz 4, 24118 Kiel, Germany.
[3]Now at: Southern University of Science and Technology, Shenzhen, China.

Contents of this section

Table S4.1. Summary of sample procedural blanks (PB), limits of detection of labile (L-pTM) and refractory (R-pTM) particulate fractions, and certified reference material (CRM) recoveries between 4 different particle leach-digestion batches. Detection Limits were determined as 3x the standard deviation (SD) of procedural blanks. Certified Reference Material (CRM) recoveries were determined using certified values and consensus values acquired from the GeoReM database at the time of publication (Jochum et al., 2005).[1]BDL = Below Detection Limit.

Procedural Blanks	***n***	**Al**	**Fe**	**Ti**	**P**	**V**	**Mn**	**Zn**	**Cu**	**Ni**	**Co**	**Cd**	**Pb**
Average PB L-pTM [pM/filter ± 1 SD]	***10***	**121 ± 113**	**119 ± 41**	**25 ± 68**	**138 ± 60**	**0.6 ± 0.3**	**2.2 ± 0.3**	**44.6 ± 31.1**	**4.8 ± 6.3**	**9.1 ± 4**	**1.2 ± 2.3**	**0.02 ± 0**	**0.24 ± 0.33**
Median Process Blank L-pTM [pM/filter]		99	99.99	2.36	128.24	0.75	2.18	33.63	2.77	7.96	0.22	0.02	0.11
L-pTM Detection Limit [pM/filter]		339	123.00	204.00	180.00	0.90	0.90	93.30	18.90	12.00	6.90	0.00	0.99
Average PB R-pTM [pM/filter ± 1 SD]	***10***	**177 ± 131**	**48 ± 36**	**102 ± 88**	**151 ± 107**	**0.4 ± 0.3**	**0.8 ± 0.6**	**21.5 ± 25.2**	**0.9 ± 0.5**	**0.8 ± 0.6**	**0.4 ± 0.2**	**0.11 ± 0.15**	**0.16 ± 0.31**
Median Process Blank R-pTM [pM/filter]		152	37.60	71.87	120.37	0.24	0.49	12.72	0.91	0.64	0.33	0.03	0.03
R-pTM Detection Limit [pM/filter]		393	108.00	264.00	321.00	0.90	1.80	75.60	1.50	1.80	0.60	0.45	0.93

Certified Reference Material	***n***	**Al**	**Fe**	**Ti**	**P**	**V**	**Mn**	**Zn**	**Cu**	**Ni**	**Co**	**Cd**	**Pb**
BCR-414 Certified/Ref. Values [ng/mg ± 1 SD]		*2673 ± 96*	1850 ± 190	*126 ± 4*	*13400 ± 3200*	**8.1 ± 0.18**	**299 ± 13**	**111.6 ± 2.5**	**29.5 ± 1.3**	**18.8 ± 0.8**	1.43 ± 0.06	**0.383 ± 0.014**	**3.97 ± 0.19**
BCR-414 Recovery [Labile, ng/mg ± 1 SD]	***9***	**344 ± 116**	**333 ± 59.9**	**BDL**	**12363 ± 250**	**2.46 ± 0.28**	**253 ± 7.56**	**94.3 ± 7.76**	**22.8 ± 1.28**	**BDL**	**0.7 ± 0.06**	**0.25 ± 0.03**	**2.62 ± 0.27**
BCR-414 Recovery [Total, % ± 1 SD]	***9***	95.7 ± 7.4	91.1 ± 2.1	93.1 ± 7.1	89.1 ± 3.3	94.6 ± 15.2	84.8 ± 2.4	85.2 ± 7.1	74.1 ± 17.8	59.9 ± 6.0	82.0 ± 10.6	65.8 ± 6.6	73.5 ± 15.2
PACS-3 Certified/Ref. Values [ng/mg ± 1 SD]		**65800 ± 1200**	**41060 ± 640**	**4420 ± 180**	**937 ± 44**	**129 ± 8**	**432 ± 16**	**376 ± 12**	**326 ± 10**	**39.5 ± 2.2**	*12.1*	**2.23 ± 0.16**	**188 ± 7.4**
PACS-3 Recovery [Total, % ± 1 SD]	***3***	84.9 ± 1.8	84.6 ± 2.2	95.4 ± 4.4	112.1 ± 7.5	109.6 ± 1.3	96.7 ± 2.2	86.9 ± 1.3	90.4 ± 2.9	79.7 ± 5.3	*110.8 ± 2.1*	113.7 ± 11.6	95.6 ± 1.5

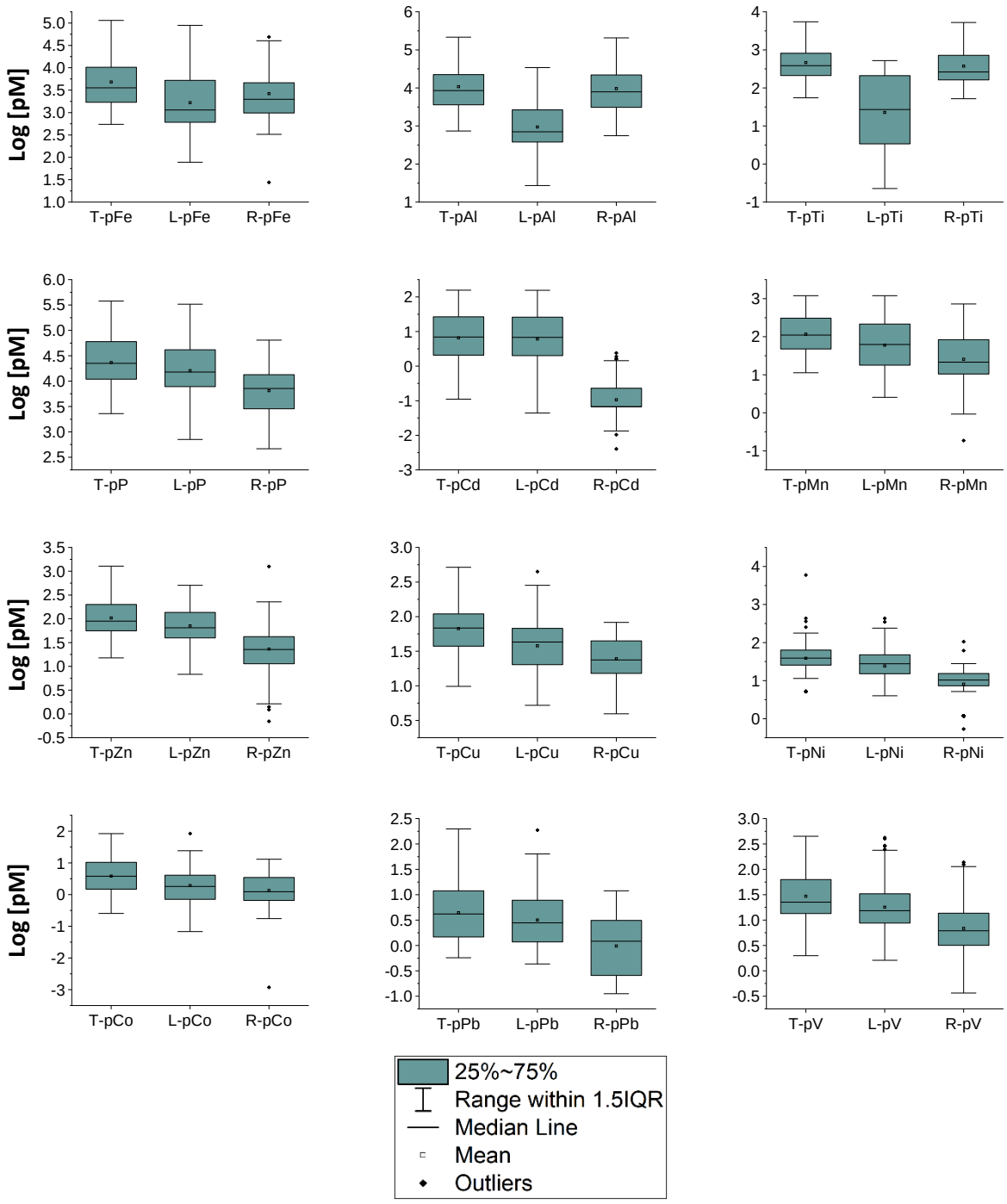

Figure S4.1 - The concentration ranges of Total (T-pTM), Labile (L-pTM) and Refractory (R-pTM) particulate trace metal fractions for samples from SO243.

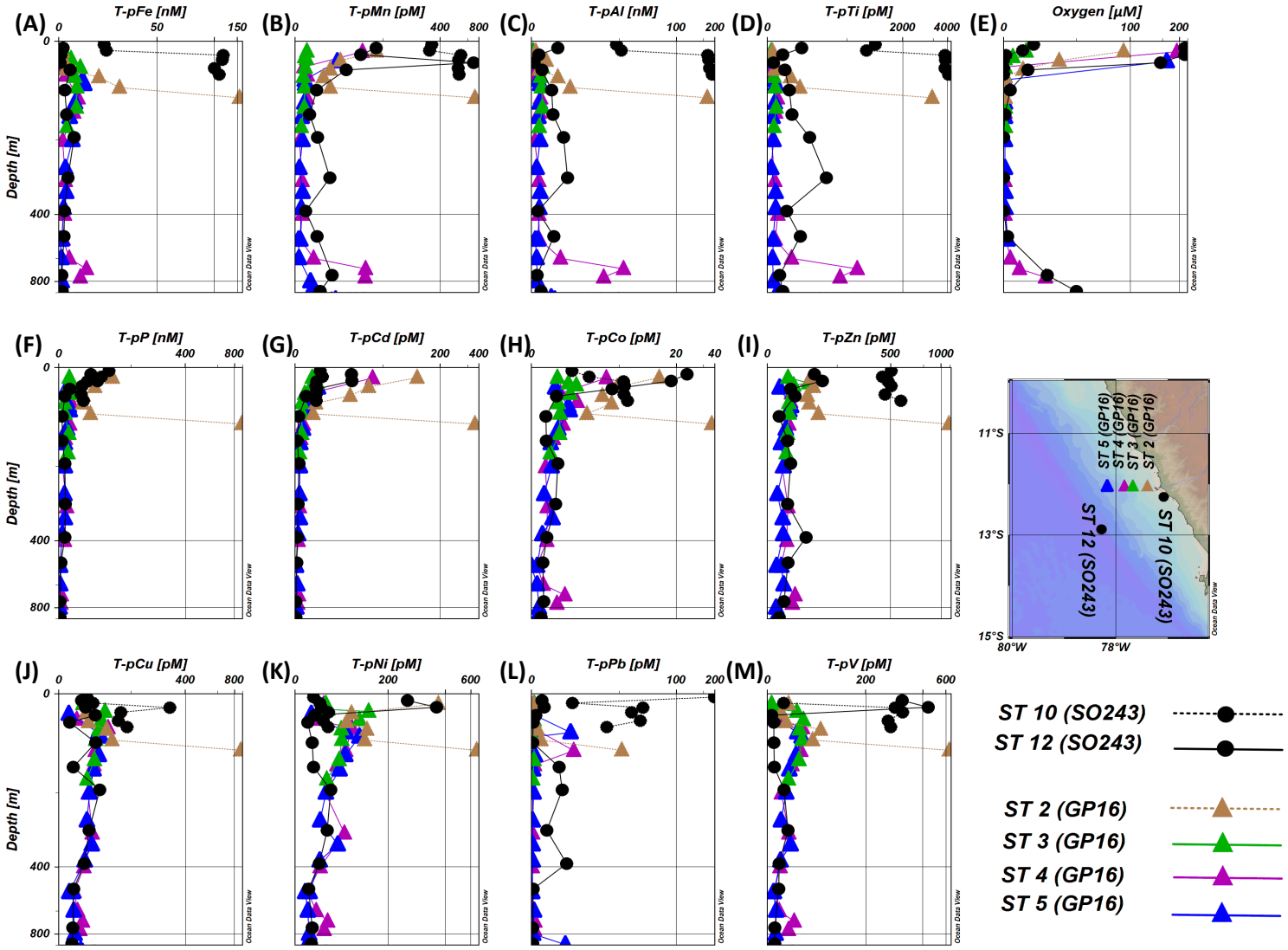

Figure S4.2 - Comparison of total particulate trace metal (T-pTM) concentrations of (A) Iron (Fe); (B) Manganese (Mn); (C) Aluminum (Al); (D) Titanium; (F) Phosphorus (P); (G) Cadmium (Cd); (H) Cobalt (Co); (I) Zinc (Zn); (J) Copper (Cu); (K) Nickel; (L) Lead (Pb); (M) Vanadium (V); and (E) dissolved oxygen concentrations for samples from nearby stations of SO243 (stations 10 and 12; circles) and GP16 (stations 2-5; triangles) (GEOTRACES IDP2021; Lee et al., 2018). Note the stretched depth and concentration scales.

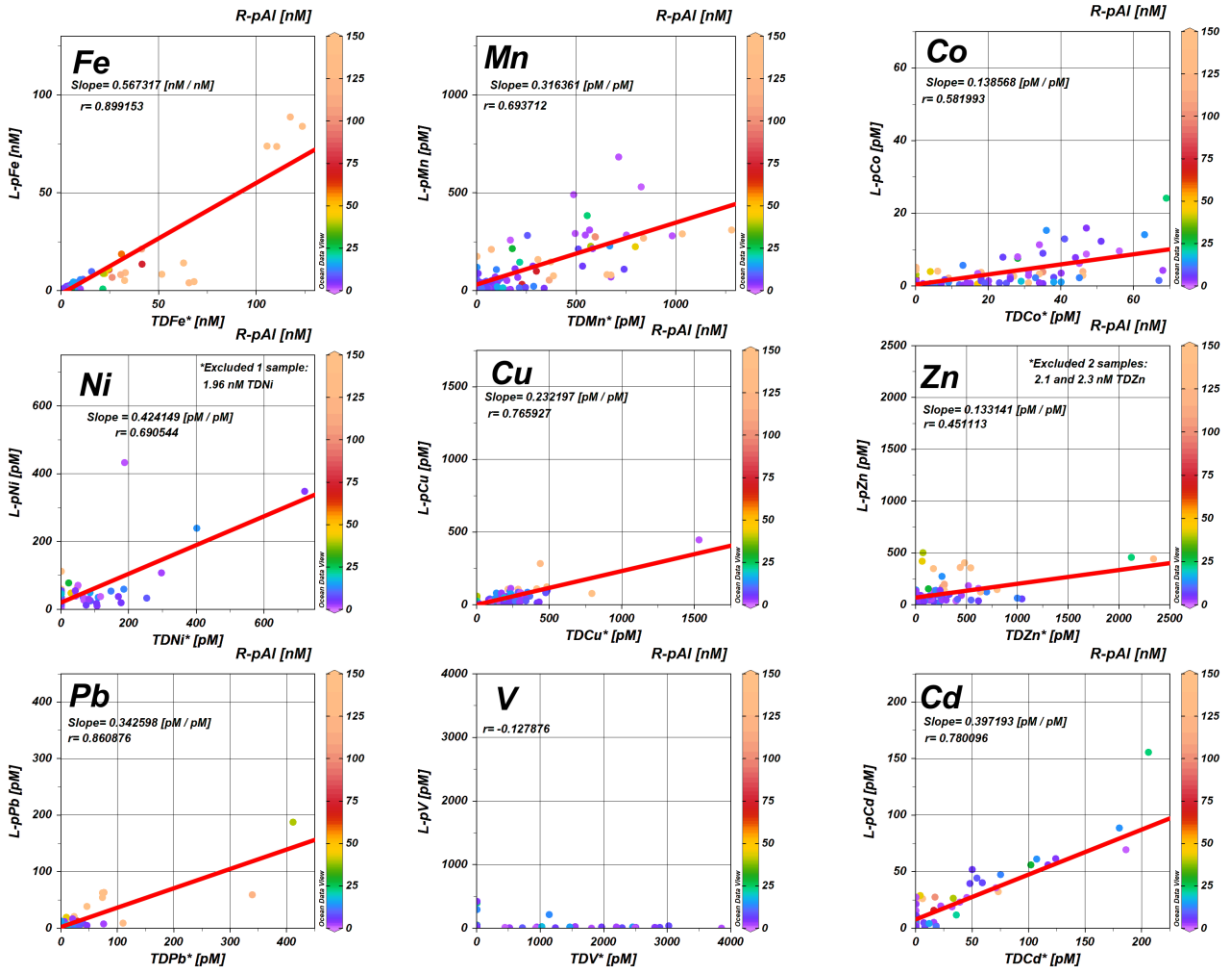

Figure S4.3 – Comparison of labile particulate trace metal (L-pTMs) and 'reactive-particulate' (TDTM*) concentrations as reported by Rapp et al., (2020). TDTM* concentrations shown were defined as the difference between unfiltered (total dissolvable) and filtered (dissolved) acidified seawater. Samples that yielded negative values are reported as "0" here. Refractory particulate aluminum (R-pAl) was plotted in the z-axis (color-scale) as a proxy for lithogenic particle concentrations.

Table S4.2 – Comparison of labile particulate fractions (% of total particulate) of samples from this study (SO243) compared to documented labile particulate fractions reported in other study sites using the same chemical leach application (Berger et al., 2008).

Sample Labile pTM fraction (%)	LpCd/TpCd [%]	LpPb/TpPb [%]	LpAl/TpAl [%]	LpP/TpP [%]	LpTi/TpTi [%]	LpMn/TpMn [%]	LpFe/TpFe [%]	LpCo/TpCo [%]	LpNi/TpNi [%]	LpCu/TpCu [%]	LpZn/TpZn [%]	L-pV/T-pV [%]	Remarks
SO243 (This study)	**96.0 - 100**	**64.0 - 83.5**	**5.4 - 14.2**	**64.0 - 77.3**	**0.7 - 5.1**	**35.5 - 84.2**	**20.3 - 52.8**	**40.7 - 73.8**	**63.1 - 81.4**	**48.8 - 68.6**	**67.2 - 87.3**	**63.1 - 82**	ETSP (Peruvian Shelf); Upper and Lower quartile ranges
(Al-Hashem et al., 2022)	94.9 - 99.9	77.2 - 95.2	6.7 - 25.1	21.1 - 55.8	0.1 - 1.5	89.2 - 96.8	15.9 - 29.9	45.5 - 71.7	49.8 - 68.1	41.3 - 64.5	75 - 93.9	-	South-East Atlantic Ocean (SW African Shelf) Upper and lower quartile values
(Twining et al., 2015)	> 70	-	< 20	~ 80	< 20	88 - 95	16 - 31	76 - 84	57 - 81	54 - 78	78 - 94	-	North Atlantic Ocean
(Milne et al., 2017)	-	-	-	-	-	-	13-52	-	-	-	-	-	North Atlantic Ocean; AVG= 24%
(Berger et al., 2008)	-	-	7 - 13	-	-	68 - 98	22-37	-	-	-	-	-	Columbia River Plume
(Twining et al., 2019)	-	79 ± 12	16.9±11.7	-	-	82 ± 2	29 ± 7	16.9 ± 11.7	-	-	75 ± 18	-	Indian Ocean
(Rauschenberg and Twining, 2015)	-	-	-	68 - 78	1 - 22	-	-	-	-	-	-	-	North Atlantic Ocean
(Little et al., 2018)							-			56 ± 11		-	South Atlantic Ocean
(Rusiecka et al., 2018)		78 ± 10					-					-	Northeast Atlantic Ocean

Table S4.3 - Bivariate Pearson's correlation matrix of Log-transformed dataset for (a) Total particulate trace metals (T-pTMs); and (b) Labile (L-pTM) and Refractory (R-pTM) particulate trace metals with ancillary measurements and indicators for the SO243 transects along the Peruvian shelf. Pearson correlation coefficient values (*r*) are shown in the white-cells, and the intensity of the colored boxes depict the strength of correlations with asterisks signifying different *p*-value thresholds, respectively. Samples with values below detection limit were excluded (pairwise) from the correlation matrix.

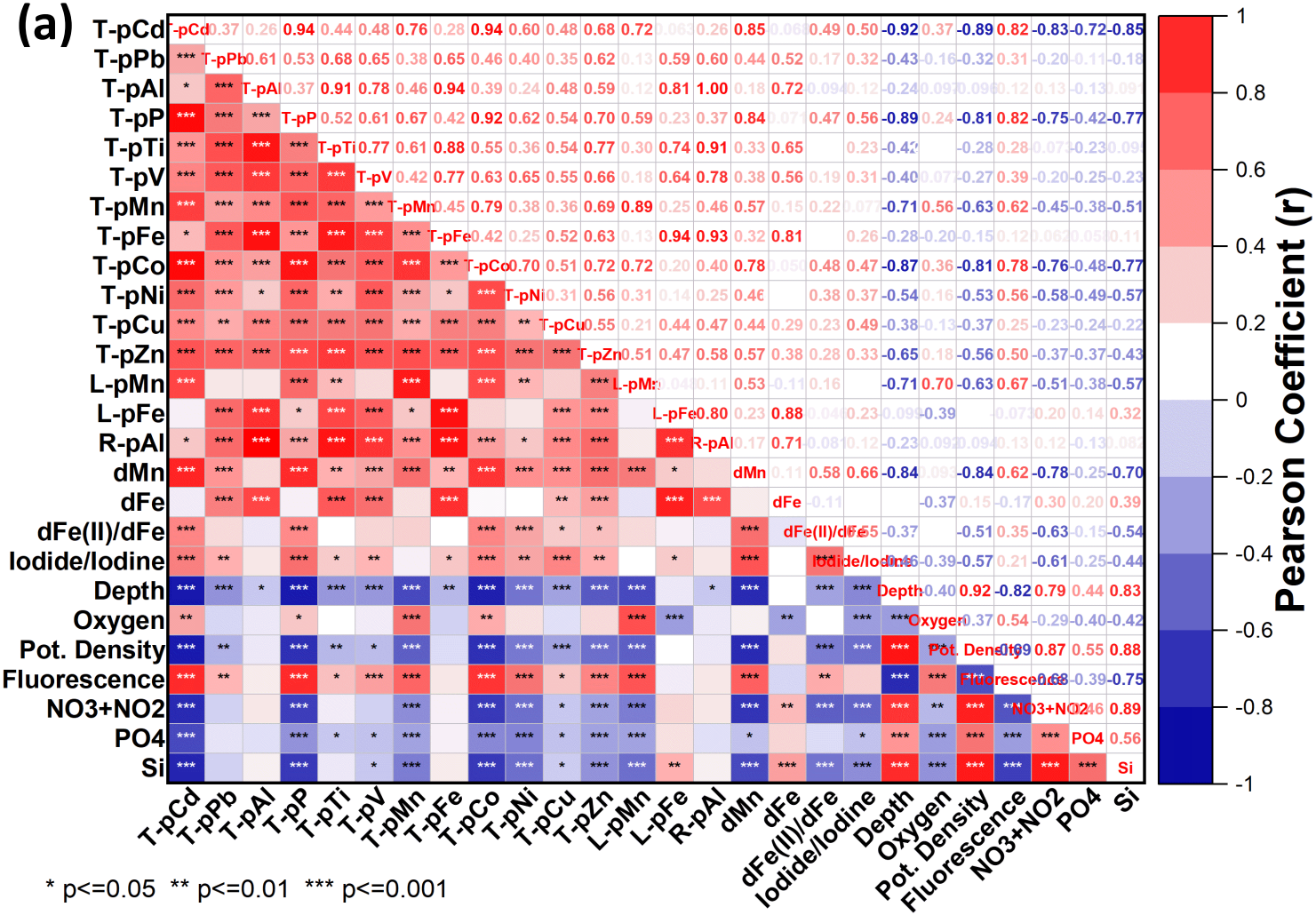

Table S4.3 *– (Continued)*

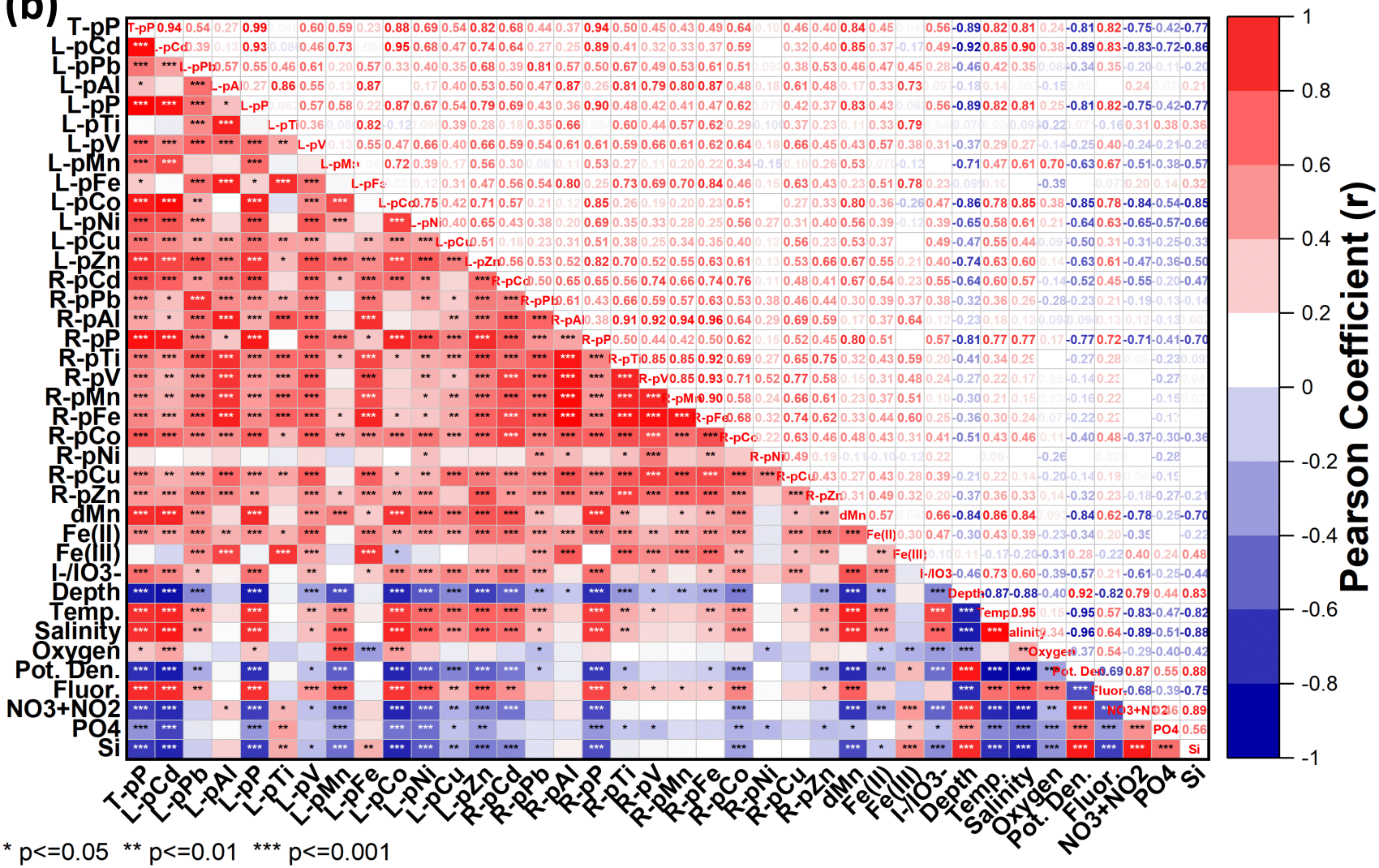

* p<=0.05 ** p<=0.01 *** p<=0.001

Figure S4.4 - Normality distributions of the entire Log transformed pTM dataset for all samples of the SO243 cruise (Top); and results of distribution fit parameter estimates (below) executed on OriginPro (Version 9.9.5).

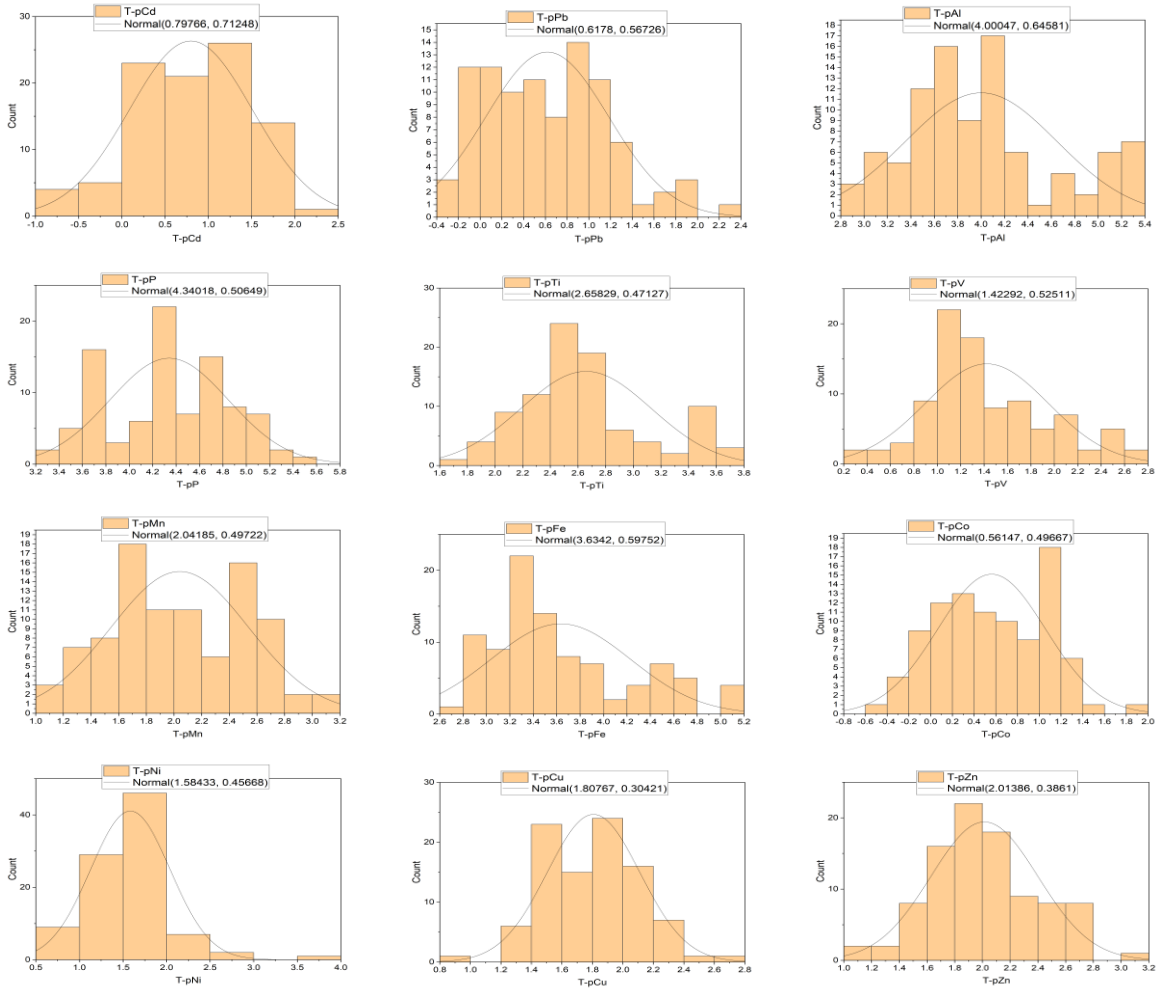

	Distribution	Parameter	Estimate	Lower 95%	Upper 95%
T-pCd	Normal	Location mu	0.79766	0.65362	0.94169
		Scale sigma	0.71248	0.61686	0.82291
T-pPb	Normal	Location mu	0.6178	0.50312	0.73247
		Scale sigma	0.56726	0.49113	0.65518
T-pAl	Normal	Location mu	4.00047	3.86992	4.13103
		Scale sigma	0.64581	0.55914	0.74591
T-pP	Normal	Location mu	4.34018	4.23779	4.44256
		Scale sigma	0.50649	0.43852	0.585
T-pTi	Normal	Location mu	2.65829	2.56302	2.75356
		Scale sigma	0.47127	0.40803	0.54432
T-pV	Normal	Location mu	1.42292	1.31677	1.52908
		Scale sigma	0.52511	0.45464	0.6065
T-pMn	Normal	Location mu	2.04185	1.94133	2.14236
		Scale sigma	0.49722	0.43049	0.57429
T-pFe	Normal	Location mu	3.6342	3.5134	3.75499
		Scale sigma	0.59752	0.51733	0.69013
T-pCo	Normal	Location mu	0.56147	0.46106	0.66187
		Scale sigma	0.49667	0.43002	0.57366
T-pNi	Normal	Location mu	1.58433	1.49201	1.67665
		Scale sigma	0.45668	0.3954	0.52747
T-pCu	Normal	Location mu	1.80767	1.74617	1.86917
		Scale sigma	0.30421	0.26339	0.35137
T-pZn	Normal	Location mu	2.01386	1.93581	2.09191
		Scale sigma	0.3861	0.33429	0.44594

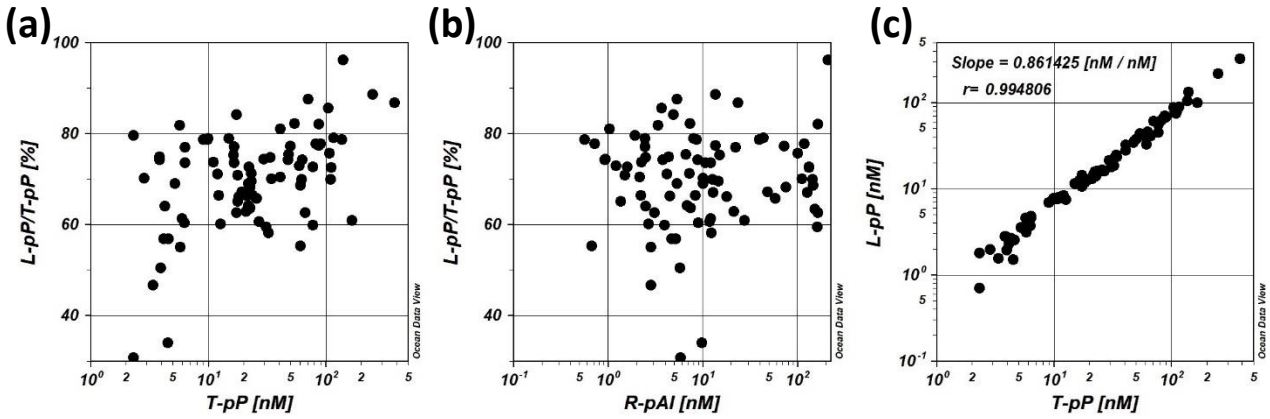

Figure S4.5- Scatterplots illustrating the variable chemical solubility of the biogenic indicator, particulate phosphorus (pP), in the top 50 m of all stations of the SO243 transects. No significant influences of particle loads on labile pP solubility (labile particulate phosphorus fraction) were evident with increasing particle indicator concentrations of (a) biogenic particles (T-pP), or (b) lithogenic particles (R-pAl). (c) Labile pP fractions of total pP remained consistent across all surface samples. Note the logarithmic scales on *x*-axis, and on *y*-axis of the plot in (c).

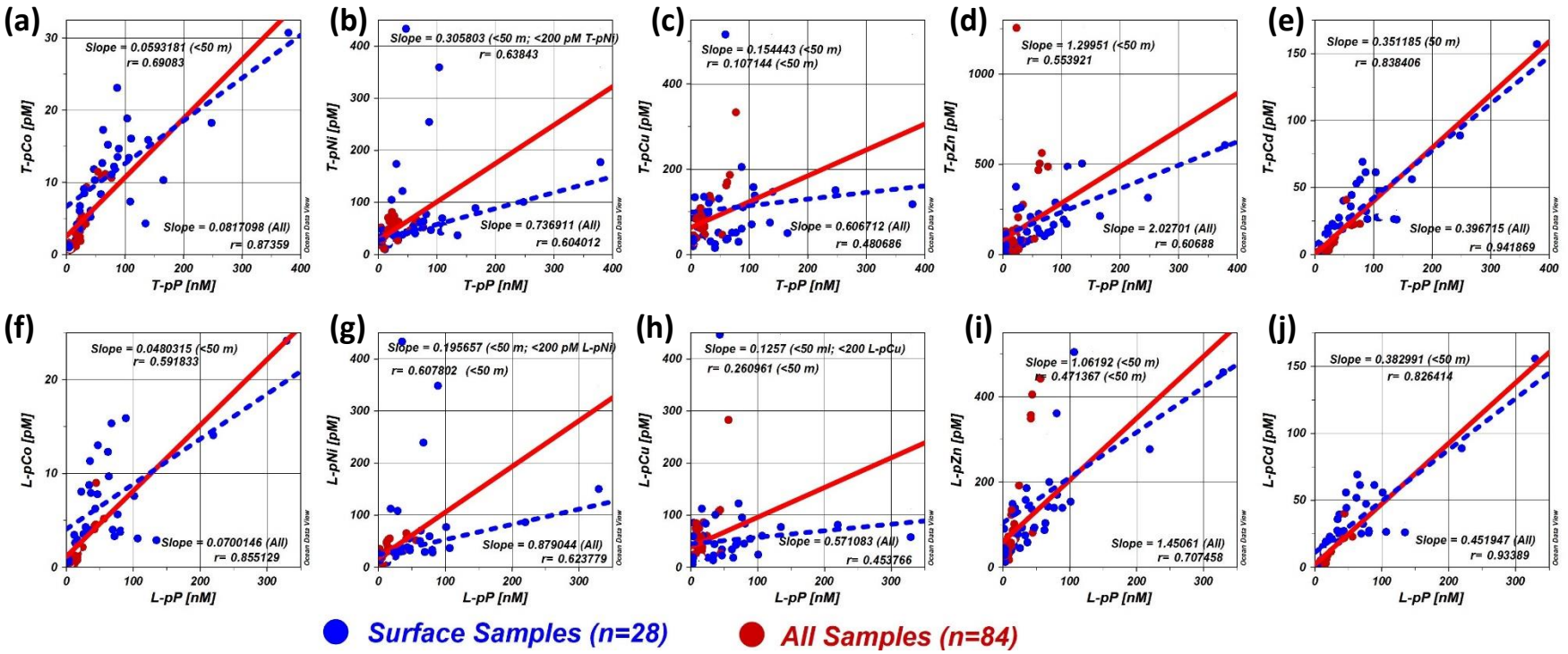

Figure S4.6 - Scatter plots showing the correlations of bio-essential T-pTMs:T-pP (Co, Ni Cu, Zn, and Cd) (a-e, respectively) and L-pTMs:L-pP (f-j, respectively). Blue dotted regression lines are of surface samples (<50 m) and red solid regression lines are of all SO243 samples.

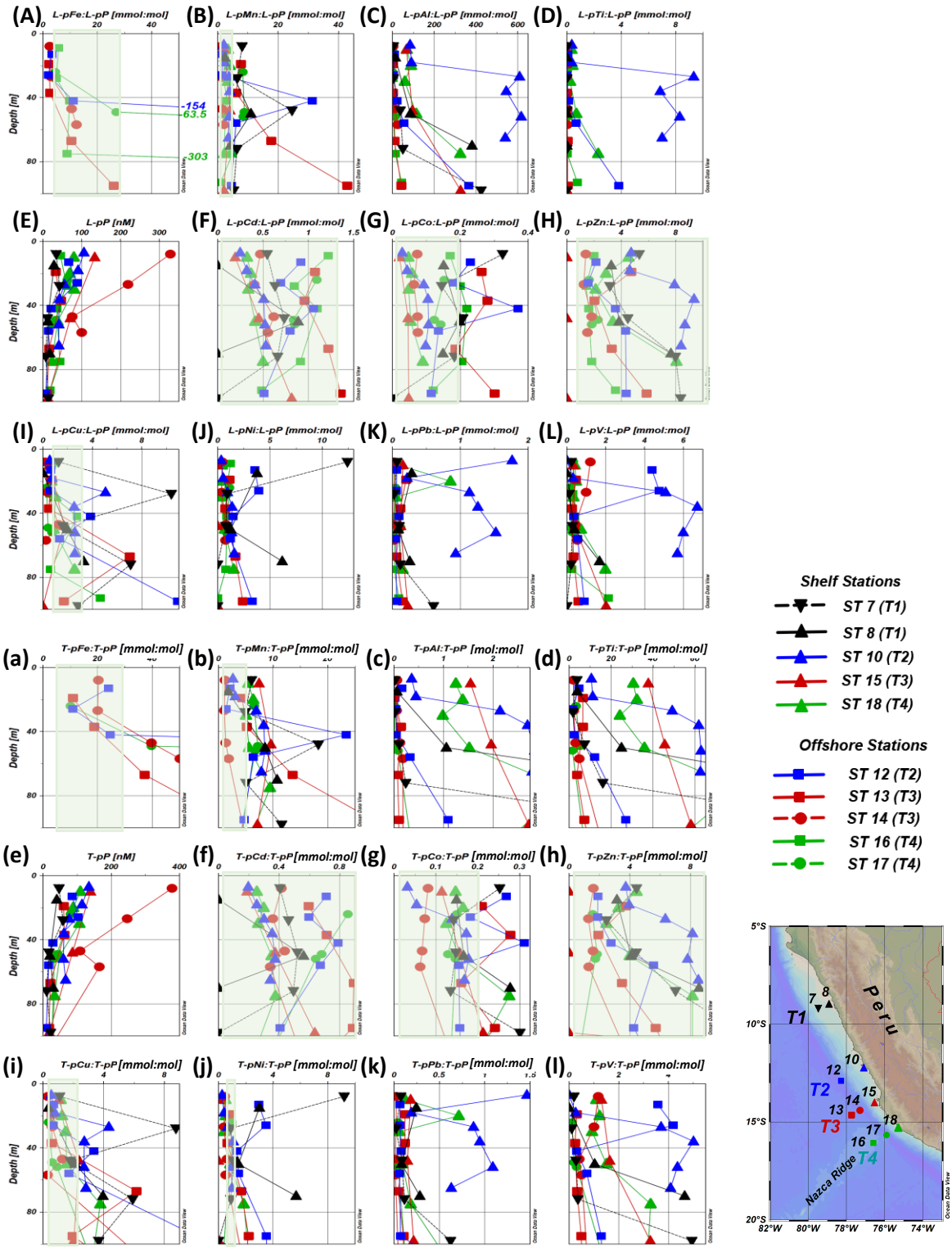

Figure S4.7 - Elemental ratios of labile particulate trace metals: labile particulate phosphorus (L-pTM:L-pP)(A-L), and total particulate trace metals (T-pTM): Total particulate phosphorus (P) (a-l) in the top 100 m of the water column across all SO243 stations. Green shaded areas within plots indicate minimum and maximum range value of reported plankton stoichiometries (summarized in Table 1), where values were available. Shelf stations were excluded from the pFe:pP plots, to enhance the resolution of lower values in offshore stations. Station (ST) and transect (T) symbols and colors are exactly as on Figure 2.

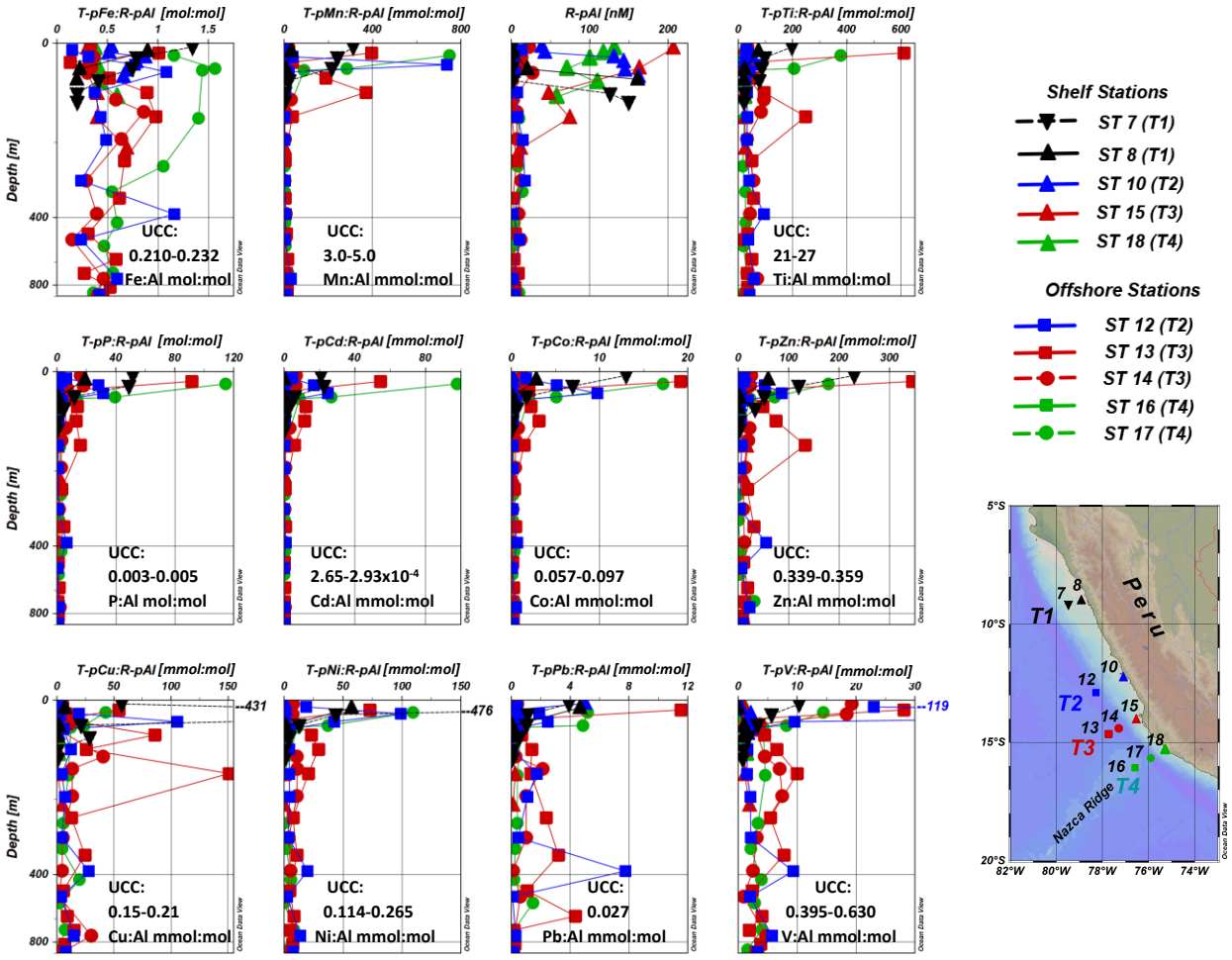

Figure S4.8 – Vertical distributions of the sample elemental ratios of total particulate trace metals (T-pTM) normalized to the lithogenic particle indicator, refractory particulate aluminum (R-pAl). Reference values ranges for canonical upper continental crust (UCC) values of each element (normalized to R-pAl) are shown within each respective plot, using the average values reported from Rudnick and Gao (2013) and Taylor and McLennan (1995).

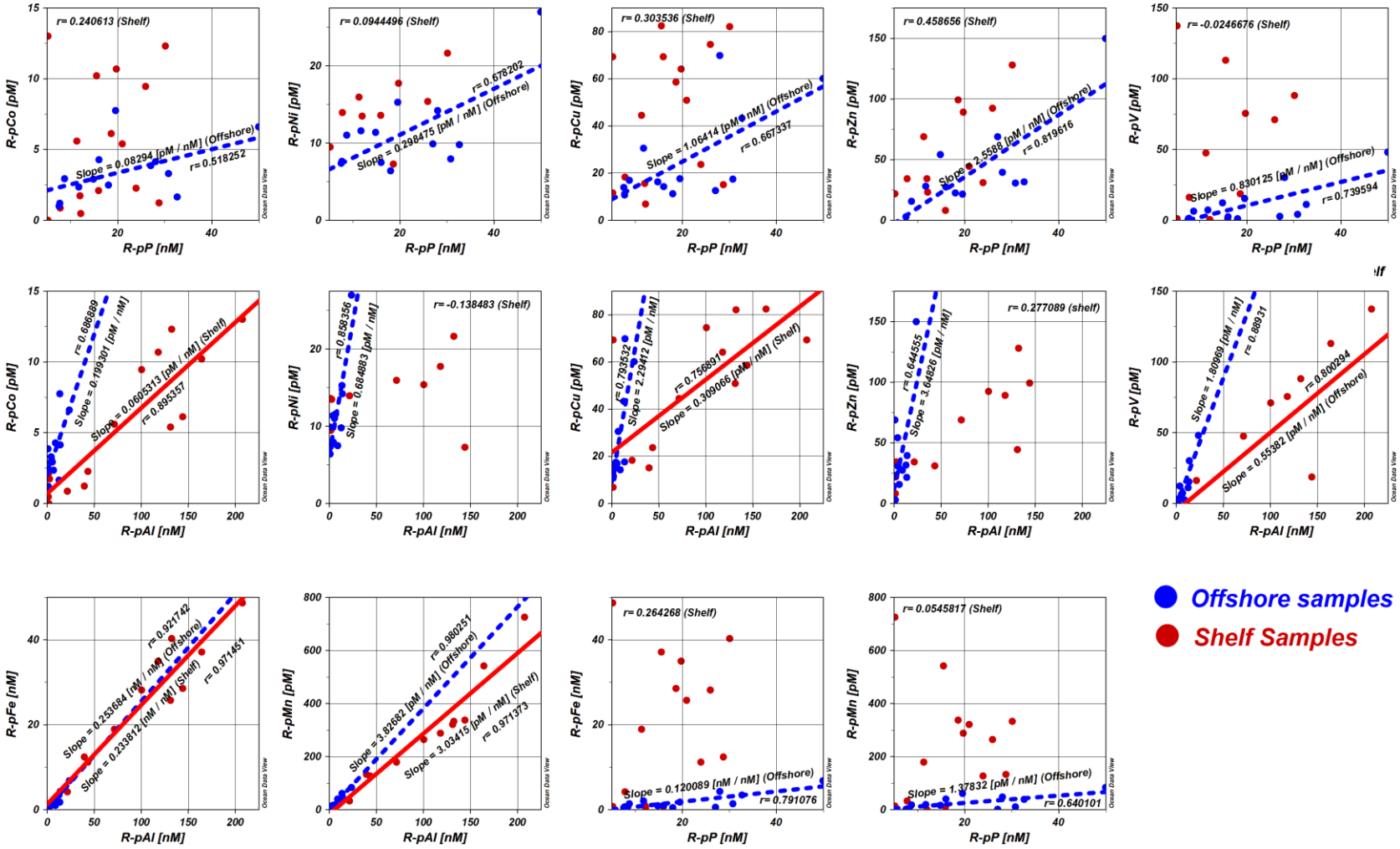

Figure S4.9 - Scatter plots showing the correlations between bio-essential refractory particulate trace metals compared against biogenic type element, refractory phosphorus (R-pP), and lithogenic particle indicator, refractory particulate aluminum (R-pAl) in surface samples (<50 m; *n*=28). Red solid regression lines are of shelf samples (<50 m), where most samples exhibited high lithogenic particle loads (>25 nM R-pAl; *n*=10 of 15 samples), and blue dotted regression lines are of offshore SO243 samples. Linear regressions lines were not drawn where *r*<0.5.

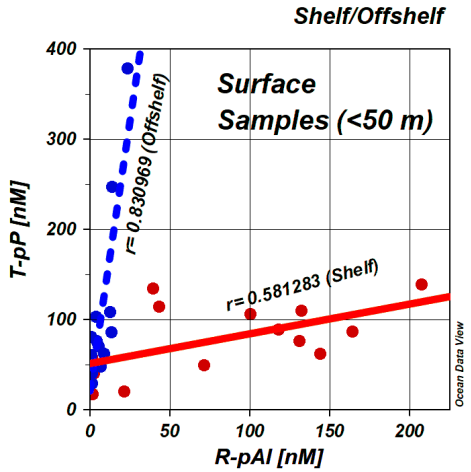

Figure S4.10 – Correlations between total particulate phosphorus (T-pP) and Refractory Particulate Aluminum (R-pAl) in surface samples (<50 m) from shelf stations (solid red regression line) and offshore stations (dotted blue regression line).

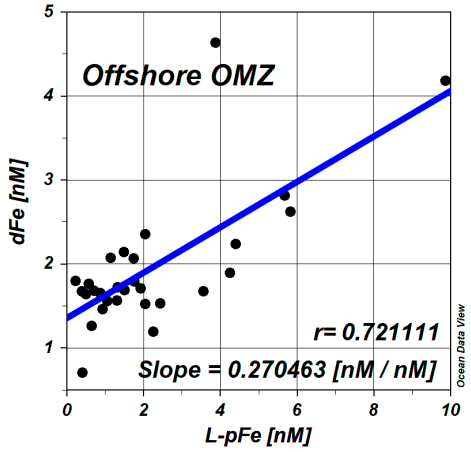

Figure S4.11 – Correlation between dissolved Fe (dFe) and labile particulate Fe (L-pFe) within the offshore oxygen minimum zone (<20 µM oxygen).

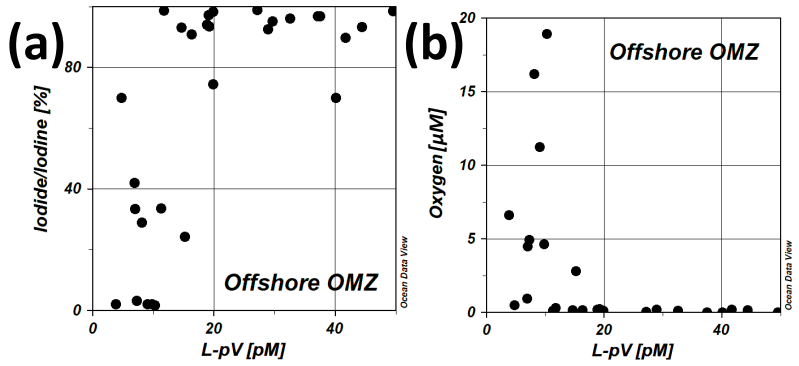

Figure S4.12 - Scatterplots illustrating the generally enhanced labile particulate vanadium (L-pV) as oxygen concentrations decreased (a) and reduced iodine fractions (I^-/IO_3^-) increased (b) in samples within the offshore oxygen minimum zone (<20 µM oxygen).

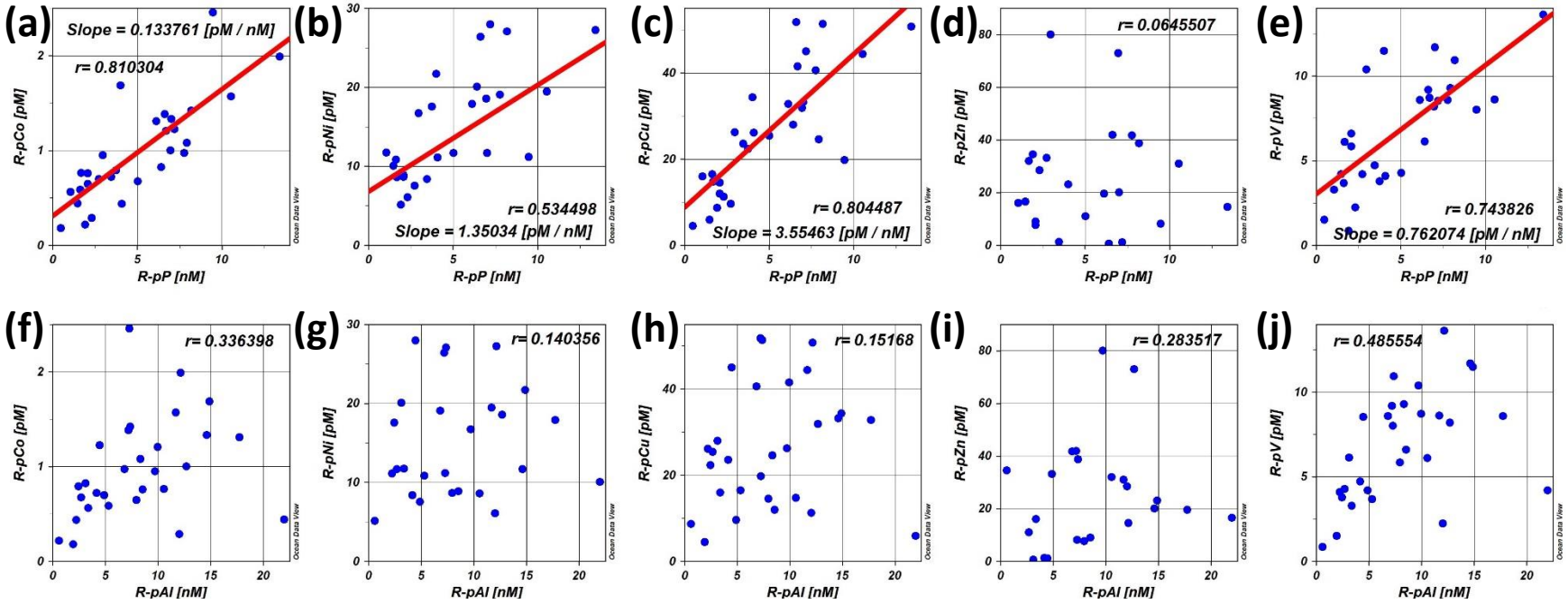

Figure S4.13 - Scatter plots showing the correlations between bio-essential refractory particulate trace metals compared against biogenic type element, refractory phosphorus (R-pP) (a-e), and lithogenic particle indicator, refractory particulate aluminum (R-pAl) (f-j) in the offshore oxygen minimum zone samples (<20 µM; *n*=29). Solid linear regression lines were drawn where *r*>0.5.

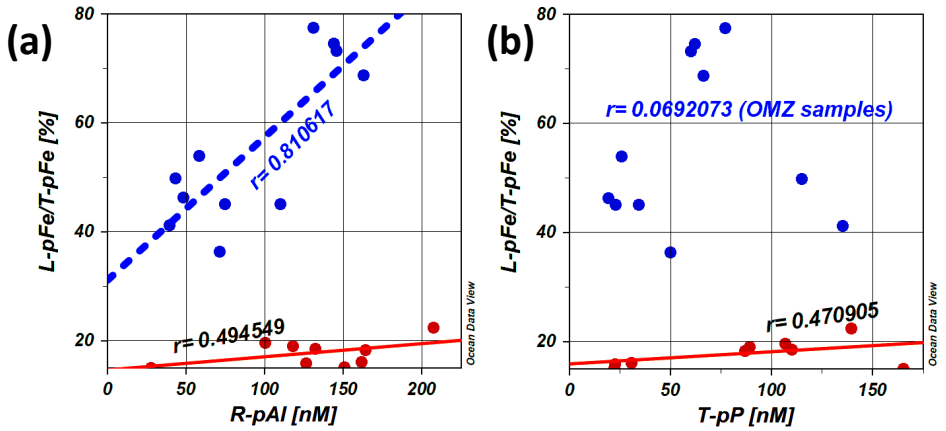

Figure S4.14 – Scatterplot of nepheloid particle samples illustrating enhanced labile particulate iron fractions (L-pFe/T-pFe, %) within oxygen minimum zone samples (≤20 µM oxygen; blue sample points) compared to non-OMZ (>20 µM oxygen; red sample points). Particle concentrations were implied using concentrations of the (a) lithogenic and (b) biogenic particle proxies, refractory particulate aluminum (R-pAl) and total particulate phosphorus (T-pP), respectively. Linear regression lines were drawn to show the strength of the correlations within OMZ samples (dotted blue line) and non-OMZ sample (solid red line).

Chapter 5: Distributions of Labile and Refractory Particulate Biogeochemical Tracers (V, Mo, W, Cr, Ba, Th, and U) on the Southwest African Shelf

Ali A. Al-Hashem[1,2*], Aaron J. Beck[1], Stephan Krisch[1,3], Te Liu[1], Tim Steffens[1], Mark J. Hopwood[1,4], Eric P. Achterberg[1,2].

[1]Marine Biogeochemistry Division, GEOMAR Helmholtz Centre for Ocean Research Kiel, Kiel 24148, Germany.

[2]Christian-Albrechts-University of Kiel, Christian-Albrechts-Platz 4 24118 Kiel, Germany.

[3]Now at: Bundesanstalt für Gewässerkunde, Am Mainzer Tor 1, 56068 Koblenz, Germany.

[4]Now at: Southern University of Science and Technology, Shenzhen, China.

The research presented in this chapter has been submitted to *Biogeochemistry.*

Abstract

The distributions of vanadium (V), molybdenum (Mo), tungsten (W), chromium (Cr), uranium (U), thorium (Th), and barium (Ba) in the ocean are understudied with only few published datasets. The mechanisms driving their distributions are not yet fully understood, particularly with respect to their particulate fractions. Here we present the labile (hereafter L-pTM) and refractory (hereafter R-pTM) particulate distributions of V, Mo, W, Cr, U, Th, and Ba along the southwest African shelf and a 3°S longitudinal transect of the GEOTRACES GA08 section cruise. The cruise traversed several contrasting biogeochemical environments with different particle sources. The average total particulate concentrations decreased in the order (average; upper and lower quartile range values in brackets): Ba (373 pM; 180-434 pM) > Cr (147 pM; 44.7-136 pM) > V (72.6 pM, 9.1-45 pM) > Mo (7.3 pM; 1.59-8.15 pM) > W (1.4 pM; 0.48-1.54 pM) > U (1.0 pM; 0.17-0.89 pM) > Th (1.2 pM; 0.08-0.57 pM). Average labile particulate fractions (L-pTM/T-pTM x 100), in descending order, were 62±19% for Ba, 58±22% for V, 54±20% for U, 33±19% for Mo, 30±21% Cr, 6.7±14% for W, and 3.7±9.8% for Th. Uranium and Mo were associated with biogenic particles over the productive Benguela shelf, with limited labile fractions of only 7% and 5%, respectively, corresponding to refractory biogenic particles, implying that particles from the water column served as significant sources of refractory pU and pMo to the underlying sediment inventory. pTh and pW mostly comprised refractory pTM phases (>90%) and were primarily associated with lithogenic particles. Some evidence for Cr, Mo, and V adsorption was evident, likely onto Fe and Mn oxides, with an apparently slight preferential affinity of Mo for adsorption onto Mn oxides and V and Cr onto Fe oxides. Biogenic particles are also likely to have comprised a significant fraction of the pV and pMo pools, particularly in surface waters. The adsorbed pCr fraction appeared driven by supply of reduced Cr, with sedimentary and the Congo River as important sources in the Angola Basin. Some evidence for barite precipitation within low oxygen mesopelagic waters (~80-1100 m) was apparent. Barite also comprised more refractory phases in the open ocean transect (51.3± 16.5% R-pBa/T-pBa), compared to shelf-adjacent deep stations (29.4±11.9%), which may be due to the presence of more chemically resistant, crystalline barite phases.

5.1 Introduction

Trace metal (TM) distributions in the ocean are governed by a variety of often interrelated biogeochemical processes, including bio-assimilation and remineralization, (dis-)aggregation, reversible-adsorption (also referred to as scavenging) onto particle surfaces, and (non-)reductive dissolution and authigenic precipitation (Anderson, 2020; Boyd et al., 2017; Close et al., 2021; Jeandel et al., 2015; Jeandel & Oelkers, 2015; Lam & Anderson, 2018). These processes often lead to transformations between operationally defined solid and dissolved TM phases and imprint upon bulk particle compositions. Marine particles determine the fate of TMs in the ocean by acting as vertical transport vectors before ultimately settling on the seafloor and becoming incorporated into sediment. The imprinting of biogeochemical processes on sinking particle and sediment composition may allow for their adoption as proxies in order to understand modern ocean processes, or to reconstruct past (paleo-)oceanographic conditions which may provide insight concerning the future state of the ocean in climatically sensitive regions. Whilst the elements vanadium (V), molybdenum (Mo), tungsten (W), chromium (Cr), uranium (U), thorium (Th), and barium (Ba) are all of some interest as tracers of biogeochemical conditions in the ocean, there is a paucity of data on their particulate distributions and their biogeochemical cycles are not fully understood (e.g., Ho et al., 2018; Horner et al., 2021; Kurzweil et al., 2021; Nasemann et al., 2020; Rahman et al., 2022).

In oxygenated seawater, dissolved vanadium (HVO_4^{2-} and $H_2VO_4^-$), molybdenum (MoO_4^{2-}), chromium (CrO_4^{2-}), tungsten (WO_4^{2-}), and uranium ($UO_2(CO_3)_3^{4-}$) exist predominantly as oxyanions (e.g., Bruland et al., 2014; Tribovillard et al., 2006 and references within). Under reducing conditions, such as in sub-oxic, anoxic, and/or sulfidic environments, the solubility of these TMs decreases as they are reduced into more particle-reactive species and are subsequently adsorbed onto particle surfaces, such as (i.e., iron [Fe] and manganese [Mn] oxides, lithogenic, biominerals and/or organic particles) with variable affinities, or fixed as sulfides (Tribovillard et al., 2006, 2012, and references therein). Thorium ($Th(OH)_4^0$) has only one stable oxidation state, Th(IV), under all naturally occurring redox conditions in seawater and is known to readily adsorb onto particle surfaces (Anderson et al., 1983; Lerner et al., 2017; Santschi et al., 2006) which makes it a useful tracer of vertical particle fluxes (e.g., Marchal & Lam, 2012). Barium

forms a divalent cation (Ba^{2+}) and its dissolved pool in seawater is mainly controlled by barite ($BaSO_4$) precipitation involving microbial oxidation of sinking organic matter (Bishop, 1988; Chow & Goldberg, 1960; Dehairs et al., 1980) which may be mediated by 'active' biological or 'passive' chemical precipitation (e.g., Gonzalez-Muñoz et al., 2012; Horner et al., 2021; Monnin et al., 1999; Rushdi et al., 2000 and references therein). Preferential affinity for Mo and W onto Mn oxides is reported (e.g., Bertine & Turekian, 1973; Horner et al., 2021; Kunzendorf & Glasby, 1992; Scott & Lyons, 2012), although adsorption onto Fe oxides is also possible (e.g., Ho et al., 2018). Mo is also known to form insoluble sulfides (i.e., thiomolybdates) under euxinic conditions (Erickson & Helz, 2000; Ho et al., 2018; Johannesson et al., 2013; Mohajerin et al., 2014, 2016), and U is fixed in the sediment following reduction by sulphate and Fe reducing bacteria (Tribovillard et al., 2006).

Several TMs serve metabolic functions and are required to varying degrees by some or all organisms (e.g., Frausto da Silva & Williams, 2001; Sunda, 2012; Twining et al., 2014; Twining & Baines, 2013). These bio-essential elements are thus incorporated into biogenic particles formed in the ocean surface mixed layer. V and Mo are known to serve biological functions in phytoplankton, such as in the enzymes nitrogenase (V and Mo), V-haloperoxidase, and nitrate reductase (Mo) (Glass et al., 2012; Hill & Manley, 2009; Johnson et al., 2011; Nuester et al., 2012; Tovar-Sanchez & Sañudo-Wilhelmy, 2011). Tungsten has been suggested to serve biological functions in enzymes (Andreesen & Makdessi, 2008; Hille, 2002; Kletzin & Adams, 1996; Lindh, 2013), and has been reported to substitute Mo in some cases (Garner & Stewart, 2002; Maia et al., 2016). Chromium (VI) can be toxic (Wong & Trevors, 1988) and is particle inert, although when reduced to Cr(III) it can readily adsorb onto particle surfaces, including mineral and organic particle phases (Achterberg & van den Berg, 1997; Cranston & Murray, 1978; Elderfield, 1970; Goring-Harford et al., 2018; Janssen et al., 2021; Nasemann et al., 2020; Semeniuk et al., 2016). Barium is strongly correlated with silicic acid concentrations in the ocean (Chan et al., 1977) but has no known biological functions in major primary producers, although intracellular precipitation of $BaSO_4$ (possibly for gravitropism) is reported for some organisms which are not abundant in seawater (Finlay et al., 1983; Gooday & Nott, 1982). Importantly, barite ($BaSO_4$) precipitation is widely suggested to occur within microenvironments of sinking organic-rich bio-

aggregated particles in the upper few hundred meters of the water column (e.g., Bishop, 1988; Chow & Goldberg, 1960; Dehairs et al., 1980, 2008; Martinez-Ruiz et al., 2019; Rahman et al., 2022) and its formation is enhanced under sub-oxic conditions (e.g., Dehairs et al., 1990). The close association between pBa (i.e., barite) precipitation with pBa sedimentation and export production (e.g., Bishop, 1988; Eagle et al., 2003), has allowed sedimentary Ba content to serve as a potential tracer of primary productivity and export production (e.g., Collier & Edmond, 1984; Dehairs et al., 1980; Eagle et al., 2003; McManus et al., 1998; Paytan & Griffith, 2007; Schoepfer et al., 2015; Thomas et al., 2011).

Particulate non-lithogenic uranium has been associated with organic matter, possibly through extracellular adsorption or incorporation into biogenic particles (Anderson, Fleisher, et al., 1989; Anderson, Lehuray, et al., 1989; McManus et al., 2006; Zheng et al., 2002). Anderson (1982) described particulate non-lithogenic uranium as 'bioauthigenic', i.e, involving either biogenic and/or an authigenic origin. The association between pU and biogenic particles appears to be stronger where sinking organic matter rates increase, and under sub-oxic conditions (e.g., McManus et al., 2005, 2006; Zheng et al., 2002), which are generally also associated with high productivity environments. This has allowed sedimentary pU to be used as a proxy for surface productivity (e.g. Anderson, Lehuray, et al., 1989; Kumar et al., 1995; McManus et al., 2006; Zheng et al., 2002). Notably though, some studies have suggested that authigenic U accumulation in sediments is primarily controlled by bottom water oxygen concentrations (Abshire et al., 2022; Francois et al., 1993; Hayes et al., 2014), making pU a potential redox (paleo-)proxy.

Although the foundations of these TMs' dissolved oceanic distributions have been sufficiently well demonstrated by prior research to facilitate a general understanding of their typical depth profiles in the Pacific and Atlantic, there are still a range of unresolved issues and pTM datasets are relatively sparse. Understanding the pTM cycling dynamics of V, Mo, W, Cr, Ba, Th, and U may help better interpret paleo-environmental records relying on these elements as modern ocean processes. To help disentangle the processes influencing the cycling, inventories, and fate of these particulate elements in the marine environment, distinguishing between labile (L-pTM) and refractory (R-pTM) particulate fractions is a powerful tool. Refractory pTM phases, which are more likely to persist through the water column and become incorporated into

sediments, are separated from comparatively labile pTM phases, which are more susceptible to solid-solution exchanges in the water column, or following deposition on the seafloor. We measured labile and refractory pTM concentrations for V, Mo, W, Cr, Ba, U, and Th using a widely adopted chemical leach (Berger et al., 2008) on marine particle samples collected along an extensive continental shelf transect that traversed several biogeochemical environments with different particle sources.

5.2 Methods and Materials

5.2.1 Study Site

Samples were collected from a total of 29 stations (*n*=318; total samples) during the GA08 GEOTRACES section cruise conducted in the austral summer of 2015 (November 22nd – December 27th) on *RV Meteor* along the southwest African coast, northward from 28.8˚S to 3˚S and westward along 3˚S from 9.8°E on the shelf to the 0° Meridian (Figure 5.1). The seafloor depths ranged from 53 to 4501 m, reflecting the occupation of shelf and off-shelf stations, with Benguela (shelf) stations generally shallower than stations positioned north of Walvis Ridge (Figure 5.1). The regional water circulation is described in greater detail by Al-Hashem et al. (2022), including the main water masses that were intersected along the transect.

Briefly, the cruise track traversed several key oceanographic features along the shelf, including the Benguela Upwelling System (BUS) (stations (ST) 43-51 and 1-4; between 18.6˚S – 28.8˚S) and the associated oxygen minimum zone (OMZ) which reached oxygen depleted conditions (<4 µM oxygen), as well as the Congo River outflow (ST 13-15; at 6.2˚S). A less intense OMZ at northern stations (ST 7-24) was present at depths of between ~50-600 m, with a minimum oxygen concentration of 20.5 µM. The Benguela (Namibian) shelf is widely reported to consist of anoxic and sulfidic sediment (Borchers et al., 2005; Inthorn et al., 2006), and phosphorite deposits are also documented, extending to Walvis Ridge (Compton & Bergh, 2016). The nearby Namib Desert is a significant source of terrestrial dust to the shelf region (Jickells, 2005; Prospero, 1996) and the Congo River plume leads to elevated concentrations of dissolved and trace elements up to ~1000 km off-shelf (Vieira et al., 2020). Continuous rain showers

generally occur during October and December across the shelf of NORTH region, possibly supplying TMs to the sea by wet depositions (Alsdorf et al., 2016).

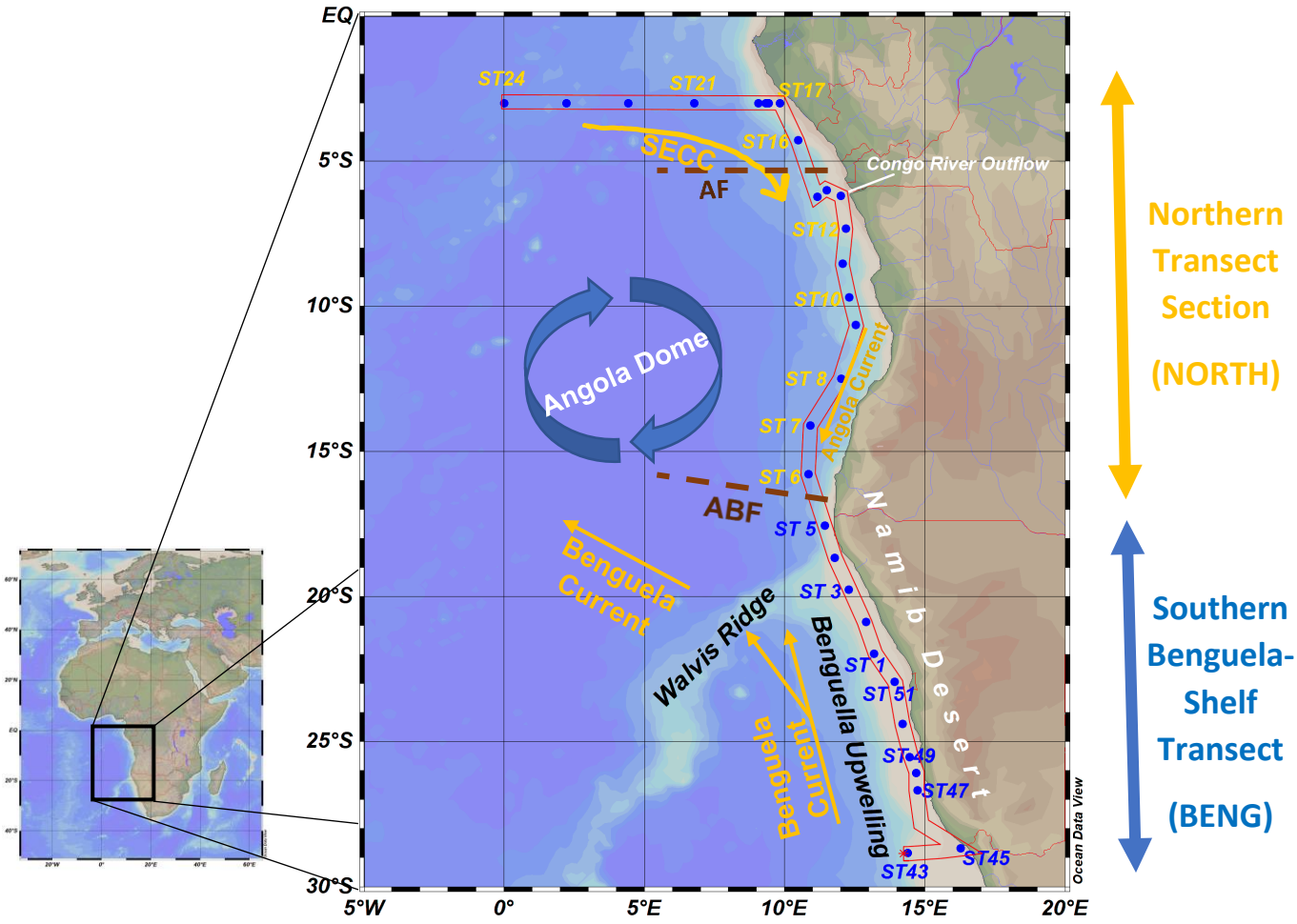

Figure 5.1. Map showing the oceanographic features that influence the Benguela ecosystem and Angola Basin, and circulation patterns that were part of the GA08 (M121) cruise track. Stations labeled in blue indicate the shallower stations within the Benguela region (BENG), and stations labeled in yellow indicate the Northern region stations (NORTH). ABF = Angola-Benguela Front; AF = Angola Front; SECC = South Equatorial Counter Current. Figure illustrations adapted from (Shannon, 2001).

5.2.2 Sample Collection and Analysis

Sample collection and analytical techniques were described in detail by Al-Hashem et al. (2022). Briefly, full water-column samples were collected following GEOTRACES protocols (Cutter et al., 2010) using Go-Flo bottles (12 Liter; Ocean Test Equipment) mounted on a dedicated GEOTRACES trace metal clean CTD rosette (Seabird). All samples were processed in a containerized clean-room while at sea immediately following each cast. Marine particle samples were collected on acid pre-cleaned polyethersulfone (PES) membrane filters (0.2 µm pore-size; 25 mm diameter, Sartorius) following the filtration of an average of 4 liters of seawater. To reduce salt from residual seawater, filters were gently misted with ultra-pure water (Milli-Q, Millipore) following filtration, and then stored frozen (-20°C) until analysis.

Labile and refractory particulate trace metals (L-pTMs and R-pTMs, respectively) were determined from each of the sample filters in series using a sequential leach-digestion procedure using modified protocols adopted from Berger et al. (2008) and Cullen and Sherrell (1999), as described in greater detail in Al-Hashem et al. (2022). The chemical leach was developed to solubilize readily reducible Fe and Mn oxides, adsorbed (scavenged), and intracellular biogenic pTMs, leaving lithogenic particle phases largely intact in the refractory phase (Berger et al., 2008; Rauschenberg & Twining, 2015). However, the inclusion of a variable fraction of refractory biogenic particles in the R-pTM pool is also possible (Al-Hashem et al., 2022).

Briefly, the samples were processed in perfluoroalkoxy (PFA) digestion vessels (Savillex) by leaching in a solution of weak acid (25% acetic acid, Optima grade, Fisher Scientific) and mild reducing agent (0.02 M hydroxylamine hydrochloride, Sigma TM grade) for a total leach time of 2 hours, including an initial 10 minute heating step (90-95°C). The leached particulate fraction was sub-sampled and processed separate from refractory particulate fraction, and subsequently dried-down. The remaining residual (refractory) particles on the filters were digested by adhering the sample filters to the inner-wall of the digestion vessels and refluxed with a strong acid mixture (50% HNO_3/10% HF v/v %; Optima grade, Fisher Scientific) at 150˚C for 15 hours, and subsequently dried-down. An internal rhenium standard (Inorganic Ventures) was added to the strong acid digestion solution to monitor sample loss. Following the respective dry-down steps,

0.5-1 ml of an oxidizing reagent solution (50% HNO_3/15% H_2O_2 (v/v%) was added before a second dry-down step, and the final residual drops (< 50 µL) were re-dissolved using 1 M nitric acid solution, with an indium spike (Inorganic Ventures) used as an analytical drift monitor. Samples were stored in acid pre-cleaned polypropylene tubes (15 ml - MetalFree™, Labcon) and analyzed using a high resolution inductively coupled mass spectrometer (HR-ICP-MS; Element XR, ThermoFisher) and quantified using external multi-element calibration with standards (Inorganic Ventures) prepared in a sample-matched matrix (Cullen et al., 2001). Particulate Th and U concentrations reported are for Thorium-232 and Uranium-238.

The consistency and quality of the leach-digestion procedure between digestion batches (*n*=13) was monitored using at least two replicates of a plankton certified reference material (BCR-414) processed alongside the particulate samples in each digestion batch. The efficacy of the refractory digestion on the lithogenic matrix was tested by carrying out the refractory digestion steps on sediment reference material (PACS-3), without the chemical leach. A summary of the procedural blank values, limits of detection, and reference material recoveries are included in Table S5.1.

Statistical analysis (bivariate Pearson's correlations and principal component analysis) was carried out on log-transformed pTM datasets using OriginPro 2022b (Version 9.9.5), and a Microsoft Excel statistical analysis add-in software (Analyse-it® for Microsoft Excel, Version 5.92), respectively. The Log-transformed pTM dataset showed normal distributions (Figure S5.1). Water column sections, station profiles, and scatterplots were prepared using Ocean Data View (Schlitzer, 2019).

5.3 Results and Discussions

We adopt the same regional definitions as previously used by Al-Hashem et al. (2022) to describe the pTM distributions for the stations across the shelf between the Benguela (BENG; ST 43-51 & 1-5) and northern non-upwelling (NORTH; ST 6-24) stations. The hydrographic parameters (oxygen, fluorescence, and macronutrients), including main water masses along the transect have been described in detail by Al-Hashem et al. (2022) (Chapter 3.3.1).

5.3.1 Particulate Trace Metal Distribution Patterns

Total pTM (T-pTM) concentrations varied over orders of magnitude between elements, ranging from 10^{-2} to 10^{4} pM (Total samples *n*=318), with average T-pTM concentrations decreasing in the order of Ba > Cr > V > Mo > W > U > Th (Figure S5.2). The highest T-pTM concentrations for Ba (5.48 nM), V (5.01 nM), Cr (5.07 nM), U (22.1 pM), and Th (92.1 pM) were all measured in bottom water samples at station 45, where R-pAl was also highest (up to 4.96 µM R-pAl) (Figure 5.2). T-pMo (124 pM) and T-pW (29.3 pM) were highest at station 9 (at 29 m depth) and station 3 (at 69 m depth), respectively. The upper and lower quartile concentration ranges of T-pV (9.1-45 pM), T-pMo (1.59-8.15 pM), T-pCr (44.7-136 pM), T-pBa (180-434 pM), T-pW (0.48-1.54 pM), T-pU (0.17-0.89 pM), and T-pTh (0.08-0.57 pM) for all samples (and also for shelf stations), were comparable to ranges that were reported in other shelf and slope regions (bottom depth <1000 m) globally (Table S5.2). Sections of L-pTMs, R-pTMs and labile particulate fractions (L-pTM/T-pTM x 100) are presented in Figures 5.3, 5.4, and 5.5, respectively.

The average pTM concentrations, in all fractions, were higher at the BENG stations (ST 43-51 & 1-5), compared to NORTH stations (ST 6-24) (T-Test; p≤0.004; Table S5.3), except for V and Th (T-Test; p>0.05; Table S5.3). Most of the high L-pTM concentrations corresponded to samples with maximum T-pTM concentrations, reaching as high as 1.38 nM L-pV, 544 pM L-pCr, 49.1 pM L-pMo, 5.29 pM L-pU, 1.18 pM for L-pW, and as high as 0.74 pM for L-pTh at station 17 (bottom sample) and 1.69 nM for L-pBa at station 1 (25 m) (Figure 5.3). All of the maximum R-pTM concentrations, which were 4.85 nM for Ba, 4.53 nM for Cr, 3.63 nM for V, 91.7 pM for Th, 86.3 pM for Mo, 28.1 pM for pW and 16.8 pM for U, corresponded to samples with maximum T-pTMs concentrations (Figure 5.4).

The average labile particulate fractions (L-pTM/T-pTM x 100) for all samples, in descending order, were 62±19% for Ba, 58±22% for V, 54±20% for U, 33±19% for Mo, 30±21% Cr, 6.7±14% for W, and 3.7±9.8% for Th (Table 5.2). The average L-pTM/T-pTM fractions for all elements were higher at NORTH stations (except Th), but the difference was only statistically significant for V, Mo, and U (T-Test; *p*<0.001; Table S5.3).

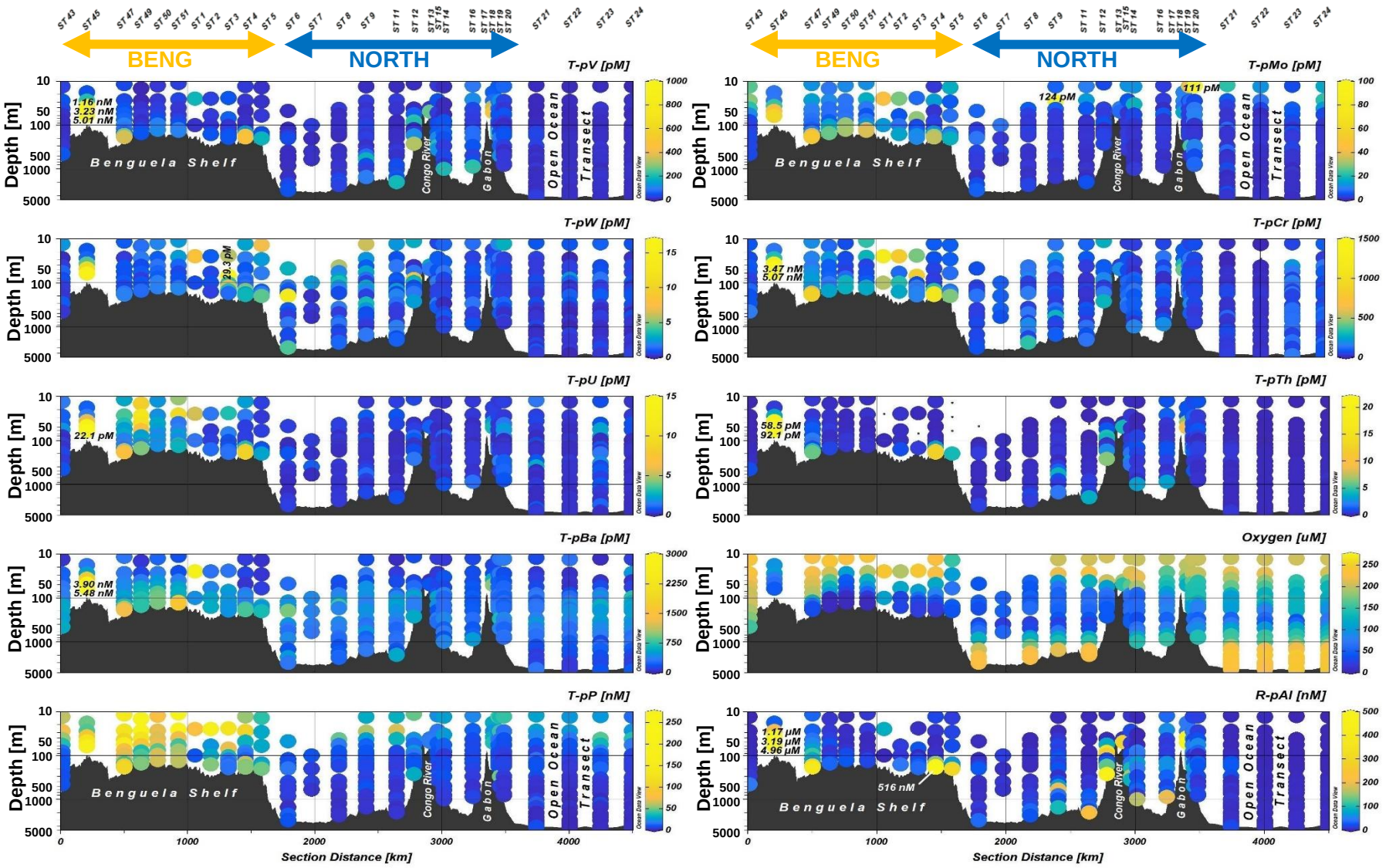

Figure 5.2 - Distribution of total particulate trace metal (pTM) concentrations along the GA08 transect. Note the logarithmic depth scales. Concentrations were annotated where values exceeded the color-bar scale (z-axis).

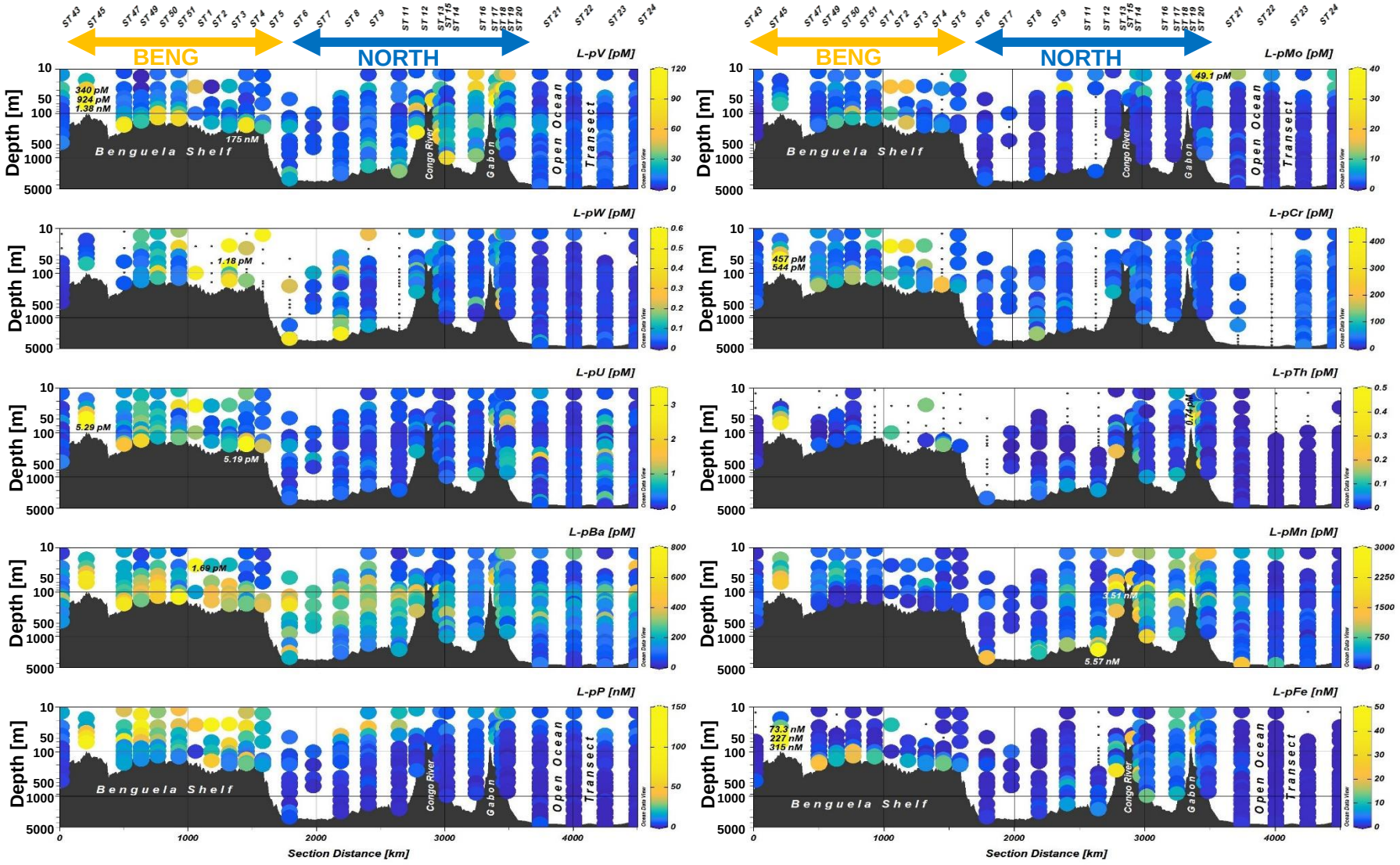

Figure 5.3 - Distribution of labile particulate trace metal (L-pTM) concentrations along the GA08 transect. Note the logarithmic depth scales. Concentrations were annotated where values exceeded the color-bar scale (z-axis).

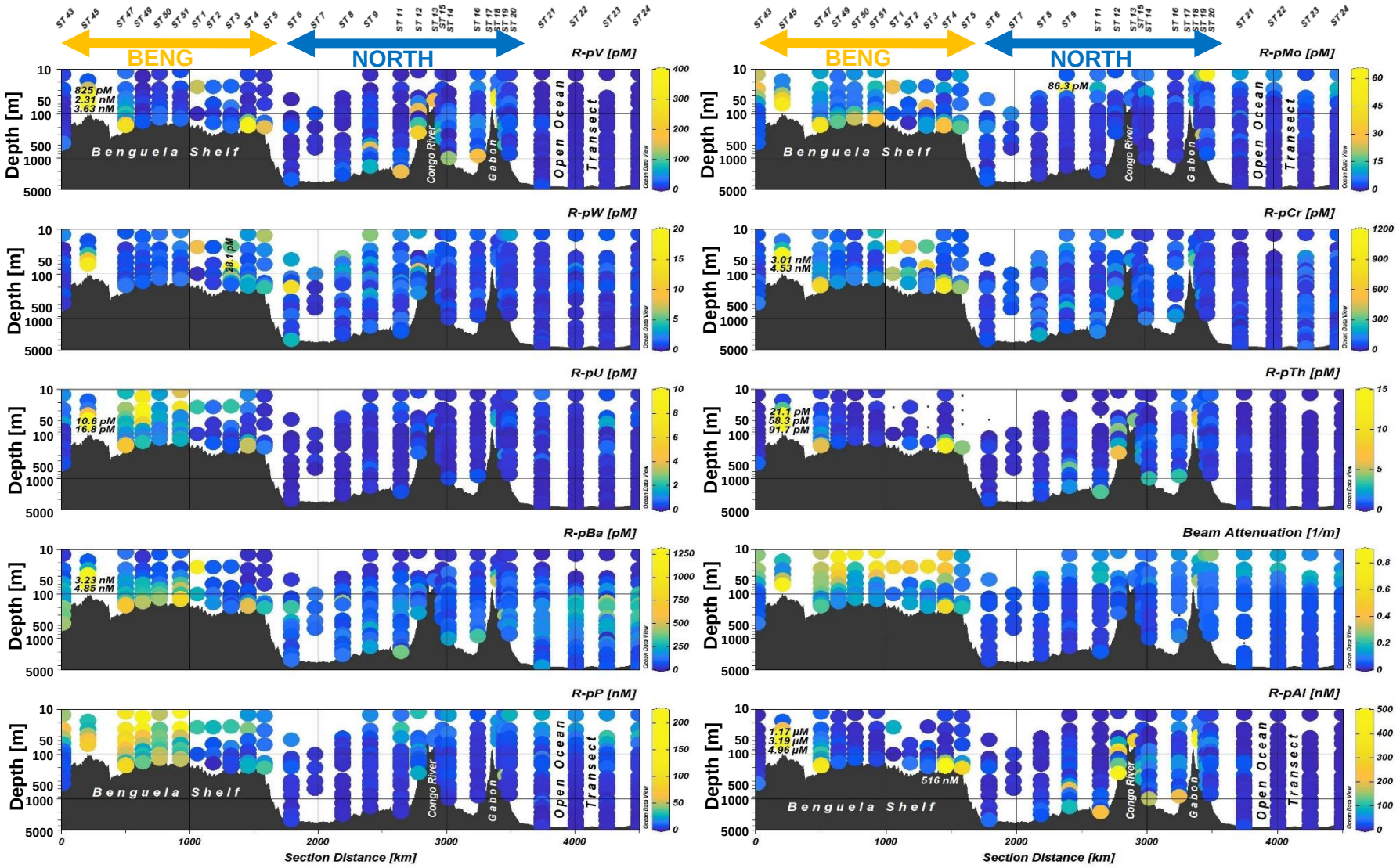

Figure 5.4 - Distribution of refractory particulate trace metal (R-pTM) concentrations along the GA08 transect. Note the logarithmic depth scales. Concentrations were annotated where values exceeded the color-bar scale (z-axis).

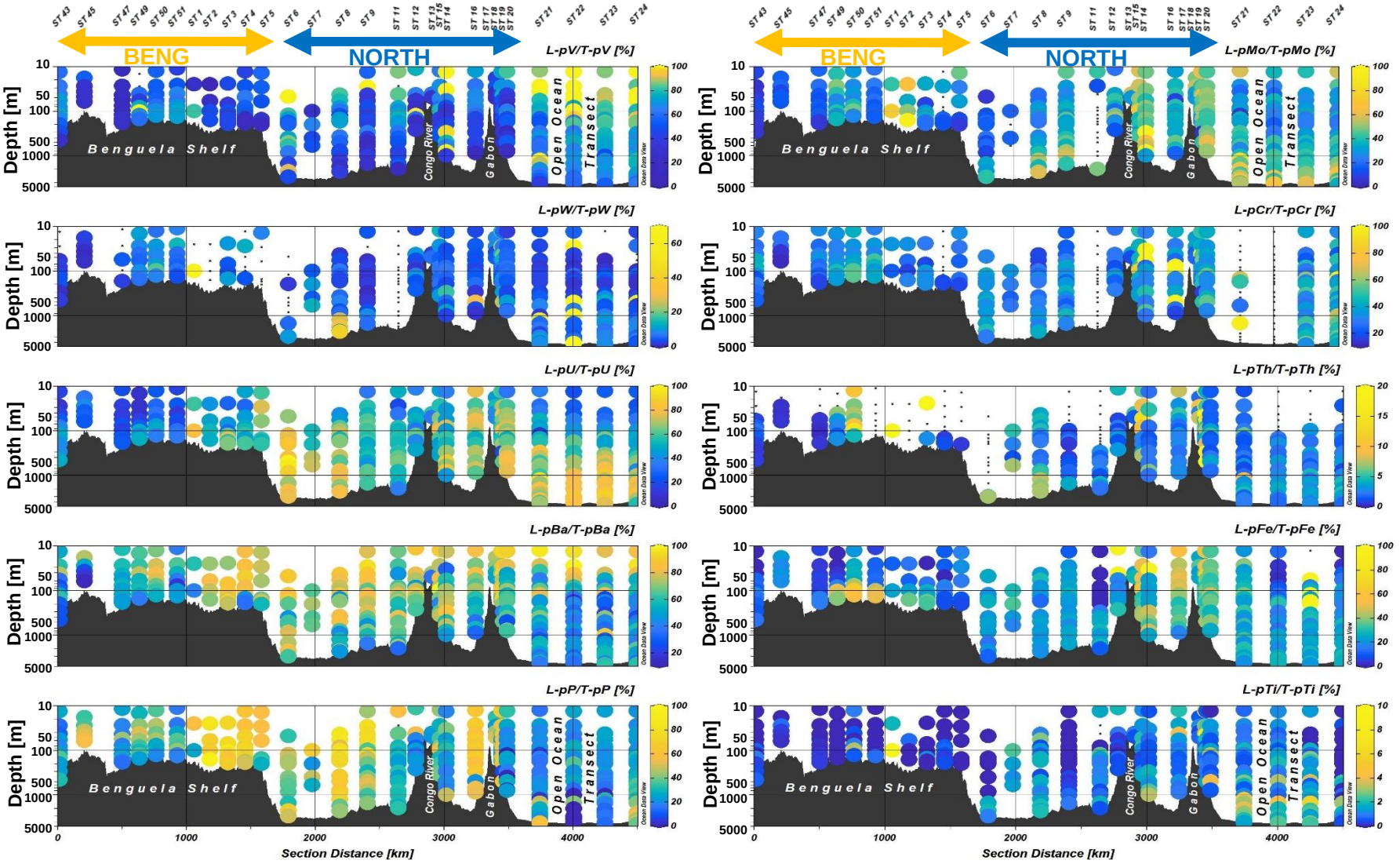

Figure 5.5 - Distribution of labile particulate fractions (%) of total particulate trace metals along the GA08 transect. Note the logarithmic depth scales.

5.3.1.1 Bivariate Correlations and Principal Component Analysis

Bivariate correlations of log-transformed datasets for T-pTMs, and L-pTMs and R-pTMs, are shown in Tables 5.1a and 5.1b, respectively, and include other particulate elements and ancillary parameters.

Total particulate Mo and U correlated well with T-pP (r= 0.80 and 0.72, respectively; p<0.001), beam attenuation (BAT) (r=0.74 and 0.71, respectively; p<0.001) and with each other (r=0.72; p<0.001), and relatively less with fluorescence (r=0.51 and 0.45, respectively; p<0.001), and R-pAl (r=0.27 and 0.42, respectively). T-pMo and T-pU also correlated relatively well with other bio-essential T-pTMs (Cd, Co, Cu, Ni, and Zn; r=0.43-0.69), suggesting an association with biogenic particles. All other T-pTMs (V, W, Th, Cr, and Ba) correlated comparatively poorly with BAT and fluorescence (r=0.01-0.38). T-pBa was the only element to exhibit close correlations with oxygen (r= -0.55; p<0.001). T-pV and T-pTh correlated well with R-pAl (r=0.86 and 0.83, respectively; p<0.001) and less with T-pP (r=0.33 and r=0.13, respectively; p<0.05), implying an association with lithogenic/benthic sources. T-pCr showed closer correlations to R-pAl than T-pP (r=0.55 and 0.45, respectively; p,0.001), and correlated relatively well with some bio-essential T-pTMs (Co, Cu, and Zn; r=0.57-0.66; p<0.001). T-pW only moderately correlated with T-pP (r=0.50; p<0.001), and relatively poorly with R-pAl (r=0.33), with the closest correlations to T-pZn and T-pCo (r=0.57; p<0.001).

Labile particulate Mo correlated most closely with BAT, T-pP, L-pP, and T-pU (r=0.54-0.61; p<0.001) and relatively poorly with R-pAl, L-pFe and L-pMn (r=0.13-0.30). L-pV and L-pTh correlated very closely with R-pAl and L-pFe (r=0.68-0.73; p<0.001), and with each other (r=0.63; p<0.001), implying common (benthic) sources (i.e., lithogenic particles and/or Fe oxides). L-pBa, L-pW, and L-pCr did not correlate well with any L-pTMs or ancillary parameters (r<0.5), except for L-pBa with oxygen (r= -0.57; p<0.001) and L-pCr with L-pU (r=0.54).

R-pAl correlated closely with R-pV and R-pTh (r=0.87 and 0.82; p<0.001) and to a lesser extent with R-pCr (r=0.53; p<0.001), and relatively poorly with R-pMo, R-pBa, R-pW, and R-pU (r=0.24-0.36). R-pMo and R-pU correlated closely with R-pP, BAT, fluorescence, and with each other (r=0.73-0.81; p<0.001), implying their association with residual (refractory) biogenic

particle fraction. R-pBa and R-pW generally did not correlate well with any other R-pTMs ($r<0.5$), except for R-pW with R-pMo ($r=0.52$; $p<0.001$).

Principal component analysis was carried out on log-transformed T-pTM, L-pTM, and R-pTM datasets for the BENG (ST 43-51 & 1-5) and NORTH (ST 6-24) regions, separately (Figures 5.6 and 5.7). Here we discuss the patterns of shared covariance that was captured within each PC between the regions, as well as where significant differences occurred.

The first component of the T-pTM datasets for both BENG and NORTH regions (40.6% and 37.1% of total variance, respectively; Figures 5.6a and 5.7a) was related to the influence of lithogenic particles, as it captured 73.4% and 82.4% of the individual variance of R-pAl, respectively. Most of the individual variances of T-pV (72% and 91%) and T-pTh were captured by PC1 in both regions, but the BENG region captured higher individual variance for T-pCr (74%), T-pBa (63%), T-pMo (50%), and T-pU (40%), compared to the NORTH region (9-24%). The second component (26.3% of total variance for BENG, and 24.4% for North regions; Figures 5.6a and 5.7a) was related to the influence of biogenic type particles, capturing individual variances of 66% and 82% for T-pP, 70% and 66% for fluorescence, and 67% and 77% for depth, in the BENG and NORTH regions, respectively. Most of the individual variance of T-pMo (61%) was captured in the NORTH region, compared to the BENG region which was much lower (<1% for T-pMo), though individual variances of oxygen (52%) and T-pU (40%) were higher in the BENG region compared to the NORTH (5% and 25%, respectively). PC3 in the BENG region (7.6% of total variance) was primarily due to the negative covariance between T-pMo (50%) and L-pMn (32%), while in the NORTH PC3 (10.7% of total variance) was primarily due to the negative covariance between oxygen (45%) and T-pBa (68%). PC4 was mostly associated with T-pW (56%) in the BENG region, while in the NORTH region, PC4 captured the highest variances for T-pU (39%), and T-pW (21%). PC5 in the BENG region captured the highest variances for T-pCr (37%) and T-pW (17%) in the NORTH region, and T-pV (10%) and T-pW (10%) in the BENG region.

Within the L-pTM datasets, the first components captured most of the individual variance for R-pAl (likely representing the influence of lithogenic particles) in the BENG (57%) and NORTH (37%) datasets (Figures 5.6b and 5.7b, respectively), with significant additional covariance with

oxygen (44%) and fluorescence (25%) within the BENG dataset. Individual variances of L-pBa (62%), L-pCr (59%), L-pU (59%) and L-pMo (29%) were higher in PC1 of the BENG dataset, while L-pV (82%), L-pTh (74%) and L-pW (45%) were higher in PC1 of the NORTH dataset. The second component of the L-pTM datasets was likely associated with biogenic particles, capturing individual variances of 76% (70%), 73% (57%), and 48% (70%) for T-pP, L-pP, and fluorescence within the BENG (NORTH) datasets. However, relatively minor individual variance was captured for all L-pTMs (≤16%) in both datasets, except for L-pMo (29%) in the NORTH, and L-pMn (46%) in the BENG regions. The third component was associated with secondary lithogenic particles in the BENG region, with individual variances of 26% for R-pAl, 49% for L-pW, 26% for L-pMo, and 20% for L-pMn, while PC3 in the NORTH dataset captured 74% and 57% variance for oxygen and L-pBa, respectively, which negatively covaried. PC4 in the BENG dataset captured the highest individual variances for L-pTh (33%), L-pW (23%), and L-pMn (13%), while PC4 in the NORTH dataset captured 45% and 25% variance for L-pCr and L-pU, respectively. PC5 in the BENG dataset captured the highest individual variance for L-pTh (14%) and <10% for all other parameters, while PC5 in the NORTH dataset captured 33% and 32% variance for L-pU and L-pCr (which negatively covaried), and 13% of L-pMo variance.

Within the R-pTM fractions, PC1 of the BENG dataset (38.5% of total variance; Figure 5.6c) was jointly associated with lithogenic particles and residual (refractory) biogenic particles, capturing 60% of the individual variance for R-pAl, and 38% and 44% of R-pP and T-pP, respectively; but almost none for fluorescence (1%). PC2 of the BENG dataset (27.4 of total variance; Figure 5.6c) captured most of the individual variance associated with fluorescence (82%), oxygen (55%), and roughly the same amount for R-pP (35%) and T-pP (40%), implying a major fraction of variance associated residual biogenic particles, while also capturing significant amounts of negative covariance for depth (76%), R-pBa (26%) and R-pV (11%). This was attributed to the higher concentration of biogenic particles over the Benguela shelf associated with the increased primary production facilitated through the upwelled supply of nutrients, and deeper penetration of biogenic particles through the underlying OMZ (Weber & Bianchi, 2020). Comparatively, PC1 in the NORTH region (34.8% of total variance; Figure 5.7c) was strongly associated with residual biogenic particles, capturing individual variances of 90%, 83%, and 58%

for T-pP, R-pP, and fluorescence, respectively, with significant variances for R-pMo (64%), R-pU (36%), R-pW (22%), and R-pBa (17%), and almost none for R-pAl (<1%). PC2 in the NORTH region dataset (27.0% of total variance; Figure 5.7c) was indicative of lithogenic particles, capturing 83% individual R-pAl variance, along with significant variances for R-pV (85%), R-pTh (79%), R-pCr (39%), and to a lesser extent for R-pU, R-pBa, and R-pW (13-19%). The third component was mostly associated with R-pW (50% variance) in the BENG dataset (Figure 5.6c), and R-pBa (29%) and oxygen (61%) in the NORTH dataset, which negatively covaried (Figure 5.7c). The fourth components captured significant individual variances for R-pMo (31%), R-pTh (16%), oxygen (15%), and R-pW (11%) in the BENG dataset (Figure 5.6c), and R-pU (24%), R-pW (23%), R-pBa (21%), and oxygen (12%) in the NORTH dataset (Figure 5.7c). The fifth component captured individual variances of 11 ± 1% for oxygen, R-pW, R-pMo, and R-pV in the BENG dataset (Figure 5.6c), and only significant individual variance for R-pCr (39%) in the NORTH dataset (Figure 5.7c).

The biplot of PC1 and PC2 vectors for the BENG L-pTM dataset (Figures 5.6e) showed two general patterns of component vectors grouping between (1) L-pFe, L-pV and L-pBa; and (2) L-pTh, L-pMo, L-pCr, L-pU, and R-pAl. In the NORTH L-pTM dataset (Figure 5.7e), some broad groups were apparent between (1) L-pTh, L-pFe, L-pMn and R-pAl, and to a lesser degree L-pV, L-pW, L-Cr and L-pU, which grouped closer together; and (2) L-pMo, L-pP, and T-pP, indicating a biogenic particle association or common source in surface waters. These covariances of L-pTMs were possibly due to either (1) a common labile particulate source, (2) increased affinity for adsorption onto similar particle surfaces, (3) and/or concomitant adsorption onto co-occurring labile particulate phases, such as labile Fe and/or Mn oxides (i.e., L-pFe and L-pMn).

Biplots for the R-pTM fractions in the BENG dataset (Figure 5.6f) showed grouping between: (1) R-pV and R-pAl (which grouped together very closely), and R-pMo, R-pTh, and R-pCr; and (2) R-pU, T-pP and R-pP. R-pBa grouped close to R-pAl and R-pV. In the NORTH dataset (Figure 5.7f) (1) R-pV, R-pTh and R-pAl grouped very closely together, and R-pCr to a lesser degree, implying a common lithogenic source; and (2) R-pMo grouped very closely with R-pP and T-pP; and (3) R-pU and R-pW were closely grouped together. The R-pBa vector negatively covaried with fluorescence and, to a lesser degree, oxygen.

Table 5.1 - Bivariate Pearson's correlation matrix of Log-transformed dataset for (a) Total particulate trace metals (T-pTMs); and (b) Labile (L-pTM) and Refractory (R-pTM) particulate trace metals with ancillary measurements and particle indicators for the GA08 transect along SW African coast and northern open ocean transect. Pearson correlation coefficient values (r) are shown in the white-cells, and the intensity of the colored boxes depict the strength of correlations with asterisks signifying different p-value thresholds, respectively. Samples with values below detection limit were excluded (pairwise) from the correlation matrix.

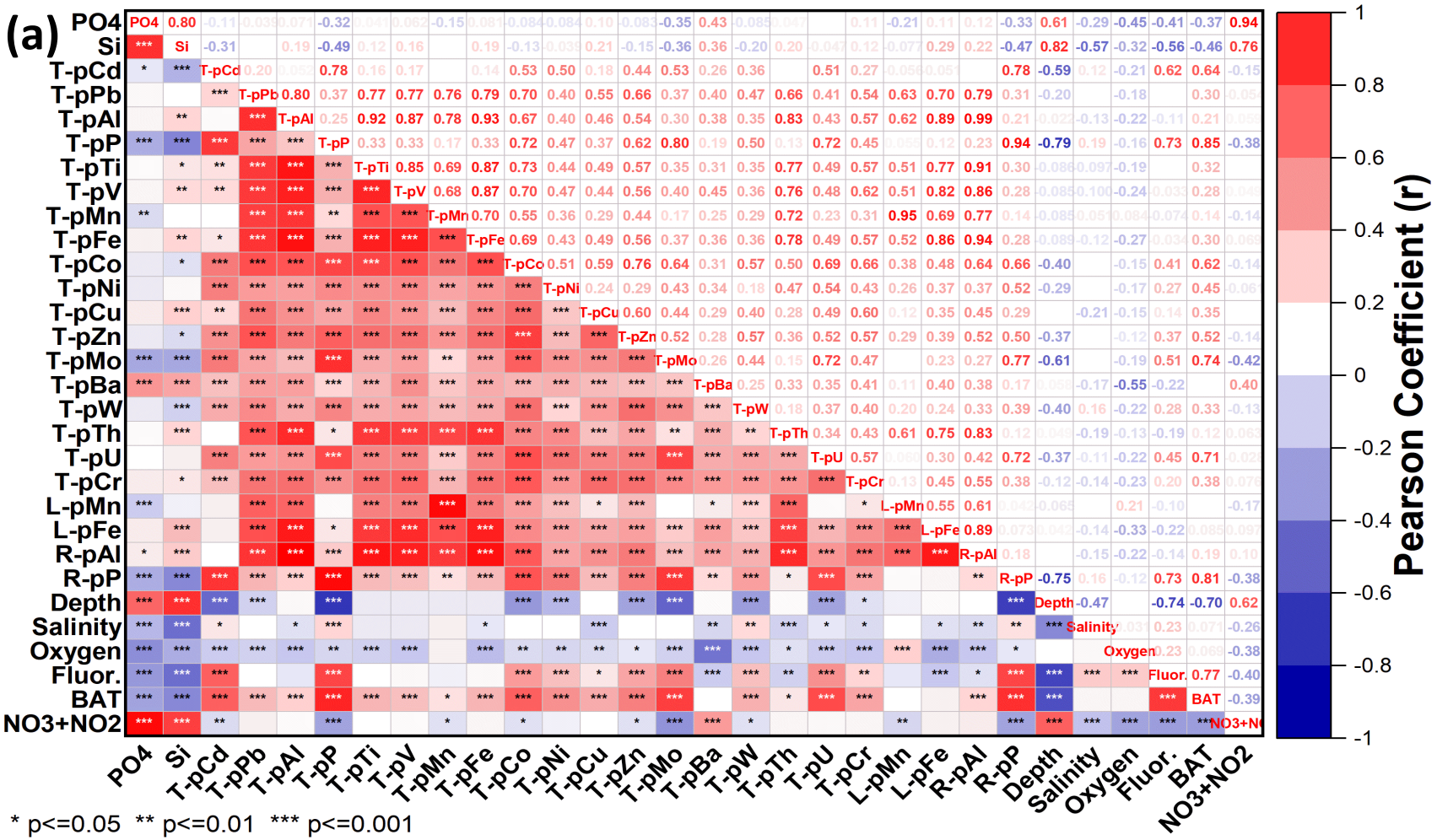

Table 5.1 - (continued)

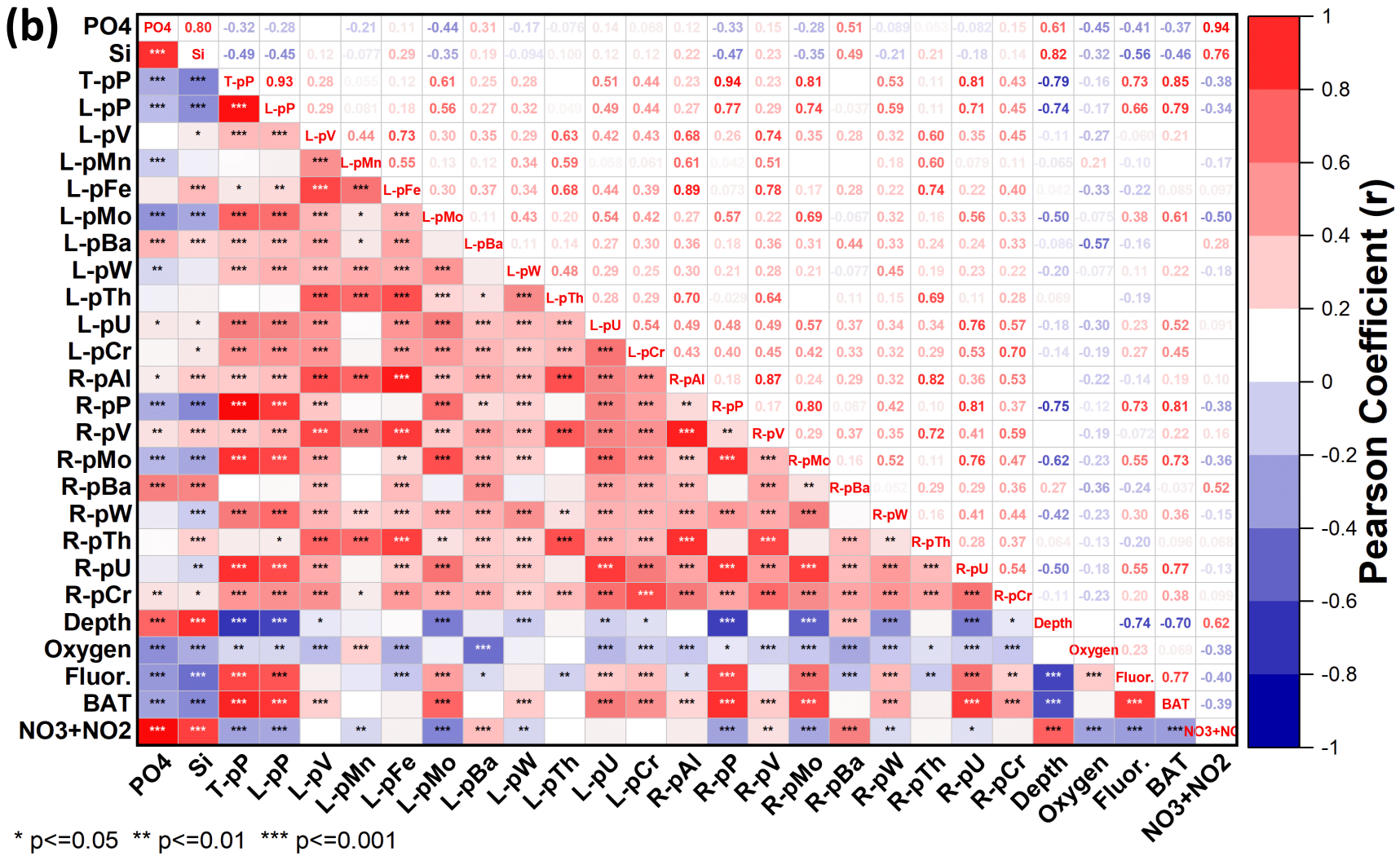

* p<=0.05 ** p<=0.01 *** p<=0.001

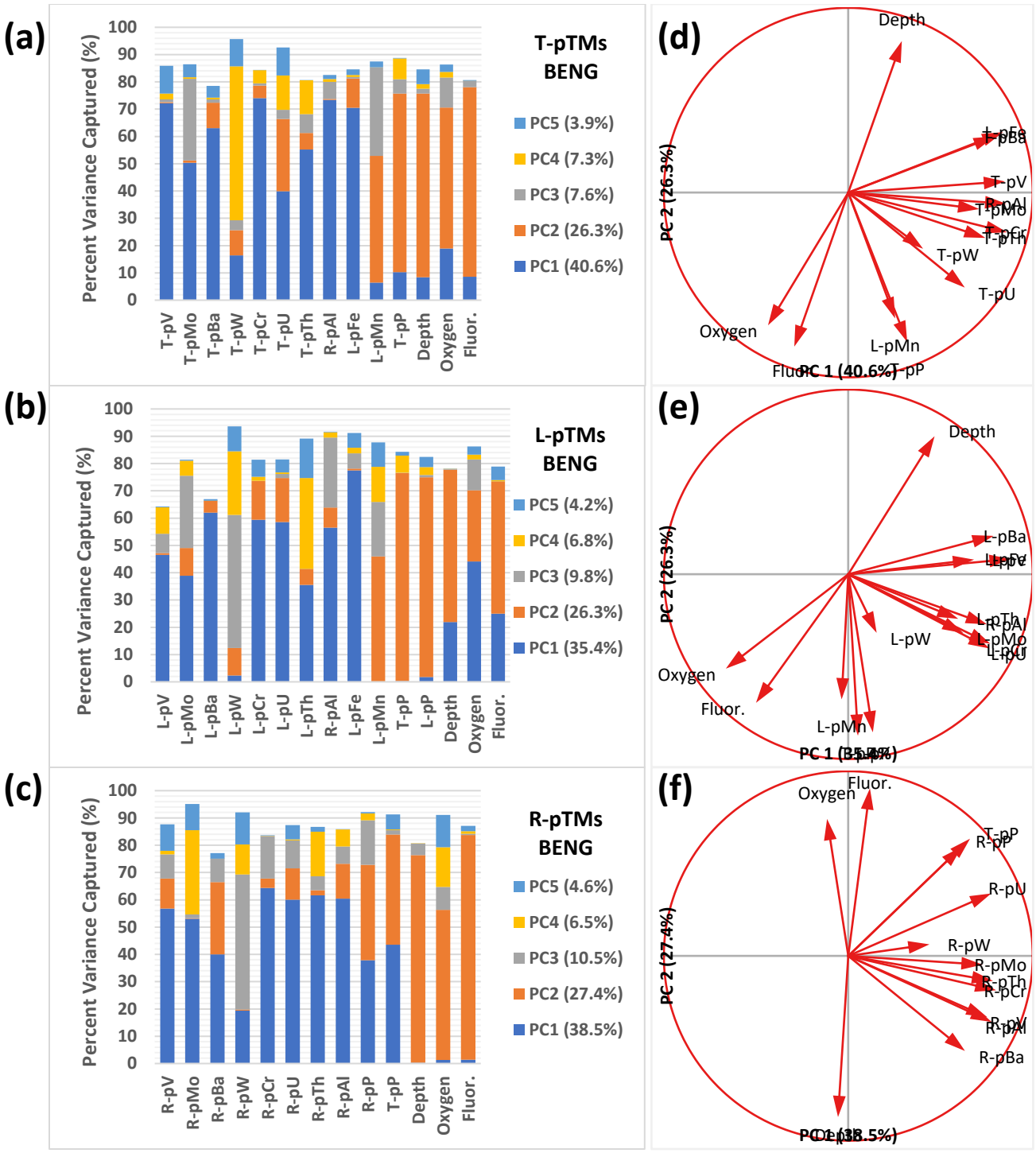

Figure 5.6 - Summary of the Principal Component Analysis (PCA) results of samples from the Benguela shelf stations (BENG; ST 43-51; 1-5). Cumulative variance explained in a 5 PC Model are shown for (a) total particulate trace metals (T-pTMs); (b) Labile particulate trace metals (L-pTMs); and (c) Refractory particulate trace metals (R-pTMs). The total variance captured by each component is indicated in the legend embedded in each chart. Biplots show the vectors of each variable against the first and second PCs of T-pTMs (d); L-pTMs (e); and R-pTMs (f).

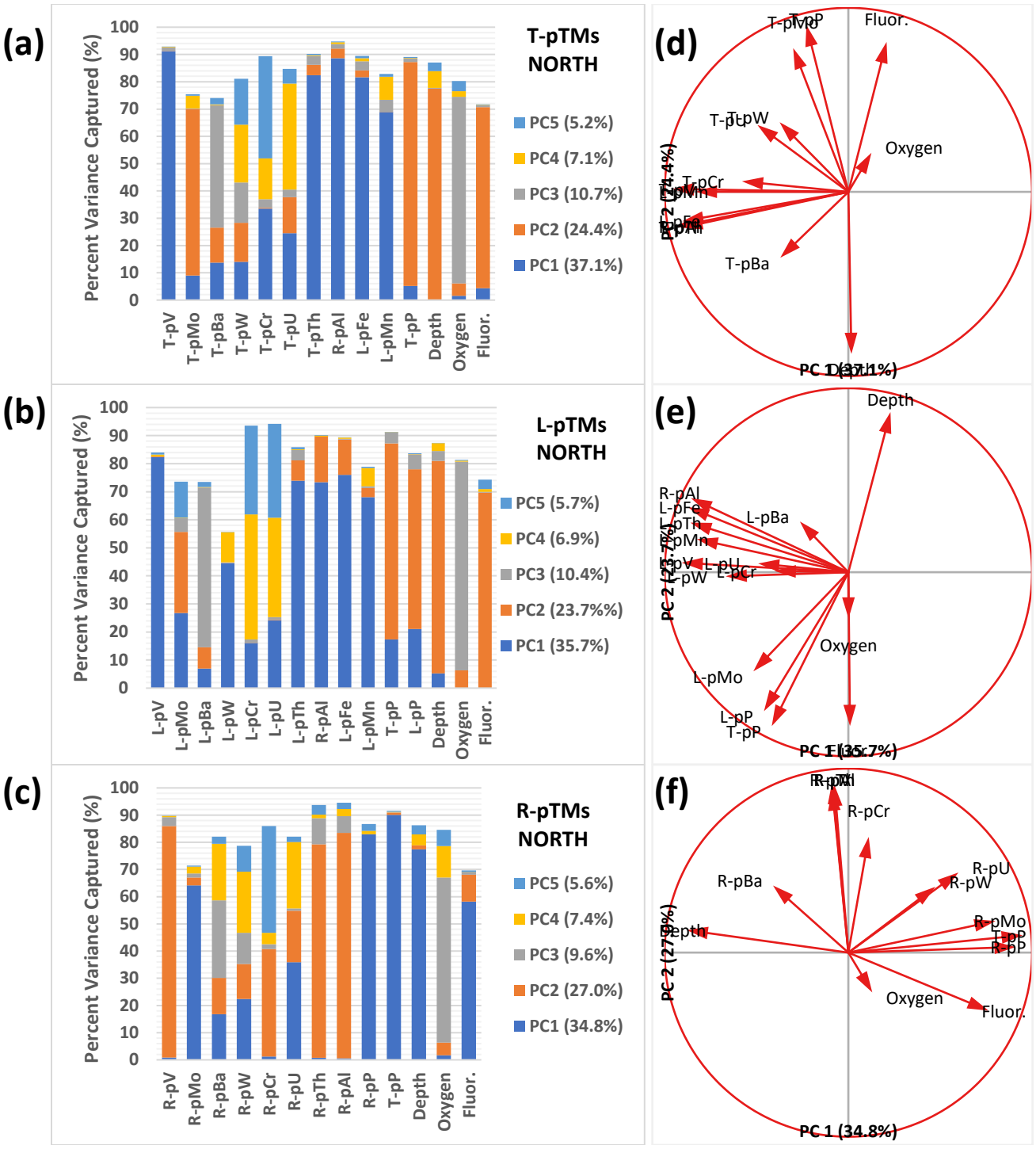

Figure 5.7 - Summary of the Principal Component Analysis (PCA) results of samples from the northern, non-upwelling stations (NORTH; stations 6-24). Cumulative variance explained in a 5 PC Model are shown for (a) total particulate trace metals (T-pTMs); (b) Labile particulate trace metals (L-pTMs); and (c) Refractory particulate trace metals (R-pTMs). The total variance captured by each component is indicated in the legend embedded in each chart. Biplots show the vectors of each variable against the first and second PCs of T-pTMs (d); L-pTMs (e); and R-pTMs (f).

5.3.1.2 Definition of Regions

The pTM distributions are described across five contrasting biogeochemical environments, and we discuss the main distribution patterns within each region. These defined regions (*n*=number of samples within each definition) include: (1) Surface layer (≤50 m, and <25 nM R-pAl; *n*=53); (2) Nepheloid layer (≥25 nM R-pAl; *n*=93); and (3) Congo River plume (ST 13-20; and ST21-22 ≤23.5 σ_{Θ}; *n*=77); (4) Open ocean (ST21-24; *n*=88); and (5) Oxygen Minimum Zone (≤60 µM oxygen; *n*=83). The defined regions are not exclusive. The defined nepheloid layer included samples with high concentrations of lithogenic particles, likely primarily derived from benthic resuspension, although possibly also including samples from other terrestrial particle sources, such as dust from the Namib Desert. Average pTM concentrations, in all fractions, and L-pTM/T-pTM fractions (%) in the defined regions are summarized in Table 5.2. Particulate trace metal stoichiometric ratios (i.e., linear regression slope values), normalized to particle-type indicators, and corresponding Pearson correlation coefficients within each respective region are summarized in Table 5.3, to help to determine the primary particle associations for each element within each of the defined regions. Upper and lower quartile stoichiometric ratio ranges of samples are referred to when Pearson correlation coefficients of the referenced parameter were poor (r<0.5) and are summarized in Table S5.2. Elemental abundance ratios normalized to biogenic and lithogenic proxies (pP and R-pAl, respectively), throughout refer to stoichiometric ratios using the respective molar concentrations.

Table 5.2 - Summary of the average total (T-pTM), labile (L-pTM), refractory (R-pTM) particulate trace metal concentratrions, and L-pTM/T-pTM fractions (%) across different biogeochemical regimes through the GA08 transect. Some overlapping of samples occurred between the defined regions. The defined 'Surface' and 'OMZ' regions exclude samples with ≥25 nM R-pAl concentrations to avoid masking effects from coinciding lithogenic sources. The river plume region includes all samples from station 13-20, and only samples <15 m from stations 21 and 22. The open ocean stations include all samples from stations 21-24. *Excluding 3 bottom samples from station 45 in 'Nepheloid Layer' samples (>1.17-4.97 µM R-pAl).

T-pTMs Average conc. (± 1 StDev)	*n*	**T-pV pM**	**T-pMo pM**	**T-pW pM**	**T-pCr pM**	**T-pBa pM**	**T-pU pM**	**T-pTh pM**
All	*318*	72.6 ± 344	7.3 ± 12.6	1.4 ± 2.4	147 ± 375	373 ± 442	1.0 ± 2.1	1.2 ± 6.5
Surface (<50 m & <25 nM R-pAl)	*53*	20.9 ± 16.7	15.6 ± 22.3	1.9 ± 2.4	106 ± 121	166 ± 114	1.5 ± 2.6	0.20 ± 0.24
Nepheloid (≥25 nM R-pAl*)	*90*	109 ± 102	8.2 ± 10.1	1.5 ± 1.9	195 ± 226	422 ± 339	1.2 ± 1.6	1.9 ± 2.3
River Plume	*77*	68.5 ± 82.3	7.6 ± 14.4	0.9 ± 0.6	84.7 ± 65.1	264 ± 144	0.5 ± 0.5	1.0 ± 1.4
Open Ocean	*88*	9.3 ± 5.6	2.9 ± 4.0	0.5 ± 0.4	59.5 ± 46.1	265 ± 166	0.4 ± 0.5	0.10 ± 0.07
OMZ (≤60 µM oxygen)	*53*	21.6 ± 21.8	5.9 ± 8.2	1.6 ± 1.4	91.8 ± 71.9	483 ± 278	0.69 ± 0.79	0.20 ± 0.13

L-pTMs Average conc. (± 1 StDev)	*n*	**L-pV [pM]**	**L-pMo [pM]**	**L-pW [pM]**	**L-pCr [pM]**	**L-pBa [pM]**	**L-pU [pM]**	**L-pTh [pM]**
All	*318*	25.5 ± 95.8	2.4 ± 4.8	0.071 ± 0.12	46.7 ± 60.8	210 ± 157	0.4 ± 0.6	0.03 ± 0.07
Surface (<50 m & <25 nM R-pAl)	*53*	14.0 ± 11.5	6.2 ± 9.4	0.14 ± 0.17	39.1 ± 40.6	131 ± 101	0.3 ± 0.4	0.04 ± 0.08
Nepheloid (≥25 nM R-pAl*)	*90*	34.4 ± 26.5	2.4 ± 3.4	0.075 ± 0.074	56.2 ± 62.2	249 ± 192	0.5 ± 0.8	0.06 ± 0.10
River Plume	*77*	27.7 ± 23.2	3.6 ± 7.0	0.059 ± 0.054	32.4 ± 25.8	178 ± 94.7	0.3 ± 0.3	0.06 ± 0.10
Open Ocean	*88*	6.6 ± 3.3	1.1 ± 1.9	0.017 ± 0.014	34.0 ± 9.9	132 ± 91.6	0.2 ± 0.3	0.003 ± 0.002
OMZ (≤60 µM oxygen)	*53*	13.6 ± 15.8	1.8 ± 2.6	0.075 ± 0.086	34.2 ± 29.2	315 ± 138	0.3 ± 0.3	0.006 ± 0.009

R-pTMs Average conc. (± 1 StDev)	*n*	**R-pV [pM]**	**R-pMo [pM]**	**R-pW [pM]**	**R-pCr [pM]**	**R-pBa [pM]**	**R-pU [pM]**	**R-pTh [pM]**
All	*318*	50.1 ± 257	5.0 ± 9.0	1.4 ± 2.4	112 ± 330	165 ± 352	0.6 ± 1.6	1.2 ± 6.5
Surface (<50 m & <25 nM R-pAl)	*53*	8.9 ± 6.7	9.7 ± 14.2	1.9 ± 2.2	76.3 ± 83.8	35.8 ± 34.5	1.2 ± 2.3	0.2 ± 0.2
Nepheloid (≥25 nM R-pAl*)	*90*	75.2 ± 82.1	6.0 ± 8.3	1.5 ± 1.9	144 ± 176	173 ± 171	0.7 ± 1.0	1.9 ± 2.2
River Plume	*77*	43.1 ± 66.2	4.1 ± 7.9	0.9 ± 0.6	58.4 ± 51.0	87.4 ± 83.8	0.2 ± 0.3	1.0 ± 1.4
Open Ocean	*88*	3.1 ± 2.9	1.8 ± 2.2	0.5 ± 0.4	40.8 ± 31.8	134 ± 105	0.2 ± 0.3	0.1 ± 0.1
OMZ (≤60 µM oxygen)	*53*	8.5 ± 7.2	4.4 ± 6.3	1.50 ± 1.32	62.8 ± 49.2	168 ± 183	0.37 ± 0.53	0.20 ± 0.12

L-pTM/T-pTM Average fraction (± 1 StDev)	*n*	**L-pV/T-pV [%]**	**L-pMo/T-pMo [%]**	**L-pW/T-pW [%]**	**L-pCr/T-pCr [%]**	**L-pBa/T-pBa [%]**	**L-pU/T-pU [%]**	**L-pTh/T-pTh [%]**
All	*318*	57.8 ± 22.2	32.8 ± 18.6	6.7 ± 14.5	29.7 ± 20.6	62.2 ± 18.8	53.9 ± 19.5	3.7 ± 9.8
Surface (<50 m & <25 nM R-pAl)	*53*	72.4 ± 19.5	34.0 ± 17.8	6.6 ± 13.9	28.1 ± 18.9	77.4 ± 15.4	37.4 ± 18.5	6.8 ± 19
Nepheloid (≥25 nM R-pAl*)	*90*	35.8 ± 15.3	31.8 ± 17.4	4.8 ± 5.5	30.0 ± 13.5	61.6 ± 15.1	50.1 ± 16.2	3.5 ± 5.1
River Plume	*77*	52.5 ± 21.9	45.5 ± 15.1	7.0 ± 5.5	42.2 ± 22.1	68.9 ± 17.3	59.5 ± 15.0	5.6 ± 6.9
Open Ocean	*88*	75.3 ± 14.5	38.3 ± 14.4	10.6 ± 24.5	24.5 ± 24.9	53.2 ± 18.7	58.6 ± 19.8	2.1 ± 1.6
OMZ (≤60 µM oxygen)	*53*	63.2 ± 17.4	26.0 ± 17.4	4.3 ± 4.5	29.2 ± 14.9	69.3 ± 17.8	58.3 ± 15.8	2.3 ± 2.9

Table 5.3 - Summary of particulate trace metal (pTM) stoichiometric ratios normalized to particle indicators, total and labile particulate phosphorus (T-pP and L-pP, respectively), refractory particulate aluminum (R-pAl), labile particulate Fe (L-pFe), and labile particulate manganese (L-pMn). Stoichiometric ratio values reported are of linear regression slopes, in mmol:mol, where correlation coefficients were statistically significant (**p<**0.05). Values in brackets show the bivariate Pearson correlation coefficient (r). Bold values indicate strong positive correlations, where r>0.7. The upper continental crust reference values were from Rudnick and Gao (2014). *Excluding 3 bottom samples from station 45 in 'Nepheloid Layer' samples (>1.17-4.97 µM R-pAl).

Surface (≤50 m & < 25 nM R-pAl) *n=53*	**V mmol:mol**	**Mo mmol:mol**	**W mmol:mol**	**Cr mmol:mol**	**Ba mmol:mol**	**U mmol:mol**	**Th mmol:mol**
L-pTM:L-pP	-	-	0.004 (0.698)	**1.044 (0.789)**	-	0.009 (0.640)	0.001 (0.375)
T-pTM:T-pP	0.110 (0.349)	-	0.012 (0.332)	1.220 (0.646)	-	**0.035 (0.861)**	-
R-pTM:R-pAl	-	-	-	-	-	-	**0.030 (0.810)**
T-pTM:R-pAl	1.262 (0.449)	-	-	-	-	-	**0.033 (0.796)**
L-pTM:L-pFe	**5.194 (0.844)**	1.795 (0.334)	-	-	-	-	**0.023 (0.743)**
L-pTM:L-pMn	13.769 (0.487)	12.885 (0.555)	-	-	71.244 (0.280)	-	0.046 (0.301)
Nepheloid samples (≥25 nM R-pAl*) *n=90*	**V mmol:mol**	**Mo mmol:mol**	**W mmol:mol**	**Cr mmol:mol**	**Ba mmol:mol**	**U mmol:mol**	**Th mmol:mol**
L-pTM:L-pP	0.462 (0.268)	0.104 (0.647)	-	1.591 (0.542)	-	0.009 (0.249)	-
R-pTM:R-pP	-	0.172 (0.595)	-	2.012 (0.331)	1.938 (0.326)	0.025 **(0.726)**	-
T-pTM:T-pP	-	0.139 (0.600)	-	2.329 (0.450)	1.908 (0.246)	0.019 (0.527)	-
UCC Reference Values TM:Al	*0.630 ± 0.069*	*0.0038±0.0011*	*0.0034±0.0019*	*0.586 ± 0.111*	*1.51 ± 0.197*	*0.0038±0.0008*	*0.015±0.0015*
L-pTM:R-pAl	0.147 (0.693)	-	-	0.153 (0.311)	-	0.003 (0.536)	0.0004 (0.550)
R-pTM:R-pAl	**0.630 (0.955)**	0.029 (0.435)	0.004 (0.235)	0.884 (0.630)	0.662 (0.483)	0.004 (0.517)	**0.017 (0.953)**
T-pTM:R-pAl	**0.778 (0.950)**	0.030 (0.364)	0.004 (0.229)	1.039 (0.573)	0.972 (0.357)	0.007 (0.573)	**0.017 (0.958)**
L-pTM:L-pFe	**3.501 (0.915)**	-	-	2.779 (0.314)	-	0.032 (0.288)	0.008 (0.608)
L-pTM:L-pMn	0.010 (0.309)	-	-	-	-	-	-
River Plume (ST13-20 & <15 m from ST21-22) *n=77*	**V mmol:mol**	**Mo mmol:mol**	**W mmol:mol**	**Cr mmol:mol**	**Ba mmol:mol**	**U mmol:mol**	**Th mmol:mol**
L-pTM:L-pP	1.976 (0.498)	0.646 (0.530)	0.004 (0.462)	1.186 (0.269)	-	-	0.008 (0.476)
T-pTM:T-pP	1.800 (0.253)	0.780 (0.628)	0.029 (0.558)	1.616 (0.288)	-	0.011 (0.256)	0.033 (0.267)
R-pTM:R-pAl	**0.662 (0.956)**	-	-	**0.480 (0.918)**	0.616 (0.695)	**0.002 (0.801)**	**0.014 (0.988)**
T-pTM:R-pAl	**0.831 (0.950)**	-	-	**0.613 (0.886)**	0.998 (0.649)	0.004 (0.684)	**0.015 (0.988)**
L-pTM:L-pFe	**3.624 (0.924)**	-	-	2.129 (0.489)	5.292 (0.330)	0.014 (0.292)	0.012 (0.695)
L-pTM:L-pMn	26.599 (0.677)	-	0.022 (0.245)	18.568 (0.430)	45.644 (0.284)	-	0.063 (0.364)
Open Ocean (ST21-24) *n=88*	**V mmol:mol**	**Mo mmol:mol**	**W mmol:mol**	**Cr mmol:mol**	**Ba mmol:mol**	**U mmol:mol**	**Th mmol:mol**
L-pTM:L-pP	-	0.338 (0.368)	-	-	-	-	-
T-pTM:T-pP	-	0.288 (0.664)	0.013 (0.294)	-	-	0.020 (0.371)	-
R-pTM:R-pAl	**0.587 (0.951)**	-	-	-	-	-	**0.015 (0.930)**
T-pTM:R-pAl	**1.065 (0.838)**	-	-	-	-	-	**0.015 (0.930)**
L-pTM:L-pFe	**6.176 (0.702)**	-	-	-	-	-	0.003 (0.586)
L-pTM:L-pMn	5.226 (0.317)	-	0.015 (0.225)	-	-	-	0.004 (0.452)
OMZ (<60 µM oxygen & <25 nM R-pAl) *n=53*	**V mmol:mol**	**Mo mmol:mol**	**W mmol:mol**	**Cr mmol:mol**	**Ba mmol:mol**	**U mmol:mol**	**Th mmol:mol**
L-pTM:L-pP	0.511 (0.300)	0.080 (0.300)	0.003 (0.345)	-	-	0.010 (0.307)	-
T-pTM:T-pP	0.704 (0.680)	**0.287 (0.734)**	-	1.614 (0.472)	7.919 (0.598)	**0.032 (0.851)**	-
R-pTM:R-pAl	0.747 (0.692)	0.280 (0.290)	-	-	-	-	**0.018 (0.952)**
T-pTM:R-pAl	1.566 (0.476)	0.403 (0.325)	-	-	-	-	**0.018 (0.957)**
L-pTM:L-pFe	**3.778 (0.874)**	**0.608 (0.925)**	0.008 (0.390)	**6.788 (0.914)**	24.011 (0.637)	0.054 (0.624)	**0.002 (0.915)**
L-pTM:L-pMn	-	-	-	-	-	-	-

5.3.2 pTM Distributions in the Surface Layer

Concentrations of the biogenic particle indicator, T-pP, R-pP, and L-pP were up to 5-fold higher over the Benguela shelf (ST 43-51 & 1-5), compared to NORTH stations (ST 6-24) reaching up to 253 nM, 212 nM, and 147 nM, respectively. Importantly, labile particulate fractions of P were relatively low (~41%) and high concentrations of refractory biogenic pP were apparent across the transect (Al-Hashem et al., 2022), particularly over the Benguela shelf. This implies that significant fractions of other biogenic associated pTMs may also be included in the biogenic R-pTM pool. Samples with high lithogenic particle concentrations in the surface layer (>25 nM R-pAl; < 50 m) are excluded in this sub-section but are mentioned in the following sub-section (Section 5.3.3).

The average concentrations of pMo and pW (in all fractions), T-pU and R-pU, as well as L-pBa/T-pBa and L-pTh/T-pTh fractions (%) were highest in the surface layer compared to the other defined regions (Table 5.2). Close correlations to the biogenic particle indicator (pP) were observed between L-pW, L-pCr, and L-pU with L-pP (r=0.64-0.79; p<0.001; Table 5.3), T-pCr and T-pU with T-pP (r=0.65-0.86; p<0.001; Table 5.3) whereas only R-pU was closely correlated with R-pP (r=0.77; p<0.001; Figure 5.8). Only R-pTh and T-pTh correlated closely with the lithogenic particle proxy, R-pAl, in the surface layer (0.81 and 0.80, respectively; p<0.001; Table 5.3).

The upper and lower quartile T-pTM:R-pAl values were at least a factor of 3, and up to 3 orders of magnitude higher than canonical upper continental crust (UCC) reference values (Rudnick & Gao, 2013) in the surface layer (Mo>>W>U>Cr>Ba>V) (Table S5.4), indicating the dominance of non-lithogenic pTM phases. The exception was for T-pTh, where upper and lower quartile T-pTh:R-pAl value ranges (0.019-0.043 mmol:mol; <50 m), and the T-pTh/R-pAl linear regression slope value (0.033 mmol:mol), were less than 3 fold higher compared to the mean UCC (0.015 ± 0.0015 mmol:mol; Rudnick and Gao, (2014)). The linear regression slope values of R-pTh:R-pAl (0.030 mmol:mol) and T-pTh:R-pAl (0.033 mmol:mol) (Table 5.3) were similar, indicating that pTh was mainly associated with refractory (lithogenic) particle sources in the surface layer, despite the exclusion of samples with high lithogenic particle concentrations. In all other regions, the linear regression slope values of T-pTh:R-pAl and R-pTh:R-pAl (0.14-0.18

mmol:mol) were comparatively lower than in the surface layer, but were consistent with UCC reference values (Rudnick & Gao, 2013). No associations between pTh and biogenic phases were apparent in any of the particulate fractions.

When normalized to the biogenic proxy, pP, the upper and lower quartile values of T-pV:T-pP (0.190-0.526 mmol:mol) and L-pV:L-pP (0.331-1.37 mmol:mol) ratios in the surface layer were comparable to, or slightly higher than, reported plankton stoichiometric ratios (0.20±0.19 mmol:mol pV:pP; Klein et al., 2013; Ohnemus et al., 2017). Higher L-pV:L-pP values compared to T-pV:T-pP suggested that biogenic pV was either associated with biogenic components that are more labile than the total biogenic pP pool, and/or that the L-pV pool included a relatively high fraction non-lithogenic and abiogenic pV phases, mainly ascribed to adsorption (see section 5.3.4). Close correlations observed between L-pV and L-pFe in the surface layer (r=0.84; p<0.001; Table 5.3) and consistently across all other regions (r=0.70-0.92; p<0.001; Table 5.3), suggested a high affinity for V adsorption onto Fe oxides (Edmonds & German, 2004; Feely et al., 1989, 1994; Ho et al., 2018; Ohnemus et al., 2019; Trefry & Metz, 1989). Correlations between L-pV and L-pMn were comparatively lower in surface waters (r=0.487; p<0.001; Table 5.3).

The upper and lower quartile values of T-pMo:T-pP (0.123-0.451 mmol:mol) and L-pMo:L-pP ratios (0.071-0.675 mmol:mol) in the surface layer were at least two-fold, and up to an order of magnitude, higher than average and median phytoplankton stoichiometric values reported by Ho et al. (2003) (0.033 mmol:mol pMo:pP) or Klein et al. (2013) (0.059-0.074 mmol:mol pMo:pP), respectively. This suggested that intracellular Mo:P quotas in bulk plankton assemblages along the GA08 transect were possibly higher than previous samples compiled from typical marine eukaryotic phytoplankton species and/or that samples included other abiogenic (i.e., primarily adsorbed) pMo phases, as similarly described for V (see section 5.3.4). Although in contrast to V, the correlations between L-pMo and L-pMn (r=0.56; p<0.001) were higher than with L-pFe (r=0.33) (Table 5.3), implying a higher affinity for Mo adsorption onto Mn oxides (Bertine & Turekian, 1973; Kashiwabara et al., 2011; Scott & Lyons, 2012) or common (biogenic) particle source. To our knowledge, no other documented references for

plankton Mo stoichiometries in the marine environment are available to compare with our results.

The highest average concentrations of L-pW (1.9 ± 2.4 pM) and close correlations between L-pW and L-pP in the surface layer (r=0.698; Table 5.3) could possibly be explained by an enzymatic role for tungsten (Garner & Stewart, 2002; Maia et al., 2016), although such a role is poorly investigated in marine plankton. Comparatively weaker correlations were observed between T-pW and T-pP (r=0.332). This implies that any biogenic pW present in the surface possibly comprised biogenic components that are comparatively more labile than the total biogenic pP. Concurrently, adsorption of W may have also occurred directly onto available biomineral or biogenic particle surfaces, or extracellular Mn (bio-)oxides (Kurzweil et al., 2021; Learman et al., 2011; Nealson et al., 1988; Tebo et al., 2004, 2005). The mechanisms controlling L-pW distribution are difficult to further resolve as L-pW correlated relatively poorly (r<0.4) with the indicators of the other prominent scavengers of Fe and Mn oxides (L-pFe and L-pMn, respectively) across all other defined regions (Table 5.3).

Total and labile particulate Cr concentrations correlated well with only T-pP and L-pP (r=0.65 and 0.79, respectively; Table 5.2) in the surface layer, suggesting a primary association with biogenic particles. This may reflect the extracellular adsorption of Cr(III) onto biogenic particles, extracellular precipitated Fe oxides, and/or bio-uptake by phytoplankton, which is possibly enhanced following the photoreduction of Cr(VI) in the photic surface layer (Achterberg & van den Berg, 1997; Janssen et al., 2020, 2021; Semeniuk et al., 2016).

Particulate U was closely associated with biogenic particles in all fractions as evidenced by close correlations between all fractions of pU and pP (r=0.64-0.86; Figure 5.8). L-pU (and R-pU, in brackets) distributions most closely resembled biogenic particle distributions in surface waters over the BENG shelf (ST 47-51 & 1-3; ≤50 m) with average concentrations of 0.91±0.79 pM (and 3.7±3.2 pM), and up to 3.21 pM (and 10.1 pM), compared to lower concentrations at stations in the North, with average concentrations of 0.225±0.205 pM (0.285±0.274 pM (ST 4-24; ≤50 m) (Figures 5.3 and 5.4). The L-pU/T-pU fractions were also lower at the same BENG

stations (23.0±14.2%; ST 47-51 & 1-3; ≤50 m), compared to the rest of the shelf stations (51.5±14.7% L-pU/T-pU; ≤50 m; ST 4-20) (Figure 5.5), corresponding with high R-pP.

R-pU was found to be closely linked to R-pP in surface waters (r=0.77; p<0.001), indicating a close relationship with refractory biogenic sources. All other R-pTMs (V, Mo, W, Cr, Ba, and Th) correlated weakly with R-pP (r= 0.02 - 0.39). Additionally, upper and lower quartile values of T-pU:R-pAl (0.25-0.60 mmol:mol) and R-pU:R-pAl (0.16-0.43 mmol:mol) in the surface layer were over 2 orders of magnitude higher than canonical lithogenic U:Al reference values (0.0038±0.00079 mmol:mol; Rudnick and Gao, (2014)), indicating that pU in the surface was predominantly comprised of non-lithogenic sources. Together these observations implied that significant fractions of particulate non-lithogenic uranium are formed in the water-column, particularly in the productive Benguela upwelling region (4.25 ± 3.35 pM R-pU; ST 47-51; <50 m; Figure 5.4) and the associated OMZ, which extended to bottom waters.

Previous studies have linked a particulate non-lithogenic uranium source from the water column to the underlying sediment, such as Zheng et al. (2002) whose observations in the Santa Barbara Basin showed similar pU compositions between sediment trap samples and surface-most sediment (Zheng et al., 2002). Our observations support Zheng et al. (2002)'s interpretations and show that R-pU comprises significant fractions of U (up to 92%; Figure 5.5) and concentrations (7.5 – 10 nM R-pU; ST 49, 14 -28 m; Figure 5.4) in surface waters. The presence of significant R-pU fractions complicates and potentially challenges interpretations using sedimentary pU as a (paleo-)proxy particularly in sediments underlying highly productive and sub-oxic regions, particularly when assuming bottom water oxygen is the primary control of particulate non-lithogenic uranium accumulation. Irrespective of whether sedimentary pU is partially or fully autochthonous in reducing sediment, the significant fractions of chemically refractory pU phases in the water column over the Benguela shelf highlights the importance for the need to differentiate between the different possible mechanisms of sedimentary pU accumulation. Extending particulate analysis in future studies to utilize uranium isotope fractionation patterns between various biogeochemical regimes may help to resolve the mechanisms and extent to which particulate non-lithogenic uranium is generated and exported from the water column (e.g., Bruggmann et al., 2022 and references therein).

No associations between pBa and biogenic particles were apparent in the surface, perhaps due to the low availability and requirement of Ba to marine organisms (Neff, 2002 and references therein), which is supported by the weak correlations of pBa with biogenic particle proxies (r≤0.28; Table 5.3). However, increasing pBa concentrations (all fractions) were observed below the surface (200-1000 m), presumably due to barite precipitation within decomposing sinking bio-aggregated particles (e.g., Rahman et al., 2022 and references therein) (see section 5.3.6).

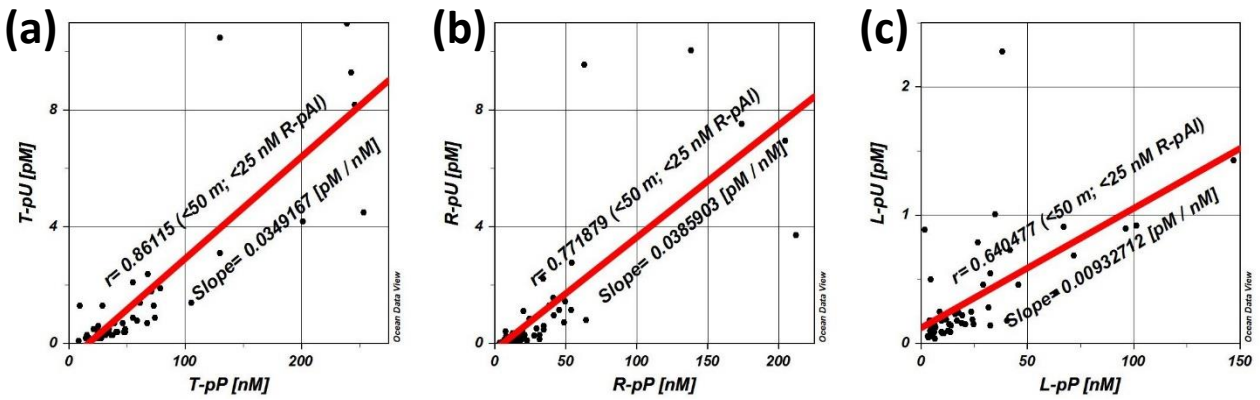

Figure 5.8 - Correlations between particulate uranium (pU) with particulate phosphorus (P) in the (a) total (T-p); (b) refractory (R-p); and (c) labile (L-p) particulate fractions in the surface layer (<50 m) across the GA08 transect. Samples with R-pAl concentrations >25 nM are not included.

5.3.3 pTMs Associated with Nepheloid Particles

Nepheloid particles (indicated by the presence of R-pAl) were generally enhanced in (near-)bottom waters (within 100 m of the seafloor), consistent with benthic resuspension and nepheloid layer distribution patterns, particularly at the shallow shelf stations 12 and 17 (up to 628 nM R-pAl), and at deep stations 9 and 11 (up to 227 nM R-pAl). Other significant lithogenic particle sources along the transect included riverine particles (between Congo plume stations 13-20) and atmospheric dust from the Namib Desert (Al-Hashem et al., 2022) (see section 5.3.4). Although notably, redox sensitive pTMs are predicted to be more abundant in the associated benthic inventory of anoxic and sulfidic sediments in the Benguela region (Borchers et al., 2005; Inthorn et al., 2006).

The highest average concentrations of pV, pCr, and pTh, in all fractions, and R-pBa, T-pU, and L-pU corresponded to nepheloid particle samples (> 25 nM R-pAl; Table 5.2). The average labile particulate fractions were lowest in nepheloid particle samples for V (35.8±15.3% L-pV/L-pV). Total and refractory particulate V and Th correlated highly with R-pAl (r=0.95-0.96), and well for pCr and pU with R-pAl (r=0.52-0.63) (Table 5.3). The corresponding linear regression slope values for total and refractory pTM:R-pAl for V and Th, and only R-pU, were consistent with UCC values, and within a factor of two for T-pU, T-pCr, and R-pCr for all nepheloid samples (Table 5.3). The correlations of pMo, pBa, and pW, in all fractions, with R-pAl, were relatively low (r<0.5).

The upper and lower quartile values of R-pW:R-pAl (0.009-0.024) and T-pW:R-pAl (0.009-0.025) were similar, suggesting a predominantly lithogenic source which is possibly more enriched with W compared to average UCC (0.0034±0.0019). Values for R-pBa:R-pAl (0.981-3.102) were generally more comparable to UCC values (1.51±0.197). Upper and lower quartile values of R-pMo:R-pAl (0.017-0.096 mmol:mol) values were approximately an order of magnitude higher than UCC values (0.004 mmol:mol Mo:Al), implying a higher abundance of Mo abundance in regional lithogenic sources, the inclusion of a higher proportion of non-lithogenic R-pMo phases, possibly as thiomolybdates from resuspended benthic particles from regional sulfidic sediment sources (Borchers et al., 2005; Erickson & Helz, 2000; Inthorn et al., 2006), and/or inclusion of biogenic R-pMo (Al-Hashem et al., 2022).

R-pU and R-pMo in nepheloid samples exhibited greater correlations with R-pP (r= 0.73 and 0.60, respectively; Table 5.3), compared to R-pAl (r= 0.52 and 0.44, respectively). This supports the hypothesis that R-pMo originates from a refractory biogenic particle source. Over the BENG shelf, R-pU and R-pMo concentrations were enriched in comparison to lithogenic proxies (R-pAl and R-pTi) (Figure 5.9), indicating a greater occurrence of refractory non-lithogenic phases. Due to the inclusion of a greater proportion of lithogenic (refractory) pU in nepheloid samples, the R-pU:R-pP linear regression slope value in nepheloid samples (0.025 mmol:mol; Table 5.3) was slightly lower than the value in surface samples (0.038 mmol:mol; Figure 5.8). Close associations between R-pU and R-pMo with R-pP show that the affiliation with refractory biogenic particle phases persisted even in lithogenic particle-rich

settings. Thus, the water column R-pTM inventory may be a significant source of R-pTM phases to the underlying sediments, particularly for R-pU and R-pMo, and their sediment inventory may not be entirely autochthonous.

In contrast to other elements, the decoupling of pW from the enrichment in pCr, pV, and pMo observed in nepheloid samples is consistent with the reported geochemical behavior of W, which shows no tendency for adsorption or (co-)precipitation in anoxic or weakly sulfidic conditions and, thus, no significant authigenic pW phases are retained in sediment (Bauer et al., 2017; Tribovillard et al., 2006 and references therein).

Adsorption of V and Mo by lithogenic and other co-occurring particles within (benthic) nepheloid samples, such as Fe and Mn oxides (Dellwig et al., 2007; Scholz et al., 2011; Whitmore et al., 2019), is likely to have further contributed to their enhanced L-pTM concentrations in nepheloid samples (Figure 5.3 and Table 5.2). This is consistent with the benthic release of these TMs during sediment resuspension and subsequent (re-)adsorption in (near-)bottom waters (Sadiq, 1988; Tribovillard et al., 2006). Enhanced adsorption is prone to occur under particle-rich environments, such as in nepheloid layers (Honeyman et al., 1988; Rutgers Van Der Loeff & Boudreau, 1997).

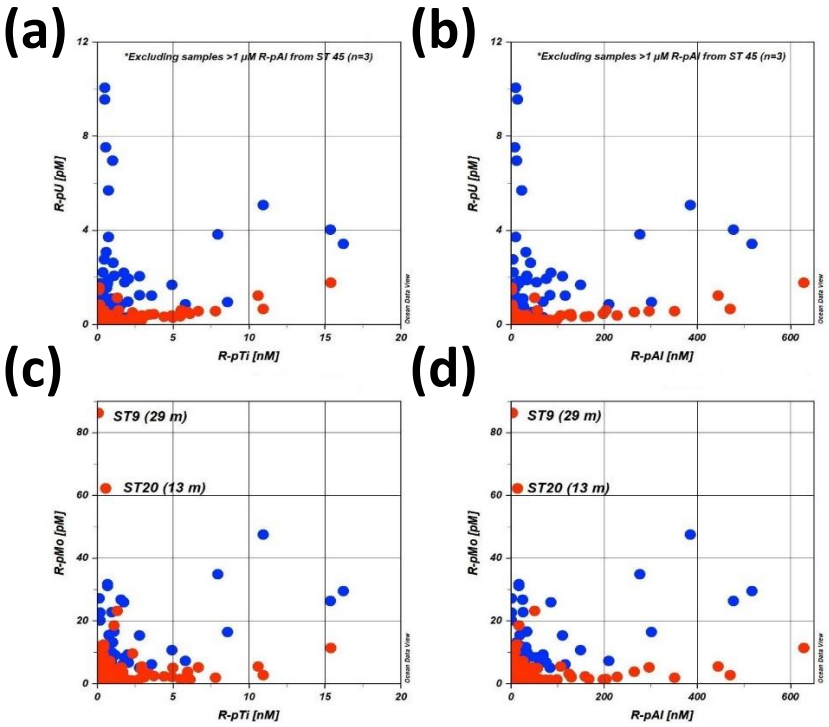

Figure 5.9 - Scatterplots showing the concentration distributions of refractory particulate uranium (R-pU) and molybdenum (R-pMo) with lithogenic particle indicators refractory particulate aluminum (R-pAl) and titanium (R-pTi): (a) R-pU:R-pTi; (b) R-pU:R-pAl; (c) R-pMo:R-pTi; (d) R-pMo:R-pAl. Scatterplots include all samples across the GA08 transect, except 3 bottom samples from station 45, which stretched the y-axes and decreased resolution. Blue points represent Benguela shelf stations (ST 43-51 & 1-5) and red points represent Northern, non-upwelling stations.

5.3.4 pTM Distributions within the Congo River Plume

Particulate TM distributions from Congo River plume associated stations (ST 13-20 & <15 m from ST 21-22) generally showed enhanced TM adsorption on suspended particles (Al-Hashem et al., 2022). Average concentrations (maximum value in brackets) of the particle indicators within the river plume samples were 56.2 ± 94.0 nM (628 nM) for R-pAl, 13.6 ± 11.6 nM (49.2 nM) for T-pP, 5.40 ± 5.91 nM (34.9 nM) for L-pFe, and 751 ± 590 pM (2894 pM) for L-pMn. In addition to labile Fe and Mn oxides, the increased L-pFe and L-pMn concentrations also likely contain considerable portions of adsorbed Fe and Mn (Al-Hashem et al., 2022).

Measurements of dissolved (<0.2 µm) and total dissolvable (unfiltered, stored acidified at pH 1.2 until analysis) TMs are available from the Congo River (*n=3*), and collected in different

seasons (May, July, and October 2017)(Vieira et al., 2020). The average dissolved TM concentrations (total dissolvable concentrations, in brackets) were 25.2±6.8 nM (40.2±7.2 nM) for V, 10.6±0.66 nM (1.77±0.87 nM) for Cr, 74.3±6.2 pM (83.1±21.2 pM) for U, and 55.4±28.7 pM for Mo.

Strong correlations with R-pAl were observed for V, Cr, and Th in both R-pTM and T-pTM fractions (*r*=0.89-0.99), and R-pU (*r*=0.8), while T-pU, T-pBa and R-pBa correlated very well with R-pAl (*r*=0.65-0.70) (Table 5.3). The corresponding linear regression slope values of T-pTMs/R-pAl for Cr, U and Th, and only R-pV/T-pAl were comparable to UCC reference sources (Rudnick & Gao, 2013), suggesting that particle sources were primarily lithogenic. Total and refractory particulate Ba and U correlated well only with R-pAl (*r*=0.65-0.70). Yet linear regression slope values of total and refractory pBa/R-pAl (0.998 and 0.616 mmol:mol, respectively) were slightly deficient compared to average UCC values (1.51±0.197 Ba:Al mmol:mol). The difference between total and refractory pBa/R-pAl ratios revealed a high fraction of labile non-lithogenic pBa phases.

Similarly, T-pTM/R-pAl regression slope values for V (0.831 mmol:mol) and Cr (0.613 mmol:mol), were higher than their respective R-pTM/R-pAl values (0.662 and 0.480 mmol:mol, respectively), indicating a relatively high proportion of labile non-lithogenic phases. The average T-pV:T-pP ratios in surface water of the river plume (3.34±3.59 mmol:mol) exceeded available plankton reference values (Klein et al., 2013; Ohnemus et al., 2017), and L-pV:L-pP ratios (4.37±4.01 mmol:mol) were even higher, compared to the average surface values of the transect (section 5.3.2). The increased L-pV concentrations and labile fractions (Figures 5.3 and 5.5, respectively) were likely caused by an additional source of V to the plume (e.g. wet atmospheric deposition) and the adsorption of V onto Fe oxides. This was evident by the strong correlation between L-pV and L-pFe (*r*= 0.924; p0.001; Table 5.3) with Fe oxides having been proposed to preferentially adsorb V from solution (e.g., Edmonds & German, 2004; Feely et al., 1994; Ho et al., 2018; Trefry & Metz, 1989). But L-pV also correlated favorably with L-pMn (*r*=0.677; Table 5.3), pointing to either a shared particle source between L-pV and L-pMn, most likely biogenic particles, or a co-occurring but somewhat lower tendency for V to adsorb onto Mn oxides (Section 5.3.2).

T-pCr and R-pCr correlated strongly with R-pAl (r= 0.92 and 0.89, respectively), weaker with all other particle indicators (r<0.5) (Table 5.3). Linear regression slope values for R-pCr:R-pAl and T-pCr:R-pAl (0.48 and 0.61 mmol:mol, respectively) were within UCC reference ranges (0.586±0.111 mmol:mol Cr:Al; Rudnick and Gao, 2014). The difference between the slope values may indicate enhanced non-lithogenic pCr phases. L-pCr/T-pCr fractions were highest in River plume stations (42.4±22.1%), compared to all other regions, implying enhanced adsorption, and were primarily enhanced in (near-)bottom waters, coinciding with enhanced R-pAl (Figure 5.5). Cr adsorption depends on reduction of Cr (VI) to particle reactive Cr (III), consistent with higher observed L-pCr and L-pCr/T-pCr near benthic reduced sources (Figures 5.3 and 5.5). Cr adsorption is also enhanced during benthic resuspension (Achterberg & van den Berg, 1997; Goring-Harford et al., 2018; Moos et al., 2020), as evident by the high coinciding R-pAl concentrations. Higher R-pCr:R-pAl ratios were observed in nepheloid samples (0.911 mmol:mol) than in the river plume (0.480 mmol:mol) (Table 5.3), possibly indicating lower Cr abundance in lithogenic particles from the Congo River compared to the rest of the nepheloid samples along the transect.

Particulate Mo, in all fractions, and T-pW correlated relatively well with all fractions of pP (r=0.53-0.63; Table 5.3) and poorly with R-pAl (r<0.2). L-pMo and L-pW also correlated poorly with L-pFe and L-pMn (r<0.25). The linear regression slope values for pMo:pP, in all fractions, exceeded plankton reference values (0.033 mmol:mol pMo:pP; Ho et al., 2003) by over an order of magnitude. Upper and lower quartile values of T-pMo:R-pAl (0.036-0.352 mmol:mol) were also higher than average UCC values by 1-2 orders of magnitude. In the surface layer of the river plume stations (ST 13–20), T-pMo:T-pP (0.538–0.561 mmol:mol) and L-pMo:L-pP (0.871–0.928 mmol:mol) ratios were particularly enhanced. This may indicate that pMo was most closely associated with biogenic particles, possibly by direct adsorption or onto extracellular Fe and/or Mn oxides (Goldberg et al., 2009; Kashiwabara et al., 2011). The upper and lower quartile values of T-pW:R-pAl (0.012-0.068 mmol:mol) and R-pW:R-pAl (0.011-0.066 mmol:mol) were very similar, indicating a refractory (lithogenic) source, although values were higher than average UCC values by about an order of magnitude.

The association between pU and biogenic particles was weaker in river plume samples with poorer correlations between pU and pP in all pTM phases (r<0.5) Instead pU correlated more closely with lithogenic particles, evident by the higher correlations with R-pAl (r=0.684-0.801), compared to pP (r<0.26). In contrast, pMo correlated most closely with pP in all phases, including R-Mo and R-pP (r=0.622; p<0.001), indicating that refractory biogenic pMo was also a significant source of pMo in river plume samples.

5.3.5 pTM Distributions in the Open Ocean Region

With the exception of pBa, all elements and major particle type proxies showed the lowest average concentrations in the open ocean region (Table 5.2). This was attributed to fewer external particle sources and lower primary production in the off-shelf surface waters. Average concentrations (maximum value in brackets) of the particle indicators in the open ocean stations (ST 21-24) were 3.34 ± 4.44 nM (25.2 nM) R-pAl, 7.66 ± 9.14 nM (45.9 nM) T-pP, 320 ± 364 pM (2165 pM) L-pFe, and 166 ± 202 pM (1519 pM) L-pMn.

Only total and refractory pV and pTh showed strong associations with R-pAl (r=0.89–0.99), and the associated linear regression slopes were consistent with UCC reference values (Rudnick & Gao, 2013), except for T-pV/R-pAl, which was greater. The elevated average L-pV/T-pV fractions seen in the open ocean region was 75.3% (Table 5.2), and the close correlation between L-pV and L-pFe (r=0.70; Table 5.3) indicated that the additional labile pV phases were adsorbed phases. Only T-pMo had a strong correlation with T-pP (r=0.664), implying a biogenic particle association, whereas W, Cr, Ba, and U had poor correlations (r<0.4) with all particle type proxies (Table 5.3).

Despite the lack of association of pBa with other particles, pBa concentrations were higher in mesopelagic depths. This observation is consistent with barite precipitation in subsurface waters (Bishop, 1988; Chow & Goldberg, 1960; Dehairs et al., 1980; Rahman et al., 2022). Similar trends of pBa enrichment in mesopelagic depths have been observed in the North Pacific (Esser & Volpe, 2002), Southern Ocean (Dehairs et al., 1992; Planchon et al., 2013), North Atlantic Ocean (le Roy et al., 2018; Martinez-Ruiz et al., 2019), and Mediterranean

Sea (Jullion et al., 2017). This distribution is attributed to barite precipitation within anoxic microenvironments in organic matter rich aggregates (Dehairs et al., 1990).

Vertical profiles of T-pBa concentrations from 80-1200 m (~25.9-27.3 σ_Θ) at open ocean stations (386±128 pM T-pBa; ST 21-24) were similar to those from the deep shelf-adjacent stations (393±130 pM; ST 6-11) (Figure 5.2). Enhanced pBa concentrations were associated with South Atlantic Central Water (25.5-27.1 σ_Θ) and Antarctic Intermediate Water (27.1-27.5 σ_Θ). However, R-pBa fractions were higher at the deeper open ocean stations, comprising 51.3±16.5% of the pBa pool (203±97.8 pM R-pBa), compared to shelf adjacent stations which comprised 29.4±11.9% (116±72.8 pM; ST 6-11). Higher R-pBa fractions may be partially caused by crystalline barite minerals that precipitate in the open ocean due to slower vertical sinking rates and lower supply of sinking particles (Jeandel et al., 2015; Lamborg et al., 2008 and references therein) and/or association with other refractory (bio-)minerals such as celestite (Bernstein et al., 1998; Bernstein & Byrne, 2004).

5.3.6 pTM Distributions within the Oxygen Minimum Zone

Within the defined OMZ (<60 µM oxygen), 30 out of 83 samples showed high lithogenic particle concentrations (> 25 µM R-pAl) and were derived primarily from (near-)bottom and river plume waters as discussed in section 5.3.3. The lowest oxygen concentrations along the transect (<10 µM oxygen; 96-150 m) were found in bottom waters over the Benguela shelf, between stations 49-51, coinciding with relatively low lithogenic (19.4±7.57 nM R-pAl) and Mn oxide (29.2±8.84 pM L-pMn) particle concentrations. However, high concentrations of Fe oxides were apparent in these waters, as suggested by the high concentrations of L-pFe and dFe (12.6±5.56 nM, and 18.2±8.81 nM, respectively). These are assumed to be derived from a benthic supply of Fe(II) which is consistent with observed Fe(II) concentrations on M121 which show enrichment close to the sediment interface (Hunt et al., 2022).

Enhanced L-pTM concentrations of Cr, V, and Mo in (near-)bottom water samples, particularly between stations 49-51 over the Benguela shelf (Figure 5.3 and S5.3), suggested a benthic source. In addition, subterranean groundwater inputs on the Benguela shelf (Emeis et

al., 2004) are a possible source of TMs, consistent with concurrent measurements of ^{223}Ra, ^{224}Ra, ^{226}Ra, and ^{228}Ra in bottom water samples (Vieira, 2019). The Benguela shelf sediments provided a substantial supply of various redox-sensitive trace metals to the overlying waters, including Fe, Co, Mn, Cd, Ni, and Cu (Liu et al., 2022). As a result, sediment release may also have contained reduced, particle reactive Cr, V, and Mo. (Tribovillard et al., 2006 and references therein). No increased adsorption of W, Ba, Th, or U was apparent in the L-pTM concentrations or L-pTM/T-pTM fractions. Furthermore, all L-pTMs correlated weakly with R-pAl (r<0.4) within the OMZ. The highest average concentrations of T-pBa and L-pBa (483±278 pM and 315±138 pM, respectively; Table 5.3) were in the OMZ, and moderate negative correlations between T-pBa and L-pBa with oxygen in all samples (r= -0.55 and -0.57, respectively; p<0.001; Tables 5.1a and 5.1b) is consistent with enhanced barite precipitation in low oxygen environments (Dehairs et al., 1990).

Resuspended benthic particles from sulfidic sediments, such as on the Benguela shelf, may include insoluble Mo sulfides formed under euxinic conditions (Erickson & Helz, 2000; Helz et al., 1996; Johannesson et al., 2013; Mohajerin et al., 2014, 2016) which accumulates in anoxic and euxinic sediment (e.g., Crusius et al., 1996; Emerson & Huested, 1991; Scott & Lyons, 2012). Additionally, organic matter is linked to increases in sedimentary Mo content (Chappaz et al., 2014; Dellwig et al., 2019). Hence, the enhanced R-pMo concentrations in (near-)bottom waters of the Benguela shelf stations (20.0 ± 9.00 pM; ST 49-51; <10 µM oxygen; n=7) may come from sulfidic sediments documented near the sampled stations (Borchers et al., 2005; Inthorn et al., 2006) (section 5.3.2).

Tungsten exhibits a similar geochemical behavior to Mo (Dellwig et al., 2019), although no enrichment in pW was apparent in bottom water particles over the BENG region. Euxinic conditions were possibly not strong enough to drive significant W-sulfide precipitation (Bauer et al., 2017; Mohajerin et al., 2014). Also, W is reported to exhibit a limited tendency for adsorption, even under anoxic conditions, and is suspected to be primarily removed by oxide minerals (Kurzweil et al., 2021). Our data show that L-pW was not significantly enhanced in samples with labile Fe oxide particles (i.e., L-pFe) and did not correlate well with L-pFe or L-pMn (r<0.4; Table 5.3). In contrast, L-pMo, L-pCr, and L-pV correlated strongly with L-pFe (r=0.87-

0.93; $p<0.001$; Table 5.3), suggesting adsorption onto Fe oxides (Cranston & Murray, 1978; Elderfield, 1970; Ho et al., 2018). This is consistent with observations in the Pacific OMZ which associated V and Mo with adsorption onto reprecipitated Fe oxide particles (Ho et al., 2018), and support the mechanism proposed by Scholz et al. (2011) for their 'shuttling' across shelf sediments due to repeated dissolution and precipitation of Fe oxides.

5.4 Conclusions

This study provides the detailed distributions of labile and refractory particulate V, Mo, W, Cr, U, Th, and Ba on a dynamic continental shelf for the first time. Our work provides insight into the behavior of the elements, in relation to proxies for lithogenic and biogenic particles, offered by separating chemically labile from refractory pTM phases.

Our observations showed that pTh and pW were predominantly associated with refractory lithogenic particles. A minor association of pW with biogenic materials in surface waters is possible, but no evidence of authigenic precipitated pW from anoxic or sulfidic sources was apparent. Particulate Mo likely included refractory thiomolybdates from benthic resuspended particles from anoxic and sulfidic sources, although significant fractions of refractory pMo were also associated with refractory biogenic sources. Datasets referencing TM stoichiometries of phytoplankton are expanding, although Mo is still largely undocumented. Future studies should consider including Mo among the suite of other elements typically studied (i.e., Fe, Mn, Co, Zn, Cu, Cd, and Ni) when examining their bio-essential TM associations to expand available references to help determine pMo associations.

Particulate U was associated with the biogenic fraction, particularly over the productive Benguela shelf, and to a lesser extent in open ocean and river plume samples. This indicated that biogenic particles in the water column may transfer refractory particulate U and Mo to sediments on productive shelves, in addition to authigenic mineral accumulation. This complicates their use as paleo-oceanographic proxies on productive shelves, potentially affecting their use as paleo-oceanographic proxies.

Total particulate Ba was largely associated with barite precipitation. Similar pBa concentrations but different labile particulate fractions at deep shelf-adjacent and open ocean stations suggested different solubilities of barite minerals and/or other pBa associated (bio-)mineral phases (possibly celestite). These patterns, which may reflect higher Ba removal in the open ocean transect compared with the Angola Basin.

L-pV distributions were enhanced in conjunction with Fe oxides that co-occur with lithogenic sources. L-pCr was mostly adsorbed, but R-pCr phases were attributed to lithogenic sources. Enhanced Cr and Mo adsorption was observed in oxygen-poor (near-)bottom waters over the Benguela shelf, where Fe oxide concentrations were particularly high and Mn oxides were lacking.

Despite the insights provided in this thesis, some open questions on particulate trace metal cycling remain and should be addressed in future work.

Future research should aim to incorporate dissolved TM fractions and isotope analysis whenever possible, as recent research has highlighted the value of using isotope fractionation patterns to improve biogeochemical cycling interpretations (e.g., Bruggmann et al., 2022; Goldberg et al., 2009; Goring-Harford et al., 2018; Horner et al., 2021; Lau et al., 2020; McManus, Poulson, et al., 2005; Miletto et al., 2021). Additionally, we recommend expanding particulate analysis to also include labile and refractory pTM phases as well where possible.

Acknowledgments

We thank the captain and crew of the RV Meteor M121 cruise/GEOTRACES GA08 section; S. Koesling, P. Lodeiro, J. Pampín Baro, J. C. Yong and C. Schlosser for cruise support and assistance in sample collection and P. Streu for technical laboratory assistance. The PhD fellowships to A. Al-Hashem, S. Krisch, and T. Liu were funded by the Kuwait Institute for Scientific Research, Kuwait, the Deutsche Forschungsgemeinschaft (AC 217/1-1 granted to Eric P. Achterberg), and the China Scholarship Council, respectively. The cruise was funded by the Deutsche Forschungsgemeinschaft (DFG). The open-access publishing charges for this publication were covered by the Helmholtz Research Centre/Association. The GEOTRACES 2021 Intermediate Data Product (IDP2021) represents an international collaboration and is endorsed by the Scientific Committee on Oceanic Research (SCOR). The many researchers and funding agencies responsible for the collection of data and quality control are thanked for their contributions to the IDP2021.

Author Contributions: A.A.A.: investigation, methodology and analysis, data curation, visualization, writing—original draft. A.J.B.: writing—review and editing. S.K.: formal analysis (dTMs). T.L.: formal analysis (dTMs). T.S.: formal analysis (TM analysis on HR-ICP-MS). M.J.H.: formal analysis (dTMs) and writing—review and editing. E.P.A.: conceptualization, funding acquisition, resources, supervision, and writing—review and editing.

Conflict of Interest

The authors declare that they have no conflicts of interest.

Data Availability

The full datasets for labile (L-pTM), refractory (R-pTM), and total (T-pTM) particulate trace metal concentrations of iron (Fe), aluminum (Al), titanium (Ti), manganese (Mn), cobalt (Co), zinc (Zn), nickel (Ni), copper (Cu), cadmium (Cd), lead (Pb), and vanadium (V), and particulate phosphorus (P) for the presented sections of the GA08 (M121) cruise transect are available at https://doi.org/10.1594/PANGAEA.945498. The dissolved TM (dTM) dataset for Fe, Co, Mn, Ni, Cd, Cu, Pb and Zn, Fe(II), and macronutrients (phosphate, nitrate + nitrite and silicic acid) are available at https://doi.org/10.1594/PANGAEA.947275. The pTM datasets for molybdenum (Mo), tungsten (W), chromium (Cr), barium (Ba), uranium (U), and thorium (Th) are available at https://doi.pangaea.de/10.1594/PANGAEA.955825.

References

Abshire, M. L., Riedinger, N., Clymer, J. M., Scott, C., Severmann, S., Romaniello, S. J., & Puckette, J. O. (2022). Reconstructing the paleoceanographic and redox conditions responsible for variations in uranium content in North American Devonian black shales. *Palaeogeography, Palaeoclimatology, Palaeoecology*, *587*, 110763. https://doi.org/10.1016/J.PALAEO.2021.110763

Achterberg, E. P., & van den Berg, C. M. G. (1997). Chemical speciation of chromium and nickel in the western Mediterranean. *Deep-Sea Research Part II: Topical Studies in Oceanography*, *44*(3–4), 693–720. https://doi.org/10.1016/S0967-0645(96)00086-0

Al-Hashem, Ali A; Beck, Aaron; Achterberg, Eric Pieter (2022): Labile, Refractory, and Total Particulate Trace Metal Concentrations from the GEOTRACES GA08 Shelf section and 3-degree Latitudinal transect. PANGAEA, https://doi.org/10.1594/PANGAEA.945498

Al-Hashem, Ali A; Beck, Aaron; Steffens, Tim; Achterberg, Eric Pieter (2023): Labile, Refractory, and Total Particulate Mo, Cr, Ba, W, Th, and U concentrations from the GEOTRACES GA08 Shelf Section and 3-degree Latitudinal Transect. PANGAEA, https://doi.org/10.1594/PANGAEA.955825

Al-Hashem, A. A., Beck, A. J., Krisch, S., Barraqueta, J.-L. M., Steffens, T., & Achterberg, E. P. (2022). Particulate Trace Metal Sources, Cycling, and Distributions on the Southwest African Shelf. *Global Biogeochemical Cycles*, e2022GB007453. https://doi.org/10.1029/2022GB007453

Alsdorf, D., Beighley, E., Laraque, A., Lee, H., Tshimanga, R., O'Loughlin, F., Mahé, G., Dinga, B., Moukandi, G., & Spencer, R. G. M. (2016). Opportunities for hydrologic research in the Congo Basin. *Reviews of Geophysics*, *54*(2), 378–409. https://doi.org/10.1002/2016RG000517

Anderson, R. F. (2020). GEOTRACES: Accelerating Research on the Marine Biogeochemical Cycles of Trace Elements and Their Isotopes. *Annual Review of Marine Science*, *12*, 49–85. https://doi.org/10.1146/annurev-marine-010318-095123

Anderson RF (1982) Concentration, vertical flux, and remineralization of particulate uranium in seawater. Geochim Cosmochim Acta 46:1293–1299. https://doi.org/10.1016/0016-7037(82)90013-8

Anderson, R. F., Bacon, M. P., & Brewer, P. G. (1983). Removal of 230Th and 231Pa from the open ocean. *Earth and Planetary Science Letters*, *62*(1), 7–23. https://doi.org/10.1016/0012-821X(83)90067-5

Anderson, R. F., Fleisher, M. Q., & LeHuray, A. P. (1989). Concentration, oxidation state, and particulate flux of uranium in the Black Sea. *Geochimica et Cosmochimica Acta*, *53*(9), 2215–2224. https://doi.org/10.1016/0016-7037(89)90345-1

Anderson, R. F., Lehuray, A. P., Fleisher, M. Q., & Murray, J. W. (1989). Uranium deposition in saanich inlet sediments, vancouver island. *Geochimica et Cosmochimica Acta*, *53*(9), 2205–2213. https://doi.org/10.1016/0016-7037(89)90344-X

Andreesen, J. R., & Makdessi, K. (2008). Tungsten, the Surprisingly Positively Acting Heavy Metal Element for Prokaryotes. *Annals of the New York Academy of Sciences*, *1125*(1), 215–229. https://doi.org/10.1196/ANNALS.1419.003

Bauer, S., Blomqvist, S., & Ingri, J. (2017). Distribution of dissolved and suspended particulate molybdenum, vanadium, and tungsten in the Baltic Sea. *Marine Chemistry*, *196*(May), 135–147. https://doi.org/10.1016/j.marchem.2017.08.010

Berger, C. J. M., Lippiatt, S. M., Lawrence, M. G., & Bruland, K. W. (2008). Application of a chemical leach technique for estimating labile particulate aluminum, iron, and manganese in the Columbia River plume and coastal waters off Oregon and Washington. *Journal of Geophysical Research*, *113*, 1–16. https://doi.org/10.1029/2007JC004703

Bernstein, R. E., & Byrne, R. H. (2004). Acantharians and marine barite. *Marine Chemistry*, *86*(1–2), 45–50. https://doi.org/10.1016/j.marchem.2003.12.003

Bernstein, R. E., Byrne, R. H., & Schijf, J. (1998). Acantharians: a missing link in the oceanic biogeochemistry of barium. *Deep Sea Research Part I: Oceanographic Research Papers*, *45*(2–3), 491–505. https://doi.org/10.1016/S0967-0637(97)00095-2

Bertine, K. K., & Turekian, K. K. (1973). Molybdenum in marine deposits. *Geochimica et Cosmochimica Acta*, *37*(6), 1415–1434. https://doi.org/10.1016/0016-7037(73)90080-X

Bishop, J. K. B. (1988). The barite-opal-organic carbon association in oceanic particulate matter. *Nature*, *332*(6162), 341–343. https://doi.org/10.1038/332341a0

Borchers, S. L., Schnetger, B., Böning, P., & Brumsack, H. J. (2005). Geochemical signatures of the Namibian diatom belt: Perennial upwelling and intermittent anoxia. *Geochemistry, Geophysics, Geosystems*, *6*(6). https://doi.org/10.1029/2004GC000886

Boyd, P. W., Ellwood, M. J., Tagliabue, A., & Twining, B. S. (2017). Biotic and abiotic retention, recycling and remineralization of metals in the ocean. In *Nature Geoscience* (Vol. 10, Issue 3, pp. 167–173). https://doi.org/10.1038/ngeo2876

Bruggmann, S., Gilleaudeau, G. J., Romaniello, S. J., Severmann, S., Canfield, D. E., Anbar, A. D., Scholz, F., & Frei, R. (2022). Uranium isotope cycling on the highly productive Peruvian margin. *Chemical Geology*, *590*. https://doi.org/10.1016/j.chemgeo.2021.120705

Bruland, K. W., Middag, R., & Lohan, M. C. (2014). Controls of Trace Metals in Seawater. In *Treatise on Geochemistry: Second Edition* (2nd ed., Vol. 8). Elsevier Ltd. https://doi.org/10.1016/B978-0-08-095975-7.00602-1

Chan, L. H., Drummond, D., Edmond, J. M., & Grant, B. (1977). On the barium data from the Atlantic GEOSECS expedition. *Deep Sea Research*, *24*(7), 613–649. https://doi.org/10.1016/0146-6291(77)90505-7

Chappaz, A., Lyons, T. W., Gregory, D. D., Reinhard, C. T., Gill, B. C., Li, C., & Large, R. R. (2014). Does pyrite act as an important host for molybdenum in modern and ancient euxinic sediments? *Geochimica et Cosmochimica Acta*, *126*, 112–122. https://doi.org/10.1016/J.GCA.2013.10.028

Chow, T. J., & Goldberg, E. D. (1960). On the marine geochemistry of barium. *Geochimica et Cosmochimica Acta*, *20*(3–4), 192–198. https://doi.org/10.1016/0016-7037(60)90073-9

Close, H. G., Lam, P. J., & Popp, B. N. (2021). Marine Particle Chemistry: Influence on Biogeochemical Cycles and Particle Export. *ACS Earth and Space Chemistry*, *5*(5), 1210–1211. https://doi.org/10.1021/acsearthspacechem.1c00091

Collier, R., & Edmond, J. (1984). The trace element geochemistry of marine biogenic particulate matter. *Progress in Oceanography*, *13*(2), 113–199. https://doi.org/10.1016/0079-6611(84)90008-9

Compton, J. S., & Bergh, E. W. (2016). Phosphorite deposits on the Namibian shelf. *Marine Geology*, *380*, 290–314. https://doi.org/10.1016/j.margeo.2016.04.006

Cranston, R. E., & Murray, J. W. (1978). The determination of chromium species in natural waters. *Analytica Chimica Acta*, *99*(2), 275–282. https://doi.org/10.1016/S0003-2670(01)83568-6

Crusius, J., Calvert, S., Pedersen, T., & Sage, D. (1996). Rhenium and molybdenum enrichments in sediments as indicators of oxic, suboxic and sulfidic conditions of deposition. *Earth and Planetary Science Letters*, *145*(1–4), 65–78. https://doi.org/10.1016/S0012-821X(96)00204-X

Cullen, J. T., Field, M. P., & Sherrell, R. M. (2001). Determination of trace elements in filtered suspended marine particulate material by sector field HR-ICP-MS. *The Royal Society of Chemistry*, *16*, 1307–1312. https://doi.org/10.1039/b104398f

Cullen, J. T., & Sherrell, R. M. (1999). Techniques for determination of trace metals in small samples of size-fractionated particulate matter: phytoplankton metals off central California. *Marine Chemistry*, *67*, 233–247. http://www.whoi.edu/science/MCG/people/jcullen/CullenandSherrell1999MarChem.pdf

Cutter, G. A., Andersson, P. S., Codispoti, L., Croot, P. L., Francois, R., Lohan, M. C., Obata, H., & Rutgers van der Loeff, M. M. (2010). *Sampling and sample-handling protocols for GEOTRACES cruises*. *December*, 1–238. https://doi.org/http://www.geotraces.org/science/intercalibration/222-sampling-and-sample-handling-protocols-for-geotraces-cruises

Dehairs, F., Baeyens, W., & Goeyens, L. (1992). Accumulation of suspended barite at mesopelagic depths and export production in the Southern Ocean. *Science*, *258*(5086), 1332–1335. https://doi.org/10.1126/SCIENCE.258.5086.1332

Dehairs, F., Chesselet, R., & Jedwab, J. (1980). Discrete suspended particles of barite and the barium cycle in the open ocean. *Earth and Planetary Science Letters*, *49*(2), 528–550. https://doi.org/10.1016/0012-821X(80)90094-1

Dehairs, F., Goeyens, L., Stroobants, N., Bernard, P., Goyet, C., Poisson, A., & Chesselet, R. (1990). On suspended barite and the oxygen minimum in the Southern Ocean. *Global Biogeochemical Cycles*, *4*(1), 85–102. https://doi.org/10.1029/GB004I001P00085

Dehairs, F., Jacquet, S., Savoye, N., van Mooy, B. A. S., Buesseler, K. O., Bishop, J. K. B., Lamborg, C. H., Elskens, M., Baeyens, W., Boyd, P. W., Casciotti, K. L., & Monnin, C. (2008). Barium in twilight zone suspended matter as a potential proxy for particulate organic carbon remineralization: Results for the North Pacific. *Deep Sea Research Part II: Topical Studies in Oceanography*, *55*(14–15), 1673–1683. https://doi.org/10.1016/J.DSR2.2008.04.020

Dellwig, O., Beck, M., Lemke, A., Lunau, M., Kolditz, K., Schnetger, B., & Brumsack, H. J. (2007). Non-conservative behaviour of molybdenum in coastal waters: Coupling geochemical, biological, and sedimentological processes. *Geochimica et Cosmochimica Acta*, *71*(11), 2745–2761. https://doi.org/10.1016/J.GCA.2007.03.014

Dellwig, O., Wegwerth, A., Schnetger, B., Schulz, H., & Arz, H. W. (2019). Dissimilar behaviors of the geochemical twins W and Mo in hypoxic-euxinic marine basins. *Earth-Science Reviews*, *193*(August 2018), 1–23. https://doi.org/10.1016/j.earscirev.2019.03.017

Eagle, M., Paytan, A., Arrigo, K. R., van Dijken, G., & Murray, R. W. (2003). A comparison between excess barium and barite as indicators of carbon export. *Paleoceanography*, *18*(1). https://doi.org/10.1029/2002PA000793

Edmonds, H. N., & German, C. R. (2004). Particle geochemistry in the Rainbow hydrothermal plume, Mid-Atlantic Ridge. *Geochimica et Cosmochimica Acta*, *68*(4), 759–772. https://doi.org/10.1016/S0016-7037(03)00498-8

Elderfield, H. (1970). Chromium speciation in sea water. *Earth and Planetary Science Letters*, *9*(1), 10–16. https://doi.org/10.1016/0012-821X(70)90017-8

Emeis, K. C., Brüchert, V., Currie, B., Endler, R., Ferdelman, T., Kiessling, A., Leipe, T., Noli-Peard, K., Struck, U., & Vogt, T. (2004). Shallow gas in shelf sediments of the Namibian coastal

upwelling ecosystem. *Continental Shelf Research*, *24*(6), 627–642. https://doi.org/10.1016/j.csr.2004.01.007

Emerson, S. R., & Huested, S. S. (1991). Ocean anoxia and the concentrations of molybdenum and vanadium in seawater. *Marine Chemistry*, *34*(3–4), 177–196. https://doi.org/10.1016/0304-4203(91)90002-E

Erickson, B. E., & Helz, G. R. (2000). Molybdenum(VI) speciation in sulfidic waters:: Stability and lability of thiomolybdates. *Geochimica et Cosmochimica Acta*, *64*(7), 1149–1158. https://doi.org/10.1016/S0016-7037(99)00423-8

Esser, B. K., & Volpe, A. M. (2002). At-sea high-resolution chemical mapping: extreme barium depletion in North Pacific surface water. *Marine Chemistry*, *79*(2), 67–79. https://doi.org/10.1016/S0304-4203(02)00037-3

Feely, R. A., Gendron, J. F., Baker, E. T., & Lebon, G. T. (1994). Hydrothermal plumes along the East Pacific Rise, 8°40′ to 11°50′N: Particle distribution and composition. *Earth and Planetary Science Letters*, *128*(1–2), 19–36. https://doi.org/10.1016/0012-821X(94)90023-X

Feely, R. A., Massoth, G., & Trefry, J. (1989). The Role of Fe Oxhydroxides in Phosphorus, Vanadium and Arsenic Scavenging over the Mid Atlantic Ridge and Juan-De-Fuca Ridge Hydrothermal systems. *Abstracts of Papers of the American Chemical Society*, *198*(ISSN: 0065-7727), 102-GEOC. https://hero.epa.gov/hero/index.cfm/reference/details/reference_id/1345913

Finlay, B. J., Hetherington, N. B., & da Vison, W. (1983). Active biological participation in lacustrine barium chemistry. *Geochimica et Cosmochimica Acta*, *47*(7), 1325–1329. https://doi.org/10.1016/0016-7037(83)90071-6

Francois, R., Bacon, M. P., Altabet, M. A., & Labeyrie, L. D. (1993). Glacial/interglacial changes in sediment rain rate in the SW Indian Sector of subantarctic Waters as recorded by 230Th, 231Pa, U, and δ15N. *Paleoceanography*, *8*(5), 611–629. https://doi.org/10.1029/93PA00784

Frausto da Silva, J. J. R., & Williams, R. J. P. (2001). The principles of the uptake and chemical speciation of the elements in biology. *The Biological Chemistry of the Elements: The Inorganic Chemistry of Life*, *02*, 29–82. https://global.oup.com/academic/product/the-biological-chemistry-of-the-elements-9780198508489

Garner, C. D., & Stewart, L. J. (2002). Tungsten-substituted molybdenum enzymes. *Metal Ions in Biological Systems*, *39*, 699–726.

Glass, J. B., Axler, R. P., Chandra, S., & Goldman, C. R. (2012). Molybdenum limitation of microbial nitrogen assimilation in aquatic ecosystems and pure cultures. *Frontiers in Microbiology*, *3*(SEP). https://doi.org/10.3389/FMICB.2012.00331

Goldberg, T., Archer, C., Vance, D., & Poulton, S. W. (2009). Mo isotope fractionation during adsorption to Fe (oxyhydr)oxides. *Geochimica et Cosmochimica Acta*, *73*(21), 6502–6516. https://doi.org/10.1016/J.GCA.2009.08.004

Gonzalez-Muñoz, M. T., Martinez-Ruiz, F., Morcillo, F., Martin-Ramos, J. D., & Paytan, A. (2012). Precipitation of barite by marine bacteria: A possible mechanism for marine barite formation. *Geology*, *40*(8), 675–678. https://doi.org/10.1130/G33006.1

Gooday, A. J., & Nott, J. A. (1982). Intracellular Barite Crystals in Two Xenophyophores, *Aschemonella Ramuliformis* and *Galatheammina* Sp. (Protozoa: Rhizopoda) With Comments on the Taxonomy of *A. Ramuliformis*. *Journal of the Marine Biological Association of the United Kingdom*, *62*(3), 595–605. https://doi.org/10.1017/S0025315400019779

Goring-Harford, H. J., Klar, J. K., Pearce, C. R., Connelly, D. P., Achterberg, E. P., & James, R. H. (2018). Behaviour of chromium isotopes in the eastern sub-tropical Atlantic Oxygen Minimum Zone. *Geochimica et Cosmochimica Acta*, *236*, 41–59. https://doi.org/10.1016/J.GCA.2018.03.004

Hayes, C. T., Martínez-García, A., Hasenfratz, A. P., Jaccard, S. L., Hodell, D. A., Sigman, D. M., Haug, G. H., & Anderson, R. F. (2014). A stagnation event in the deep south atlantic during the last interglacial period. *Science*, *346*(6216), 1514–1517. https://doi.org/10.1126/SCIENCE.1256620/SUPPL_FILE/HAYES.SM.PDF

Helz, G. R., Miller, C. v., Charnock, J. M., Mosselmans, J. F. W., Pattrick, R. A. D., Garner, C. D., & Vaughan, D. J. (1996). Mechanism of molybdenum removal from the sea and its concentration in black shales: EXAFS evidence. *Geochimica et Cosmochimica Acta*, *60*(19), 3631–3642. https://doi.org/10.1016/0016-7037(96)00195-0

Hill, V. L., & Manley, S. L. (2009). Release of reactive bromine and iodine from diatoms and its possible role in halogen transfer in polar and tropical oceans. *Limnology and Oceanography*, *54*(3), 812–822. https://doi.org/10.4319/LO.2009.54.3.0812

Hille, R. (2002). Molybdenum and tungsten in biology. *Trends in Biochemical Sciences*, *27*(7), 360–367. https://doi.org/10.1016/S0968-0004(02)02107-2

Ho, P., Lee, J. M., Heller, M. I., Lam, P. J., & Shiller, A. M. (2018). The distribution of dissolved and particulate Mo and V along the U.S. GEOTRACES East Pacific Zonal Transect (GP16): The roles of oxides and biogenic particles in their distributions in the oxygen deficient zone and the hydrothermal plume. *Marine Chemistry*, *201*(October), 242–255. https://doi.org/10.1016/j.marchem.2017.12.003

Ho, T.-Y., Finkel, Z. v, Milligan, A. J., Wyman, K., Falkowski, P. G., & Morel, F. M. M. (2003). The elemental composition of some marine phytoplankton. *Journal of Phycology*, *39*, 1145–1159.

Honeyman, B. D., Balistrieri, L. S., & Murray, J. W. (1988). Oceanic trace metal scavenging: the importance of particle concentration. *Deep Sea Research Part A, Oceanographic Research Papers*, *35*(2), 227–246. https://doi.org/10.1016/0198-0149(88)90038-6

Horner, T. J., Little, S. H., Conway, T. M., Farmer, J. R., Hertzberg, J. E., Janssen, D. J., Lough, A. J. M., McKay, J. L., Tessin, A., Galer, S. J. G., Jaccard, S. L., Lacan, F., Paytan, A., & Wuttig, K. (2021). Bioactive Trace Metals and Their Isotopes as Paleoproductivity Proxies: An Assessment Using GEOTRACES-Era Data. *Global Biogeochemical Cycles*, *35*(11), 1–86. https://doi.org/10.1029/2020gb006814

Hunt, H. R., Summers, B. A., Sieber, M., Krisch, S., Al-Hashem, A., Hopwood, M. J., Achterberg, E. P., & Conway, T. M. (2022). Distinguishing the influence of sediments, the Congo River, and water-mass mixing on the distribution of iron and its isotopes in the Southeast Atlantic Ocean. *Marine Chemistry*, 104181. https://doi.org/10.1016/J.MARCHEM.2022.104181

Inthorn, M., Mohrholz, V., & Zabel, M. (2006). Nepheloid layer distribution in the Benguela upwelling area offshore Namibia. *Deep-Sea Research Part I: Oceanographic Research Papers*, *53*(8), 1423–1438. https://doi.org/10.1016/j.dsr.2006.06.004

Janssen, D. J., Rickli, J., Abbott, A. N., Ellwood, M. J., Twining, B. S., Ohnemus, D. C., Nasemann, P., Gilliard, D., & Jaccard, S. L. (2021). Release from biogenic particles, benthic fluxes, and deep water circulation control Cr and δ53Cr distributions in the ocean interior. *Earth and Planetary Science Letters*, *574*. https://doi.org/10.1016/j.epsl.2021.117163

Janssen, D. J., Rickli, J., Quay, P. D., White, A. E., Nasemann, P., & Jaccard, S. L. (2020). Biological Control of Chromium Redox and Stable Isotope Composition in the Surface Ocean. *Global Biogeochemical Cycles*, *34*(1). https://doi.org/10.1029/2019GB006397

Jeandel, C., & Oelkers, E. H. (2015). The influence of terrigenous particulate material dissolution on ocean chemistry and global element cycles. *Chemical Geology*, *395*, 50–66. https://doi.org/10.1016/j.chemgeo.2014.12.001

Jeandel, C., Rutgers van der Loeff, M., Lam, P. J., Roy-Barman, M., Sherrell, R. M., Kretschmer, S., German, C., & Dehairs, F. (2015). What did we learn about ocean particle dynamics in the GEOSECS-JGOFS era? *Progress in Oceanography*, *133*, 6–16. https://doi.org/10.1016/j.pocean.2014.12.018

Jickells, T. D. (2005). Global Iron Connections Between Desert Dust, Ocean Biogeochemistry, and Climate. *Science*, *308*(5718), 67–71. https://doi.org/10.1126/science.1105959

Jochum, K. P., Nohl, U., Herwig, K., Lammel, E., Stoll, B., & Hofmann, A. W. (2005). GeoReM: A new geochemical database for reference materials and isotopic standards. *Geostandards and Geoanalytical Research*, *29*(3), 333–338. https://doi.org/10.1111/j.1751-908x.2005.tb00904.x

Johannesson, K. H., Dave, H. B., Mohajerin, T. J., & Datta, S. (2013). Controls on tungsten concentrations in groundwater flow systems: The role of adsorption, aquifer sediment Fe(III) oxide/oxyhydroxide content, and thiotungstate formation. *Chemical Geology*, *351*, 76–94. https://doi.org/10.1016/J.CHEMGEO.2013.05.002

Johnson, T. L., Palenik, B., & Brahamsha, B. (2011). CHARACTERIZATION OF A FUNCTIONAL VANADIUM-DEPENDENT BROMOPEROXIDASE IN THE MARINE CYANOBACTERIUM SYNECHOCOCCUS SP. CC9311(1). *Journal of Phycology*, *47*(4), 792–801. https://doi.org/10.1111/J.1529-8817.2011.01007.X

Jullion, L., Jacquet, S. H. M., & Tanhua, T. (2017). Untangling biogeochemical processes from the impact of ocean circulation: First insight on the Mediterranean dissolved barium dynamics. *Global Biogeochemical Cycles*, *31*(8), 1256–1270. https://doi.org/10.1002/2016GB005489

Kashiwabara, T., Takahashi, Y., Tanimizu, M., & Usui, A. (2011). Molecular-scale mechanisms of distribution and isotopic fractionation of molybdenum between seawater and ferromanganese oxides. *Geochimica et Cosmochimica Acta*, *75*(19), 5762–5784. https://doi.org/10.1016/J.GCA.2011.07.022

Klein, N. J., Beck, A. J., Hutchins, D. A., & Sañudo-Wilhelmy, S. A. (2013). Regression modeling of the North East Atlantic Spring Bloom suggests previously unrecognized biological roles for V and Mo. *Frontiers in Microbiology*, *4*(MAR), 1–12. https://doi.org/10.3389/fmicb.2013.00045

Kletzin, A., & Adams, M. W. W. (1996). Tungsten in biological systems. *FEMS Microbiology Reviews*, *18*(1), 5–63. https://doi.org/10.1111/J.1574-6976.1996.TB00226.X

Kumar, N., Anderson, R. F., Mortlock, R. A., Froelich, P. N., Kubik, P., Dittrich-Hannen, B., & Suter, M. (1995). Increased biological productivity and export production in the glacial Southern Ocean. *Nature 1995 378:6558*, *378*(6558), 675–680. https://doi.org/10.1038/378675a0

Kunzendorf, H., & Glasby, G. P. (1992). Tungsten accumulation in Pacific ferromanganese deposits. *Mineralium Deposita 1992 27:2*, *27*(2), 147–152. https://doi.org/10.1007/BF00197100

Kurzweil, F., Archer, C., Wille, M., Schoenberg, R., Münker, C., & Dellwig, O. (2021). Redox control on the tungsten isotope composition of seawater. *Proceedings of the National Academy of Sciences of the United States of America*, *118*(18), e2023544118. https://doi.org/10.1073/PNAS.2023544118/SUPPL_FILE/PNAS.2023544118.SD05.XLSX

Lam, P. J., & Anderson, R. F. (2018). GEOTRACES: The Marine Biogeochemical Cycle of Trace Elements and Their Isotopes. *Elements*, *14*(6), 377–378. https://doi.org/10.2138/GSELEMENTS.14.6.377

Lamborg, C. H., Buesseler, K. O., & Lam, P. J. (2008). Sinking fluxes of minor and trace elements in the North Pacific Ocean measured during the VERTIGO program. *Deep-Sea Research Part II: Topical Studies in Oceanography*, *55*(14–15), 1564–1577. https://doi.org/10.1016/j.dsr2.2008.04.012

Lau, K. v., Lyons, T. W., & Maher, K. (2020). Uranium reduction and isotopic fractionation in reducing sediments: Insights from reactive transport modeling. *Geochimica et Cosmochimica Acta*, *287*, 65–92. https://doi.org/10.1016/j.gca.2020.01.021

le Roy, E., Sanial, V., Charette, M. A., van Beek, P., Lacan, F., Jacquet, H. M. S., Henderson, P. B., Souhaut, M., García-Ibáñez, M. I., Jeandel, C., Pérez, F. F., & Sarthou, G. (2018). The 226Ra-Ba relationship in the North Atlantic during GEOTRACES-GA01. *Biogeosciences*, *15*(9), 3027–3048. https://doi.org/10.5194/BG-15-3027-2018

Learman, D. R., Voelker, B. M., Vazquez-Rodriguez, A. I., & Hansel, C. M. (2011). Formation of manganese oxides by bacterially generated superoxide. *Nature Geoscience 2010 4:2*, *4*(2), 95–98. https://doi.org/10.1038/ngeo1055

Lerner, P. E., Marchal, O., Lam, P. J., Buesseler, K. O., & Charette, M. A. (2017). Kinetics of thorium and particle cycling along the U.S. GEOTRACES North Atlantic Transect. *Deep-Sea Research Part I: Oceanographic Research Papers*, *125*. https://doi.org/10.1016/j.dsr.2017.05.003

Lindh, U. (2013). Biological functions of the elements. *Essentials of Medical Geology: Revised Edition*, 129–177. https://doi.org/10.1007/978-94-007-4375-5_7/COVER

Liu, Te; Krisch, Stephan; Hopwood, Mark James; Achterberg, Eric Pieter; Mutzberg, André (2022): Trace metal data from water samples during METEOR cruise M121. PANGAEA, https://doi.org/10.1594/PANGAEA.947275

Liu, T., Krisch, S., Xie, R. C., Hopwood, M. J., Dengler, M., & Achterberg, E. P. (2022). Sediment Release in the Benguela Upwelling System Dominates Trace Metal Input to the Shelf and Eastern South Atlantic Ocean. *Global Biogeochemical Cycles*, *36*(9). https://doi.org/10.1029/2022GB007466

Maia, L. B., Moura, I., & Moura, J. J. G. (2016). CHAPTER 1:Molybdenum and Tungsten-Containing Enzymes: An Overview. *RSC Metallobiology*, *2017-January*(5), 1–80. https://doi.org/10.1039/9781782623915-00001

Marchal, O., & Lam, P. J. (2012). What can paired measurements of Th isotope activity and particle concentration tell us about particle cycling in the ocean? *Geochimica et Cosmochimica Acta*, *90*, 126–148. https://doi.org/10.1016/J.GCA.2012.05.009

Martinez-Ruiz, F., Paytan, A., Gonzalez-Muñoz, M. T., Jroundi, F., Abad, M. M., Lam, P. J., Bishop, J. K. B., Horner, T. J., Morton, P. L., & Kastner, M. (2019). Barite formation in the

ocean: Origin of amorphous and crystalline precipitates. *Chemical Geology*, *511*, 441–451. https://doi.org/10.1016/j.chemgeo.2018.09.011

McManus, J., Berelson, W. M., Klinkhammer, G. P., Hammond, D. E., & Holm, C. (2005). Authigenic uranium: Relationship to oxygen penetration depth and organic carbon rain. *Geochimica et Cosmochimica Acta*, *69*(1), 95–108. https://doi.org/10.1016/J.GCA.2004.06.023

McManus, J., Berelson, W. M., Klinkhammer, G. P., Johnson, K. S., Coale, K. H., Anderson, R. F., Kumar, N., Burdige, D. J., Hammond, D. E., Brumsack, H. J., McCorkle, D. C., & Rushdi, A. (1998). Geochemistry of barium in marine sediments: implications for its use as a paleoproxy. *Geochimica et Cosmochimica Acta*, *62*(21–22), 3453–3473. https://doi.org/10.1016/S0016-7037(98)00248-8

McManus, J., Berelson, W. M., Severmann, S., Poulson, R. L., Hammond, D. E., Klinkhammer, G. P., & Holm, C. (2006). Molybdenum and uranium geochemistry in continental margin sediments: Paleoproxy potential. *Geochimica et Cosmochimica Acta*, *70*(18), 4643–4662. https://doi.org/10.1016/J.GCA.2006.06.1564

McManus, J., Poulson, R. L., Siebert, C., & Berelson, W. M. (2005). The Molybdenum Isotope Paleoproxy: Defining Signatures of Reducing Conditions in Marine Sediments. *AGUFM*, *2005*, PP34A-01. https://ui.adsabs.harvard.edu/abs/2005AGUFMPP34A..01M/abstract

Miletto, M., Wang, X., Planavsky, N. J., Luther, G. W., Lyons, T. W., & Tebo, B. M. (2021). Marine microbial Mn(II) oxidation mediates Cr(III) oxidation and isotope fractionation. *Geochimica et Cosmochimica Acta*, *297*, 101–119. https://doi.org/10.1016/j.gca.2021.01.008

Mohajerin, T. J., Helz, G. R., & Johannesson, K. H. (2016). Tungsten–molybdenum fractionation in estuarine environments. *Geochimica et Cosmochimica Acta*, *177*, 105–119. https://doi.org/10.1016/J.GCA.2015.12.030

Mohajerin, T. J., Helz, G. R., White, C. D., & Johannesson, K. H. (2014). Tungsten speciation in sulfidic waters: Determination of thiotungstate formation constants and modeling their distribution in natural waters. *Geochimica et Cosmochimica Acta*, *144*, 157–172. https://doi.org/10.1016/J.GCA.2014.08.037

Monnin, C., Jeandel, C., Cattaldo, T., & Dehairs, F. (1999). The marine barite saturation state of the world's oceans. *Marine Chemistry*, *65*(3–4), 253–261. https://doi.org/10.1016/S0304-4203(99)00016-X

Moos, S. B., Boyle, E. A., Altabet, M. A., & Bourbonnais, A. (2020). Investigating the cycling of chromium in the oxygen deficient waters of the Eastern Tropical North Pacific Ocean and the Santa Barbara Basin using stable isotopes. *Marine Chemistry*, *221*, 103756. https://doi.org/10.1016/J.MARCHEM.2020.103756

Nasemann, P., Janssen, D. J., Rickli, J., Grasse, P., Frank, M., & Jaccard, S. L. (2020). Chromium reduction and associated stable isotope fractionation restricted to anoxic shelf waters in the Peruvian Oxygen Minimum Zone. *Geochimica et Cosmochimica Acta*, *285*, 207–224. https://doi.org/10.1016/j.gca.2020.06.027

Nealson, K. H., Tebo, B. M., & Rosson, R. A. (1988). Occurrence and Mechanisms of Microbial Oxidation of Manganese. *Advances in Applied Microbiology*, *33*(C), 279–318. https://doi.org/10.1016/S0065-2164(08)70209-0

Neff, J. M. (2002). Barium in the Ocean. *Bioaccumulation in Marine Organisms*, *December 2002*, 79–87. https://doi.org/10.1016/b978-008043716-3/50005-1

Nuester, J., Vogt, S., Newville, M., Kustka, A. B., & Twining, B. S. (2012). The unique biogeochemical signature of the marine diazotroph Trichodesmium. *Frontiers in Microbiology*, *3*(APR), 1–15. https://doi.org/10.3389/fmicb.2012.00150

Ohnemus, D. C., Rauschenberg, S., Cutter, G. A., Fitzsimmons, J. N., Sherrell, R. M., & Twining, B. S. (2017). Elevated trace metal content of prokaryotic communities associated with marine oxygen deficient zones. *Limnology and Oceanography*, *62*(1), 3–25. https://doi.org/10.1002/LNO.10363

Ohnemus, D. C., Torrie, R., & Twining, B. S. (2019). Exposing the Distributions and Elemental Associations of Scavenged Particulate Phases in the Ocean Using Basin-Scale Multi-Element Data Sets. *Global Biogeochemical Cycles*, *33*(6), 725–748. https://doi.org/10.1029/2018GB006145

Paytan, A., & Griffith, E. M. (2007). Marine barite: Recorder of variations in ocean export productivity. *Deep Sea Research Part II: Topical Studies in Oceanography*, *54*(5–7), 687–705. https://doi.org/10.1016/J.DSR2.2007.01.007

Planchon, F., Cavagna, A. J., Cardinal, D., André, L., & Dehairs, F. (2013). Late summer particulate organic carbon export and twilight zone remineralisation in the Atlantic sector of the Southern Ocean. *Biogeosciences*, *10*(2), 803–820. https://doi.org/10.5194/bg-10-803-2013

Rahman, S., Shiller, A. M., Anderson, R. F., Charette, M. A., Hayes, C. T., Gilbert, M., Grissom, K. R., Lam, P. J., Ohnemus, D. C., Pavia, F. J., Twining, B. S., & Vivancos, S. M. (2022). Dissolved and Particulate Barium Distributions Along the US GEOTRACES North Atlantic and East Pacific Zonal Transects (GA03 and GP16): Global Implications for the Marine Barium Cycle. *Global Biogeochemical Cycles*, *36*(6), 1–33. https://doi.org/10.1029/2022gb007330

Rauschenberg, S., & Twining, B. S. (2015). Evaluation of approaches to estimate biogenic particulate trace metals in the ocean. *Marine Chemistry*, *171*, 67–77. https://doi.org/10.1016/j.marchem.2015.01.004

Rudnick, R. L., & Gao, S. (2013). Composition of the Continental Crust. In *Treatise on Geochemistry: Second Edition* (2nd ed., Vol. 4, Issue November). Elsevier Ltd. https://doi.org/10.1016/B978-0-08-095975-7.00301-6

Rushdi, A. I., McManus, J., & Collier, R. W. (2000). Marine barite and celestite saturation in seawater. *Marine Chemistry*, *69*(1–2), 19–31. https://doi.org/10.1016/S0304-4203(99)00089-4

Rutgers Van Der Loeff, M. M., & Boudreau, B. P. (1997). The effect of resuspension on chemical exchanges at the sediment-water interface in the deep sea - A modelling and natural radiotracer approach. *Journal of Marine Systems*, *11*(3–4), 305–342. https://doi.org/10.1016/S0924-7963(96)00128-5

Sadiq, M. (1988). Thermodynamic solubility relationships of inorganic vanadium in the marine environment. *Marine Chemistry*, *23*(1–2), 87–96. https://doi.org/10.1016/0304-4203(88)90024-2

Santschi, P. H., Murray, J. W., Baskaran, M., Benitez-Nelson, C. R., Guo, L. D., Hung, C. C., Lamborg, C., Moran, S. B., Passow, U., & Roy-Barman, M. (2006). Thorium speciation in seawater. *Marine Chemistry*, *100*(3–4), 250–268. https://doi.org/10.1016/J.MARCHEM.2005.10.024

Schlitzer, R., Ocean Data View, https://odv.awu.de, 2019.

Schoepfer, S. D., Shen, J., Wei, H., Tyson, R. v., Ingall, E., & Algeo, T. J. (2015). Total organic carbon, organic phosphorus, and biogenic barium fluxes as proxies for paleomarine productivity. *Earth-Science Reviews*, *149*, 23–52. https://doi.org/10.1016/J.EARSCIREV.2014.08.017

Scholz, F., Hensen, C., Noffke, A., Rohde, A., Liebetrau, V., & Wallmann, K. (2011). Early diagenesis of redox-sensitive trace metals in the Peru upwelling area - response to ENSO-related oxygen fluctuations in the water column. *Geochimica et Cosmochimica Acta*, *75*(22), 7257–7276. https://doi.org/10.1016/j.gca.2011.08.007

Scott, C., & Lyons, T. W. (2012). Contrasting molybdenum cycling and isotopic properties in euxinic versus non-euxinic sediments and sedimentary rocks: Refining the paleoproxies. *Chemical Geology*, *324–325*, 19–27. https://doi.org/10.1016/J.CHEMGEO.2012.05.012

Semeniuk, D. M., Maldonado, M. T., & Jaccard, S. L. (2016). Chromium uptake and adsorption in marine phytoplankton – Implications for the marine chromium cycle. *Geochimica et Cosmochimica Acta*, *184*, 41–54. https://doi.org/10.1016/J.GCA.2016.04.021

Shannon, L. (2001). Benguela current. In *Encyclopedia of Ocean Sciences* (1st ed., pp. 225–267).

Sunda, W. G. (2012). Feedback interactions between trace metal nutrients and phytoplankton in the ocean. *Frontiers in Microbiology*, *3*(JUN), 1–22. https://doi.org/10.3389/fmicb.2012.00204

Tebo, B. M., Bargar, J. R., Clement, B. G., Dick, G. J., Murray, K. J., Parker, D., Verity, R., & Webb, S. M. (2004). Biogenic manganese oxides: Properties and mechanisms of formation. *Annual Review of Earth and Planetary Sciences*, *32*(Goldberg 1954), 287–328. https://doi.org/10.1146/annurev.earth.32.101802.120213

Tebo, B. M., Johnson, H. A., McCarthy, J. K., & Templeton, A. S. (2005). Geomicrobiology of manganese(II) oxidation. *Trends in Microbiology*, *13*(9), 421–428. https://doi.org/10.1016/j.tim.2005.07.009

Thomas, H., Shadwick, E., Dehairs, F., Lansard, B., Mucci, A., Navez, J., Gratton, Y., Prowe, F., Chierici, M., Fransson, A., Papakyriakou, T. N., Sternberg, E., Miller, L. A., Tremblay, J. R., & Monnin, C. (2011). Barium and carbon fluxes in the Canadian Arctic Archipelago. *Journal of Geophysical Research: Oceans*, *116*(C9), 0–08. https://doi.org/10.1029/2011JC007120

Tovar-Sanchez, A., & Sañudo-Wilhelmy, S. A. (2011). Influence of the Amazon River on dissolved and intra-cellular metal concentrations in Trichodesmium colonies along the western boundary of the sub-tropical North Atlantic Ocean. *Biogeosciences*, *8*(1), 217–225. https://doi.org/10.5194/bg-8-217-2011

Trefry, J. H., & Metz, S. (1989). Role of hydrothermal precipitates in the geochemical cycling of vanadium. *Nature 1989 342:6249*, *342*(6249), 531–533. https://doi.org/10.1038/342531a0

Tribovillard, N., Algeo, T. J., Baudin, F., & Riboulleau, A. (2012). *Analysis of marine environmental conditions based on molybdenum-uranium covariation-Applications to Mesozoic paleoceanography*. https://doi.org/10.1016/j.chemgeo.2011.09.009

Tribovillard, N., Algeo, T. J., Lyons, T., & Riboulleau, A. (2006). Trace metals as paleoredox and paleoproductivity proxies: An update. *Chemical Geology*, *232*(1–2), 12–32. https://doi.org/10.1016/J.CHEMGEO.2006.02.012

Twining, B. S., & Baines, S. B. (2013). The Trace Metal Composition of Marine Phytoplankton. *Annu. Rev. Mar. Sci*, *5*, 191–215. https://doi.org/10.1146/annurev-marine-121211-172322

Twining, B. S., Nodder, S. D., King, A. L., Hutchins, D. A., Lecleir, G. R., Debruyn, J. M., Maas, E. W., Vogt, S., Wilhelm, S. W., & Boyd, P. W. (2014). Differential remineralization of major and trace elements in sinking diatoms. *Limnology and Oceanography*, *59*(3), 689–704. https://doi.org/10.4319/lo.2014.59.3.0689

Vieira, L. H. (2019). *Radium isotopes as tracers of element cycling at ocean boundaries* [Christian-Albrechts-Universitat zu Kiel]. https://macau.uni-kiel.de/receive/diss_mods_00025629

Vieira, L. H., Krisch, S., Hopwood, M. J., Beck, A. J., Scholten, J., Liebetrau, V., & Achterberg, E. P. (2020). Unprecedented Fe delivery from the Congo River margin to the South Atlantic Gyre. *Nature Communications*, *11*(1), 1–8. https://doi.org/10.1038/s41467-019-14255-2

Weber, T. S., & Bianchi, D. (2020). Efficient Particle Transfer to Depth in Oxygen Minimum Zones of the Pacific and Indian Oceans. *Frontiers in Earth Science*, *8*(September), 1–11. https://doi.org/10.3389/feart.2020.00376

Whitmore, L. M., Morton, P. L., Twining, B. S., & Shiller, A. M. (2019). Vanadium cycling in the Western Arctic Ocean is influenced by shelf-basin connectivity. *Marine Chemistry*, *216*, 103701. https://doi.org/10.1016/J.MARCHEM.2019.103701

Wong, P., & Trevors, J. (1988). Chromium toxicity to algae and bacteria. *Undefined*.

Zheng, Y., Anderson, R. F., van Geen, A., & Fleisher, M. Q. (2002). Preservation of particulate non-lithogenic uranium in marine sediments. *Geochimica et Cosmochimica Acta*, *66*(17), 3085–3092. https://doi.org/10.1016/S0016-7037(01)00632-9

Supporting Information for

Distributions of Labile and Refractory Particulate Biogeochemical Tracers (V, Mo, W, Cr, Ba, Th, and U) on the Southwest African Shelf

Ali A. Al-Hashem[1,2*], Aaron J. Beck[1], Stephan Krisch[1,3], Te Liu[1], Tim Steffens[1], Mark J. Hopwood[1,4], Eric P. Achterberg[1,2].

[1]Marine Biogeochemistry Division, GEOMAR Helmholtz Centre for Ocean Research Kiel, Kiel 24148, Germany.
[2]Christian-Albrechts-University of Kiel, Christian-Albrechts-Platz 4 24118 Kiel, Germany.
[3]Now at: Bundesanstalt für Gewässerkunde, Am Mainzer Tor 1, 56068 Koblenz, Germany.
[4]Now at: Southern University of Science and Technology, Shenzhen, China.

*Corresponding author: Ali A. Al-Hashem (aalhashem@geomar.de)

Contents of this section

Keywords: Marine Particles; Trace Elements; Oxygen Minimum Zone; Continental Shelf; GEOTRACES; Congo River.

Table S5.1 - Sample procedural blanks, limits of detection, average sample relative standard deviations (RSD%) and percent of samples that were below the detection limit (BDL) of labile (L-pTM) and refractory (R-pTM) particulate fractions. Samples were processed in 13 separate leach-digestion batches. Limits of Detection were determined as 3x the standard deviation (SD) of procedural blanks. Certified Reference Material (CRM) recoveries were compared to certified values and consensus values from the GeoReM database (Jochum et al., 2005).

	n	V	Mo	Cr	W	Ba	U	Th	Al	Fe	Ti	P	Mn
Average Process Blank L-pTM (pM/filter ± 1 SD)	***30***	**0.07 ± 0.12**	**0.32 ± 0.28**	**45.0 ± 28.9**	**0.013 ± 0.01**	**1.72 ± 0.82**	**0.006 ± 0.001**	**0.0009 ± 0.0011**	**116 ± 117**	**119 ± 128**	**0.9 ± 1.6**	**415 ± 973**	**2.7 ± 1.8**
Median Process Blank L-pTM (pM/filter)		0.02	0.31	36.29	0.013	1.47	0.006	0.0003	103	103	0.2	44	2.3
L-pTM Detection Limit (pM/filter)		0.02	0.84	86.6	0.04	2.47	0.0034	0.0032	351	384	4.9	2920	5.4
Percent Samples BDL		1%	7%	20%	21%	0%	0%	28%	0%	6%	27%	3%	0%
Average (L-pTM) Sample RSD (%) (1 SD)		3%	4%	3%	15%	3%	4%	6%	3%	2%	8%	7%	2%
Average Process Blank R-pTM (pM/filter ± 1 SD)	***30***	**0.12 ± 0.2**	**0.37 ± 0.28**	**10.2 ± 14.9**	**0.14 ± 0.13**	**0.34 ± 0.34**	**0.002 ± 0.005**	**0.007 ± 0.008**	**130 ± 125**	**165 ± 616**	**115 ± 148**	**128 ± 198**	**1.1 ± 2.6**
Median Process Blank R-pTM (pM/filter)		0.61	0.31	4.64	0.08	0.28	0.001	0.004	120	68	79	91	0.37
R-pTM Detection Limit (pM/filter)		0.61	0.84	44.5	0.40	1.02	0.01	0.025	376	1849	445	595	7.9
Percent Samples BDL		7%	1%	3%	2%	1%	0%	5%	0%	3%	1%	0%	14%
Average (R-pTM) Sample RSD (%) (1 SD)		7%	8%	5%	37%	8%	12%	11%	5%	4%	10%	19%	5%
	N	**V**	**Mo**	**Cr**	**W**	**Ba**	**U**	**Th**	**Al**	**Fe**	**Ti**	**P**	**Mn**
BCR-414 Certified/Ref. Values (ng/mg ± 1 SD)		**8.1 ± 0.18**	**1.35 ± 0.2**	**23.8 ± 1.2**	n/a	**31 ± 7**	**0.14 ± 0.01**	**n/a**	*2673 ± 96*	1850 ± 190	*126 ± 4*	*13400 ± 3200*	**299 ± 13**
BCR-414 Recovery (Labile, ng/mg ± 1 SD)	***25***	3.06 ± 0.28	0.20 ± 0.08	1.54 ± 0.22	0.02 ±0.007	20.0 ± 1.89	0.025 ± 0.004	0.032 ± 0.009	51.6 ± 5.30	346 ± 35.2	0.44 ± 0.09	14687 ± 3027	262 ± 17.5
BCR-414 Recovery (Total, % ± 1 SD)	***25***	110 ± 10.8	129 ± 26.4	107 ± 8.9	n/a	109 ± 25.4	94.2 ± 26.2	n/a	108.6 ± 7.8	103.6 ± 14	109.4 ± 8.9	113.1 ± 20.7	92.5 ± 8.3
PACS-3 Certified/Ref. Values (ng/mg ± 1 SD)		**129 ± 8**	***5.9***	**90.6 ± 4**	*n/a*	**n/a**	***2.6***	n/a	***65800 ± 1200***	**41060 ± 640**	**4420 ± 180**	**937 ± 44**	**432 ± 16**
PACS-3 Recovery (Total, % ± 1 SD)	***3***	110 ± 1.3	129 ± 8.7	105 ± 0.8	*n/a*	n/a	95.3 ± 1.8	**n/a**	84.9 ± 1.8	84.6 ± 2.2	95.4 ± 4.4	112.1 ± 7.5	96.7 ± 2.2

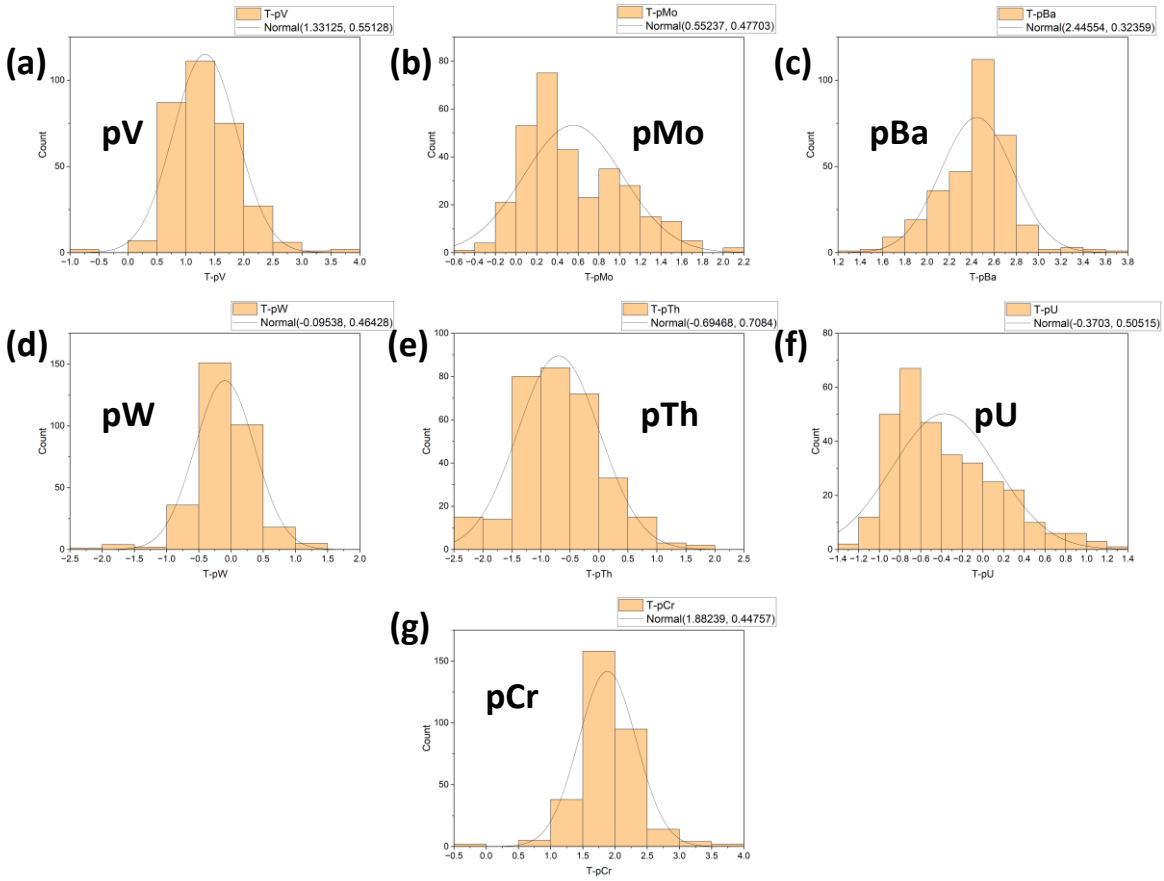

	Distribution	Parameter	Estimate	Lower 95%	Upper 95%
T-pV	Normal	Location mu	1.33125	1.27066	1.39184
		Scale sigma	0.55128	0.50997	0.59594
T-pMo	Normal	Location mu	0.55237	0.49994	0.6048
		Scale sigma	0.47703	0.44128	0.51568
T-pBa	Normal	Location mu	2.44554	2.40998	2.48111
		Scale sigma	0.32359	0.29934	0.3498
T-pW	Normal	Location mu	-0.09538	-0.14641	-0.04435
		Scale sigma	0.46428	0.42948	0.50189
T-pTh	Normal	Location mu	-0.69468	-0.77254	-0.61682
		Scale sigma	0.7084	0.65531	0.7658
T-pU	Normal	Location mu	-0.3703	-0.42582	-0.31478
		Scale sigma	0.50515	0.46729	0.54608
T-pCr	Normal	Location mu	1.88239	1.8332	1.93158
		Scale sigma	0.44757	0.41403	0.48383

Figure S5.1 - Distributions of Log Transformed total particulate trace metal datasets for (a) Vanadium (V); (b) Molybdenum (Mo); (c) Barium (Ba); (d) Tungsten (W); (e) Thorium (Th); (f) Uranium (U); and (g) Chromium (Cr); and (table) results of distribution fit parameter estimates executed on OriginPro (Version 9.9.5).

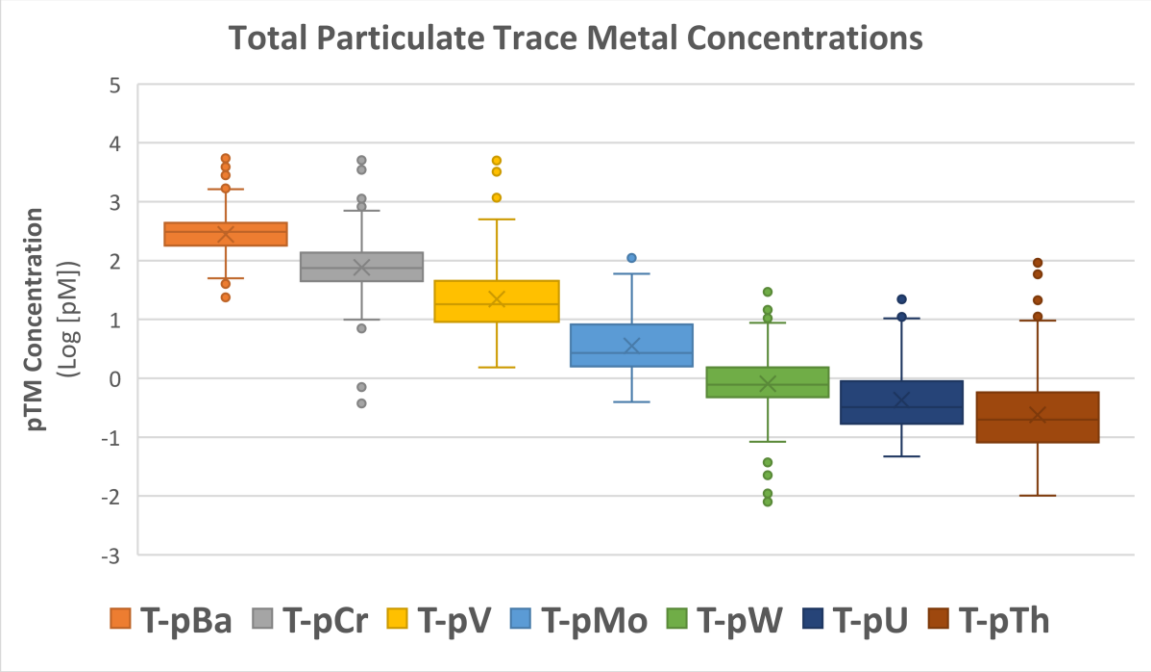

Figure S5.2 - Total particulate trace metal (T-pTM) concentration ranges for (left to right) Barium (Ba), Chromium (Cr), Vanadium (V), Molybdenum (Mo), Tungsten (W), Uranium (U), and Thorium (Th) in samples across the GA08 shelf region. Note the logarithmic concentration scale (pM). The ends of boxes and whiskers represent the 25th and 75th percentiles and the 5th and 95th percentiles, respectively. The points beyond the whiskers represent outliers. The horizontal line and "X" within each box represent the median and mean, respectively. Total particulate concentrations shown are the sum of the sample labile and refractory particulate concentrations.

Table S5.2 - Total particulate trace metal (pTM) concentrations of samples from our study area (GA08) compared to other reported shelf and slope regions (< 1000 m bottom depth). The ranges reported are of the upper and lower quartile values of all particulate samples within the respective stations referenced. Reference values were compiled from the GEOTRACES IDP2021 or where noted in remarks.

Region		pV [pM]	pMo [pM]	pW [pM]	pCr [pM]	pBa [pM]	pU [pM]	pTh [pM]	pAl [nM]	pFe [nM]	pTi [nM]	pP [nM]	Remarks
SW Africa Shelf	**1st-3rd Quart**	**20.6 - 94.6**	**2.66 - 13.1**	**0.71 - 1.81**	**66.0 - 200**	**205 - 540**	**0.32 - 2.01**	**0.18 - 1.19**	**10.1 - 71.4**	**4.29 - 23.9**	**0.37 - 1.76**	**10.7 - 62.6**	GA08
(This Study)	*MAX conc.*	**5010**	**59.7**	**29.2**	**5071**	**5478**	**22.1**	**92.1**	**5111**	**1697**	**138**	**253**	
Peruvian Shelf	**1st-3rd Quart**	24.5 – 62.1	n/a	n/a	n/a	278 – 586	n/a	0.055 - 0.118	3.01 - 7.47	3.52 - 9.68	0.07 - 0.12	27.4 - 79.5	GP16 (ST 2-4)
	MAX conc.	660	n/a	n/a	n/a	3435	n/a	2.15	162	159	2.96	983	
South Africa	**1st-3rd Quart**	14.9 – 167	2.93 – 8.37	n/a	n/a	215 – 395	n/a	n/a	2.28 - 26.2	0.1 - 6.60	0.14 - 0.65	8.1 - 47.4	GA10
	MAX conc.	520	23.4	n/a	n/a	687	n/a	n/a	131	37.8	3.61	131	(ST 8)
Uruguay	**1st-3rd Quart**	87.0 - 529	31.7 – 130	n/a	n/a	1589 – 2804	n/a	n/a	50.1 - 501	10.8 - 144	1.66 - 18.1	54.8 - 75.4	GA10
	MAX conc.	718	172	n/a	n/a	2178	n/a	n/a	1005	280	23.8	81.7	(ST 24)
Portugal	**1st-3rd Quart**	13.3 – 37.8	1.04 – 4.34	n/a	8.69 - 22.6	174 – 326	n/a	n/a	7.88 - 50.8	2.01 - 10.0	0.13 - 0.87	2.05 - 16.4	GA01
	MAX conc.	951	12.1	n/a	666	1496	n/a	n/a	1544	304	21.5	34.2	(ST 2+4)
Greenland	**1st-3rd Quart**	41.0 – 53.0	0.71 – 3.02	n/a	20.2 – 23.7	161 – 293	n/a	n/a	21.9 - 58.8	4.37 - 16.5	0.55 - 1.79	17.7 - 47.3	GA01
	MAX conc.	70.9	4.12	n/a	38.8	568	n/a	n/a	75.3	22.1	2.39	161	(ST 53+56)
Senegal	**1st-3rd Quart**	n/a	15.0 – 23.4	n/a	n/a	171 – 249	n/a	n/a	366 - 595	75.9 - 114	11 - 19.2	56.3 - 78	GA06
	MAX conc.	n/a	25.2	n/a	n/a	569	n/a	n/a	779	134	26.1	83.6	(ST 4+5)
Bering Sea	**1st-3rd Quart**	13.8 - 1042	4.78 – 14.3	n/a	138 – 585	414 – 766	n/a	0.03 – 7.82	2.75 - 454	1.15 - 213	0.29 - 20.1	12.7 - 83.6	GN01
	MAX conc.	10996	53.2	n/a	4929	2839	n/a	57.0	5213	2246	262	308	(ST1-3)
Chukchi Sea	**1st-3rd Quart**	168 – 2571	6.41 - 20.1	n/a	195 – 1668	412 – 2706	n/a	1.21 – 22.2	89.4 - 1759	23.4 - 500	2.38 - 52.7	27.0 - 173	GN01
	MAX conc.	10135	135	n/a	5094	12705	n/a	80.3	6170	2262	207	336	(ST 4-6; 8; 10; 61; 66)
Newfoundland	**1st-3rd Quart**	42.4 – 238	1.61 – 3.56	n/a	97.7 – 229	361 – 664	n/a	n/a	25.1 - 248	8.14 - 75.8	0.77 - 7.44	17.3 - 32.8	GA01
	MAX conc.	514	4.7	n/a	465	1350	n/a	n/a	559	168	16.7	96.8	(ST 78)
***Southern**	**1st-3rd Quart**	n/a	n/a	n/a	n/a	n/a	0.37 - 0.75	n/a	n/a	n/a	n/a	n/a	GIPY02
Ocean	*MAX conc.*	n/a	n/a	n/a	n/a	n/a	5.11	n/a	n/a	n/a	n/a	n/a	*(Deep stations)
Baltic Sea	***Total Range**	10-6500	30-500	1.0-60	n/a	n/a	n/a	n/a	n/a	n/a	n/a	n/a	Bauer et al., (2017)
	MAX conc.			n/a	n/a	n/a	n/a	n/a	n/a	n/a	n/a	n/a	

Table S5.3 - Summarized results of two-tailed unequal variance student t-test between samples from BENG stations (ST 43-51 & 1-5) and NORTH stations (ST 6-20) for each element in the total particulate trace metal (T-pTM), labile particulate trace metal (L-pTM), refractory particulate trace metal (R-pTM) fractions, as well as L-pTM/T-pTM fractions (%). Bold: highlights *p*-values < 0.05.

Student's T-Test Results
2-Tailed Unequal Variance

	T-pTM	L-pTM	R-pTM	L-pTM/T-pTM
V	0.064	0.060	0.065	**0.000**
Mo	**0.000**	**0.001**	**0.000**	**0.000**
Ba	**0.000**	**0.000**	**0.004**	0.083
W	**0.003**	**0.001**	**0.003**	0.934
Cr	**0.001**	**0.000**	**0.002**	0.322
U	**0.000**	**0.000**	**0.000**	**0.000**
Th	0.072	0.155	0.071	0.328

Table S5.4 - Summary of the upper and lower quartile values of the labile (L-pTM), refractory (R-pTM), and total (T-pTM) particulate trace metal ratios, normalized to the biogenic particle indicator, particulate phosphorus (pP), and lithogenic particle indicator, refractory particulate aluminum (R-pAl) from samples within the respective regions along the GA08 transect.

Surface (≤50 m & < 25 nM R-pAl) *n=53*	**V mmol:mol**	**Mo mmol:mol**	**W mmol:mol**	**Cr mmol:mol**	**Ba mmol:mol**	**U mmol:mol**	**Th mmol:mol**
L-pTM:L-pP	0.33 - 1.37	0.07 - 0.68	0.000 - 0.006	0.57 - 2.75	2.91 - 14.7	0.009 - 0.020	0.000 - 0.000
T-pTM:T-pP	0.19 - 0.53	0.12 - 0.45	0.016 - 0.056	0.89 - 3.31	1.63 - 5.77	0.010 - 0.023	0.001 - 0.005
R-pTM:R-pAl	0.31 - 1.89	0.66 - 4.51	0.161 - 0.816	3.11 – 48.0	2.04 - 16.9	0.020 - 0.432	0.018 - 0.040
T-pTM:R-pAl	2.18 - 10.29	1.19 - 8.06	0.16 - 0.82	5.01 - 52.3	13.1 - 83.4	0.06 - 0.60	0.02 - 0.04
Nepheloid samples (≥25 nM R-pAl*) *n=90*	**V mmol:mol**	**Mo mmol:mol**	**W mmol:mol**	**Cr mmol:mol**	**Ba mmol:mol**	**U mmol:mol**	**Th mmol:mol**
L-pTM:L-pP	3.35 - 11.47	0.115 - 0.401	0.000 - 0.018	3.99 - 12.7	20.6 - 86.3	0.032 - 0.106	0.001 - 0.014
T-pTM:T-pP	2.70 - 12.26	0.203 - 0.441	0.037 - 0.138	5.01 - 15.9	12.9 - 46.3	0.026 - 0.076	0.033 - 0.198
UCC Reference Values TM:Al	*0.630 ± 0.069*	*0.0038±0.0011*	*0.0034±0.0019*	*0.586 ± 0.111*	*1.51 ± 0.197*	*0.0038±0.0008*	*0.015±0.0015*
R-pTM:R-pAl	0.613 - 0.796	0.017 - 0.096	0.009 - 0.024	0.811 - 1.90	0.981 - 3.10	0.002 - 0.010	0.014 - 0.019
T-pTM:R-pAl	0.903 - 1.376	0.028 - 0.147	0.009 - 0.025	1.34 - 2.51	2.93 - 8.98	0.005 - 0.018	0.015 - 0.020
River Plume (ST13-20 & <15 m from ST21-22) *n=77*	**V mmol:mol**	**Mo mmol:mol**	**W mmol:mol**	**Cr mmol:mol**	**Ba mmol:mol**	**U mmol:mol**	**Th mmol:mol**
L-pTM:L-pP	3.94 - 9.48	0.199 - 0.732	0.007 - 0.021	4.21 - 15.3	23.6 - 82.2	0.021 - 0.102	0.003 - 0.013
T-pTM:T-pP	2.72 - 9.55	0.225 - 0.498	0.055 - 0.124	3.60 - 13.1	11.9 - 44.0	0.017 - 0.062	0.034 - 0.126
R-pTM:R-pAl	0.580 - 0.827	0.020 - 0.163	0.011 - 0.066	0.755 - 2.19	0.945 - 4.00	0.002 - 0.010	0.016 - 0.024
T-pTM:R-pAl	1.12 - 2.03	0.036 - 0.361	0.012 - 0.069	1.38 - 4.28	3.70 - 18.0	0.006 - 0.027	0.017 - 0.026
Open Ocean (ST21-24) *n=88*	**V mmol:mol**	**Mo mmol:mol**	**W mmol:mol**	**Cr mmol:mol**	**Ba mmol:mol**	**U mmol:mol**	**Th mmol:mol**
L-pTM:L-pP	2.06 - 12.8	0.302 - 1.02	0.006 - 0.024	0.00 - 30.7	55.2 – 200	0.045 - 0.241	0.000 - 0.005
T-pTM:T-pP	0.585 - 5.39	0.257 - 0.677	0.038 - 0.183	4.36 - 31.1	36.7 – 119	0.024 - 0.107	0.005 - 0.063
R-pTM:R-pAl	0.632 - 1.20	0.151 - 1.75	0.067 - 0.549	6.41 - 30.5	14.9 – 134	0.011 - 0.123	0.028 - 0.052
T-pTM:R-pAl	2.32 - 5.96	0.325 - 2.36	0.072 - 0.563	7.35 - 42.6	41.1 – 239	0.045 - 0.256	0.029 - 0.053
OMZ (<60 µM oxygen & <25 nM R-pAl) *n=53*	**V mmol:mol**	**Mo mmol:mol**	**W mmol:mol**	**Cr mmol:mol**	**Ba mmol:mol**	**U mmol:mol**	**Th mmol:mol**
L-pTM:L-pP	1.08 - 4.83	0.078 - 0.329	0.002 - 0.016	1.40 - 8.97	35.1 – 129	0.023 - 0.090	0.000 - 0.002
T-pTM:T-pP	0.87 - 2.62	0.22 - 0.41	0.044 - 0.251	3.62 - 10.7	26.6 - 70.8	0.023 - 0.046	0.006 - 0.037
R-pTM:R-pAl	0.66 - 1.53	0.20 - 0.98	0.067 - 0.316	4.85 - 11.7	7.5 - 49.4	0.007 - 0.061	0.020 - 0.028
T-pTM:R-pAl	1.54 - 4.70	0.27 - 1.29	0.073 - 0.337	7.12 - 18.2	36.6 – 143	0.028 - 0.113	0.020 - 0.028

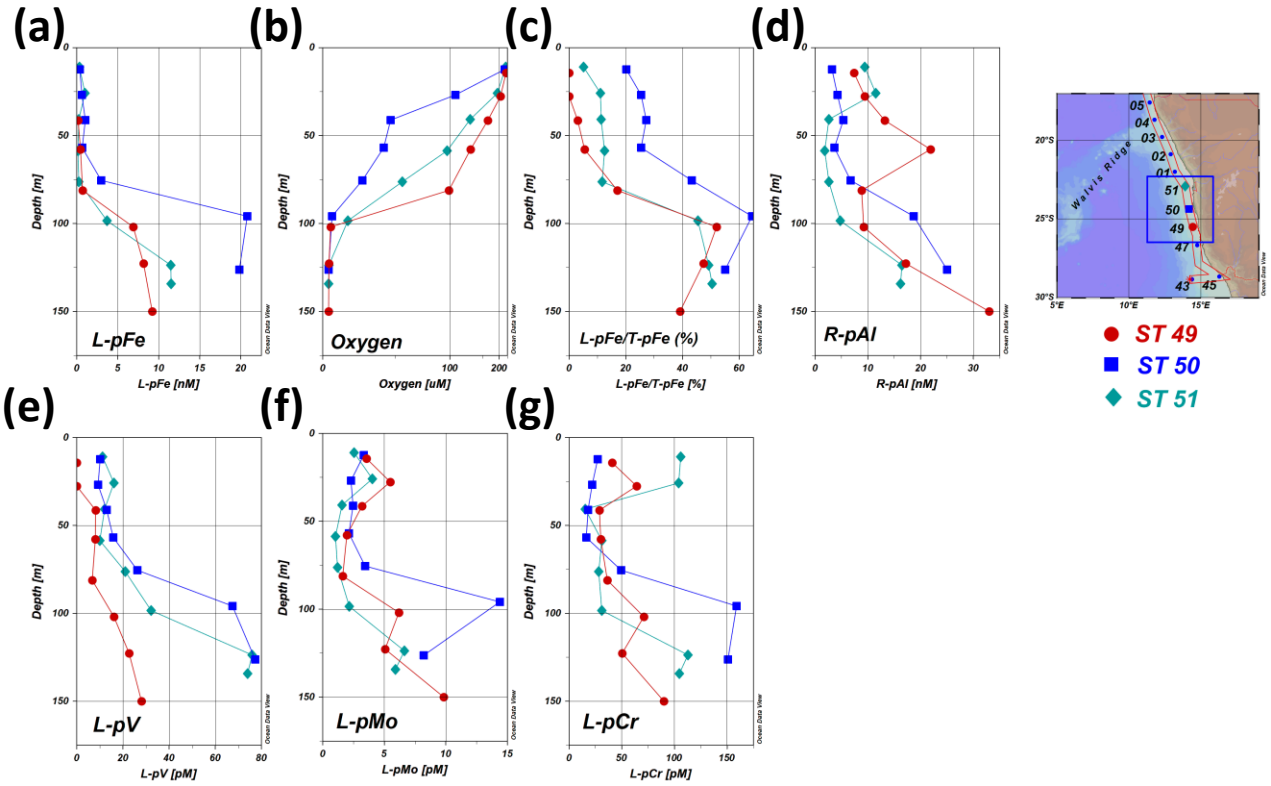

Figure S5.3 - Vertical concentration profiles of labile particulate V (L-pV), L-pMo and L-pCr (e, f, and g respectively) in Benguela shelf stations 49-51, where the lowest oxygen concentration was observed. Labile particulate Fe (L-pFe) (a) and refractory particulate Al (d) are shown as proxies for Fe oxides and lithogenic particles, respectively, as well as and oxygen concentrations (b) and L-pFe/total particulate Fe fractions (c). Note the stretched oxygen concentration (x-axis) scale on (b).

Chapter 6: Conclusions and Future Directions

The overarching goal of this PhD thesis research is to improve our understanding of the marine biogeochemical cycles of particulate trace metals, focusing on the distributions of 17 pTMs (Fe, Mn, Al, Ti, Co, Zn, Cd, Ni, Pb, Cu, V, Mo, Ba, W, Cr, U, and Th) and particulate phosphorus (pP) from the understudied regions of the Southwest African and Peruvian shelves. This was achieved while demonstrating the feasibility of producing high quality full ocean depth profiles of labile and refractory pTM (L-pTM and R-pTM, respectively) data with a relatively simple sequential leach and total digestion method. Different biogeochemical regimes and particle sources were encountered on the shelves of the Southwest African and Peru regions, and included the longest continental shelf transect focusing on TM distributions to date. The study regions provided unique insights into the critical mechanisms that govern trace metal distributions, availability, and solid-solution interactions in the water column. The key takeaways that were learned following the studies are summarized below, highlighting some of the similarities and differences between the regions, and some potential considerations for future work are also discussed.

The predominant carriers of particulate elements in surface waters of the Southwest African and Peruvian regions were biogenic particles with enhanced concentrations in the Benguela and Humboldt upwelling systems, driven by increased primary production (maximum pP concentrations of 253 nM and 380 nM, respectively). The elemental stoichiometries of bio-essential T-pTMs (Zn, Cu, Ni, Cd, Co, and V) relative T-pP (T-pTMs:T-pP) were mostly consistent with phytoplankton biomass across both regions. The T-pTMs were mostly labile (>50% L-pTM/T-pTM) in samples with low lithogenic material (<25 nM R-pAl) and hence likely to be recycled on short time timescales. The mean and upper and lower quartile L-pP/T-pP fractions were much lower in the Southwest African region (49.7±24.3% and 23.5-49.2%, respectively) compared to the Peruvian region (76.1±8.7% and 72.2-79.7%, respectively), despite the higher surface mean pP concentrations in the Peruvian region (91.0±72.6 nM compared to 29.0±51.4 nM T-pP). As a result, the remineralization time scales are more likely to be longer and greater fractions of biogenic pP reach the bottom of the productive Southwest African shelf compared to the

Peruvian shelf, at least during our cruises. The difference in the biogenic phosphorus lability was attributed to the likely differing lability of phytoplankton taxa comprising the bulk biomass between the regions. Particulate U and Mo were closely associated with biogenic particles in the productive Benguela upwelling region of Southwest African shelf, particularly in the refractory fractions, also implying the transfer of substantial fractions of R-pU and R-pMo to underlying sediments of the productive margin. This observation has implications for paleo-oceanographic interpretations of sediment composition when studying paleo-productivity and paleo-redox cycles using pU and pMo. Only a minor association of L-pW with biogenic material (i.e., L-pP) was apparent in surface waters. Enhanced concentrations of bio-essential L-pTMs which persisted at or below the surface were attributed to the inclusion of higher proportions of scavenged phases, and were most apparent within the Congo River plume, or to longer remineralization length scales within the oxygen minimum zones (OMZs). Occasionally, lithogenic particle concentrations were also high in surface waters (>25 nM R-pAl; *n*=30 of 102) of both regions, particularly at shallow coastal stations and were attributed mainly to resuspended benthic nepheloid particles, which also further enhanced the scavenging of TMs.

Though Fe and Mn are bio-essential (e.g., Morel & Price, 2003; Twining & Baines, 2013), their labile particulate pools in surface waters often comprised substantial proportions of abiogenic particle phases largely including Fe and Mn oxides, and adsorbed phases, as pFe:pP and pMn:pP ratios were often in far in excess of intracellular phytoplankton quotas. The only exceptions occurred in the offshore surface waters of the Peruvian shelf where pFe and pMn ratios (normalized to pP) were consistent with phytoplankton biomass. Labile pFe and pMn concentrations were enhanced in the surface waters of the Congo River plume, although only at coastal stations, with L-pMn persisting in the surface layer further offshore. This suggested a distinct stabilization mechanism for particulate Mn, possibly via reversible adsorption involving biogenic particles, as Mn oxides are typically low in surface waters due to their photo-reductive dissolution (Sunda & Huntsman, 1988, 1994). Particulate Mn was mostly labile in surface waters (>90% L-pMn/T-pMn) and decreased (to <60% L-pMn/T-pMn) where lithogenic particle concentrations were exceptionally high, or within low oxygen waters (<20 µM oxygen). The low L-pMn concentrations and labile particulate fractions within the OMZs of both regions (<360 pM

and <100 pM L-pMn in Benguela and Peruvian OMZs, respectively) were attributed to the reducing environments of the OMZs which retarded Mn oxide precipitation. The low abundance of Mn oxides within the OMZs may thus permit typically (co-)precipitated pTMs, such as Co, from being removed from solution, allowing OMZs to serve as conduits for TM transfer from continental shelves to the open ocean. This mechanism is supported by observations of elevated dCo within the OMZ further offshore in the South Atlantic (e.g., Noble et al., 2012, 2017).

Particulate Fe was generally less labile compared to other bio-essential pTMs, due to a relatively higher proportion of refractory Fe in lithogenic particles compared to other bio-essential TMs (e.g., Rudnick & Gao, 2013). On the productive Benguela shelf, the combination of a large reactive pool of Fe and nearby sulfidic sources (Böning et al., 2020; Borchers et al., 2005; Inthorn et al., 2006) may have permitted the formation of refractory Fe sulfides which were subsequently sequestrated into the underlying sediment, thus driving the enhanced R-pFe abundance distinctly observed over the Benguela shelf. Similar pFe enrichment was not apparent over the Peruvian shelf (0.215 mol:mol R-pFe:R-pAl; 9.55 mol:mol R-pFe:R-pTi), which were instead consistent with canonical upper continental crust values (0.199-0.269 mol:mol Fe:Al and 6.97-11.1 mol:mol Fe:Ti; (Rudnick & Gao, 2013). L-pFe concentrations were frequently elevated in (near-) bottom waters of both regions and often in conjunction with elevated dFe, particularly where resuspended benthic particles were abundant. Enhanced concentrations also extended to areas with relatively low nepheloid particle abundance, such as the (near-) bottom waters of the Benguela shelf (up to 39.6 nM and 65%, respectively), suggesting the presence of high proportions of (nano-)particulate Fe oxides in both dissolved and particulate phases. The close coupling of L-pFe and dFe distributions that were widely apparent throughout the different biogeochemical regimes in both regions inferred a buffering effect between the particulate and dissolved Fe pools, as similarly described in the North Atlantic (Achterberg et al., 2018, 2021; Milne et al., 2017). This reinforces that the pFe pool is an important component for the available Fe pool in the water column, and that similar buffering mechanisms may also be an important component to the distributions of other TMs. Furthermore, it also signifies that the reactive pTM fraction should be properly incorporated into biogeochemical models to account for available

TM inventories and to predict the fate TMs more accurately, which may be challenging at present due to the limited availability of such datasets.

The frequent association of L-pV with L-pFe throughout both regions implied that V had a strong propensity to adsorb onto Fe oxides or other common particle surfaces as Fe, in line with previous reports from the Peruvian margin (Scholz et al., 2011) and in the Western Arctic (Whitmore et al., 2019). Particulate Pb was mostly labile (>70% L-pPb/T-pPb) throughout both regions and primarily attributed to adsorbed phases. No preferential affinities to specific particle substrates were apparent, as L-pPb was generally enhanced in particle rich environments of different types such as nepheloid layers, productive upwelling regions, and where a high abundance of Fe or Mn oxides were presumed. The close connection of L-pMo and L-pCr to L-pFe in the Benguela OMZ was attributed to adsorption onto Fe oxide particles, supporting similar associations that were proposed in the Pacific OMZ (Ho et al., 2018; Scholz et al., 2011). As a result, the biogeochemical cycling and fate of Fe oxides within the OMZs have direct implications for the cycling and co-transport of other associated TMs, which may be carried alongside sinking Fe oxides particles out of the OMZ and deposited into the underlying sediment, or laterally advected off the shelf and into the open ocean within via nano-particulate suspended particles or colloidal Fe oxides.

Labile pAl/T-pAl fractions were reasonably consistent across both regions, and normally less than 20%, but were markedly enhanced within the Congo River plume (up to 77.5% L-pAl/T-pAl and 21.6nM L-pAl), indicating greater adsorption onto riverine particles. Although this feature may also be a result of the Congo River's exceptionally high supply of dissolved Al (up to 784 nM dAl in plume waters) promoting enhanced adsorption onto particles.

Particulate Barium concentrations were primarily enhanced in mesopelagic waters and largely associated with barite, although higher refractory pBa fractions were observed at the shallow shelf stations compared to deep open ocean stations (51.3±16.5% compared to 29.4±11.9%), despite similar concentrations of T-pBa (203±97.8 nM and 116±72.8 nM T-pBa, respectively). This observation may be attributable to differing barite minerology but this could not be resolved in my study. Nonetheless, higher fractions of R-pBa are likely to be incorporated

into the sediment further off the Angola margin compared to the shelf, which paleo-oceanographers who aim to use pBa as a paleo proxy in ocean sediment should consider.

Particulate Ti, W, and Th predominantly comprised of refractory phases (>90% R-pTM/T-pTM) and associated with lithogenic material across all biogeochemical settings studied. This highlights the potential utility for their stoichiometric abundance ratio compositions to be used to help discern between the contributions of different lithogenic sources (i.e., terrestrial, atmospheric, or benthic resuspension). However, this is predicated on sufficiently identifying end member source composition.

6.1 Suggestions for Future Work

This research emphasized the importance of studying both labile and refractory pTM fractions to gain a comprehensive understanding of their cycling in the water column. The sequential leach and total digestion method has proven to be a valuable tool in this regard, although there is still room for optimization of this technique to allow more accurate comparisons between different ocean basins and seasons in future studies, and to account for the chemical lability of major phytoplankton taxa. The research presented in chapter 4 builds a case for more thoroughly studying phytoplankton lability in dedicated future studies, ideally while utilizing the same leach and digestion approach. The Berger leach (Berger et al., 2008), which is adopted in the work of this dissertation, is perhaps the most suitable as it is recommended in the GEOTRACES sampling and sample-handling protocols (i.e., the GEOTRACES 'Cookbook'; Cutter et al., 2017)) and is currently adopted by various research groups (e.g. Lippiatt et al., 2010; Little et al., 2018; Milne et al., 2017; Twining et al., 2015, 2019). However, an intercomparison study of the Berger leach by different independent laboratories using the same leach procedure is yet to be published. This may be achieved by comparing the leach consistency across different digestion batches and between laboratories by applying the leach to a standard sample, such as BCR-414 (Quevauviller et al., 1993), a plankton certified reference material which has already been the *de facto* reference material used in most labs applying the Berger leach. The availability of such a study, if indeed shown to be consistent, would provide a more unified characterization of labile particulate fractions and allow for a reliable extension of TM

biogeochemical cycling interpretations and insights to other biogeochemical settings and regions of the global ocean.

Furthermore, separate studies on the lability of TMs in specific phytoplankton taxa groups will also aid in accounting for changes in bulk plankton community composition that occur seasonally or are induced by climate change (such as ocean acidification or rising surface seawater temperatures) or anthropogenic perturbations. Hence, the integration of these activities alongside expeditions and research efforts part of the developing BioGeoSCAPES program (built upon the model of the GEOTRACES program) would be a sensible strategy to maximize the efficiency of outcomes.

In addition to leaching particulate samples, future research should also include expanding the scope of investigation to other regions of the global ocean, and incorporate other analytical parameters, such as major particle phase composition, isotopic fractionation, and particle size fractionation to fill the knowledge gaps of trace metal dynamics in the marine environment. The lack of particle morphology data in the work of this thesis limited the ability to qualitatively assess the affinities for TMs to adsorb onto specific particle substrates, relying on particle type proxies rather than direct measurements of key major particle phases such as $CaCO_3$, biogenic silica, and particulate organic carbon. Inclusion of major particle phase analysis would help unravel the preferential affinities associated between TMs with different particles, as well as help identify particle sources, and characterize the processes of carbon export, remineralization, and sequestration in the deep ocean (e.g., Lam et al., 2011; McDonnell et al., 2015).

Isotope fractionation patterns of elements such as Fe (e.g., Hunt et al., 2022; Marsay et al., 2018), Cu (e.g., Little et al., 2018; Packman et al., 2022), Cd (e.g., Xie et al., 2019), Ba (e.g., Cao et al., 2020) have been demonstrated to provide insights into the sources, sinks, and transformation processes involved in trace metal cycling. Separating the small and large size fractions (e.g., 0.2-51 µm and >51 µm, respectively; e.g., Lam et al., 2015; Lee et al., 2018; Xiang & Lam, 2020) of marine particles allows for distinguishing between sinking and suspended particulate pools, helping account for the extent of vertical sinking or lateral transport of pTM pools through the water column. Ideally, dissolved TM samples, which are collected in conjunction with marine particles, should also be size fractionated to separate 'truly' soluble

(<0.02 µm) and colloidal size fractions (0.02-0.2 µm) if possible (e.g., Birchill et al., 2017), to account for (dis-)aggregation and transformation dynamics between solid-solution phases. The collection of sediment and porewater samples underlying each station where the full water column is sampled will allow a more direct approach for connecting the water column with benthic TM cycling (e.g., Plass et al., 2021). Furthermore, coupling these analyses with advanced imaging techniques, such as scanning electron microscopy and synchrotron-based techniques (e.g., Synchrotron X-ray fluorescence [SXRF] microscopy or X-ray Absorption Near-Edge Structure [XANES]; Lam, Twining, et al., 2015; Twining et al., 2015), can reveal the microscale distribution of trace metals within particles, shedding light on the underlying mechanisms controlling their speciation and behavior.

Given the significant resources required to carry out the additional sampling and analytical operations suggested, these efforts should focus on samples from dynamic ocean regions. The anticipated expansion of OMZs (Schmidtko et al., 2017; Stramma et al., 2008) emphasizes the importance of focusing attention on OMZ systems; however, other dynamic environments such as continental shelves, upwelling zones, and near river discharge and hydrothermal vent systems will also provide vital insights that are still needed. Laboratories that are limited in their abilities to analyze any of the above parameters may explore collaborations with other research groups with established practices to enhance results. Ultimately, a multidisciplinary approach integrating several analytical techniques will allow for a better understanding of the intricate biogeochemical interactions which govern TM distributions in the ocean.

The findings contributed by this dissertation are an incremental step towards understanding the marine biogeochemical mechanisms that control the TM inventories in the global ocean. The far-reaching implications for the findings contributed by this dissertation, as well as any further advancements gained in the future, are that they ultimately help build a robust knowledge base to help direct policymakers to more confidently support effective environmental policies to mitigate and counter negative impacts of climate change and other anthropogenic perturbations occurring in the environment.

References

Achterberg, E. P., Steigenberger, S., Klar, J. K., Browning, T. J., Marsay, C. M., Painter, S. C., Vieira, L. H., Baker, A. R., Hamilton, D. S., Tanhua, T., & Moore, C. M. (2021). Trace Element Biogeochemistry in the High-Latitude North Atlantic Ocean: Seasonal Variations and Volcanic Inputs. *Global Biogeochemical Cycles*, *35*(3). https://doi.org/10.1029/2020GB006674

Achterberg, E. P., Steigenberger, S., Marsay, C. M., Lemoigne, F. A. C., Painter, S. C., Baker, A. R., Connelly, D. P., Moore, C. M., Tagliabue, A., & Tanhua, T. (2018). Iron Biogeochemistry in the High Latitude North Atlantic Ocean. *Scientific Reports*, *8*(1). https://doi.org/10.1038/s41598-018-19472-1

Berger, C. J. M., Lippiatt, S. M., Lawrence, M. G., & Bruland, K. W. (2008). Application of a chemical leach technique for estimating labile particulate aluminum, iron, and manganese in the Columbia River plume and coastal waters off Oregon and Washington. *Journal of Geophysical Research*, *113*, 1–16. https://doi.org/10.1029/2007JC004703

Birchill, A. J., Milne, A., Woodward, E. M. S., Harris, C., Annett, A. L., Rusiecka, D., Achterberg, E. P., Gledhill, M., Ussher, S. J., Worsfold, P. J., Geibert, W., & Lohan, M. C. (2017). Seasonal iron depletion in temperate shelf seas. *Geophysical Research Letters*, *44*(17), 8987–8996. https://doi.org/10.1002/2017GL073881

Böning, P., Schnetger, B., Belz, L., Ferdelman, T. G., Brumsack, H. J., & Pahnke, K. (2020). Sedimentary iron cycling in the Benguela upwelling system off Namibia. *Earth and Planetary Science Letters*, *538*, 116212. https://doi.org/10.1016/j.epsl.2020.116212

Borchers, S. L., Schnetger, B., Böning, P., & Brumsack, H. J. (2005). Geochemical signatures of the Namibian diatom belt: Perennial upwelling and intermittent anoxia. *Geochemistry, Geophysics, Geosystems*, *6*(6). https://doi.org/10.1029/2004GC000886

Cao, Z., Li, Y., Rao, X., Yu, Y., Hathorne, E. C., Siebert, C., Dai, M., & Frank, M. (2020). Constraining barium isotope fractionation in the upper water column of the South China Sea. *Geochimica et Cosmochimica Acta*, *288*, 120–137. https://doi.org/10.1016/j.gca.2020.08.008

Cutter, G. A., Casciotti, K., Croot, P. L., Geibert, W., Heimbürger, L.-E., Lohan, M. C., Planquette, H., & van de Flierdt, T. (2017). Sampling and Sample-handling Protocols for GEOTRACES Cruises. Version 3, August 2017. *GEOTRACES Community Practices*, *August*, 139pp. & Appendices. http://www.geotraces.org/images/stories/documents/intercalibration/Cookbook.pdf

Ho, P., Lee, J. M., Heller, M. I., Lam, P. J., & Shiller, A. M. (2018). The distribution of dissolved and particulate Mo and V along the U.S. GEOTRACES East Pacific Zonal Transect (GP16): The roles of oxides and biogenic particles in their distributions in the oxygen deficient

zone and the hydrothermal plume. *Marine Chemistry*, *201*(October), 242–255. https://doi.org/10.1016/j.marchem.2017.12.003

Hunt, H. R., Summers, B. A., Sieber, M., Krisch, S., Al-Hashem, A., Hopwood, M. J., Achterberg, E. P., & Conway, T. M. (2022). Distinguishing the influence of sediments, the Congo River, and water-mass mixing on the distribution of iron and its isotopes in the Southeast Atlantic Ocean. *Marine Chemistry*, 104181. https://doi.org/10.1016/J.MARCHEM.2022.104181

Inthorn, M., Mohrholz, V., & Zabel, M. (2006). Nepheloid layer distribution in the Benguela upwelling area offshore Namibia. *Deep-Sea Research Part I: Oceanographic Research Papers*, *53*(8), 1423–1438. https://doi.org/10.1016/j.dsr.2006.06.004

Lam, P. J., Doney, S. C., & Bishop, J. K. B. (2011). The dynamic ocean biological pump: Insights from a global compilation of particulate organic carbon, CaCO 3, and opal concentration profiles from the mesopelagic. *Global Biogeochemical Cycles*, *25*(3). https://doi.org/10.1029/2010GB003868

Lam, P. J., Ohnemus, D. C., & Auro, M. E. (2015). Size-fractionated major particle composition and concentrations from the US GEOTRACES North Atlantic Zonal Transect. *Deep-Sea Research Part II: Topical Studies in Oceanography*, *116*, 303–320. https://doi.org/10.1016/j.dsr2.2014.11.020

Lam, P. J., Twining, B. S., Jeandel, C., Roychoudhury, A., Resing, J. A., Santschi, P. H., & Anderson, R. F. (2015). Methods for analyzing the concentration and speciation of major and trace elements in marine particles. *Progress in Oceanography*, *133*, 32–42. https://doi.org/10.1016/j.pocean.2015.01.005

Lee, J. M., Heller, M. I., & Lam, P. J. (2018). Size distribution of particulate trace elements in the U.S. GEOTRACES Eastern Pacific Zonal Transect (GP16). *Marine Chemistry*, *201*, 108–123. https://doi.org/10.1016/j.marchem.2017.09.006

Lippiatt, S. M., Lohan, M. C., & Bruland, K. W. (2010). The distribution of reactive iron in northern Gulf of Alaska coastal waters. *Marine Chemistry*, *121*(1–4), 187–199. https://doi.org/10.1016/j.marchem.2010.04.007

Little, S. H., Archer, C., Milne, A., Schlosser, C., Achterberg, E. P., Lohan, M. C., & Vance, D. (2018). Paired dissolved and particulate phase Cu isotope distributions in the South Atlantic. *Chemical Geology*, *502*(June), 29–43. https://doi.org/10.1016/j.chemgeo.2018.07.022

Marsay, C. M., Lam, P. J., Heller, M. I., Lee, J. M., & John, S. G. (2018). Distribution and isotopic signature of ligand-leachable particulate iron along the GEOTRACES GP16 East Pacific Zonal Transect. *Marine Chemistry*, *201*, 198–211. https://doi.org/10.1016/j.marchem.2017.07.003

McDonnell, A. M. P., Lam, P. J., Lamborg, C. H., Buesseler, K. O., Sanders, R., Riley, J. S., Marsay, C. M., Smith, H. E. K., Sargent, E. C., Lampitt, R. S., & Bishop, J. K. B. (2015). The oceanographic toolbox for the collection of sinking and suspended marine particles. *Progress in Oceanography*, *133*, 17–31. https://doi.org/10.1016/j.pocean.2015.01.007

Milne, A., Schlosser, C., Wake, B. D., Achterberg, E. P., Chance, R., Baker, A. R., Forryan, A., & Lohan, M. C. (2017). Particulate phases are key in controlling dissolved iron concentrations in the (sub)tropical North Atlantic: Particulate Phases Control dFe. *Geophysical Research Letters*. https://doi.org/10.1002/2016GL072314

Morel, F. M. M., & Price, N. M. (2003). The biogeochemical cycles of trace metals in the oceans. *Science*, *300*(5621), 944–947. https://doi.org/10.1126/science.1083545

Noble, A. E., Lamborg, C. H., Ohnemus, D. C., Lam, P. J., Goepfert, T. J., Measures, C. I., Frame, C. H., Casciotti, K. L., DiTullio, G. R., Jennings, J., & Saito, M. A. (2012). Basin-scale inputs of cobalt, iron, and manganese from the Benguela-Angola front to the South Atlantic Ocean. *Limnology and Oceanography*, *57*(4), 989–1010. https://doi.org/10.4319/lo.2012.57.4.0989

Noble, A. E., Ohnemus, D. C., Hawco, N. J., Lam, P. J., & Saito, M. A. (2017). Coastal sources, sinks and strong organic complexation of dissolved cobalt within the US North Atlantic GEOTRACES transect GA03. *Biogeosciences*, *14*(11), 2715–2739. https://doi.org/10.5194/bg-14-2715-2017

Packman, H., Little, S. H., Baker, A. R., Bridgestock, L., Chance, R. J., Coles, B. J., Kreissig, K., Rehkämper, M., & van de Flierdt, T. (2022). Tracing natural and anthropogenic sources of aerosols to the Atlantic Ocean using Zn and Cu isotopes. *Chemical Geology*, 121091. https://doi.org/10.1016/J.CHEMGEO.2022.121091

Plass, A., Dale, A. W., & Scholz, F. (2021). Sedimentary cycling and benthic fluxes of manganese, cobalt, nickel, copper, zinc and cadmium in the Peruvian oxygen minimum zone. *Marine Chemistry*, *233*, 103982. https://doi.org/10.1016/J.MARCHEM.2021.103982

Quevauviller, P., Vercoutere, K., Muntau, H., & Griepink, B. (1993). Certified reference material (CRM 414) for the quality control of trace element analysis in plankton. *Fresenius' Journal of Analytical Chemistry*, *345*(1), 12–17. https://doi.org/10.1007/BF00323319

Rudnick, R. L., & Gao, S. (2013). Composition of the Continental Crust. In *Treatise on Geochemistry: Second Edition* (2nd ed., Vol. 4, Issue November). Elsevier Ltd. https://doi.org/10.1016/B978-0-08-095975-7.00301-6

Schmidtko, S., Stramma, L., & Visbeck, M. (2017). Decline in global oceanic oxygen content during the past five decades. *Nature*, *542*(7641), 335–339. https://doi.org/10.1038/nature21399

Scholz, F., Hensen, C., Noffke, A., Rohde, A., Liebetrau, V., & Wallmann, K. (2011). Early diagenesis of redox-sensitive trace metals in the Peru upwelling area - response to ENSO-related oxygen fluctuations in the water column. *Geochimica et Cosmochimica Acta*, *75*(22), 7257–7276. https://doi.org/10.1016/j.gca.2011.08.007

Stramma, L., Johnson, G. C., Sprintall, J., & Mohrholz, V. (2008). Expanding Oxygen-Minimum Zones in the Tropical Oceans. *Science*, *320*(5876), 655–658. https://doi.org/10.1126/SCIENCE.1153847

Sunda, W. G., & Huntsman, S. A. (1988). Effect of sunlight on redox cycles of manganese in the southwestern Sargasso Sea. *Deep Sea Research Part A, Oceanographic Research Papers*, *35*(8), 1297–1317. https://doi.org/10.1016/0198-0149(88)90084-2

Sunda, W. G., & Huntsman, S. A. (1994). Photoreduction of manganese oxides in seawater. *Marine Chemistry*, *46*(1–2), 133–152. https://doi.org/10.1016/0304-4203(94)90051-5

Twining, B. S., & Baines, S. B. (2013). The Trace Metal Composition of Marine Phytoplankton. *Annu. Rev. Mar. Sci*, *5*, 191–215. https://doi.org/10.1146/annurev-marine-121211-172322

Twining, B. S., Rauschenberg, S., Baer, S. E., Lomas, M. W., Martiny, A. C., & Antipova, O. (2019). A nutrient limitation mosaic in the eastern tropical Indian Ocean. *Deep-Sea Research Part II: Topical Studies in Oceanography*, *166*(November 2018), 0–1. https://doi.org/10.1016/j.dsr2.2019.05.001

Twining, B. S., Rauschenberg, S., Morton, P. L., & Vogt, S. (2015). Metal contents of phytoplankton and labile particulate material in the North Atlantic Ocean. *Progress in Oceanography*, *137*, 261–283. https://doi.org/10.1016/j.pocean.2015.07.001

Whitmore, L. M., Morton, P. L., Twining, B. S., & Shiller, A. M. (2019). Vanadium cycling in the Western Arctic Ocean is influenced by shelf-basin connectivity. *Marine Chemistry*, *216*, 103701. https://doi.org/10.1016/J.MARCHEM.2019.103701

Xiang, Y., & Lam, P. J. (2020). Size-Fractionated Compositions of Marine Suspended Particles in the Western Arctic Ocean: Lateral and Vertical Sources. *Journal of Geophysical Research: Oceans*, *125*(8), 1–33. https://doi.org/10.1029/2020JC016144

Xie, R. C., Rehkämper, M., Grasse, P., van de Flierdt, T., Frank, M., & Xue, Z. (2019). Isotopic evidence for complex biogeochemical cycling of Cd in the eastern tropical South Pacific. *Earth and Planetary Science Letters*, *512*, 134–146. https://doi.org/10.1016/J.EPSL.2019.02.001

Statement of declaration

I, Ali Abdulhameed Al-Hashem, hereby declare that the work present in this PhD thesis titled "The Biogeochemical Cycling of Particulate Trace Metals off the Southwest African and Peruvian Shelves" is entirely my own, independently conducted and written, apart from the guidance of my supervisors. This work was conducted under compliance of the Rules of Good Scientific Practice of the German Research Foundation. All resources that were utilized during the research and writing of this thesis are explicitly acknowledged and referenced. Moreover, I affirm that no part of this PhD thesis has been submitted for the conferral of a degree elsewhere. Manuscripts that were published or submitted for publication are identified at the relevant places. Lastly, I have never had an academic degree withdrawn due to any violation of academic ethics or any other reason.

(Ali A. Al-Hashem) Kiel, 19.06.2023